

# **Finite-Element Simulations of Earthquakes**

Thesis by

**Brad Thomas Aagaard**

In Partial Fulfillment of the Requirements

for the Degree of

Doctor of Philosophy



California Institute of Technology

Pasadena, California

2000

(Submitted October 13, 1999)

© 2000  
Brad Thomas Aagaard  
All Rights Reserved

## Acknowledgements

When I arrived at Caltech, I had little idea which area of earthquake engineering would pique my interest. I would like to thank my advisor, John Hall, for his excellent guidance in helping me settle upon simulations of seismic ground motions as a research topic. I am grateful for the freedom he has given me to explore this area and his indispensable expertise in numerical modeling. I would also like to thank Tom Heaton for his insightful comments and suggestions along the way, which have greatly improved my knowledge of seismology. I would also like to acknowledge my family for their interest in my research, their helpful advice, and most of all, their constant support. In particular, my father provided invaluable advice and instilled in me from an early age the importance and satisfaction of striving to do my very best.

## Abstract

This thesis discusses simulations of earthquake ground motions using prescribed ruptures and dynamic failure. Introducing sliding degrees of freedom led to an innovative technique for numerical modeling of earthquake sources. This technique allows efficient implementation of both prescribed ruptures and dynamic failure on an arbitrarily oriented fault surface. Off the fault surface the solution of the three-dimensional, dynamic elasticity equation uses well known finite-element techniques. We employ parallel processing to efficiently compute the ground motions in domains containing millions of degrees of freedom.

Using prescribed ruptures we study the sensitivity of long-period near-source ground motions to five earthquake source parameters for hypothetical events on a strike-slip fault ( $M_W$  7.0–7.1) and a thrust fault ( $M_W$  6.6–7.0). The directivity of the ruptures creates large displacement and velocity pulses in the ground motions in the forward direction. We found a good match between the severity of the shaking and the shape of the near-source factor from the 1997 Uniform Building Code for strike-slip faults and thrust faults with surface rupture. However, for blind thrust faults the peak displacement and velocities occur up-dip from the region with the peak near-source factor. We assert that a simple modification to the formulation of the near-source factor improves the match between the severity of the ground motion and the shape of the near-source factor.

For simulations with dynamic failure on a strike-slip fault or a thrust fault, we examine what constraints must be imposed on the coefficient of friction to produce realistic ruptures under the application of reasonable shear and normal stress distributions with depth. We found that variation of the coefficient of friction with the shear modulus and the depth produces realistic rupture behavior in both homogeneous and layered half-spaces. Furthermore, we observed a dependence of the rupture speed on the direction of propagation and fluctuations in the rupture speed and slip rate as the rupture encountered changes in the stress field. Including such behavior in prescribed ruptures would yield more realistic ground motions.

# Contents

<b>Acknowledgements</b>	<b>iii</b>
<b>Abstract</b>	<b>iv</b>
<b>Notation</b>	<b>xvii</b>
<b>1 Introduction</b>	<b>1</b>
1.1 Background . . . . .	1
1.2 Organization . . . . .	5
<b>2 General Methodology</b>	<b>6</b>
2.1 Governing Equations . . . . .	6
2.2 Integration of Differential Equation . . . . .	6
2.2.1 Boundary Conditions . . . . .	7
2.3 Discretization . . . . .	8
2.3.1 Mass Matrix . . . . .	10
2.3.2 Stiffness Matrix . . . . .	10
2.3.3 Damping Matrix . . . . .	11
2.4 Model of Fault . . . . .	15
2.4.1 Slip Degrees of Freedom . . . . .	15
2.4.2 Modification to Element Matrices . . . . .	18
2.4.3 Average Slip and Moment Magnitude . . . . .	20
2.5 Spatial Interpolation . . . . .	21
2.6 Finite-Element Mesh Creation . . . . .	24
<b>3 Implementation of Parallel Processing</b>	<b>26</b>
3.1 The Center for Advanced Computing Research Supercomputers . . . . .	26
3.2 Domain Partitioning among Processors . . . . .	26
3.3 Parallel Computation . . . . .	28
3.4 Parallel Input and Output . . . . .	29
3.5 Global Mesh Refinement . . . . .	30
3.5.1 Element Splitting . . . . .	30

<b>4 Dynamic Energy Balance for Earthquakes</b>	<b>33</b>
4.1 Derivation of Dynamic Energy Balance . . . . .	33
4.2 Radiated Energy . . . . .	33
4.3 Change in Thermal Energy . . . . .	34
4.3.1 Change in Temperature on the Fault . . . . .	35
4.4 Change in Potential Energy . . . . .	35
4.4.1 Topography and Changes in Gravitational Potential Energy . . . . .	37
<b>5 Prescribed Rupture</b>	<b>39</b>
5.1 Earthquake Source . . . . .	39
5.2 Slip Time History . . . . .	39
5.3 Slip Distribution . . . . .	41
5.4 Rupture Speed . . . . .	43
<b>6 Validation of Simulation Software</b>	<b>45</b>
6.1 Domain Geometry . . . . .	45
6.2 Validation of Ground Motion Time Histories . . . . .	46
6.3 Validation of Static Displacements . . . . .	46
6.4 Discussion . . . . .	48
<b>7 Sensitivity Study of Near-Source Ground Motion with Prescribed Ruptures</b>	<b>51</b>
7.1 Strike-Slip Fault . . . . .	51
7.1.1 Finite-Element Model . . . . .	51
7.1.2 Earthquake Source Parameters . . . . .	52
7.1.3 Simulation Results . . . . .	56
7.2 Thrust Fault . . . . .	75
7.2.1 Finite-Element Model . . . . .	75
7.2.2 Earthquake Source Parameters . . . . .	77
7.2.3 Simulation Results . . . . .	78
7.3 Discussion . . . . .	98
7.3.1 Ground Motion Characteristics . . . . .	98
7.3.2 Sensitivity of Ground Motions to Variations in Parameters . . . . .	98
7.3.3 Implications for Earthquake Engineering . . . . .	100
7.3.4 Geophysical Implications . . . . .	104
<b>8 Dynamic Failure</b>	<b>107</b>
8.1 Earthquake Source . . . . .	107
8.1.1 Governing Equations with Friction . . . . .	107

8.1.2	Forces on Slip Degrees of Freedom . . . . .	108
8.1.3	Initiation of Sliding . . . . .	109
8.1.4	Condition for Termination of Sliding . . . . .	110
8.1.5	Average Stress Drop . . . . .	110
8.2	Initial Traction on Fault . . . . .	111
8.2.1	Effective Normal Traction . . . . .	111
8.2.2	Shear Traction . . . . .	112
8.2.3	Effect of Gravity . . . . .	112
8.2.4	Spatial Distribution of Parameters for Dynamic Failure . . . . .	114
8.3	Overview of Rupture Dynamics . . . . .	114
8.3.1	Stress and Rupture Dynamics . . . . .	115
8.3.2	Energy and Rupture Dynamics . . . . .	116
8.4	Friction Models . . . . .	117
8.4.1	Constant . . . . .	118
8.4.2	Two-Phase . . . . .	118
8.4.3	Slip-Weakening I . . . . .	119
8.4.4	Slip-Weakening II . . . . .	119
8.4.5	Rate-Weakening I . . . . .	120
8.4.6	Rate-Weakening II . . . . .	120
8.4.7	Slip- and Rate-Weakening . . . . .	120
8.4.8	Shear Melting-Refreezing . . . . .	120
<b>9</b>	<b>Dynamic Failure in a Homogeneous Half-Space</b>	<b>123</b>
9.1	Finite-Element Models . . . . .	123
9.1.1	Strike-Slip Fault . . . . .	123
9.1.2	Thrust Fault . . . . .	124
9.2	General Features of Dynamic Rupture . . . . .	125
9.2.1	Base Case: Scenario ssbase . . . . .	125
9.2.2	Role of Fracture Energy . . . . .	129
9.2.3	Effect of Discretization Size . . . . .	129
9.3	Effective Normal Stresses . . . . .	131
9.3.1	Uniform Stresses with a Uniform Friction Model: Scenario ssbase . . . . .	131
9.3.2	Lithostatic Stresses with a Uniform Friction Model: Scenario sslithouni . . . . .	131
9.3.3	Lithostatic Stresses with a Variable Friction Model: Scenario sslithovar . . . . .	134
9.3.4	Lithostatic-Hydrostatic Stresses with a Variable Friction Model: Scenario sslithohydro	138
9.4	Thrust Fault . . . . .	139

9.4.1	Uniform Stresses with a Uniform Friction Model: Scenario thbase . . . . .	140
9.4.2	Lithostatic Stresses with a Variable Friction Model: Scenario tlithovar . . . . .	142
9.5	Rupture Behavior with Different Friction Models . . . . .	144
9.5.1	Slip- and Rate-Weakening Friction Model: Scenario sscombo . . . . .	144
9.5.2	Shear Melting-Refreezing Friction Model: Scenario ssmelt . . . . .	146
9.6	Effect of the Free Surface . . . . .	147
9.6.1	Slip Rate and Hypocenter Location . . . . .	147
9.6.2	Bifurcation of the Rupture on a Long Fault . . . . .	149
9.7	Discussion . . . . .	154
9.7.1	Modeling of Dynamic Failure . . . . .	154
9.7.2	Effective Normal Stresses . . . . .	154
9.7.3	Friction Models . . . . .	155
9.7.4	Effect of Free Surface . . . . .	155
<b>10</b>	<b>Dynamic Failure in a Layered Half-Space</b>	<b>157</b>
10.1	Strike-Slip Fault . . . . .	157
10.1.1	Earthquake Source Parameters . . . . .	158
10.1.2	Uniform Stress Versus Uniform Strain . . . . .	158
10.1.3	Variation of Friction Parameters with Material Properties . . . . .	164
10.1.4	Sensitivity Study . . . . .	172
10.1.5	Comparison with Prescribed Ruptures . . . . .	187
10.2	Thrust Fault . . . . .	191
10.2.1	Earthquake Source Parameters . . . . .	191
10.2.2	Sensitivity Study . . . . .	192
10.2.3	Comparison with Prescribed Ruptures . . . . .	219
10.3	Discussion . . . . .	224
10.3.1	Summary of Rupture Behavior and Ground Motions . . . . .	224
10.3.2	Sensitivity of Ground Motion to Variations in Parameters . . . . .	225
10.3.3	Dynamic Failure versus Prescribed Ruptures . . . . .	227
10.3.4	Implications for Earthquake Engineering . . . . .	229
10.3.5	Geophysical Implications . . . . .	230
<b>11</b>	<b>Conclusions and Future Work</b>	<b>234</b>
11.1	Conclusions . . . . .	234
11.2	Future Work . . . . .	236

## List of Figures

2.1	Tetrahedral finite-element. . . . .	9
2.2	Storage example for a 5x5 sparse, symmetric matrix. . . . .	12
2.3	Model of the fault plane in the finite-element mesh. . . . .	16
2.4	Fault geometry relative to the global coordinate axes. . . . .	17
2.5	Different topologies of the data set. . . . .	22
2.6	Interpolation schemes for the various topologies. . . . .	23
3.1	Example of partitioning of the mesh using inertial bisection. . . . .	28
3.2	Example of partitioning of the mesh using METIS library. . . . .	29
3.3	Diagram of element splitting in the 2x refinement procedure. . . . .	31
3.4	Diagram of element splitting in the 4x refinement procedure. . . . .	32
4.1	Configurations of the two fluid containers. . . . .	37
5.1	Slip and slip rate as a function of time for the three slip time history shapes. . . . .	40
5.2	Fast Fourier transforms of the three slip time history shapes. . . . .	41
5.3	Strike and dip coordinates used in the slip tapering function. . . . .	42
5.4	Cross-section of an asperity with height $D_a$ and radius $r_a$ . . . . .	42
5.5	Diagram of the quantities used to propagate the rupture front through an element. . . . .	44
6.1	Domain geometry used in the validation. . . . .	45
6.2	Velocity time histories at site A. . . . .	47
6.3	Velocity time histories at site B. . . . .	47
6.4	Velocity time histories at site C. . . . .	48
6.5	Velocity time histories at site D. . . . .	48
6.6	Static horizontal displacements along two lines on the ground surface. . . . .	49
6.7	Static vertical and north-south displacements along a line on the ground surface. . . . .	49
6.8	Static vertical and east-west displacements along a line on the ground surface. . . . .	50
7.1	Domain geometry for the strike-slip fault. . . . .	52
7.2	Material properties as a function of depth for the layered half-space. . . . .	53
7.3	Partitioning of the finite-element model among 256 processors. . . . .	53
7.4	Hypocenter locations on the fault plane. . . . .	54
7.5	Homogeneous slip distribution unitaper. . . . .	55

7.6	Homogeneous slip distribution semitaper. . . . .	56
7.7	Homogeneous slip distribution semitaper3. . . . .	56
7.8	Weakly heterogeneous slip distribution weakupper. . . . .	56
7.9	Weakly heterogeneous slip distribution weaklower. . . . .	57
7.10	Strong heterogeneous slip distribution strongerter. . . . .	57
7.11	Snapshots of slip rate on the fault surface for scenario baseII. . . . .	58
7.12	Snapshots of velocity on the ground surface for scenario baseII. . . . .	59
7.13	Maximum displacements and velocities on the ground surface for scenario baseII. . . . .	60
7.14	Displacement and velocity time histories at two sites for scenario baseII. . . . .	61
7.15	Acceleration response spectra at two sites for scenario baseII. . . . .	62
7.16	Displacement time histories at two sites for different material properties. . . . .	62
7.17	Maximum displacements and velocities on the ground surface for scenario vr90. . . . .	63
7.18	Velocity time histories at two sites for the three rupture speeds. . . . .	64
7.19	Maximum displacements and velocities along an east-west line for the three rupture speeds.	65
7.20	Velocity time histories at two sites for the three maximum slip rates. . . . .	66
7.21	Maximum displacements and velocities along an east-west line for the three maximum slip rates. . . . .	66
7.22	Maximum displacements and velocities on the ground surface for scenario hybq. . . . .	67
7.23	Displacement time histories at two sites for the four hypocenter locations. . . . .	68
7.24	Maximum displacements and velocities along an east-west line for the four hypocenter locations. . . . .	69
7.25	Maximum displacements and velocities on the ground surface for scenario sliphet. . . . .	70
7.26	Maximum displacements and velocities along an east-west line for the five slip distributions. . . . .	71
7.27	Displacement time histories at two sites for the five slip distributions. . . . .	71
7.28	Displacement time histories at two sites for the two values of average slip. . . . .	72
7.29	Maximum displacements and velocities along an east-west line for the two values of average slip. . . . .	73
7.30	Displacement time histories at two sites for the three fault depths. . . . .	74
7.31	Domain geometry for the thrust fault. . . . .	75
7.32	Material properties as a function of depth for the layered half-space. . . . .	76
7.33	Partitioning of the finite-element model among 256 processors. . . . .	76
7.34	Hypocenter locations on the fault plane. . . . .	78
7.35	Homogeneous slip distribution unitaper. . . . .	79
7.36	Homogeneous slip distribution unitaper2. . . . .	79
7.37	Weakly heterogeneous slip distribution weakupper. . . . .	80
7.38	Weakly heterogeneous slip distribution weaklower. . . . .	80

7.39	Snapshots of velocity on a vertical slice for scenario base. . . . .	81
7.40	Snapshots of velocity on the ground surface for scenario base. . . . .	82
7.41	Maximum displacements on the ground surface for scenario base. . . . .	82
7.42	Maximum velocities on the ground surface for scenario base. . . . .	83
7.43	Displacement and velocity time histories at two sites for scenario base. . . . .	84
7.44	Acceleration response spectra at two sites for scenario base. . . . .	84
7.45	Velocity time histories at two sites for different material properties. . . . .	85
7.46	Velocity time histories at two sites for the three rupture speeds. . . . .	86
7.47	Maximum displacements and vectors along a north-south line for the three rupture speeds. .	87
7.48	Velocity time histories at two sites for the three maximum slip rates. . . . .	87
7.49	Maximum displacements and velocities along a north-south line for the three maximum slip rates. . . . .	88
7.50	Maximum velocities on the ground surface for scenario hyme. . . . .	89
7.51	Displacement time histories at two sites for the four hypocenter locations. . . . .	90
7.52	Maximum displacements and velocities along a north-south line for the four hypocenter locations. . . . .	91
7.53	Maximum velocities on the ground surface for scenario sliptop. . . . .	91
7.54	Displacement time histories at two sites for the three slip distributions. . . . .	92
7.55	Maximum displacements and velocities along a north-south line for the three slip distributions. .	93
7.56	Displacement time histories at two sites for the two values of average slip. . . . .	94
7.57	Maximum displacements and velocities along a north-south line for the two values of average slip. . . . .	94
7.58	Maximum velocities on the ground surface for scenario fault4km. . . . .	95
7.59	Velocity time histories at two sites for the three fault depths. . . . .	96
7.60	Maximum displacements and velocities along a north-south line for the three fault depths. .	97
7.61	Areas where the maximum displacements and velocities exceed a given value. . . . .	101
7.62	Modified version of the 1997 UBC near-source factor. . . . .	104
7.63	Maximum displacements and velocities along a north-south line for the three fault depths. .	105
7.64	Radiated energy as a function of moment magnitude. . . . .	106
8.1	Analogy between a thrust fault and an incline plane. . . . .	112
8.2	Pushing a block up an incline plane with and without gravity. . . . .	113
8.3	Control points that define the variation of the mass density with depth. . . . .	115
8.4	Diagrams of the concentration of shear stress near the rupture front. . . . .	115
8.5	Illustration of two slip-weakening friction models with the same fracture energy. . . . .	117
8.6	Slip-weakening I friction model. . . . .	119

8.7	Slip-weakening II friction model. . . . .	120
8.8	Slip- and rate-weakening friction model. . . . .	121
8.9	Shear melting-refreezing friction model. . . . .	122
9.1	Domain geometry for the strike-slip fault. . . . .	124
9.2	Domain geometry for the thrust fault. . . . .	125
9.3	Shear and normal tractions on the fault surface for the base case. . . . .	127
9.4	Snapshots of slip rate on the strike-slip fault for the base case. . . . .	128
9.5	Distributions of final slip and maximum slip rate for the base case. . . . .	129
9.6	Comparison of slip time histories for ruptures with and without fracture energy. . . . .	130
9.7	Comparison of displacement time histories for the two spatial resolutions. . . . .	130
9.8	Variations of tractions with depth for the case of uniform effective normal stresses and a uniform coefficient of friction. . . . .	131
9.9	Variations of tractions with depth for the case of lithostatic effective normal stresses and a uniform coefficient of friction. . . . .	132
9.10	Shear and normal tractions on the fault surface for scenario sslithouni. . . . .	133
9.11	Distributions of final slip and maximum slip rate for scenario sslithouni. . . . .	133
9.12	Depth variations of the coefficient of the friction parameters. . . . .	136
9.13	Variations of tractions with depth for the case of lithostatic effective normal stresses and a variable coefficient of friction. . . . .	137
9.14	Shear and normal tractions on the fault surface for scenario sslithovar. . . . .	138
9.15	Distributions of final slip and maximum slip rate for scenario sslithovar. . . . .	138
9.16	Comparison of the velocity time histories for the three cases of effective normal stresses. . . .	139
9.17	Shear and normal tractions on the fault surface for scenario thbase. . . . .	141
9.18	Snapshots of slip rate on the fault surface for scenario thbase. . . . .	141
9.19	Distributions of final slip and maximum slip rate for scenario thbase. . . . .	142
9.20	Shear and normal tractions on the fault surface for scenario tlithovar. . . . .	143
9.21	Distributions of final slip and maximum slip rate for scenario tlithovar. . . . .	143
9.22	Comparison of velocity time histories for the two cases of effective normal stresses. . . .	144
9.23	Distributions of final slip and maximum slip rate for scenario sscombo. . . . .	145
9.24	Comparison of velocity time histories for the three friction models. . . . .	146
9.25	Distributions of final slip and maximum slip rate for scenario ssmelt. . . . .	147
9.26	Diagram of starting asperity locations on the fault surface. . . . .	148
9.27	Distributions of final slip and maximum slip rate with hypocenter HB. . . . .	149
9.28	Distributions of final slip and maximum slip rate with hypocenter HC. . . . .	149
9.29	Shear and normal tractions on the fault surface of the large homogeneous half-space. . . . .	150

9.30	Snapshots of slip rate on the fault surface of the large homogeneous half-space. . . . .	151
9.31	Distributions of final slip and maximum slip rate for the large homogeneous half-space. . .	152
9.32	Orientation of spherical coordinates relative to a double couple in whole-space. . . . .	153
10.1	Partitioning of the finite-element model among 16 processors. . . . .	157
10.2	Shear and normal tractions on the fault surface for scenario unistress. . . . .	159
10.3	Parameters of the slip-weakening I friction model as a function of depth. . . . .	160
10.4	Initial, failure, and minimum sliding shear stresses as a function of fault dip for scenario unistress. . . . .	161
10.5	Distributions of final slip and maximum slip rate for scenario unistress. . . . .	161
10.6	Shear and normal tractions on the fault surface for scenario unistrain. . . . .	162
10.7	Initial, failure, and minimum sliding shear stresses as a function of fault dip for scenario unistrain. . . . .	163
10.8	Distributions of final slip and maximum slip rate for scenario unistrain. . . . .	163
10.9	Normalized slip for different variations of the coefficient of friction with depth and material properties. . . . .	166
10.10	Parameters of the slip-weakening I friction model as a function of depth. . . . .	167
10.11	Initial, failure, and minimum sliding shear stresses as a function of fault dip for scenario unistrain2. . . . .	167
10.12	Snapshots of slip rate on the fault surface for scenario unistrain2. . . . .	168
10.13	Distributions of final slip and maximum slip rate for scenario unistrain2. . . . .	169
10.14	Final change in temperature on the fault surface for scenario unistrain2. . . . .	170
10.15	Maximum displacements and velocities on the ground surface for scenario unistrain2. . . .	170
10.16	Displacement and velocity time histories at two sites for scenario unistrain2. . . . .	171
10.17	Initial, failure, and minimum sliding shear stresses as a function of fault dip for scenarios comboB and meltC. . . . .	174
10.18	Maximum displacements and velocities on the ground surface for scenario comboB. . . .	175
10.19	Velocity time histories at two sites for the three friction models. . . . .	175
10.20	Maximum displacements and velocities along an east-west line for the three friction models.	176
10.21	Displacement time histories at two sites for the two fault depths. . . . .	177
10.22	Maximum displacements and velocities along an east-west line for the two fault depths. .	178
10.23	Displacement time histories at two sites for the two hypocenter locations. . . . .	179
10.24	Maximum displacements and velocities along an east-west line for the two hypocenter locations. . . . .	180
10.25	Initial, failure, and minimum sliding shear stresses on the fault surface for scenario shearstrong. .	180
10.26	Distributions of final slip and maximum slip rate for scenario shearstrong. . . . .	181

10.27 Maximum displacements and velocities on the ground surface for scenario shearstrong. . . . .	182
10.28 Distributions of final slip and maximum slip rate for scenario meltstrong. . . . .	183
10.29 Displacement time histories at two sites for the four cases of heterogeneity in the initial shear tractions. . . . .	184
10.30 Maximum displacements and velocities along an east-west line for the four cases of heterogeneity in the initial shear tractions. . . . .	185
10.31 Initial, failure, and minimum sliding shear stresses on the fault surface for scenario frictionstrong. . . . .	185
10.32 Distributions of final slip and maximum slip rate for scenario frictionstrong. . . . .	186
10.33 Displacement time histories at two sites for the three cases of heterogeneity in the friction model. . . . .	187
10.34 Maximum displacements and velocities along an east-west line for the three cases of heterogeneity in the friction model. . . . .	188
10.35 Velocity time histories at two sites for a dynamic failure simulation and a prescribed rupture simulation. . . . .	189
10.36 Maximum displacements and velocities along an east-west line for a dynamic failure simulation and a prescribed rupture simulation. . . . .	190
10.37 Partitioning of the finite-element model among 16 processors. . . . .	191
10.38 Initial, failure, and minimum sliding shear stresses as a function of fault dip for scenario unistrain. . . . .	194
10.39 Shear and normal tractions on the fault surface for scenario unistrain. . . . .	194
10.40 Snapshots of slip rate on the fault surface for scenario unistrain. . . . .	195
10.41 Distributions of final slip and maximum slip rate for scenario unistrain. . . . .	196
10.42 Final change in temperature on the fault surface for scenario unistrain. . . . .	196
10.43 Maximum displacements on the ground surface for scenario unistrain. . . . .	197
10.44 Maximum velocities on the ground surface for scenario unistrain. . . . .	197
10.45 Displacement and velocity time histories at two sites for scenario unistrain. . . . .	198
10.46 Maximum displacements on the ground surface for scenario unistrain2. . . . .	199
10.47 Maximum velocities on the ground surface for scenario unistrain2. . . . .	200
10.48 Velocity time histories at two sites for the two values of initial shear stress. . . . .	201
10.49 Maximum displacements and velocities along a north-south line for the two values of initial shear stress. . . . .	202
10.50 Displacement time histories at two sites for the three friction models. . . . .	204
10.51 Maximum displacements and velocities along a north-south line for the three friction models. .	205
10.52 Initial, failure, and minimum sliding shear stresses as a function of fault dip for scenario fault0km. . . . .	205

10.53 Snapshots of velocity on a vertical slice for scenario fault0km. . . . .	206
10.54 Maximum displacements on the ground surface for scenario fault0km. . . . .	207
10.55 Snapshots of velocity on a vertical slice for scenario combo0km. . . . .	208
10.56 Maximum displacements on the ground surface for scenario combo0km. . . . .	208
10.57 Displacement time histories at two sites for the three fault depths. . . . .	209
10.58 Maximum displacements and velocities along a north-south line for the three fault depths. .	210
10.59 Velocity time histories at two sites for the two hypocenter locations. . . . .	211
10.60 Maximum displacements and velocities along a north-south line for the two hypocenter locations. . . . .	212
10.61 Initial, failure, and minimum sliding shear stresses on the fault surface for scenario shearstrong.	213
10.62 Distributions of final slip and maximum slip rate for scenario shearstrong. . . . .	214
10.63 Distributions of final slip and maximum slip rate for scenario meltstrong. . . . .	214
10.64 Maximum velocities on the ground surface for scenario meltstrong. . . . .	215
10.65 Velocity time histories at two sites for the four cases of heterogeneity in the initial shear tractions. . . . .	216
10.66 Maximum displacements and velocities along a north-south line for the four cases of heterogeneity in the initial shear tractions. . . . .	216
10.67 Initial, failure, and minimum sliding shear stresses on the fault surface for scenario frictionstrong. . . . .	217
10.68 Distributions of final slip and maximum slip rate for scenario frictionstrong. . . . .	218
10.69 Displacement time histories at two sites for the three cases of heterogeneity in the friction model. . . . .	218
10.70 Maximum displacements and velocities along a north-south line for the three cases of heterogeneity in the friction model. . . . .	219
10.71 Velocity time histories at two sites for a dynamic failure simulation and a prescribed rupture simulation. . . . .	221
10.72 Maximum displacements and velocities along a north-south line for a dynamic failure simulation and a prescribed rupture simulation. . . . .	221
10.73 Displacement time histories at two sites for dynamic failure and prescribed rupture simulations with surface slip. . . . .	223
10.74 Areas where the maximum displacements and velocities exceed a given value. . . . .	229
10.75 Maximum displacements and velocities along a north-south line for the three fault depths. .	230
10.76 Average stress drop as a function of average slip. . . . .	231
10.77 Energy balance for a strike-slip simulation and a thrust fault simulation. . . . .	232
10.78 Radiated energy as a function of moment magnitude. . . . .	233

## List of Tables

5.1	Functional forms of the three slip time history shapes. . . . .	40
7.1	Material property control elevations for the layered half-space. . . . .	52
7.2	Sizes of the two finite-element models at coarse and fine resolution. . . . .	52
7.3	Summary of the parameters for the prescribed rupture simulations on the strike-slip fault. . .	54
7.4	Asperity parameters used in the heterogeneous slip distributions on the strike-slip fault. . . .	55
7.5	Sizes of the four finite-element models at coarse and fine resolution. . . . .	76
7.6	Summary of the parameters for the prescribed rupture simulations on the thrust fault. . . . .	77
7.7	Asperity parameters used in heterogeneous slip distributions on the thrust fault. . . . .	78
7.8	Variations in the peak maximum displacements and velocities with moment magnitude. . . .	103
8.1	Description of the variables involved in the friction models. . . . .	118
9.1	Sizes of the finite-element models at various resolutions for the domain containing the strike-slip fault. . . . .	124
9.2	Sizes of the finite-element models at various resolutions for the domain containing the thrust fault. . . . .	124
9.3	Friction model parameters and initial tractions for scenario ssbase. . . . .	127
9.4	Friction model parameters for scenario thbase. . . . .	140
10.1	Summary of the parameters for each scenario in the sensitivity study of the strike-slip fault. .	172
10.2	Summary of the ruptures in the scenarios that we use in the sensitivity study of the strike-slip fault. . . . .	173
10.3	Summary of the parameters for each scenario in the sensitivity study of the thrust fault. . . .	192
10.4	Summary of the ruptures in the scenarios that we use in the sensitivity study of the thrust fault.	193

## Notation

$\{ \}$	Column vector
$\langle \rangle$	Row vector
$[ ]$	Matrix
$[ ]^T$	Transpose of a matrix
$A$	Area
$\alpha$	Dilatational wave speed
$[B]$	Matrix of the derivatives of the shape functions
$\beta$	Shear wave speed
$[C]$	Damping matrix
$C_v$	Heat capacity per unit mass
$[D]$	Elasticity matrix relating the stresses and strains
$D$	Slip
$\overline{D}$	Average slip
$\delta$	Angle of fault dip
$E_R$	Radiated energy
$\varepsilon_{ij}$	Components of the infinitesimal strain tensor
$F_f$	Friction force
$F_t$	Tectonic force
$F_n$	Normal force
$G$	Fracture energy per unit area
$[K]$	Stiffness matrix
$l$	Length of the fault
$\lambda$	Rake angle, Lame's constant
$[M]$	Mass matrix
$\mu$	Lame's constant or shear modulus
$\mu_f$	Coefficient of friction
$\mu_{max}$	Coefficient of friction at failure
$\mu_{min}$	Minimum coefficient of friction during sliding
$\mu_{post}$	Coefficient of friction upon the termination of sliding

$[N]$	Matrix of the shape (nodal interpolation) functions
$N_i$	Shape function for node $i$
$\phi$	Azimuth of the strike direction or the strike angle of the fault
$(p, q)$	Location of a point on the fault plane
$Q$	Thermal energy
$\rho$	Material mass density
$\sigma_{ij}$	Components of the stress tensor
$\sigma_0$	Initial shear stress at a point
$\sigma_1$	Final shear stress at a point
$\Delta\sigma$	Stress drop ( $\sigma_0 - \sigma_1$ )
$\sigma_d$	Dynamic stress drop ( $\sigma_0 - \sigma_f$ )
$\sigma_{dff}$	Distance from failure or the difference between the shear stress at failure and the initial shear stress
$\sigma_f$	Friction stress at a point
$\sigma_{fail}$	Shear stress at failure
$\sigma_n$	Normal stress
$S$	Surface
$T$	Absolute temperature
$t$	Time
$(u_x, u_y, u_z)$	Displacement of a point in space
$V$	Volume
$v_r$	Velocity of the rupture
$w$	Width of the fault
$W$	Potential energy
$W_G$	Gravitational potential energy
$(x, y, z)$	Location of a point in space

# Chapter 1 Introduction

In the last five years two earthquakes have reminded us that we still have much to learn about how faults rupture and the resulting ground motions. On January 17, 1994, the Northridge earthquake hinted at the destruction possible when faults rupture below a densely populated area. Fortunately, most of the energy propagated away from the center of population. A year later, on January 17, 1995, the city of Kobe, Japan, did not fair as well: a fault rupture propagated toward the city. These earthquakes provided another demonstration that even moderate earthquakes can cause substantial damage. Records from these two events significantly increased our limited knowledge of how the ground moves close to rupturing faults. We need more information, however, about the robustness of the characteristics of near-source ground motions. Inversions of strong ground motions allow us to identify the area where slip occurred, the speed of the fault rupture, and the maximum slip rates. Inversions do not provide information about the sensitivity of the ground motions to variations in the source parameters.

We focus on investigating such sensitivities by computing the ground motion time histories for many hypothetical scenarios on a strike-slip fault and a shallow dipping thrust fault using finite-element models. Using prescribed ruptures, we assess the sensitivity of the ground motions to variations in the earthquake parameters. We improve our understanding of the dynamics of the rupture process by modeling the ruptures with dynamic failure through frictional sliding on the fault surface, instead of prescribing the ruptures. Based on simulations in homogeneous and layered half-spaces, we develop a simple, functional form for the coefficient of friction as a function of the material properties and the depth. Additionally, we conduct a second sensitivity study to gauge the influence of the initial conditions and friction model on the rupture behavior and the resulting ground motions.

## 1.1 Background

The sporadic occurrence of moderate to large earthquakes makes the task of understanding near-source ground motions difficult. Additionally, the sparse coverage of recording stations limits our ability to capture ground motions close to fault ruptures. The location of the 1992 Landers earthquake in a sparsely populated desert area resulted in only one record of near-source ground motion. While this record has been carefully studied (Iwan and Chen 1994), it shows how the ground moved at only one location. Modeling of the long-period ground motions from this event suggests that larger peak velocities occurred farther south along the fault (Wald and Heaton 1994). The location of the 1994 Northridge and 1995 Kobe earthquakes near large centers of population, where the station coverage is generally more dense, added many records

of near-source ground motions to the database. During the Northridge earthquake, ten stations within five kilometers of the surface projection of the rupture recorded ground motions (Hall et al. 1995). The limited number of near-source ground motions that have been recorded for large thrust earthquakes made it impossible to determine if the near-source records from the Northridge earthquake were anomalous (Somerville et al. 1996); however, Somerville et al. used a simulation procedure that was validated with many California earthquakes to reproduce the departure of the Northridge records from the empirical attenuation relations. They concluded that the Northridge near-source ground motions are representative of the near-source ground motions from large thrust earthquakes.

With the limited number of near-source records, seismologists have relied on simulations to reproduce ground motions from actual events and to predict the ground motions for hypothetical ones. Researchers have successfully modeled the near-source ground motions at periods of one second and longer from ten California earthquakes (Hall et al. 1995). These include, among others, the 1989 Loma Prieta (Wald et al. 1991), 1992 Landers (Wald and Heaton 1994), and the 1994 Northridge (Wald et al. 1996) earthquakes. Additionally, Kamae and Irikura (1998) and Wald (1996) reproduced the near-source ground motions from the 1995 Kobe earthquake. The source models associated with these simulations provide valuable information for dissecting past earthquakes. Olsen and Archuleta (1996) approximated the Northridge rupture to examine basin and directivity effects. Pitarka et al. (1998) and Hisada et al. (1998) have studied the directivity and basin edge effects for the 1995 Kobe earthquake to explain the zones of concentrated damage.

On the other hand, simulations of past events give little insight into how the ground motions compare to those from future events. We would also like to know if earthquakes on similar faults will produce comparable ground motions. Thus, the variability of the ground motions to changes in the seismic source parameters becomes important when predicting ground motions for hypothetical events. Saikia (1993) examined the ground motions at a network of sites in the greater Los Angeles area for a  $M_W$  7.0 event on the Elysian Park fault. In order to gauge the uncertainty of the ground motions, he examined several random distributions of slip and found wide variations in the peak accelerations. Based on the moderate to strong sensitivity of the ground motions to variations in the seismic moment, source rise time, and heterogeneity of the slip distribution for simulations of hypothetical earthquakes on a section of the San Andreas fault, Graves (1998) suggested that appropriate values for the source parameterization are essential for realistic predictions of ground motions. Additionally, while studying the accuracy of three-dimensional seismic velocity models, Wald and Graves (1998) demonstrated the variability exhibited by ground motions in response to changes in the material properties of the simulation domain.

We will expand on these studies and study the sensitivity of the long-period near-source ground motions on a strike-slip fault and a thrust fault to systematic variations of five earthquake source parameters, including the rupture speed, maximum slip rate, hypocenter location, fault depth, and distribution of slip. We also investigate how the shape of the near-source factor from the 1997 Uniform Building Code matches the distribution of the shaking.

Furthermore, we can improve the accuracy of our modeling of near-source ground motions if we better understand the dynamics of the rupture process. Including the rupture dynamics in simulations of earthquakes generally involves modeling the frictional sliding on the fault surface. Two distinct efforts of modeling the frictional sliding on faults have emerged in recent years. One focuses on modeling the evolution of stress on the fault leading up to the nucleation of earthquakes (Marone 1998; Rice and Ben-Zion 1996; Scholz 1998; Tullis 1996), and the other concentrates on modeling the dynamics of the rupture during the earthquake (Fukuyama and Madariaga 1998; Harris and Day 1999; Madariaga and Cochard 1996; Magistrale and Day 1999; Oglesby et al. 1998; Olsen et al. 1997).

Those researchers who model the evolution of stress on the fault almost exclusively use state- and rate-dependent friction models. Review articles by Marone (1998) and Scholz (1998) summarize the development of the friction models and some of the features of their behavior. These models are based on laboratory experiments of sliding at slip rates between  $10^{-7}$  mm/sec and 1 mm/sec, which are appropriate for the nucleation of earthquakes (Rice and Ben-Zion 1996). Additionally, analytical models of creep behavior yield friction models of the same form (Persson 1997). Consequently, researchers apply these models to studies of the nucleation of earthquakes and creep behavior on faults. Using an elastodynamic model of a half-space, Rice and Ben-Zion (1996) examined nucleation of earthquakes on a strike-slip fault. Tullis (1996) conducted a similar study on a segment of the San Andreas fault near Parkfield. Both groups use realistic distributions of the effective normal stresses with depth: the effective normal stresses are the difference between the lithostatic pressures and the hydrostatic pressures.

Rundle et al. (1997) suggested that the laboratory experiments used to create the state- and rate-dependent friction models do not adequately represent sliding on faults, and, in particular sliding dominated by inertial effects. Rundle et al. also noted that several predictions implied by these friction models have yet to be observed in nature. These include high shear stresses that generate large amounts of heat on the fault surface and significant precursory and inter-seismic creep between earthquakes. The first of these predictions is often referred to as the heat paradox. Several mechanisms have been suggested to explain why the friction stress drops to low levels during sliding and prevents melting. These include fluid pressurization prior to slip (Sleep 1997), wrinkle-like slip pulses associated with a contrast in material properties (Ben-Zion and Andrews 1998), acoustic fluidization (Melosh 1996), and normal vibrations (Tworzdylo and Hamzeh 1997).

The uncertainty in the behavior of how faults rupture has led researchers to create simple, *ad hoc* models that produce reasonable behavior. These models generally include either slip-weakening behavior, i.e., the shear strength decreases as slip occurs, or a combination of slip-weakening and rate-weakening, i.e., initially, the shear strength drops with slip in response to slip-weakening and then returns near its original level as the slip rate decreases. For over twenty years the slip-weakening friction model has been used to study the frictional sliding associated with earthquakes. Burridge et al. (1979) used a slip-weakening friction model to study stable propagation of mode-II shear cracks. More recently, Langer et al. (1996) postulated that inertial dynamics played an integral role in the complex distributions of slip in earthquakes, based on

observations of chaotic sequences of large and small events in two-dimensional elastodynamics models with slip-weakening friction. Using the boundary integral method, Madariaga and Cochard (1996) examined a two-dimensional anti-plane crack and discovered heterogeneity occurred on smooth faults with slip- and rate-weakening friction. Madariaga and Cochard suggested that stress heterogeneity occurs when the friction model allows a dynamic stress drop significantly larger than the average stress drop.

With an improved boundary integral method, Fukuyama and Madariaga (1998) successfully examined the three-dimensional features of slip on a planar crack in a homogeneous elastic medium. They concluded that, in friction models with slip- and rate-weakening, the slip-weakening friction is important at the leading edge of the rupture, while the rate-weakening friction influences the healing stage. Furthermore, Fukuyama and Madariaga found that healing (recovery of the shear stress on the fault) may occur in simulations without rate-weakening in the presence of shear stress asperities. The use of boundary integrals limits the applicability of the method to simple geometrical domains and variations in the material properties. Madariaga et al. (1998) formulated appropriate boundary conditions for the finite-difference method to study dynamic failure on planar faults in three-dimensional domains and demonstrated that the method reproduces the well known behavior of simple rupture models. The use of finite-differences marked a dramatic improvement in the applicability of the methods used to implement dynamic ruptures because it allowed heterogeneous material properties; however, the formulation restricted the alignment of the fault plane to the finite-difference grid. Consequently, the method did not allow rupture on faults inclined with respect to the finite-difference grid.

A simulation of the 1992 Landers earthquake by Olsen et al. (1997) demonstrated the ability of this finite-difference method and a slip-weakening friction model to produce reasonable rupture behavior. The simulation generated a confined rupture pulse consistent with the kinematic source models and reproduced the main long-period features of the waveforms. Olsen et al. could not determine whether or not a friction model with slip- and rate-weakening or variation of the characteristic slip-weakening distance would improve the fit of the ground motions to the recorded data. Other simulations with a slip-weakening friction model also generate realistic ruptures. Oglesby et al. (1998) used the finite-element method to study the difference between ruptures on two-dimensional normal faults and thrust faults in a homogeneous medium. They found larger motions on the hanging wall compared to the footwall that are consistent with recorded ground motions. Harris and Day (1999) explained the propagation across an echelon of faults for the rupture in the 1992 Landers earthquake using a three-dimensional finite-difference method. Using the same technique, Magistrale and Day (1999) investigated ruptures propagating across an echelon of thrust faults. In both cases the boundary conditions associated with the implementation of the earthquake source forced alignment of the faults along the finite-difference grids.

In contrast to the simulations using state-rate friction models, all of the simulations with slip-weakening or slip- and rate-weakening friction models assume uniform effective normal stresses. The use of the slip-weakening friction model and the slip- and rate-weakening friction model do not constrain the variations of the effective normal stresses with depth. Consequently, we will examine what constraints on the friction

model may be required to produce realistic ruptures when we apply reasonable shear and normal stress distributions with depth. Additionally, we will show that introducing sliding degrees of freedom in the finite-element models allows simulation of dynamic failure on an arbitrarily oriented fault surface. Using this implementation of the earthquake source and following the constraints imposed on the friction model, we will determine the sensitivity of the rupture behavior and ground motions to systematic variations of the initial shear stresses, friction model, fault depth, and location of the hypocenter. With this information we compare the rupture behavior from the dynamic failure simulations with our prescribed ruptures and propose modifications to the prescribed ruptures that would lead to more realistic ground motions.

## 1.2 Organization

Chapters 2–4 discuss the framework that we use in the earthquake simulations in the later chapters. Chapter 2 outlines the general methodology of the simulations. Chapter 3 focuses on the issues related to parallel execution of the software. We discuss the energy balance of earthquakes in chapter 4 and determine which forms of energy we can compute in our simulations. Chapter 6 summarizes the validation of the simulation software with both dynamic and static solutions. In chapter 7 we present the results from a sensitivity study of long-period near-source ground motions computed using prescribed ruptures. We assess the sensitivity of the ground motions to five earthquake source parameters and discuss the implications for earthquake engineering.

Chapter 8 begins our study of dynamic failure simulations by outlining the software implementation of the dynamic ruptures and discussing some of the general features of the rupture dynamics. Using a homogeneous half-space, chapter 9 summarizes several of the numerical aspects of dynamic ruptures, including the effects of changing the distribution of the effective normal stresses with depth. We demonstrate how variation of the coefficient of friction with depth produces realistic behavior when the effective normal stresses increase with depth. Chapter 10 extends our discussion of dynamic failure to a layered half-space. We examine some of the implications of using a layered versus a homogeneous half-space and conduct a sensitivity study of near-source ground motions using dynamic failure with variations in the initial conditions and the friction model. Finally, chapter 11 summarizes the findings of the sensitivity studies and suggests areas for further study.

## Chapter 2 General Methodology

We want to simulate slip on a fault in an efficient manner and to compute the ground motions in a given domain. Because we are focusing primarily on near-source ground motions, the domain of interest includes the ground surface in the region surrounding the fault, the fault itself, and everything in between. We model the slip on the fault to create the earthquake and model the wave propagation to compute the ground motions in the domain.

### 2.1 Governing Equations

We solve for the displacement time histories in the three-dimensional dynamic elasticity equation as given in index notation by equation (2.1) where  $\lambda$  and  $\mu$  are Lame's constants,  $u$  denotes displacement, and  $\rho$  denotes mass density. We subject the domain to the appropriate boundary conditions as discussed in section 2.2.1.

$$\lambda u_{k,kj} \delta_{ij} + \mu(u_{i,jj} + u_{j,ij}) = \rho \ddot{u}_i \quad (2.1)$$

In practice we cannot find closed-form solutions to equation (2.1) for geometrically complex media with heterogeneous properties. We must turn to numerical methods, such as the finite-element method, to find the displacement time histories. Although several computationally efficient methods have been developed to synthesize ground motions on finite faults with prescribed slip in a layered half-space (Heaton 1995), we use the finite-element method because we intend to extend the software to simulations with dynamic rupture and three-dimensional material properties. Using Lagrange equations and the finite-element method, the dynamic elasticity equation becomes the matrix equation given by equation (2.2), where  $[M]$ ,  $[C]$ , and  $[K]$  denote the mass, damping, and stiffness matrices, respectively, and  $\{F\}$  is the force vector.<sup>1</sup> We will discuss each term in detail below.

$$[M]\{\ddot{u}(t)\} + [C]\{\dot{u}(t)\} + [K]\{u(t)\} = \{F(t)\} \quad (2.2)$$

### 2.2 Integration of Differential Equation

The central-difference scheme provides an efficient means by which to numerically integrate the matrix differential equation. Equation (2.3) gives the expressions for the velocity,  $\{\dot{u}(t)\}$ , and acceleration,  $\{\ddot{u}(t)\}$ , at

---

<sup>1</sup>The details are given in most finite-element texts, such as Rao (1999).

time  $t$  as a function of the displacements at time  $t - \Delta t$ ,  $t$ , and  $t + \Delta t$ , where  $\Delta t$  denotes the time step.

$$\{\dot{u}(t)\} = \frac{1}{2\Delta t} (\{u(t + \Delta t)\} - \{u(t - \Delta t)\}) \quad (2.3)$$

$$\{\ddot{u}(t)\} = \frac{1}{\Delta t^2} (\{u(t - \Delta t)\} - 2\{u(t)\} + \{u(t + \Delta t)\}) \quad (2.4)$$

Substituting into the equation of motion (equation (2.2)) and solving for the displacements at time  $t + \Delta t$  yields

$$\begin{aligned} \left( \frac{1}{\Delta t^2} [M] + \frac{1}{2\Delta t} [C] \right) \{u(t + \Delta t)\} &= \{F(t)\} + \left( \frac{2}{\Delta t^2} [M] - [K] \right) \{u(t)\} \\ &\quad - \left( \frac{1}{\Delta t^2} [M] - \frac{1}{2\Delta t} [C] \right) \{u(t - \Delta t)\}. \end{aligned} \quad (2.5)$$

If we take the mass and damping matrices to be diagonal and constant, the left-hand side of equation (2.5) involves a constant, diagonal matrix, so that solving for the displacement vector at time  $t + \Delta t$  does not require matrix factorization. Additionally, computing the right-hand side necessitates only one matrix-vector multiplication; all of the other computations are operations on either vectors or diagonal matrices. Because the central-difference scheme minimizes the number of matrix-vector calculations and matrix-vector computations require significantly more operations than vector computations, in this case, the central-difference scheme provides an efficient technique for numerical integration. For stability of the numerical integration, the time step must be less than the time necessary for the fastest traveling wave to propagate between nodes—that is, the Courant-Friedrich-Lowy parameter must be less than 1.0. Consequently, in order to avoid unnecessarily small time steps, we want the elements to be as large as possible, which is also desirable from the standpoint of minimizing the number of elements in the mesh.

### 2.2.1 Boundary Conditions

Our domain encompasses only a minuscule fraction of the earth. We must therefore apply appropriate boundary conditions to compensate for the truncation of the domain. We model the ground surface as a free surface and create non-reflecting boundaries on the lateral sides and bottom of the domain. The non-reflecting boundaries approximate the behavior of the waves continuing to propagate past the edges of the domain. We absorb the outgoing waves by placing dampers on the absorbing boundaries as discussed below in section 2.3.3. While the dampers absorb nearly all of the energy of the propagating waves, they do not provide the stiffness that would exist if we did not truncate the domain; the absorbing boundaries act as free surfaces when the velocities on the boundary are zero. As a result, the final displacements depend on the size of the domain. But this dependency becomes small as the domains become large. Furthermore, the ground motion time histories, not the final displacements, are most important, and the lack of stiffness at the absorbing boundaries has minimal impact on the dynamic displacements. Consequently, the absorbing boundaries allow truncation

of the domain with minimal adverse effects on the solution.

## 2.3 Discretization

Efficient computation with the finite-element method requires choosing the appropriate type of finite-element. Choosing the appropriate element will, in most cases, reduce the errors in the computation, the memory storage requirements, and the computation time. The constraints imposed by solving the dynamic elasticity equation include the need to vary the node spacing to match variations in the material properties and to minimize the memory storage requirements of the global matrices. For linear elements, such as a hexahedron with six nodes and a tetrahedron with four nodes, reducing interpolation errors to less than five percent requires using ten nodes per shear wavelength (Bao et al. 1998). Ideally, we want the finite-elements to satisfy this criterion of ten nodes per wavelength throughout the entire domain.

We could use elements of the same size throughout the domain with the appropriate node spacing for the slowest shear wave speed. This would be the most stringent option. But this leads to meshes that contain many times the optimal number of elements and nodes and requires extremely small time steps in the numerical integration. This phenomenon is the major shortcoming of using the finite-difference method, which relies on uniform grid spacing. Because wavelength is proportional to wave speed, we want the node spacing to vary directly with the shear wave speed. Typically the shear wave speed varies from 4500 m/sec at the top of the mantle (at a depth of 30 km) to less than 700 m/sec at the surface. As a result, to minimize the mesh size and computational effort when simulating wave propagation with minimal artificial dispersion requires the node spacing at the surface to be less than one-sixth the node spacing at a depth of 30 km. We also wish to impose the constraint that the mesh should not lead to inefficient use of memory or to excessive computation time. The stiffness matrix which is the only non-diagonal matrix, dominates the memory storage requirements, so we wish to minimize its size by minimizing the total number of degrees of freedom and the average number of coupled degrees of freedom.

When modeling three-dimensional domains with finite-elements, the two main choices include hexahedral (six-sided) elements and tetrahedral (four-sided) elements. Hexahedral elements generally result in meshes with repeating structures, which make mesh generation simple, while tetrahedral elements generally result in meshes with little or no repeating structure and make mesh generation extremely complex, especially in three dimensions. The use of mesh generation software, such as Structural Dynamic Research Corporation's IDEAS, alleviates this difficulty. Several significant advantages lead to the choice of using tetrahedral elements. The most compelling reason to use tetrahedra over hexahedra is the improved ability to vary the node spacing within the domain. The structured nature of hexahedral meshes inhibits adjusting local element sizes independently of the surrounding elements, while the unstructured nature of tetrahedral meshes allows adjusting the local node spacing with minimal effects on the surrounding elements. A second advantage involves the coupling among the degrees of freedom. A linear hexahedral element in a uniform grid shares

nodes with 26 other elements. With three translational degrees of freedom per node and all degrees of freedom coupled within an element, each degree of freedom is typically coupled to 81 degrees of freedom. In a mesh of approximately uniformly sized tetrahedral elements, each degree of freedom is typically coupled to only 40 degrees of freedom. This means that the stiffness matrix for a tetrahedral mesh requires roughly half the memory as that for a hexahedral mesh with the same number of nodes. For these reasons we use a tetrahedral finite-element.

If we compare a linear tetrahedral element, which has four nodes, to a parabolic tetrahedral element (ten nodes), we find that use of the parabolic element requires more memory. For a parabolic element, limiting interpolation errors to less than five percent requires 9.4 nodes per wavelength (Bao et al. 1998), so the element edges are approximately twice as long but the node spacing is nearly the same. With ten nodes per element, the number of coupled degrees of freedom increases dramatically compared to the linear tetrahedral element, so that the stiffness matrix for a mesh with parabolic tetrahedral elements requires much more memory than the one for a mesh with linear tetrahedral elements. We therefore choose the linear tetrahedral element over the parabolic tetrahedral element.

With a linear tetrahedral element as shown in figure 2.1, we may exactly represent a linear variation in displacement within the element with the shape functions given in equation (2.6), where  $V$  is the volume of the element, and  $V_i$  is the volume of the tetrahedron formed by the point  $P$  and all nodes except node  $i$ . For example,  $V_1$  denotes the volume of the tetrahedron formed by point  $P$  and nodes 2, 3, and 4.

$$N_1 = \frac{V_1}{V} \quad N_2 = \frac{V_2}{V} \quad N_3 = \frac{V_3}{V} \quad N_4 = \frac{V_4}{V} \quad (2.6)$$

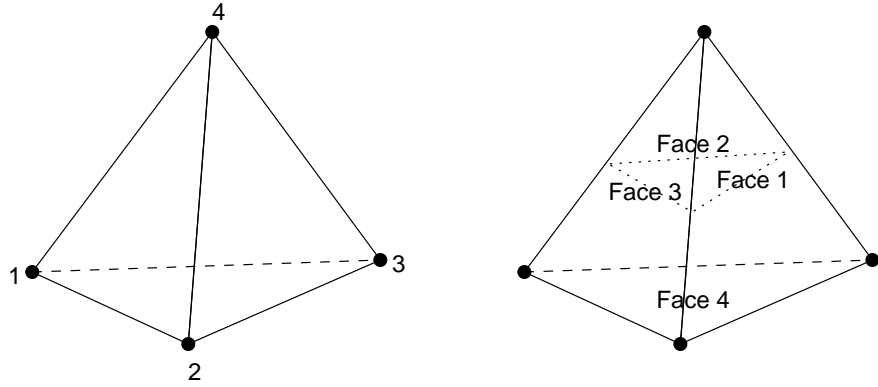


Figure 2.1: Node and face numbering of a tetrahedral finite-element.

The process of converting the three-dimensional elasticity equation (equation (2.1)) into the matrix differential equation (equation (2.2)) yields the expressions for the element matrices. Rao (1999) provides detailed development of the calculations, so in the following sections we will discuss only the final implementation of the matrix computations. We assume that the material properties do not vary significantly within an element, so that we may assume homogeneous material properties within the element and use the material properties

at the element centroid.

### 2.3.1 Mass Matrix

For efficient integration of the differential equation using the central-difference scheme we want a diagonal mass matrix. We convert the consistent element mass matrix to the lumped element mass matrix (diagonal matrix) given in equation (2.7) by requiring that both matrices yield the same inertial forces for rigid body accelerations along each global coordinate direction.

$$\langle M^e \rangle = \frac{\rho V^e}{4} \langle 1 \ 1 \ 1 \ 1 \ 1 \ 1 \ 1 \ 1 \ 1 \ 1 \ 1 \ 1 \rangle \quad (2.7)$$

Note that this matrix depends only on the volume of the element,  $V^e$ , and not explicitly on the relative locations of the nodes. We store the diagonal matrix using a row vector as indicated by the notation in equation (2.7).

### 2.3.2 Stiffness Matrix

The same method that produced the consistent mass matrix also gives us the expression for the element stiffness matrix shown in equation (2.8), where  $V^e$  is the volume of an element,  $[D]$  is the elasticity matrix relating the stresses to the strains (equation (2.9)), and  $[B]$  is the matrix of the derivatives of the shape functions (equation (2.10)). We assume that the strains and rotations remain small everywhere so that we may use linear elasticity.

$$[K^e] = V^e [B]^T [D] [B] \quad (2.8)$$

$$[D] = \begin{bmatrix} \lambda + 2\mu & \lambda & \lambda & 0 & 0 & 0 \\ \lambda & \lambda + 2\mu & \lambda & 0 & 0 & 0 \\ \lambda & \lambda & \lambda + 2\mu & 0 & 0 & 0 \\ 0 & 0 & 0 & \mu & 0 & 0 \\ 0 & 0 & 0 & 0 & \mu & 0 \\ 0 & 0 & 0 & 0 & 0 & \mu \end{bmatrix} \quad (2.9)$$

$$[B] = \frac{1}{6V^e} \begin{bmatrix} b_1 & 0 & 0 & b_2 & 0 & 0 & b_3 & 0 & 0 & b_4 & 0 & 0 \\ 0 & c_1 & 0 & 0 & c_2 & 0 & 0 & c_3 & 0 & 0 & c_4 & 0 \\ 0 & 0 & d_1 & 0 & 0 & d_2 & 0 & 0 & d_3 & 0 & 0 & d_4 \\ c_1 & b_1 & 0 & c_2 & b_2 & 0 & c_3 & b_3 & 0 & c_4 & d_4 & 0 \\ 0 & d_1 & c_1 & 0 & d_2 & c_2 & 0 & d_3 & c_3 & 0 & d_4 & c_4 \\ d_1 & 0 & b_1 & d_2 & 0 & b_2 & d_3 & 0 & b_3 & d_4 & 0 & b_4 \end{bmatrix} \quad (2.10)$$

The constants in the expression for  $[B]$  ( $a_i$ ,  $b_i$ ,  $c_i$ , and  $d_i$ ) are the cofactors of the terms in the determinant for the volume of an element given by equation (2.11), where  $(x_i, y_i, z_i)$  denotes the coordinates of node  $i$ . Equation (2.12) shows the expressions for four of the cofactors; the other cofactors may be found from permutations of these four.

$$V^e = \frac{1}{6} \begin{bmatrix} 1 & x_1 & y_1 & z_1 \\ 1 & x_2 & y_2 & z_2 \\ 1 & x_3 & y_3 & z_3 \\ 1 & x_4 & y_4 & z_4 \end{bmatrix} \quad (2.11)$$

$$a_1 = \begin{vmatrix} x_2 & y_2 & z_2 \\ x_3 & y_3 & z_3 \\ x_4 & y_4 & z_4 \end{vmatrix} \quad b_1 = - \begin{vmatrix} 1 & y_2 & z_2 \\ 1 & y_3 & z_3 \\ 1 & y_4 & z_4 \end{vmatrix} \quad c_1 = - \begin{vmatrix} x_2 & 1 & z_2 \\ x_3 & 1 & z_3 \\ x_4 & 1 & z_4 \end{vmatrix} \quad d_1 = - \begin{vmatrix} x_2 & y_2 & 1 \\ x_3 & y_3 & 1 \\ x_4 & y_4 & 1 \end{vmatrix} \quad (2.12)$$

Because the material property matrix is symmetric, we have a symmetric element stiffness matrix, and assembly into the global stiffness matrix also produces a symmetric matrix. As mentioned previously, in a finite-element mesh with linear tetrahedral elements, typically each degree of freedom is coupled to approximately 40 others. For a stiffness matrix with anywhere from hundreds of thousands to millions of degrees of freedom, relatively few entries in the matrix are nonzero. The unstructured nature of the finite-element mesh makes it nearly impossible to number the degrees of freedom in such a way as to create a uniformly banded stiffness matrix. Therefore, we choose to store as a row vector (data vector) only the nonzero terms in the upper half of the symmetric, sparse stiffness matrix. In order to find the location of each entry in the full matrix in the data vector, we also store the index where each row in the full matrix begins in the data vector and the column in the full matrix of each entry in the data vector. Figure 2.2 demonstrates the storage of a 5x5 symmetric, sparse matrix.

### 2.3.3 Damping Matrix

The damping matrix contains contributions from two sources: material damping and dampers placed on the boundaries to prevent artificial reflections of the propagating waves. We assume that the material damping

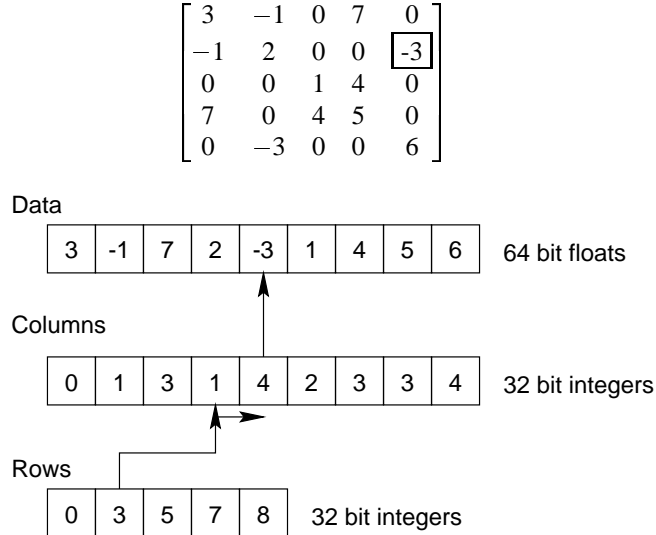


Figure 2.2: Storage example for a  $5 \times 5$  symmetric, sparse matrix. We follow the C/C++ convention and number the rows and columns starting with 0. We find the entry  $-3$  in row 1, column 4 (highlighted by the box) by looking up in the Rows array where row 1 starts. We then perform a linear search until we find column 4. The index in the Columns array in which we found column 4 indicates which index in the data array contains the entry we want.

may be created from scaling the mass and stiffness matrices as shown by equation (2.13).

$$[C] = C_m[M] + C_k[K] \quad (2.13)$$

We need not restrict ourselves to using the global matrices in equation (2.13); using the element mass and stiffness matrices allows local variations in the damping independent of variations in mass and stiffness.

### Mass-Proportional Damping

Mass-proportional damping applies more damping to the lowest modes of the domain. Equation (2.14) illustrates how the percent of critical damping,  $\zeta_m$ , varies as a function of frequency,  $\omega$ , for a given level of mass-proportional damping,  $C_m$ .

$$\zeta_m = \frac{C_m}{2\omega} \quad (2.14)$$

This means that waves with longer wavelengths are subjected to more damping than those with shorter wavelengths. The earth attenuates higher frequencies more than lower frequencies, so we use little or no mass-proportional damping. Because we use a diagonal mass matrix, mass-proportional damping contributes only terms on the diagonal to the damping matrix, whether or not we allow local variations in  $C_m$  (using equation (2.13) with the element matrices). This does not adversely affect the computational efficiency of the

central-difference scheme because a diagonal damping matrix does not introduce any additional matrix-vector multiplications which dominate the computation effort at each time step.

### Stiffness-Proportional Damping

Stiffness-proportional damping more effectively damps higher modes of the domain. Equation (2.15) shows how the percent of critical damping,  $\zeta_k$ , varies as a function of frequency,  $\omega$ , for a given level of stiffness-proportional damping,  $C_k$ .

$$\zeta_k = \frac{1}{2} C_k \omega \quad (2.15)$$

In other words, stiffness-proportional damping has the opposite trend with respect to frequency that mass-proportional damping has; with stiffness-proportional damping, the shorter wavelengths receive more damping than the longer wavelengths, so it more closely resembles what occurs in the earth. Unfortunately, stiffness-proportional damping greatly reduces the efficiency of the central-difference integration scheme, because it contributes off-diagonal terms to the damping matrix. If we allow local variations in  $C_k$ , we must formulate an additional sparse matrix to store the damping matrix, which nearly doubles the memory storage requirements. It also destroys the efficiency of the central-difference equation because we must factor the left-hand side of equation (2.5). Therefore, we do not allow local variations in  $C_k$ . If we restrict ourselves to a uniform  $C_k$ , we may solve the matrix differential equation without storing an additional sparse matrix. We do so by adjusting the formulation of the central-difference scheme as shown by equation (2.16), where  $[C_m]$  denotes the diagonal damping matrix coming from mass-proportional damping.

$$\begin{aligned} \left( \frac{1}{\Delta t^2} [M] + \frac{1}{2\Delta t} [C_m] \right) \{u(t + \Delta t)\} &= \{F(t)\} + \left( \frac{2}{\Delta t^2} [M] - [K] \right) \{u(t)\} \\ &\quad - \left( \frac{1}{\Delta t^2} [M] - \frac{1}{2\Delta t} [C_m] - \frac{1}{\Delta t} C_k [K] \right) \{u(t - \Delta t)\}. \end{aligned} \quad (2.16)$$

We have approximated the velocity for the stiffness-proportional damping term at time  $t$  using the displacements at time  $t$  and  $t - \Delta t$  as shown by equation (2.17), instead of the usual times  $t + \Delta t$  and  $t - \Delta t$ , to prevent the stiffness-proportional damping term from appearing on the left-hand side.

$$\{\dot{u}(t)\} = \frac{1}{\Delta t} (\{u(t)\} - \{u(t - \Delta t)\}) \quad (2.17)$$

Notice that each time step now involves two matrix-vector multiplications, effectively doubling the computation time. For this reason, the software does not currently implement stiffness-proportional damping.

### Absorbing Boundary

Dampers placed on the lateral sides and bottom of the mesh prevent propagating waves from reflecting off the boundaries and contaminating the solution inside the domain. For plane dilatational and shear waves propagating normal to the boundary, the dampers may absorb the waves completely if the dampers for the normal degrees of freedom are tuned to the dilatational wave speed and the dampers for the tangential degrees of freedom are tuned to the shear wave speed. This method also works reasonably well for incident angles other than 90 degrees (Cohen 1980). For an element with face 3 (see figure 2.1) on an absorbing boundary aligned with the  $yz$  plane, equation (2.18) gives the element damping matrix, where  $\rho$  denotes the mass density,  $A$  denotes the area of the face on the boundary, and  $\alpha$  and  $\beta$  denote the dilatational and shear wave speeds, respectively.

$$[C^e] = \frac{\rho A}{12} \begin{bmatrix} 2\alpha & 0 & 0 & \alpha & 0 & 0 & 0 & 0 & 0 & \alpha & 0 & 0 \\ 0 & 2\beta & 0 & 0 & \beta & 0 & 0 & 0 & 0 & 0 & \beta & 0 \\ 0 & 0 & 2\beta & 0 & 0 & \beta & 0 & 0 & 0 & 0 & 0 & \beta \\ \alpha & 0 & 0 & 2\alpha & 0 & 0 & 0 & 0 & 0 & \alpha & 0 & 0 \\ 0 & \beta & 0 & 0 & 2\beta & 0 & 0 & 0 & 0 & 0 & \beta & 0 \\ 0 & 0 & \beta & 0 & 0 & 2\beta & 0 & 0 & 0 & 0 & 0 & \beta \\ 0 & 0 & 0 & 0 & 0 & 0 & 0 & 0 & 0 & 0 & 0 & 0 \\ 0 & 0 & 0 & 0 & 0 & 0 & 0 & 0 & 0 & 0 & 0 & 0 \\ 0 & 0 & 0 & 0 & 0 & 0 & 0 & 0 & 0 & 0 & 0 & 0 \\ \alpha & 0 & 0 & \alpha & 0 & 0 & 0 & 0 & 0 & 2\alpha & 0 & 0 \\ 0 & \beta & 0 & 0 & \beta & 0 & 0 & 0 & 0 & 0 & 2\beta & 0 \\ 0 & 0 & \beta & 0 & 0 & \beta & 0 & 0 & 0 & 0 & 0 & 2\beta \end{bmatrix} \quad (2.18)$$

Although we require the absorbing boundaries to be aligned with a coordinate axis as discussed in section 2.6, we choose to formulate the boundary condition without this artificial constraint. Consequently, we formulate the element damping matrix based on the normal direction of the face, so that we completely absorb shear and dilatational waves propagating normal to the boundary. Because we use tetrahedral elements, three nodes define a face of the tetrahedron, so knowing the location of the three nodes for a face uniquely determines the normal direction. We form the element damping matrix in the normal and tangential coordinate frame of the face and then transform the element damping matrix to the global coordinate frame.

The above procedure results in a non-diagonal damping matrix, which we wish to avoid so that we may use the central-difference scheme without factoring any matrices. We know that the node spacing will be chosen to satisfy the ten nodes per wavelength requirement, so we may assume that the wavelength of the wave hitting the boundary will be much greater than the node spacing. This means that the velocities at the nodes of an element face on the absorbing boundary will be approximately the same, and we may use

equivalent rigid body velocities to convert the full damping matrix to a lumped (diagonal) damping matrix without significantly decreasing the effectiveness of the absorbing boundary. This is the same method that we used to lump the mass matrix in section 2.3.1, except that here we use rigid body velocities instead of rigid body accelerations.

## 2.4 Model of Fault

Realistic ground motions require accurate modeling of the slip on the fault. Prescribed ruptures necessitate explicit control of the slip at every point on the fault at all times. Similarly, simulations with dynamic failure require control of the friction on the fault. Double couples typically are used to model the earthquake source by applying forces to create large strains that approximate dislocations on the fault surface. A discretized domain requires applying the forces over a discrete length to create the couples. This distributes the slip across a discrete length, which is usually the node spacing, creating a “fault zone.” For a node spacing with ten nodes per wavelength and shear waves with periods of one second or more, the slip will be distributed over a much wider region than we observe in nature. Additionally, in an unstructured mesh the nodes do not naturally lie where we want to place the forces to generate the double couples. Using double couples also does not lend itself to implementing dynamic failure on the fault. These shortcomings of double couples inspired the development of an alternative method for modeling the earthquake source. The following sections outline the use of slip degrees of freedom to model slip on the fault in a way that works well both for simulations with prescribed ruptures and for simulations with dynamic failure.

### 2.4.1 Slip Degrees of Freedom

For slip on the fault we want to impose a dislocation in the finite-element model. In the case of a prescribed rupture we wish to specify the relative motion of one side of the fault with respect to the other side while allowing propagation of waves across the fault. We may accomplish these tasks by incorporating the fault plane into the geometry of the finite-element model. This interior surface gives structure to the finite-element mesh so that no elements straddle the fault plane. Instead, elements on either side share common faces on the fault plane, as illustrated by figure 2.3. We give double the usual number of degrees of freedom to all the nodes on the fault plane to allow one side to move relative to the other side; each fault node has six translational degrees of freedom that are split such that each side of the fault has three degrees of freedom, as shown in figure 2.3.

If we transform to relative and average degrees of freedom, we gain explicit control of the relative motion across the fault. We will denote the three degrees of freedom corresponding to the positive side of the fault plane<sup>2</sup> by  $u_{x_1}$ ,  $u_{y_1}$ , and  $u_{z_1}$ , and those corresponding to the negative side of the fault plane by  $u_{x_2}$ ,  $u_{y_2}$ , and  $u_{z_2}$ .

---

<sup>2</sup>We follow the convention that the normal vector for the fault points towards the hanging wall, and the hanging wall lies on the positive side of the fault plane.

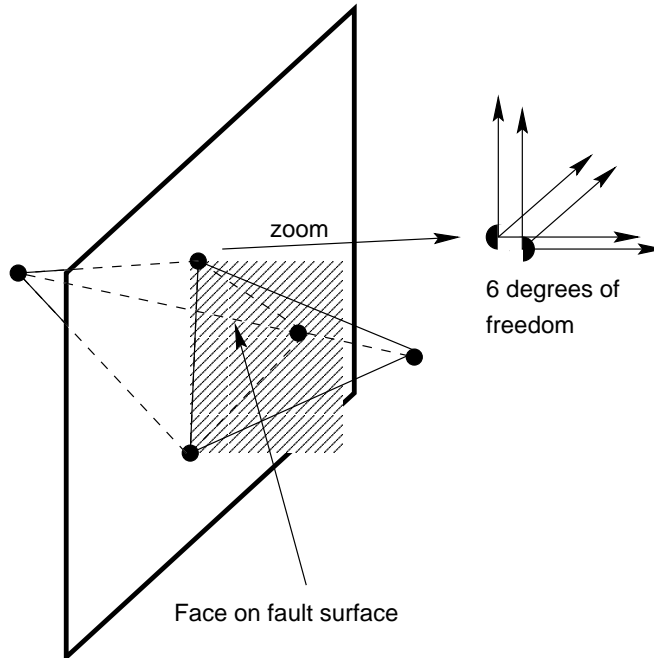


Figure 2.3: Model of the fault plane in the finite-element mesh. The left portion shows the alignment of the elements on the fault plane. The right portion provides a closeup of a node to demonstrate how each node contains six translational degrees of freedom to allow the sides of the fault to move relative to each other.

Equation (2.19) shows how to transform from the global degrees of freedom to relative and average degrees of freedom using an orthogonal matrix. Using an orthogonal matrix allows us to use the transpose to invert the transformation.

$$\begin{Bmatrix} u_{x_1-x_2} \\ u_{y_1-y_2} \\ u_{z_1-z_2} \\ u_{x_1+x_2} \\ u_{y_1+y_2} \\ u_{z_1+z_2} \end{Bmatrix} = \begin{bmatrix} \frac{1}{\sqrt{2}} & 0 & 0 & -\frac{1}{\sqrt{2}} & 0 & 0 \\ 0 & \frac{1}{\sqrt{2}} & 0 & 0 & -\frac{1}{\sqrt{2}} & 0 \\ 0 & 0 & \frac{1}{\sqrt{2}} & 0 & 0 & -\frac{1}{\sqrt{2}} \\ \frac{1}{\sqrt{2}} & 0 & 0 & \frac{1}{\sqrt{2}} & 0 & 0 \\ 0 & \frac{1}{\sqrt{2}} & 0 & 0 & \frac{1}{\sqrt{2}} & 0 \\ 0 & 0 & \frac{1}{\sqrt{2}} & 0 & 0 & \frac{1}{\sqrt{2}} \end{bmatrix} \begin{Bmatrix} u_{x_1} \\ u_{y_1} \\ u_{z_1} \\ u_{x_2} \\ u_{y_2} \\ u_{z_2} \end{Bmatrix} \quad (2.19)$$

We do not want to restrict the alignment of the fault plane to any one of the global coordinate planes. If we rotate from the global coordinate frame to the fault coordinate frame before transforming to slip and relative degrees of freedom, we will allow arbitrary orientation of the fault plane. Given the predominant slip direction in the fault plane and the fault normal, we define the fault coordinate frame by a fixed direction in the fault plane, selected to coincide with the direction of dominant slip (first coordinate), the direction in the fault plane perpendicular to the dominant slip direction (second coordinate), and the positive fault normal (third coordinate). In prescribed ruptures we set the slip in the dominant slip direction. In simulations with dynamic failure we apply the shear tractions on the fault surface in the direction of the dominant slip, although slip

may occur in any direction on the fault plane. Equation (2.20) demonstrates how to transform from the global coordinates to the relative and average coordinates in the fault plane, where  $[T_{slip}]$  is the 6x6 orthogonal matrix given in equation (2.19) and  $T_{fault}$  is the 6x6 rotation matrix given in equation (2.21), which transforms the degrees of freedom from the global coordinates,  $(x, y, z)$ , into the fault plane coordinates,  $(p, q, r)$ . Figure 2.4 shows the orientation of the fault plane coordinates relative to the global coordinates.

$$\begin{pmatrix} u_{p_1-p_2} \\ u_{q_1-q_2} \\ u_{r_1-r_2} \\ u_{p_1+p_2} \\ u_{q_1+q_2} \\ u_{r_1+r_2} \end{pmatrix} = [T_{slip}] \begin{pmatrix} [T_{fault}] & [0] \\ [0] & [T_{fault}] \end{pmatrix} \begin{pmatrix} u_{x_1} \\ u_{y_1} \\ u_{z_1} \\ u_{x_2} \\ u_{y_2} \\ u_{z_2} \end{pmatrix} \quad (2.20)$$

$$[T_{fault}] = \begin{bmatrix} \cos \lambda \sin \phi - \sin \lambda \cos \delta \cos \phi & \cos \lambda \cos \phi + \sin \lambda \cos \delta \sin \phi & \sin \lambda \sin \delta \\ -\sin \lambda \sin \phi - \cos \lambda \cos \delta \cos \phi & -\sin \lambda \cos \phi + \cos \lambda \cos \delta \sin \phi & \cos \lambda \sin \delta \\ \sin \delta \cos \phi & -\sin \delta \sin \phi & \cos \delta \end{bmatrix} \quad (2.21)$$

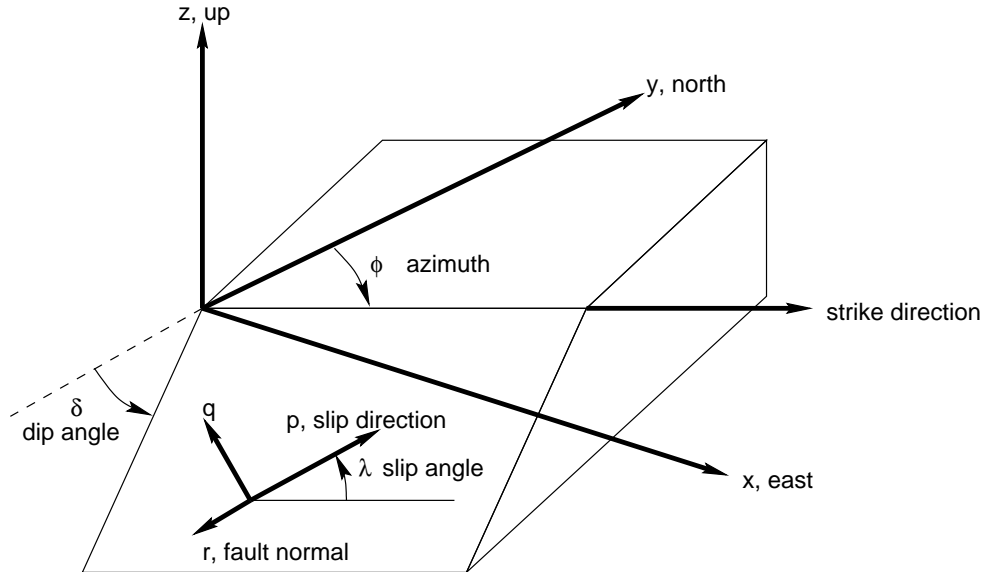


Figure 2.4: Fault geometry relative to the global coordinate axes.

The use of the slip degrees of freedom allows explicit control of the relative motion. In prescribed ruptures we simply set the slip degrees of freedom at each time step as described in chapter 5, while in simulations involving dynamic failure we set the forces acting on the slip degrees of freedom based on frictional sliding as described in section 8.1. In both cases we prevent the fault from opening by setting the relative degree of

freedom in the direction normal to the fault to zero at all time steps.

### 2.4.2 Modification to Element Matrices

For elements that contain one or more nodes on the fault, the slip degrees of freedom do not match those used for the element matrices, so we must transform the element mass and stiffness matrices derived in section 2.3.1 and section 2.3.2 to account for the slip degrees of freedom. We assume no damping is associated with elements that have slip degrees of freedom, so that these elements do not contribute to the global damping matrix. We transform the usual twelve element degrees of freedom aligned with the global coordinate axes to the modified element degrees of freedom using the transformation matrix given by equation (2.22), where  $[T_{fault}]$  is defined above by equation (2.21). If the element lies on the positive side of the fault plane, then  $C = +1$ , and if the element lies on the negative side of the fault plane, then  $C = -1$ .

$$[T_{el}] = \begin{bmatrix} [T_1] & [0] & [0] & [0] \\ [0] & [T_2] & [0] & [0] \\ [0] & [0] & [T_3] & [0] \\ [0] & [0] & [0] & [T_4] \end{bmatrix} \text{ where} \quad (2.22)$$

$$[T_i] = \begin{cases} \begin{bmatrix} 1 & 0 & 0 \\ 0 & 1 & 0 \\ 0 & 0 & 1 \end{bmatrix} & \text{if node } i \text{ is not on the fault} \\ \begin{bmatrix} C & 0 & 0 \\ 0 & C & 0 \\ 0 & 0 & C \end{bmatrix} [T_{fault}] & \text{if node } i \text{ is on the fault} \end{cases} \quad (2.23)$$

#### Modified Element Mass Matrix

We want the modified element mass matrix to give the same inertial forces for the same accelerations. In other words, if we transform a given acceleration in the usual twelve element degrees of freedom into the modified element degrees of freedom, we want the inertial forces in the modified coordinate system to be equal to transformation of the inertial forces in the original coordinate system,

$$[M_{slip}^e]\{\ddot{u}_{slip}^e\} = [T_{el}][M^e]\{\ddot{u}^e\}, \quad (2.24)$$

where  $[T_{el}]$  is given by equation (2.22). After some simple manipulation we find that

$$[M_{slip}^e] = [T_{el}][M^e][T_{el}]^T. \quad (2.25)$$

In section 2.3.1 we chose to use a lumped element mass matrix for efficient time stepping, so that  $[M]$  is diagonal. In general, the transformation of the lumped (diagonal) mass matrix given by equation (2.25) leads to a mass matrix with off-diagonal terms. The following example shows that we may neglect the off-diagonal terms because they will be small.

Consider a system with two degrees of freedom and a lumped mass matrix,

$$\{u\} = \begin{Bmatrix} u_1 \\ u_2 \end{Bmatrix} \quad (2.26)$$

$$[M] = \begin{bmatrix} m_1 & 0 \\ 0 & m_2 \end{bmatrix}. \quad (2.27)$$

Transforming to slip degrees of freedom gives

$$\{u_{slip}\} = \begin{Bmatrix} \frac{1}{\sqrt{2}}(u_1 - u_2) \\ \frac{1}{\sqrt{2}}(u_1 + u_2) \end{Bmatrix}, \text{ where} \quad (2.28)$$

$$\{u_{slip}\} = [T]\{u\}, \text{ and} \quad (2.29)$$

$$[T] = \begin{bmatrix} \frac{1}{\sqrt{2}} & -\frac{1}{\sqrt{2}} \\ \frac{1}{\sqrt{2}} & \frac{1}{\sqrt{2}} \end{bmatrix}. \quad (2.30)$$

Using equation (2.25) to transform the mass matrix to the slip coordinate frame yields

$$[M_{slip}] = \begin{bmatrix} \frac{1}{2}(m_1 + m_2) & \frac{1}{2}(m_1 - m_2) \\ \frac{1}{2}(m_1 - m_2) & \frac{1}{2}(m_1 + m_2) \end{bmatrix}. \quad (2.31)$$

If the masses on each side of the slip plane are equal, i.e., if  $m_1 = m_2$ , then we have a diagonal mass matrix. In our unstructured mesh this may or may not be true. Nevertheless, the off-diagonal terms involve the differences between the masses on opposite sides of the slip plane, while the diagonal terms involve the sum of the masses; this means that the off-diagonal terms will be much smaller than the diagonal terms, so that we may neglect the off-diagonal terms to create the diagonal (lumped) mass matrix as desired. To create the lumped modified element mass matrix, we simply distribute the lumped masses from the degrees of freedom for nodes on the fault equally between the relative and average degrees of freedom.

### Modified Element Stiffness Matrix

We follow the same analysis to find the modified element stiffness matrix that we used to determine the modified element mass matrix. We want the forces in the slip coordinate frame to be equal to the transformed forces in the original coordinate frame for a given displacement field,

$$[K_{\text{slip}}^e]\{u_{\text{slip}}^e\} = [T_{el}][K^e]\{u^e\}. \quad (2.32)$$

After some simple manipulation we find that

$$[K_{\text{slip}}^e] = [T_{el}][K^e][T_{el}]^T. \quad (2.33)$$

This transformation neither adds any additional constraints nor adversely modifies the stiffness matrix, as we will see by examining the eigenvalue and eigenvectors of the original and modified element stiffness matrices. The eigenvalues,  $\lambda_i$ , and eigenvectors,  $\{v_i\}$ , of the original element stiffness matrix satisfy

$$[K^e]\{v_i\} = \lambda_i\{v_i\}. \quad (2.34)$$

Denoting the eigenvalues and eigenvectors in the slip coordinate frame by  $\lambda_i^*$  and  $\{v_i^*\}$ , we have

$$[K_{\text{slip}}^e]\{v_i^*\} = \lambda_i^*\{v_i^*\}. \quad (2.35)$$

Substituting the expression of the modified stiffness matrix given by equation (2.33) and simplifying produces

$$[K^e][T_{el}]^T\{v_i^*\} = \lambda_i^*[T_{el}]^T\{v_i^*\}. \quad (2.36)$$

This is simply the eigenvalue problem for the original stiffness matrix, where

$$\{v_i^*\} = [T_{el}]\{v_i\}, \text{ and} \quad (2.37)$$

$$\lambda_i = \lambda_i^*. \quad (2.38)$$

Hence, the eigenvalues of the stiffness matrix do not change, and the eigenvectors are simply the original eigenvectors transformed to the slip coordinate frame.

### 2.4.3 Average Slip and Moment Magnitude

We often categorize seismic events using the fault area, the average slip, and the moment magnitude. We define the fault area to be the sum of the tributary areas on the fault plane of each node at which slip occurred. With an unstructured mesh the tributary areas will likely vary significantly from node to node, especially

where the material properties vary over the fault plane. Equation (2.39) indicates how we compute the average slip from the slip degrees of freedom by finding the weighted sum of the slip at each node and dividing by the fault area, where  $N$  is the number of nodes at which slip occurred and  $A_i$  is the fault tributary area for node  $i$ .

$$\bar{D} = \frac{\sum_{i=1}^N D_i A_i}{\sum_{i=1}^N A_i} \quad (2.39)$$

The moment magnitude which is defined by

$$M = \frac{\log M_o - 16.05}{1.5}, \text{ where} \quad (2.40)$$

$$M_o = \mu A \bar{D} \text{ (all in CGS units)}, \quad (2.41)$$

depends on the shear modulus on the fault plane. For heterogeneous material properties we cannot use the above expression for the moment,  $M_o$ , as it stands; we must sum the moments at each node at which slip occurs as shown by equation (2.42).

$$M_o = \sum_{i=1}^N \sum_{j=1}^{N^e} D_i \mu_j A_j \quad (2.42)$$

The tributary area for each node comes from all elements that contain the node and that also have a face on the fault surface. Each element may have a different shear modulus, so we sum the product of the tributary fault area and shear modulus over all  $N^e$  elements that contain the fault node. This expression for seismic moment accurately captures the variation in the moment over the fault for heterogeneity in both slip and shear modulus, and reduces to the usual expression (equation (2.41)) in the case of uniform slip and homogeneous material properties.

## 2.5 Spatial Interpolation

The simulation software requires several input parameters that may or may not be described by simple functions. In some cases we may only have a numerical picture of the data as defined by a set of locations and values. This data may be distributed along a line, e.g., material properties as a function of depth, an area, e.g., slip as a function of dip and strike on the fault plane, or a volume, e.g., material properties as a function of location in the domain. In any case, we want to use the values and locations given by the data set to determine values at other locations inside the domain, usually nodes or element centroids. This section describes the method used to interpolate values from a given spatial distribution of data. The procedure accounts for the topology of the data set and works for any location where we want to find the values.

The data set provides a list of values and locations in the global coordinate frame. Additionally, we require the data set to provide a flag indicating the topology of the data. Figure 2.5 shows the different topologies;

the data points as a group describe variations in zero dimensions (one point), one dimension (line), two dimensions (area), or three dimensions (volume). We assume the values vary linearly between data points (as explained below), so that we interpolate using the closest points and the corresponding values. The number of points that we need depends on the spatial variation of the values. For a one-dimensional data set, we need two points (line segment) to describe a linear variation in the values, for a two-dimensional data set we need three points (triangle), and for a three-dimensional data set we need four points (tetrahedron). For each given location at which we wish to know a value, we order the points in the data set based on the distance from the given location. We use the closest points that allow interpolation to find the value. If the given location lies outside the region covered by the data, we extrapolate using the nearest locations.

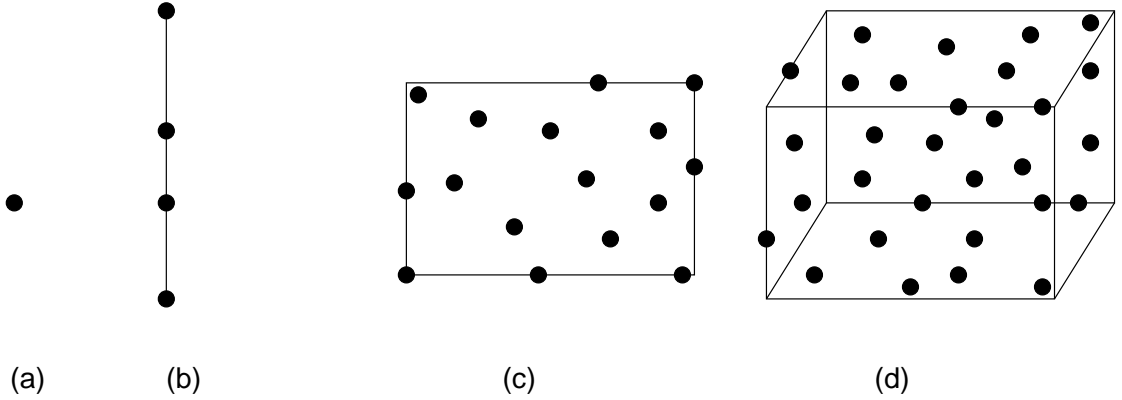


Figure 2.5: Different topologies of the data set. (a) Zero-dimensional data set (b) One-dimensional data set (c) Two-dimensional data set (d) Three-dimensional data set

We now describe the algorithm used in the interpolation. Point  $P$  denotes the location where we wish to know the value of some quantity  $s$ , and  $s_i$  denotes the value of  $s$  at point  $i$ .

1. If the data set contains only one point, then the value at point  $P$  is simply the value at the data set point, and we are done.
2. Order the data set based on the distance from point  $P$ .
3. Select the nearest point in the data set as point 1.
4. Select the next nearest point in the data set as point 2 subject to the constraint that point  $P$  lies between point 1 and point 2. If no such point 2 exists, we choose point 2 as the next closest point in the data set after point 1.
5. If the data set is one-dimensional, then

$$s_p = \frac{1}{d} \sum_{i=1}^2 s_i d_i, \quad (2.43)$$

where  $d$  is the distance between point 1 and point 2, and  $d_i$  is the distance between point  $P$  and the point other than point  $i$  as shown in figure 2.6. We are done.

6. Select the next nearest point in the data set as point 3, subject to the constraint that point  $P$  lies inside the triangle formed by point 1, point 2, and point 3. If no such point 3 exists, we choose point 3 as the next closest point in the data set after point 2.
7. If the data set is two-dimensional, then

$$s_p = \frac{1}{A} \sum_{i=1}^3 s_i A_i, \quad (2.44)$$

where  $A$  is the area of the triangle formed by point 1, point 2, and point 3, and  $A_i$  is the area of the triangle formed by point  $P$  and the other two points besides point  $i$  as indicated in figure 2.6(b). We are done.

8. Select the next nearest point in the data set as point 4 subject to the constraint that point  $P$  lies inside the tetrahedron formed by point 1, point 2, point 3, and point 4. If no such point exists, we choose point 4 as the next closest point in the data set after point 3.
9. If the data set is three-dimensional, then

$$s_p = \frac{1}{V} \sum_{i=1}^4 s_i V_i, \quad (2.45)$$

where  $V$  is the volume of the tetrahedron formed by point 1, point 2, point 3, and point 4, and  $V_i$  is the volume of the tetrahedron formed by point  $P$  and the three other points besides point  $i$ .  $V_1$  is shaded in figure 2.6(c). We are done.

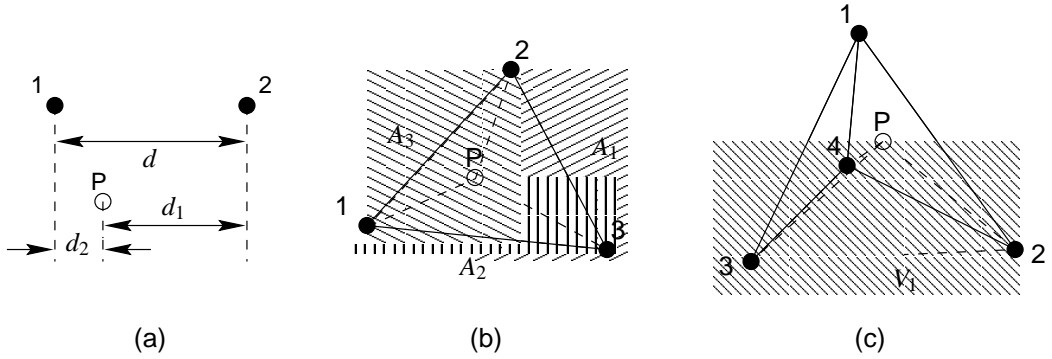


Figure 2.6: Interpolation schemes for the various topologies of the data sets. (a) Linear interpolation. (b) Area interpolation. (c) Volume interpolation.

## 2.6 Finite-Element Mesh Creation

We do not attempt to write software to generate the unstructured finite-element meshes with tetrahedral finite-elements. It is not easy to discretize a domain into tetrahedra, and the complexity of the problem increases significantly when we constrain the node spacing to match changes in material properties, include the fault plane as part of the domain geometry, and force the tetrahedra to be as regular as possible. Consequently, we use the IDEAS software from the Structural Dynamics Research Corporation to generate the finite-element mesh.

The first step involves inputting the geometry into the IDEAS solid modeler. In addition to the basic domain geometry, we also include the fault plane on which we align the element faces as described in section 2.4.1 and other surfaces on which we want to force alignment of the element faces. For example, we usually include the surface that slices through the centerline of the fault so that we may output information on this surface. For faster mesh generation we subdivide the domain into smaller chunks, allowing the mesh generator to work on only one chunk of the domain at a time. We define the finite-element model from the geometry by selecting the four-node tetrahedral finite-element and specifying the node spacing at appropriate locations in the domain.

We generate the mesh one sub-domain at a time and use the auto-checking feature of IDEAS to insure the quality of the elements in the mesh. Poor-quality elements include those with distorted shapes, which lead to larger numerical errors, and elements with non-optimal node spacing, which lead to interpolation errors when the spacing is too large and to reduced time steps when the node spacing is unnecessarily small. We export the mesh in universal file format, which is a plain text file that is easily read by the simulation software.

We also use IDEAS to extract information regarding which nodes and element faces lie on given lines and surfaces. For example, we want to identify all of the nodes on the fault plane, because we use them to implement slip of the fault. Similarly, we often want to output displacement time histories on the ground surface or along strategically placed lines. For planar surfaces, only one face of an element lies on the surface, and a list of the element's three nodes on the surface uniquely determines the element face on the surface. However, for multiple faces on a surface, all four nodes of an element lie on the surface and anywhere between two and four faces may lie on the surface.

We must use an additional criterion to separate the extraneous faces from the ones that we want. We require the fault to be a planar surface, so that only one face of an element may lie on the fault surface, and we do not need an additional criterion. The surfaces on which we choose to output information may or may not be planar. Because outputting information on these extra surfaces does not affect the solution and because the penalty for outputting this additional information is negligible, we allow the extraneous surfaces to remain. The absorbing boundaries usually have planar surfaces that meet with elements on the intersection having multiple faces on the absorbing boundary, with the extraneous faces arbitrarily oriented relative to the boundary. These extra faces could hamper the effectiveness of the absorbing boundary. We eliminate them

by constraining the lateral sides of the domain and bottom (absorbing boundaries) to coincide with one of the coordinate axes. When we formulate the absorbing boundary we ignore any faces that do not coincide with one of the coordinate axes. We use IDEAS to create the groups of nodes that coincide with the desired geometric entity and export them as part of the universal file.

## Chapter 3 Implementation of Parallel Processing

Simulations that involve hundreds of thousands to millions of degrees of freedom require hundreds of megabytes to gigabytes of memory and billions of floating point operations. State of the art workstations still lack the memory storage and processing power to effectively handle such large problems. Luckily, parallel computing provides a suitable environment for solving such problems by distributing both the storage and computation among many processors. We do not seek the optimum parallel software implementation, but do strive for efficient parallel computation.

Several methods and libraries exist to aid in writing parallel computing software. We chose to use the Message Passing Interface (MPI) which is not a library in itself, but a standard interface which libraries may follow. Some manufacturers develop their own implementation of the MPI in order to optimize the code for the architecture of the supercomputer, such as Intel's MPI on the Intel Paragon. In other cases, a third party implementation, such as MPICH from Argonne National Laboratory, is used. The MPI standard defines numerous functions to pass information among processors and facilitate initializing parallel execution.

### 3.1 The Center for Advanced Computing Research Supercomputers

The Center for Advanced Computing Research (CACR) at the California Institute of Technology oversees the use of several supercomputers. Initially, we used the CACR's Intel Paragon that has a total of 512 compute nodes. Each compute node contains an Intel i860 XP microprocessor and 32 megabytes of RAM and is capable of executing a maximum of 60 Mflops. The CACR decided to retire the Intel Paragon supercomputer in the spring of 1999, so we switched to the CACR's Hewlett Packard Exemplar. The Exemplar contains 16 hypernodes with each hypernode containing 16 Hewlett Packard PA 8000 RISC microprocessors running at 180 MHz with a peak capacity of 720 Mflops per processor; the processors within a hypernode share four gigabytes of RAM. Currently, it is the largest cache-coherent shared memory computer in the world.

### 3.2 Domain Partitioning among Processors

We distribute the computation among the processors by parceling the domain among the processors. Ideally we want the computation load evenly distributed among the processors, so that we achieve maximum parallel performance (processors do not sit idle and they spend negligible time communicating with each other). The software follows the single program-multiple data (SPMD) model of parallel execution in which every processor follows the same algorithm but operates on a different portion of the domain. In other words, we divide the finite-element mesh into small groups of elements and give each processor one group of elements.

We map each element to one processor, while the nodes may be mapped to more than one processor; nodes that lie on the boundaries between groups must be shared by the processors containing elements with those nodes. The lack of a repeating structure in meshes with tetrahedral elements tends to complicate the problem of partitioning the mesh. We have used two different partitioning strategies: a strategy that parcels the elements based a simple geometric approach and a more refined strategy more appropriate for unstructured meshes that balances the load and minimizes the communication among the processors.

Inertial bisection provides a simple and very fast method for partitioning the elements among the processors (Williams 1991; Williams 1994). We assume that the number of elements in each processor correlates with the computation time, so that we partition the domain based solely on the locations of the elements. Inertial bisection recursively divides the domain until the number of partitions equals the number of processors. We consider each element as a point mass with the mass of the element proportional to the computation effort of the degrees of freedom of that element. In this way, we give the elements with slip degrees of freedom more mass to compensate for their additional computational effort.<sup>1</sup>

Any number of partitions may be created by recursively dividing each partition. By adjusting the distribution of the load at each division, we ultimately create a load (mass) balanced partitioning of the domain. For example, to partition a mesh among three processors, we first divide the mesh into two groups, one with a load (mass) that is one-half of the second one, and then subdivide the larger of the two groups. The three resulting partitions all have the same load (mass). Each division requires computing the maximum principle moment of inertia of the current partition and finding the origin of the bisecting plane normal to the maximum principle moment of inertia to separate the elements into two groups with the desired loads (masses). Figure 3.1 gives an example of how inertial bisection partitions an unstructured mesh with nearly uniform element sizes. An example of partitioning an unstructured mesh with large variations in element sizes is shown in chapter 7. The inertial bisection method comes from a statistical approximation to the spectral bisection method. As a result, it may produce partitions that require significantly more interprocessor communication than other methods.

The METIS software library (Karypis et al. 1999) from the University of Minnesota provides the tools to efficiently partition unstructured meshes while evenly distributing the computation load and minimizing the total communication among processors. As in the case of inertial bisection, we assign a computation effort to each element, and adjust the weights of elements with slip degrees of freedom accordingly in order to account for the additional computational effort they require. Figure 3.2 gives an example of an unstructured mesh with nearly uniform element sizes partitioned using the METIS library.

---

<sup>1</sup>The amount of additional mass required to balance the load depends on the architecture of the supercomputer and the efficiency of the interprocessor communication libraries.

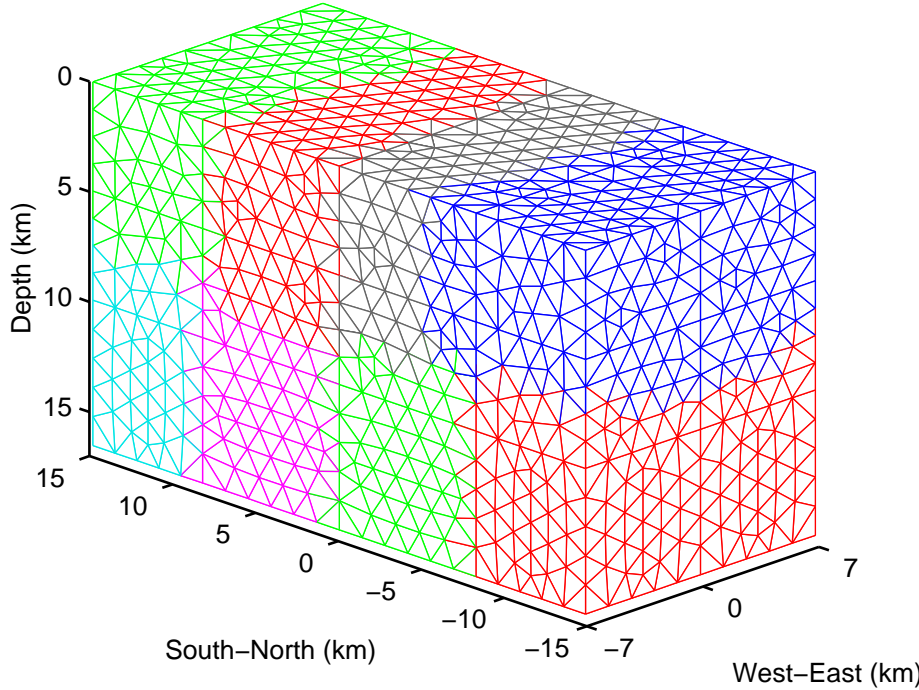


Figure 3.1: Example of partitioning of an unstructured mesh among eight processors using inertial bisection. Each patch of color identifies the elements of a single processor. The domain contains homogeneous material properties so the element sizes are nearly uniform.

### 3.3 Parallel Computation

Efficiently implementing parallel computation requires minimizing the communication among the processors. Bottlenecks occur when processors must pass information to each other, especially when they must pass information to all of their neighbors. Each processor formulates matrices and vectors for its degrees of freedom in the same fashion as we would normally formulate the global matrices and vectors. In order to couple the matrices and vectors over the entire domain (across the processors), we assemble the matrices and vectors by having each processor pass the entries for those degrees of freedom it shares with other processors to the appropriate neighbor. Note that it is much more efficient to assemble vectors, which require passing one entry per shared degree of freedom, than to assemble matrices, which require passing an entire row per shared degree of freedom.

One reason we choose to numerically integrate the dynamic elasticity equation using the central-difference scheme is that it is well suited for parallel processing. Upon examining equation (2.5) we see that the factor  $\frac{1}{\Delta t^2}[M] + \frac{1}{2\Delta t}[C]$  on the left-hand side does not change with time, so we need to formulate it only once; each processor computes the local portion of the term, and then we assemble the vector (diagonal matrix stored as a row vector) across the processors. The right-hand side changes significantly from time step to time step, so at each time step each processor formulates the local version of the entire right-hand side of equation (2.5) before assembling it across the processors. As a result, the numerical integration involves interprocessor

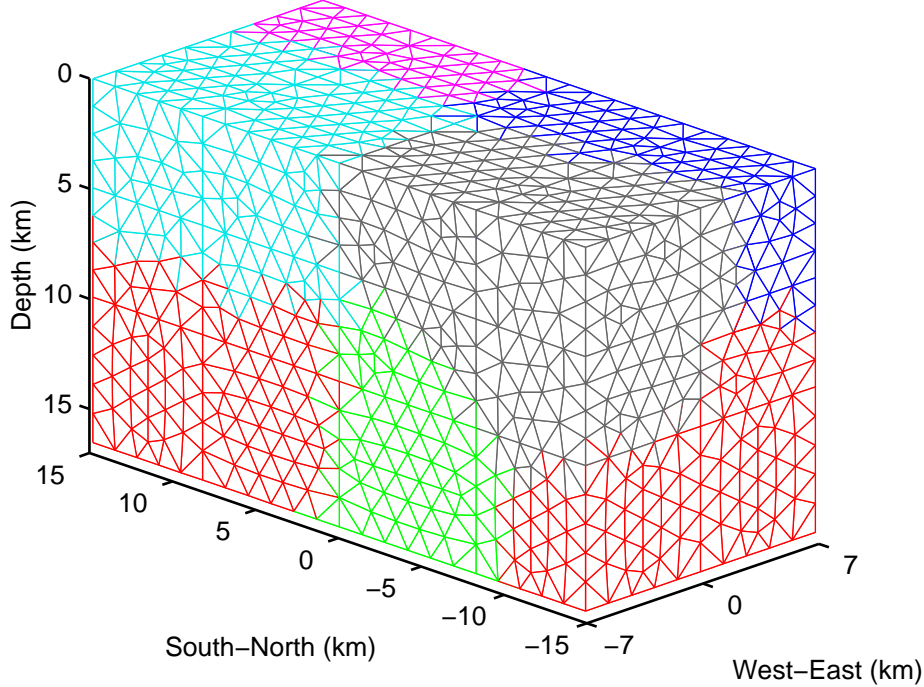


Figure 3.2: Example of partitioning of an unstructured mesh among eight processors using the METIS library. Each patch of color identifies the elements of a single processor. The domain contains homogeneous material properties so the element sizes are nearly uniform.

communication only when we assemble the vector on the right-hand side, which occurs just once per time step.

### 3.4 Parallel Input and Output

File input and output becomes slightly more complicated when executing a program on multiple processors. One strategy involves letting each processor read and write to its own file; however, this may lead to operating system panics when there are hundreds of processors. Additionally, post-processing becomes cumbersome because we must compile data from hundreds of files. An alternative strategy involves parallel input and output, or letting each processor read and write from the same file. This strategy is particularly effective when the supercomputer contains a parallel file system, e.g., the Intel Paragon. The simulation software includes a simple parallel input/output library which interfaces with the MPI and, in the case of the Intel Paragon, the parallel file system.

The parallel input/output library gives control of the file pointer to a master processor. We allow the master processor to read and write from the file as it wishes, during which it updates the file pointer. When we want to output information contained on multiple processors, the master processor coordinates the reading and writing to insure that each processor reads and writes from the proper place in the file. When multiple processors

write information, we order the data based on the rank of each processor, so the data from processor  $i$  follows the data from processor  $i - 1$  and immediately precedes the data from processor  $i + 1$ . When we want to write in parallel, we follow the algorithm below (reading in parallel is similar).

1. Each processor sends the master processor the number of bytes it wants to write.
2. The master processor computes the file position where each processor should begin writing based on the current file position (which it stores).
3. The master sends to each processor the file position where it should begin writing its data.
4. All processors write their data at the designated locations.

## 3.5 Global Mesh Refinement

As discussed in section 2.6, we use IDEAS to generate the finite-element meshes, and even with small meshes we must subdivide the domain to expedite the mesh generation process. To further reduce the load on the mesh generator, we create the mesh at a coarse resolution in IDEAS, and then globally refine the mesh to the desired resolution at the beginning of the simulation. Each processor refines its own portion of the domain, and by following the same refinement strategy, the element faces match along all interprocessor boundaries. The global refinement does not require extensive computation effort, so it is simply a matter of convenience to refine the meshes in parallel; the input file for the simulation may remain at coarse resolution which reduces disk storage. This allows IDEAS to create a mesh that contains only a fraction of the number of nodes and elements we use in the simulation. We currently implement two different resolutions of refinement: one that reduces the node spacing by a factor of two (2x refinement) and one that reduces the node spacing by a factor of four (4x refinement). We apply the refinement strategy to all elements in the same manner, so the resolution of the coarse mesh must be fine enough to capture the proper variations in node spacing; we satisfy this requirement by carefully selecting the locations of the element size control points and the designated element sizes when we create the coarse mesh.

If we choose to output information at the coarse resolution, we substantially reduce the file sizes with minimal losses of information. For example, we expect the final displacements and stresses to be much smoother than the shortest propagating wave, so the coarse mesh, even with four times the node spacing of the fine mesh, presents an accurate picture of the final displacements and stresses, but requires less than 2% of the disk space needed to store the displacements and stresses at the complete resolution.

### 3.5.1 Element Splitting

In 2x refinement we split each element in the mesh into eight elements as shown in figure 3.3. We add new nodes at the midpoints of the edges of the original tetrahedron. For a regular tetrahedron with edges of length

$l$  in the coarse mesh, we create four regular tetrahedra with edges of length  $\frac{l}{2}$  and four irregular tetrahedra with edges of length  $\frac{l}{2}$  and  $\frac{l}{\sqrt{2}}$ . Consequently, the global refinement algorithm does slightly degrade the quality of the elements, but not enough to adversely affect the solution. In this case, the mesh generated in IDEAS contains only one-eighth of the number of elements of the mesh used in the simulation.

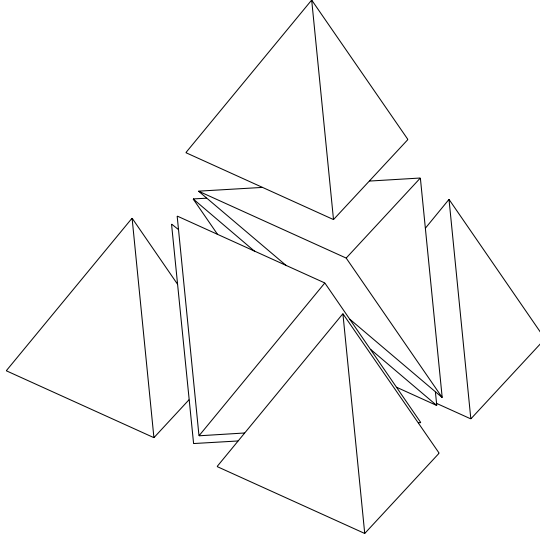


Figure 3.3: Diagram of element splitting in 2x refinement procedure during which we divide each element into eight elements and reduce the node spacing by a factor of two.

In 4x refinement we split each element in the mesh into 64 elements as shown in figure 3.4. During the 4x refinement we do not recursively refine the element using the 2x refinement procedure, because the quality of the elements would continue to degrade at the second level of refinement. Instead, we follow a different procedure that adds new nodes on both the edges and in the interior of the original element. We add new nodes such that each node lies exactly between two other nodes. From a regular tetrahedron with edges of length  $l$ , we create 24 regular tetrahedra with edges of length  $\frac{l}{4}$  and 40 tetrahedra with edges of length  $\frac{l}{4}$  and  $\frac{l}{2\sqrt{2}}$ . The disparity between the lengths of the edges of the tetrahedra remains the same as the 2x refinement. In this case, the number of elements in the coarse mesh generated in IDEAS is approximately 1.6% of the number of elements in the fine mesh used in the simulation. This gives a tremendous reduction in the time and effort needed to generate a mesh.

When we globally refine the mesh and create new nodes and elements, we must adjust the boundary conditions accordingly. As discussed in section 2.6, we use lists of nodes or nodal groups to uniquely determine the element faces composing the boundary conditions, e.g., the absorbing boundaries and the fault plane. During the mesh refinement, whenever we create new nodes on an element face associated with a boundary condition, we add the nodes to the list of nodes for that boundary condition. We also follow this procedure to modify lists of nodes associated with the surfaces on which we output time histories, when we select to output the information at the fine resolution.

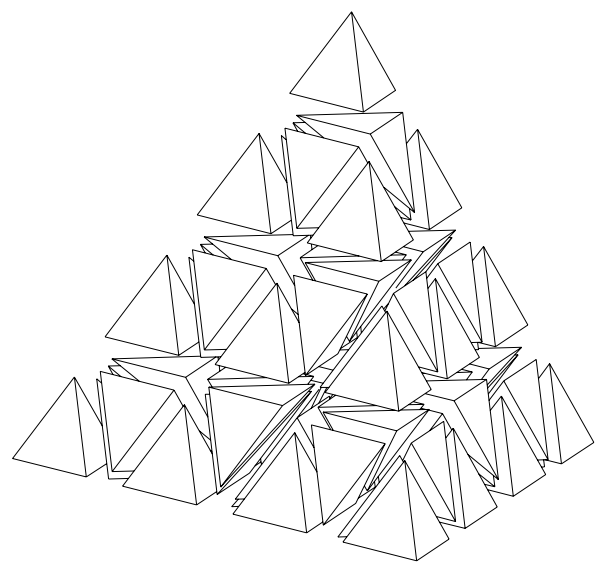


Figure 3.4: Diagram of element splitting in 4x refinement procedure during which we divide each element into 64 elements and reduce the node spacing by a factor of four.

## Chapter 4 Dynamic Energy Balance for Earthquakes

We compute the energy balance for our simulated earthquakes with the objective of learning more about the physics of the rupture process. As we will discuss below, the only forms of energy available from the simulations are the radiated energy, the change in potential energy of the earth, and the change in thermal energy of the earth. The energy balance also provides an additional tool to measure the size of the earthquake, and the change in thermal energy allows estimation of the degree of melting on the fault.

### 4.1 Derivation of Dynamic Energy Balance

We start with the conservation of energy for the entire earth. We neglect all external forces, such as the gravitational forces from the sun and the other planets; therefore, we have no change in the internal energy of the earth. As given by equation (4.1), the internal energy of the earth involves the radiated energy ( $E_R$ ), the change in thermal energy ( $\Delta Q$ ), and the change in the potential energy ( $\Delta W$ ).

$$E_R + \Delta Q + \Delta W = 0 \quad (4.1)$$

The change in potential energy involves changes in the strain energy, changes in the gravitational potential energy, and changes in the rotational energy of the entire earth. For prescribed ruptures we do not model the sliding friction on the fault, so we can determine neither the change in thermal energy nor the change in potential energy. The only quantity in the energy balance that we can compute is the radiated energy. When we use dynamic failure to model the slip on the fault, we do model the frictional sliding, so we can compute each term of the energy balance given by equation (4.1).

### 4.2 Radiated Energy

When we think about energy and earthquakes, we often only consider the radiated energy, because we associate it with the ground motions and can estimate it from ground motion records. Similarly, in numerical models the radiated energy is readily available from the earthquake simulation by finding the energy of the waves propagating away from the seismic source. The earth eventually dissipates all of the radiated energy through material damping. When we truncate the edges of the domain in order to model only a small portion of the earth, the absorbing boundaries, as discussed in section 2.3.3, mimic the waves propagating through the boundaries by absorbing the waves through the use of dampers. As a result, in our discretized models the damping matrix contains a complete description of how the domain dissipates the radiated energy, so we use

it to compute the radiated energy. Generally, we do not specify enough time steps in the time integration for the absorbing boundaries to completely absorb all of the radiated energy, and a small amount of the radiated energy remains in the domain as kinetic energy. We add this kinetic energy to the energy absorbed through the damping matrix to find the total radiated energy. For the domain discretized in both space and time, equation (4.2) gives the total energy radiated from the seismic source, where  $\{\dot{u}(t)\}$  is the velocity vector at time  $t$ ,  $[C]$  is the damping matrix,  $[M]$  is the mass matrix,  $\Delta t$  is the time step, and  $N$  is the number of time steps.

$$E_R = \Delta t \sum_{m=1}^N \langle \dot{u}(m\Delta t) \rangle [C] \{\dot{u}(m\Delta t)\} + \frac{1}{2} \langle \dot{u}(m\Delta t) \rangle [M] \{\dot{u}(m\Delta t)\} \quad (4.2)$$

### 4.3 Change in Thermal Energy

Earthquakes change the thermal energy of the earth in four ways. The primary contribution comes from the generation of heat by the frictional sliding on the fault. Additionally, the fracturing of materials in the fault zone creates latent heat. The radiated energy eventually dissipates into heat, but we choose to consider it separately as discussed above. If we assume that the strain increments throughout the earth occur adiabatically, then they cause changes in temperature in the same fashion that the adiabatic expansion of a gas causes a drop in temperature (Fung 1965). We will assume that the strain increments cause a negligible change in temperature, so that we may neglect the change in thermal energy imposed by the adiabatic change in strain. Therefore, we are left with the change in thermal energy caused by frictional sliding and the fracturing of materials.

We choose to include both the fracture behavior and the sliding behavior in the friction model. Consequently, the energy dissipated through frictional sliding includes both the latent heat associated with the fracture energy and the heat generated by sliding. To find the energy dissipated as heat during frictional sliding on the fault, we begin with the increment of heat,  $dQ(t)$ , created during an increment of slip,  $dD(t)$ ,

$$dQ(t) = \sigma_f(t) dD(t) dS, \quad (4.3)$$

where  $\sigma_f(t)$  is the frictional stress at a point on the fault surface and  $dS$  is the differential fault area. Integrating over the fault surface and slip yields

$$\Delta Q(t) = \int_{D(t)} \int_S \sigma_f(t) dD dS. \quad (4.4)$$

Converting the integral over slip to an integral over time produces

$$\Delta Q(t) = \int_t \int_S \sigma_f(t) \dot{D}(t) dS dt, \quad (4.5)$$

where  $\dot{D}$  is the slip rate. Finally, for a domain discretized in time and space, equation (4.6) gives the total

change in thermal energy for an earthquake, where  $\Delta t$  is the time step,  $\langle F_f(t) \rangle$  is the friction force vector at time  $t$ , and  $N$  is the number of time steps.

$$\Delta Q(t) = \Delta t \sum_{m=1}^N \langle F_f(m\Delta t) \rangle \{ \dot{D}(m\Delta t) \} \quad (4.6)$$

### 4.3.1 Change in Temperature on the Fault

The heat generated during sliding on the fault will increase the temperature in a region surrounding the fault. The total change in thermal energy on the fault, which we compute from the friction and sliding on the fault as discussed above, includes both the fracture energy and the heat generated by sliding. We will assume that the fracture energy is much smaller than the heat generated by sliding, so that we may use the change in total thermal energy at each point on the fault to compute the change in temperature. We find the increment in temperature,  $dT$ , at a point on the fault from the increment in heat,  $dQ$ , using

$$dT = \frac{dQ(t)}{C_v \rho d ds}, \quad (4.7)$$

where  $C_v$  is the heat capacity per unit mass,  $\rho$  is the density,  $d$  is the distance perpendicular to the fault where the heat is trapped, and  $ds$  is the differential fault area. Substituting in the expression for the increment in heat at a point on the fault (equation (4.3)) and converting the increment in slip to a slip rate over an increment in time yields

$$dT = \frac{\sigma_f(t) \dot{D}(t) dt}{C_v \rho d}. \quad (4.8)$$

Integrating over time to find the change in temperature produces

$$\Delta T = \int_t \frac{\sigma_f(t) \dot{D}(t)}{C_v \rho d} dt. \quad (4.9)$$

After discretizing the domain in space and time, we find that equation (4.10) gives the change in temperature at a point on the fault, where  $F_f(t)$  is the friction force at time  $t$ ,  $\Delta t$  is the time step, and  $N$  is the number of time steps.

$$\Delta T = \frac{\Delta t}{C_v \rho d} \sum_{m=1}^N \langle F_f(m\Delta t) \rangle \{ \dot{D}(m\Delta t) \} \quad (4.10)$$

## 4.4 Change in Potential Energy

We define the change in potential energy as the energy released by the slip on the fault assuming that the slip occurs quasi-statically and that the domain behaves according to linear elasticity. Because both the radiated energy and the change in heat energy must be positive, conservation of energy dictates that the change in

potential energy must be negative. This drop in the potential energy allows earthquakes to release energy as propagating waves and generate heat through frictional sliding.

We follow a procedure similar to that of Savage and Walsh (1978) and Dahlen (1977) to find the change in potential energy due to an earthquake. We start with the change in energy for an increment of slip,

$$dW = -\sigma(D) dD dS, \quad (4.11)$$

where  $dW$  is the incremental change in potential energy,  $\sigma$  is the shear stress at a point on the fault,  $D$  is the slip at a point on the fault,  $dD$  is the increment of slip, and  $dS$  is the differential fault area. The negative sign indicates the shear stress opposes slip. Assuming a linearly elastic medium, the stress follows

$$\sigma(D(t)) = -\sigma_0 + \frac{D(t)}{D} \Delta\sigma, \quad (4.12)$$

where  $\sigma_0$  is the shear stress just prior to the earthquake,  $\sigma(D(t))$  is the shear stress after the fault has slipped an amount  $D(t)$ ,  $D(t)$  is the slip at time  $t$ ,  $D$  is the final slip, and  $\Delta\sigma$  is the final stress drop. We follow the convention that a decrease in stress gives a positive stress drop. Substituting the stress at slip  $D(t)$  into the expression for the incremental change in potential energy and integrating over both the slip and the fault area produces

$$\Delta W = - \int_D \int_S (\sigma_0 - \frac{D(t)}{D} \Delta\sigma) dD dS. \quad (4.13)$$

Integrating over the slip and simplifying produces

$$\Delta W = -\frac{1}{2} \int_S (\sigma_0 + \sigma_1) D dS, \quad (4.14)$$

where  $D$  and  $\sigma_1$  are the slip and stress at a point on the fault after the earthquake. After discretizing in time and space, equation (4.15) gives the change in potential energy caused by an earthquake, where  $\langle F(0) \rangle$  is the friction force vector on the fault at zero slip and  $\langle F_t(D) \rangle$  is the friction force vector on the fault at the completion of slip.

$$\Delta W = -\frac{1}{2} (\langle F_t(0) \rangle + \langle F_t(D) \rangle) \{D\} \quad (4.15)$$

From the point of view of understanding the physics of the rupture, we would like to decompose the change in potential energy into the change in strain energy and change in gravitational potential energy. As shown by Savage and Walsh (1978) and Dahlen (1977), we cannot determine these changes in energy when we truncate the domain, because all points in the earth contribute equally to the computations; the domain must encompass the entire earth in order to compute the change in strain energy and the change in gravitational potential energy. Additionally, we neglect the change in Earth's rotational energy caused by

earthquakes for the same reason.<sup>1</sup>

#### 4.4.1 Topography and Changes in Gravitational Potential Energy

If we could determine the change in gravitational potential energy, it might lead us to a better understanding of the creation of mountains due to thrust earthquakes. The following simple thought experiment illustrates the general mechanism by which earthquakes change the gravitational potential energy of the earth. Consider two containers of an incompressible fluid with widths  $b_1$  and  $b_2$  as shown in Figure 4.1. Figure 4.1(a) shows the containers filled with fluid to heights of  $h_1$  and  $h_2$ . We may think of the two containers of fluid as the two sides of a thrust fault with the heights of the fluid corresponding to the level of the surface topography. The gravitational potential energy of this configuration is

$$W_{G_0} = \frac{1}{2}h_1(\rho gh_1 b_1) + \frac{1}{2}h_2(\rho gh_2 b_2). \quad (4.16)$$

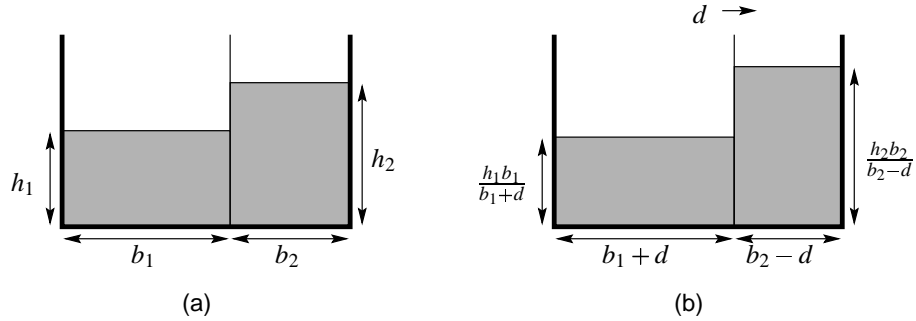


Figure 4.1: Configurations of the two fluid containers. (a) Original configuration (b) Configuration after the divider moves a distance  $d$  to the right.

We move the divider a distance  $d$  to the right. This represents a slip of  $d$  that generates the upward movement of the hanging wall and the subsidence of the footwall in a thrust earthquake. The gravitational potential energy of the fluid in the containers becomes

$$W_{G_1} = \frac{1}{2} \left( \frac{h_1 b_1}{b_1 + d} \right) (\rho g h_1 b_1) + \frac{1}{2} \left( \frac{h_2 b_2}{b_2 - d} \right) (\rho g h_2 b_2). \quad (4.17)$$

The change in gravitational potential energy is

$$\begin{aligned} \Delta W_G &= W_{G_1} - W_{G_0} \\ &= \frac{1}{2} \rho g d \left( \frac{h_2^2 b_2}{b_2 - d} - \frac{h_1^2 b_1}{b_1 + d} \right). \end{aligned} \quad (4.18)$$

---

<sup>1</sup>Chao and Gross (1995) computed the change in the rotational energy of the earth for a catalog of earthquakes using modal techniques and point sources.

The movement of the divider increases the gravitational potential energy if

$$\frac{h_2^2 b_2}{b_2 - d} > \frac{h_1^2 b_1}{b_1 + d}, \quad (4.19)$$

which is nonlinear in the movement of the divider,  $d$ . Even for this simple analogy, the gravitational potential energy changes in a nonlinear fashion. If we start with equal heights and widths of the fluid containers ( $h_1 = h_2$  and  $b_1 = b_2$ ), the expression for the change in gravitational potential energy reduces to

$$\Delta W_G = \rho g d h_1^2 b_1 \frac{d^2}{b_1^2 - d^2}, \quad (4.20)$$

and the change in gravitational energy is second order. This corresponds to no surface topography being present before the earthquake. On the other hand, when surface topography does exist, the change in gravitational potential energy is first order.

For the same slip distribution on a given fault, the greater the differences in topographic features, the larger the change in gravitational potential energy. In other words, for mountain-building thrust fault earthquakes with the same amount of slip, each successive earthquake leads to greater changes in the gravitational potential energy. If the change in potential energy is the same for each event, the change in strain energy must become more negative to balance the ever greater changes in gravitational potential energy. We do not know how the seismic behavior changes with these progressively larger changes in the strain energy and the gravitational potential energy, because we cannot compute the change in strain energy and change in gravitational potential energy. We must rely on the stress state as discussed in section 8.2.3 for insight into the roles of gravity and topography in seismic events.

## Chapter 5 Prescribed Rupture

When we simulate earthquakes using prescribed ruptures, we set the slip time history at each point on the fault according to some predetermined set of parameters. This method works well when we want to compute the ground motions for scenarios with well known source parameters, such as the final distribution of slip on the fault, rupture speed, and maximum slip rate. On the other hand, we ignore the dynamics of the rupture process by not modeling the frictional sliding on the fault surface. Instead, we focus on the ground motions resulting from the choice of the earthquake source parameters.

### 5.1 Earthquake Source

With the use of slip degrees of freedom to model the earthquake source as described in section 2.4.1, at each time step we set the displacements of the slip degrees of freedom to create the appropriate relative motion between the sides of the fault. In the numerical integration (equation (2.5)) we set the displacements of the slip degrees of freedom at time  $t + \Delta t$ , so we must subtract the known values of the left-hand side from the right-hand side. We subtract the term  $\left(\frac{1}{\Delta t^2}[M] + \frac{1}{2\Delta t}[C]\right)\{u(t + \Delta t)\}$  from the right-hand side where the only nonzero entries in  $\{u(t + \Delta t)\}$  are the displacements for the slip degrees of freedom. By using the already assembled version of  $\frac{1}{\Delta t^2}[M] + \frac{1}{2\Delta t}[C]$ , this calculation does not require any interprocessor communication, and we subtract this product from the already assembled right-hand side.

### 5.2 Slip Time History

The slip time history controls the progression of slip over time. The slip time history at each point on the fault has the same functional form, but we set the time constants that control the precise time history at each point based on the specified values of the final slip and maximum slip rate. We use a uniform maximum slip rate but allow spatial variation of the final slip as we will discuss below in section 5.3. Allowing variations in final slip while using a uniform maximum slip rate produces variations in the slip rise times with longer rise times at points with larger values of final slip.

For the slip time history in a given scenario, we choose one of the three shapes shown in table 5.1 and figure 5.1. One-half of a period of the cosine function gives an extremely simple slip time history. To create a causal slip time history from the non-causal functional form of the error function, we truncate the beginning portion of error function time history. With two time constants in the error function, we may select both the maximum slip rate and the time when it occurs. However, the time of the maximum slip rate must be late enough, so that the portion we truncate remains negligible. Olsen and Archuleta (1996) often use this

Shape	Slip function	Maximum Slip Rate
cosine	$\frac{t-t_0}{\tau} - \frac{1}{2\pi} \sin(2\pi \frac{t-t_0}{\tau})$	$\frac{2}{\tau}$
erf	$\frac{1}{2} \left( 1 + \text{erf} \left( \frac{t-t_0-\tau_1}{\sqrt{2}\tau_2} \right) \right)$	$\frac{1}{\sqrt{\pi}\tau_2}$
Brune	$1 - \exp \left( \frac{-(t-t_0)}{\tau} \right) \left( 1 + \frac{t-t_0}{\tau} \right)$	$\frac{1}{\tau e}$

Table 5.1: Functional forms of the three slip time history shapes. Slip begins at time  $t = t_0$ , and  $\tau$ ,  $\tau_1$ , and  $\tau_2$  are all time constants.

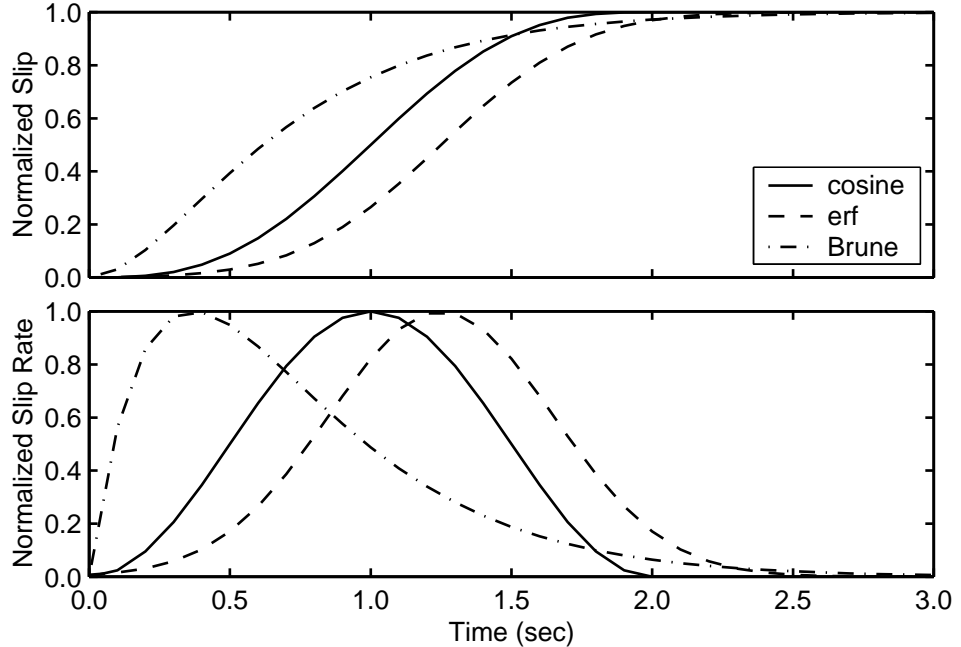


Figure 5.1: Slip and slip rate as a function of time for the three shapes of the slip time history functions. Each slip time history has the same maximum slip rate. We have set  $t_o = 0$  for convenience so slip begins at  $t = 0$ .

shape when simulating earthquakes with prescribed ruptures. Typically, we use the third shape, the integral of Brune's (1970) far field time function, for the slip time history. In contrast to the other two shapes, the acceleration is nonzero when slip begins. Additionally, the maximum slip rate occurs early in the time history, which leads to a non-symmetric slip rate. When a point starts to slip, we expect a nonzero acceleration, so this third shape matches more closely with what we expect physically.

The shape of the slip time history along with the rupture speed controls the frequency content of the waves generated in the domain. As discussed in section 2.3, we need ten nodes per wavelength for the shortest period shear wave. We now examine the frequency content of the slip time histories using the magnitude of the Fourier coefficients. Figure 5.2 shows the magnitude of the Fourier coefficients for each slip time history as a function of frequency. As we approach 0.75 Hz from the left, each distribution falls off at a different rate with the error function falling most rapidly and the integral of Brune's far field time function falling gradually. Above about 0.75 Hz, all three have nearly identical frequency distributions. The band limited

features of these three slip time histories match well with our constraint of simulating only the long-period ground motion due to the limited resolution of the finite-element mesh.

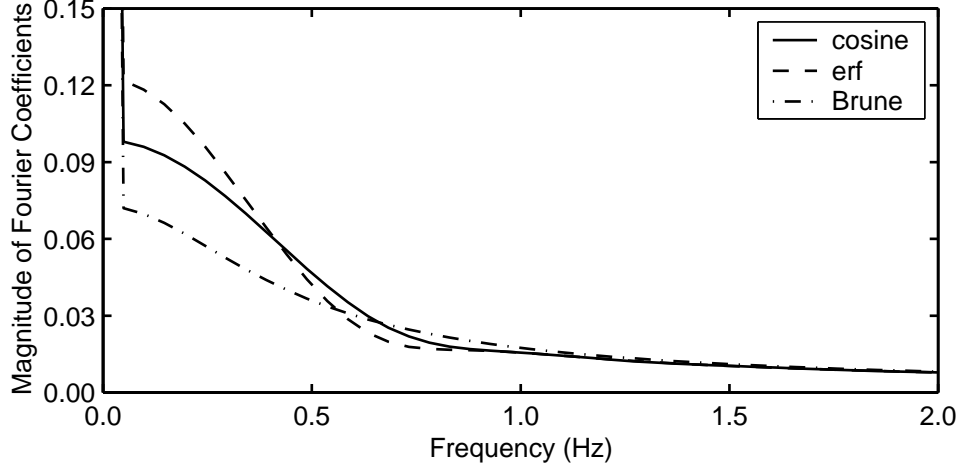


Figure 5.2: Fast Fourier transforms of the three shapes of slip time history functions using time histories with 1024 points, a time step of 0.02 sec, and the same time constants as those used in figure 5.1.

### 5.3 Slip Distribution

We use the spatial interpolation procedure outlined in section 2.5 to specify the final distribution of slip on the fault surface. With a dense population of points, we may independently specify the final slip at each node on the fault surface. In general, we want a relatively uniform distribution of slip that is tapered at the edges and may or may not contain some degree of heterogeneity. Consequently, we nearly always use three simple construction techniques to generate the spatial distribution. We taper the slip at three or four of the edges using an exponential function. Scaling the nominal value of slip produces the desired average value. Introducing circular asperities of various sizes and values gives heterogeneity to the distribution.

We taper the slip at the edges of the fault to emulate the smothering of the rupture at the boundaries of the fault surface. We taper all four edges when we bury the fault, but may allow the rupture to reach the surface when the fault reaches the surface by tapering only three edges, i.e., the lateral edges and the bottom. Equation (5.1) gives the final slip as a function of location along the strike,  $p$ , and location along the dip,  $q$ , where  $D_o$  denotes the nominal value of final slip and  $d$  denotes a distance which controls the rate of decay of slip. Figure 5.3 illustrates the coordinate system with the center of the fault given by  $(p_o, q_o)$ . The constant  $C$  controls on how many edges we taper the slip. We set  $C = 0$  when  $q > q_o$  and we want to taper the slip on only three edges, and we set  $C = 1$  when we want to taper the slip along all four edges.

$$D = D_o \left( 1 - \exp \left( \frac{-(p_o - |p - p_o|)}{d} \right) \right) \left( 1 - C \exp \left( \frac{-(q_o - |q - q_o|)}{d} \right) \right) \quad (5.1)$$

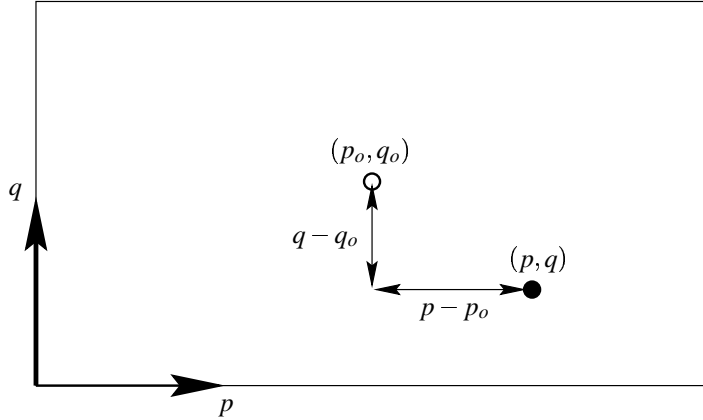


Figure 5.3: Strike and dip coordinates used in the slip tapering function.

We add circular asperities with different radii and heights to give heterogeneity to the distribution. Equation (5.2) gives the height of the asperity as a function of radius. The radius  $r_a$  denotes the radius at which the height has decayed to 5% of the peak value. Figure 5.4 illustrates the cross-section of an asperity of height  $D_a$  and radius  $r_a$ .

$$D = D_a \exp\left(-\frac{r^2}{r_o^2}\right), \text{ where} \quad (5.2)$$

$$r_o^2 = \frac{r_a^2}{\ln 20}$$

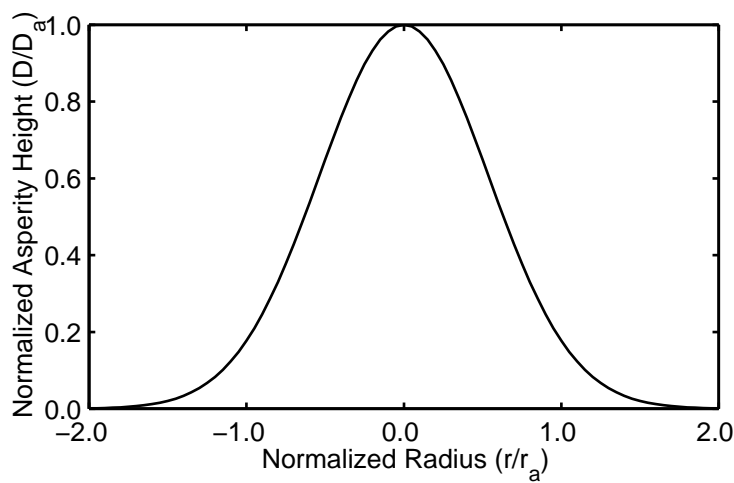


Figure 5.4: Cross-section of an asperity with height  $D_a$  and radius  $r_a$ .

## 5.4 Rupture Speed

We set the rupture speed relative to the local shear wave speed. If, instead, we choose to ignore variations in material properties and enforce a uniform rupture speed, we will have large variations in the rupture speed relative to the shear wave speed. Numerical modeling, such as that in chapter 8 and that by Burridge et al. (1979), suggests stable ruptures tend to propagate at nearly uniform speeds relative to the local shear wave speed. Consequently, we impose a uniform rupture speed relative to the local shear wave speed. The speed of the rupture governs when adjacent points on the fault should start to slip. This means that specifying the rupture speed involves setting the time when each point on the fault begins to slip. The rupture starts at the hypocenter, which we require to coincide with a node in the finite-element model. The following algorithm outlines how we prescribe the time when the sides of the fault begin to move relative to each other at each node on the fault.

1. Set the hypocenter node to start slipping at time  $t = 0$  ( $t_0 = 0$  in table 5.1).
2. Set the time when slip begins for all nodes adjacent to the hypocenter node. We use the finite-element faces on the fault plane to define adjacent nodes, which in this case means that the nodes lie on an edge of an element face on the fault plane. For node  $i$  adjacent to the hypocenter node, which lies on an edge of length  $l$  contained in element  $j$ , the time when slip begins is

$$t_0 = \min\left(\frac{l}{v_r \beta_j}, j = 1 \dots N\right), \quad (5.3)$$

where  $v_r$  is the rupture speed as a fraction of the local shear wave speed ( $\beta$ ) and  $N$  is the number of elements with edges on the fault plane containing the hypocenter node and node  $i$ .

3. Iterate to propagate the rupture front (start times) along each element face on the fault surface.
  - (a) For each element face on the fault plane, we check to see if we changed any of the start times for its nodes in the last iteration. If we did change at least one start time and have assigned start times to at least two nodes on the face (which we will denote as node A and node B), then we set the start time at the node with the latest start time (which we will denote as node C) using equation (5.4). We change the start time at node C only if the new start time is earlier than the previous one. We denote the start time at node A as  $t_A$ , the start time at node B as  $t_B$ , and the distance between node

$i$  and node  $j$  as  $d_{ij}$ . Figure 5.5 illustrates the other quantities used in equation (5.4).

$$t_0 = \frac{d_{CD}}{v_r \beta}, \text{ where} \quad (5.4)$$

$$d_{CD}^2 = r_b^2 + d_{BC}^2 - 2r_B d_{BC} \cos(\theta_1 + \theta_2)$$

$$r_A = v_r t_A$$

$$r_B = v_r t_B$$

$$b = \frac{1}{2} \left( d_{AB} + \frac{r_B^2 - r_A^2}{d_{AB}} \right)$$

$$\theta_2 = \arccos \left( \frac{b}{r_B} \right) \text{ from } \triangle ABC$$

$$\theta_1 = \arccos \left( \frac{d_{AB}^2 + d_{BC}^2 - d_{AC}^2}{2d_{AB}d_{BC}} \right) \text{ from } \triangle BCD$$

- (b) Find the number of start times we changed this iteration. If we did not change any start times, then we are done. Otherwise, continue iterating.

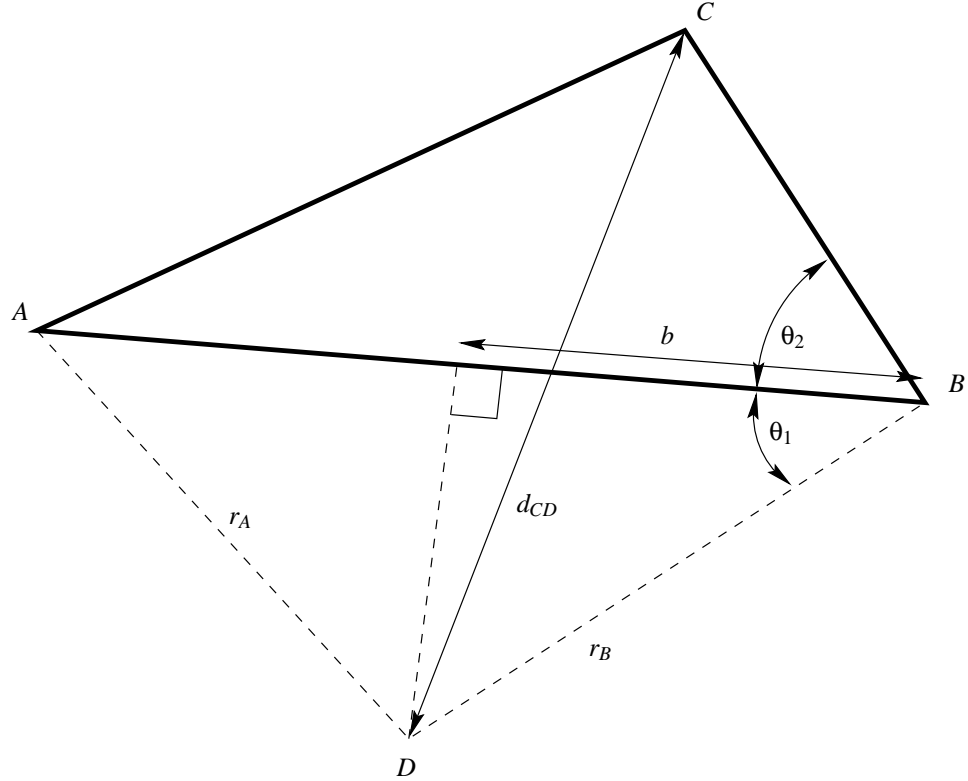


Figure 5.5: Diagram of the quantities used to propagate rupture front along an element face. The element face is  $\triangle ABC$ , point D is the apparent hypocenter, and we set the start time at node C.

## Chapter 6 Validation of Simulation Software

In this chapter we discuss the validation of the simulation software in terms of how well it succeeds in modeling the wave propagation. We check the ground motion time histories to verify that they accurately predict both the arrivals and amplitudes of the various phases. Additionally, we examine the final displacements in the ground motions to see how well they match those predicted by a static analysis. The performance of the absorbing boundary will also be evident in the ground motions. For the validation we solve the problem of a propagating rupture on a buried, dipping, finite fault in a homogeneous half-space.

### 6.1 Domain Geometry

We model a region 60 km long by 60 km wide down to a depth of 24 km. As shown by figure 6.1, we bury the 28 km long and 18 km wide fault 8.6 km below the surface. The fault strikes west and dips 23 degrees to the north. We impose a rake angle of 105 degrees from the strike; this corresponds to  $\phi = 270$  degrees,  $\delta = 23$  degrees, and  $\lambda = 105$  degrees in figure 2.4. We use homogeneous material properties with a dilatational wave speed of 5.85 km/sec, a shear wave speed of 3.40 km/sec, and a density of 2500 kg/m<sup>3</sup>. These material properties correspond to those typically found at depths of 10–20 km.

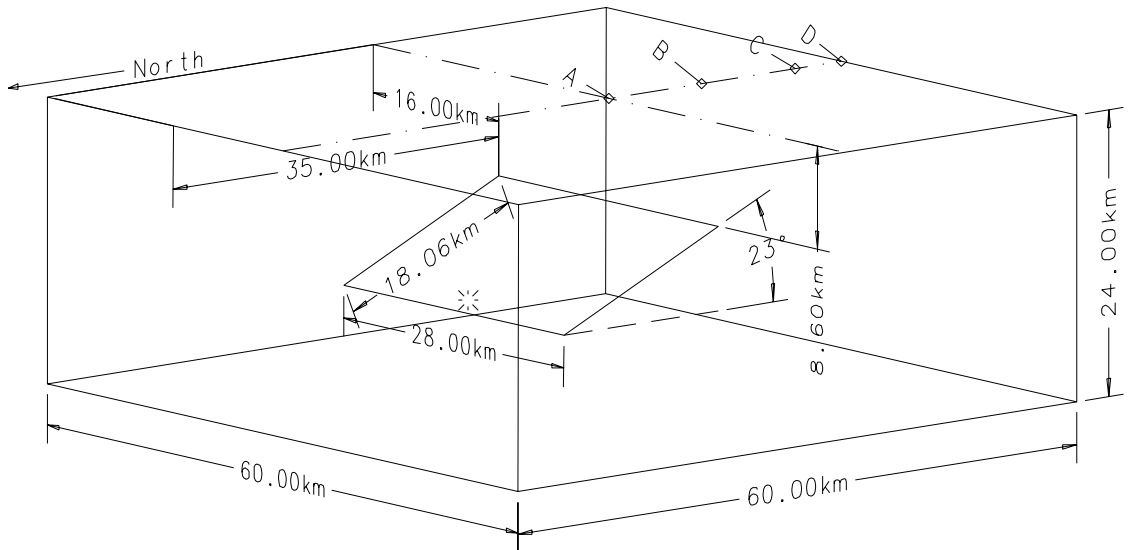


Figure 6.1: Orthographic view of domain geometry used for validation of the simulation software. The star denotes the hypocenter. We examine the final displacements along the two dash-dotted lines on the ground surface and velocity time histories at sites A–D.

We created the finite-element model at a coarse resolution and used the 2x refinement procedure discussed in section 3.5 to globally refine the mesh to a resolution of ten nodes per wavelength for a shear wave with a period of 2.0 sec. The coarse mesh contains 6389 nodes and 31,879 elements; the mesh at fine resolution contains approximately 400,000 nodes and two million elements. The simulation took 1.2 hours using 64 processors on the Intel Paragon or 40 minutes using 12 processors on the Hewlett Packard Exemplar at the CACR.

## 6.2 Validation of Ground Motion Time Histories

We prescribed the slip at each point on the fault using the integral of Brune's far field time function with a final slip of 1.0 m and a maximum slip rate of 0.74 m/sec. The hypocenter lies along the east-west centerline of the fault at a depth of 15 km. The rupture propagates away from the hypocenter at a uniform speed of 2.7 km/sec, which is 80% of the shear wave speed. We compare the ground motions generated using the finite-element model with ones generated using point dislocation solutions obtained by discrete-wave-number finite-element techniques.<sup>1</sup>

We compare velocity time histories at four sites on the ground surface, labeled A, B, C, and D in figure 6.1. Site A lies directly above the top of the fault, and site D lies at the absorbing boundary. Figures 6.2–6.5 show the north-south and vertical components of the velocity time histories at each site for the two simulation methods. All of the time histories have been low-pass filtered using a Butterworth filter with a corner frequency of 0.5 Hz. We do not see any evidence of delays in arrival of the phases, and the velocity amplitudes agree reasonably well. We want the best accuracy where the motion is most severe, and, indeed, this is the case. The time histories for the vertical component match very well, especially close to the fault. The limited amount of energy arriving late in the velocity time histories of the finite-element simulation confirms that the absorbing boundaries adequately prevent reflections from the lateral sides and the bottom of the domain. At the absorbing boundary, site D, the velocity time histories agree less well, but as we noted, the absorbing boundary does its job. Therefore, we find the level of accuracy of the ground motions acceptable, provided that we don't use the sites on the absorbing boundary in any analysis.

## 6.3 Validation of Static Displacements

In addition to verifying the velocity time histories, we also compare the final displacements from the finite-element simulation with the displacements computed from a static analysis. For the static analysis we compute the displacements from point source dislocations using the analytical solution given by Heaton and Heaton (1989). We uniformly distribute 2016 point sources over the fault surface to mimic the uniform slip of 1.0 m in the finite-element model. We examine all three components of displacement along the north-south

---

<sup>1</sup>David Wald at the United States Geological Survey office in Pasadena provided these time histories. More details regarding the method he used may be found in the paper by Hall et al. (1995).

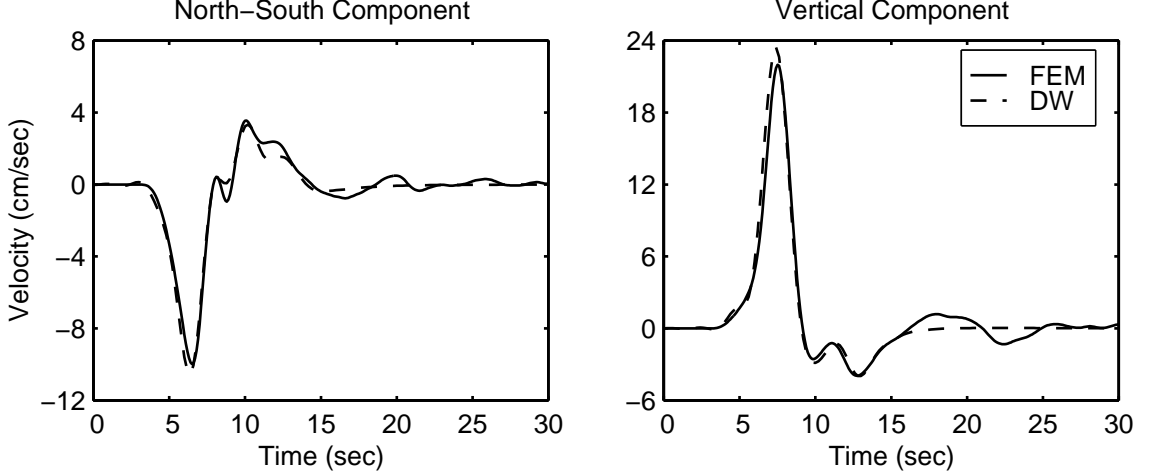


Figure 6.2: Velocity time histories in the north-south and vertical directions at site A, which is located directly above the top of the fault. The solid lines indicate the time histories from the finite-element solution, and the dashed lines indicate the time histories from the discrete-wave-number solution.

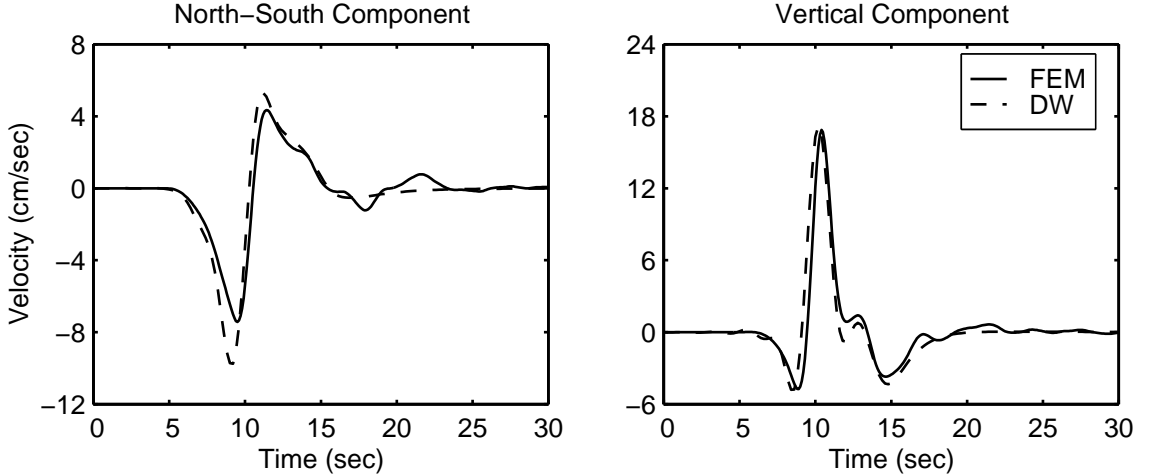


Figure 6.3: Velocity time histories in the north-south and vertical directions at site B, which is located 10 km south of the top of the fault. The solid lines indicate the time histories from the finite-element solution, and the dashed lines indicate the time histories from the discrete-wave-number solution.

running centerline of the domain and along the east-west line along the top of the fault, as denoted by the dash-dotted lines in figure 6.1.

Figure 6.6 shows the comparison between the horizontal components along both lines. Figure 6.7 and figure 6.8 demonstrate the vertical displacements also match well along the north-south and east-west lines. The rake angle of 105 degrees deforms the ground surface to the south and slightly to the east (visible in figure 6.6 and figure 6.8). Approaching the edges of the domain, the north-south displacements from the finite-element model gradually diverge from those of the static analysis, because the absorbing boundaries do not model the stiffness of the truncated portion of the domain as discussed in section 2.3.3. This leads to a slightly slower decay with distance from the source in the final displacements of the finite-element model

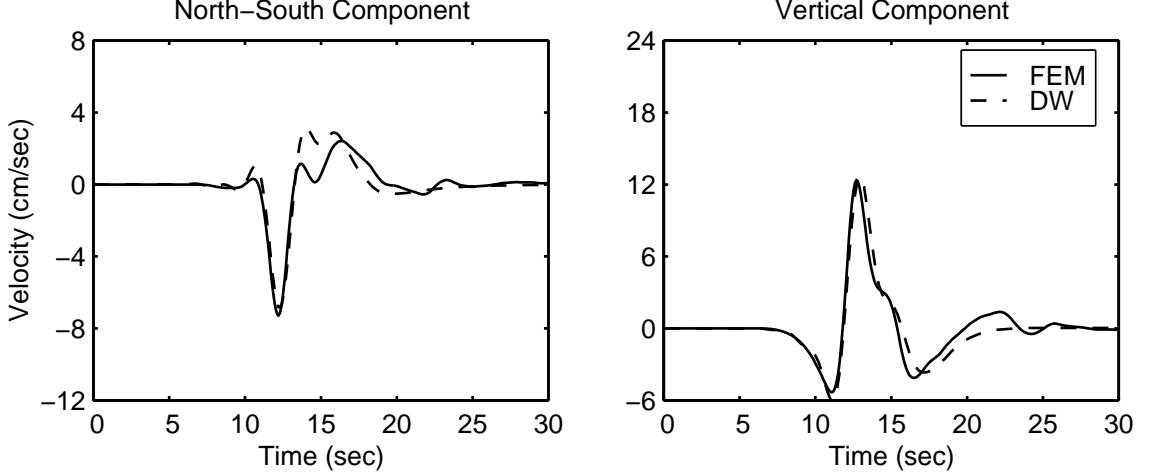


Figure 6.4: Velocity time histories in the north-south and vertical directions at site C, which is located 20 km south of the top of the fault. The solid lines indicate the time histories from the finite-element solution, and the dashed lines indicate the time histories from the discrete-wave-number solution.

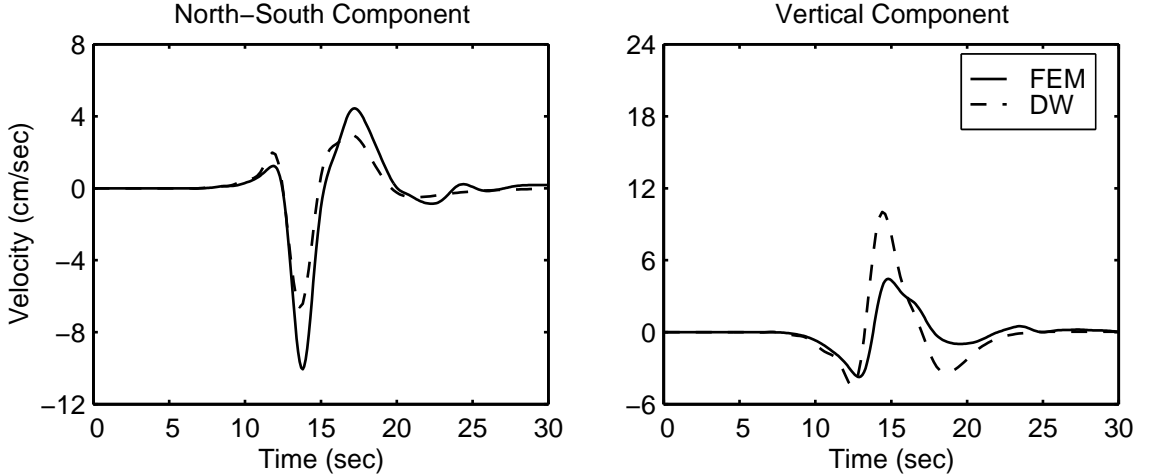


Figure 6.5: Velocity time histories in the north-south and vertical directions at site D, which is located on the absorbing boundary and 25 km south of the top of the fault. The solid lines indicate the time histories from the finite-element solution, and the dashed lines indicate the time histories from the discrete-wave-number solution.

compared to the analytical solution. The east-west displacements exhibit excellent agreement across the domain.

## 6.4 Discussion

The results from the finite-element simulation show close agreement with those from the discrete-wave-number technique and the static analysis. The absorbing boundary effectively prevents contamination of the solution in the interior of the domain from reflections off the lateral sides and the bottom of the domain.

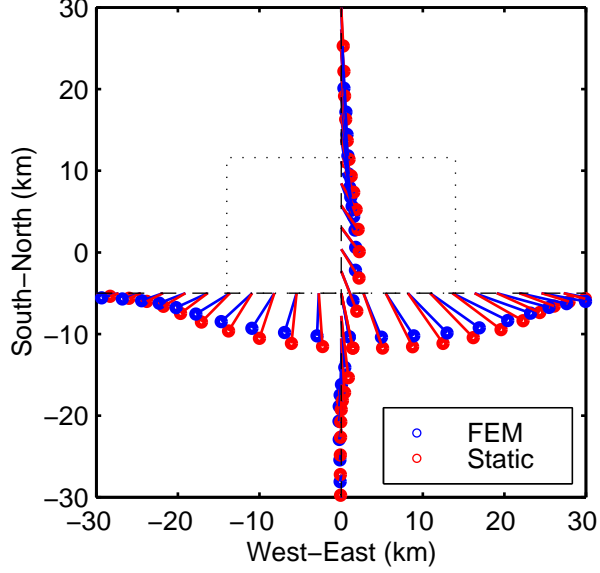


Figure 6.6: Horizontal components of the final (static) displacements along two lines on the ground surface. The dotted line indicates the projection of the fault plane onto the ground surface. The north-south line passes through the center of the domain, and the east-west line along the top of the fault. The thin, solid lines show the original locations of the lines. The displacements have been scaled by a factor of 50,000.

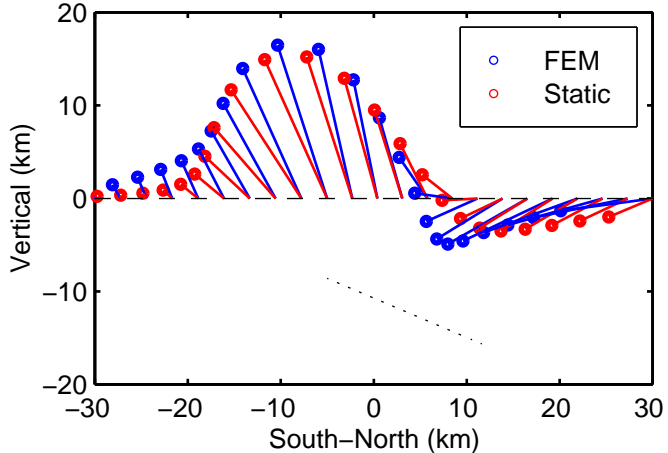


Figure 6.7: Vertical and north-south components of the final (static) displacements on the ground surface along the north-south line passing through the center of the domain. The dotted line indicates the projection of the fault plane onto the vertical slice. The displacements have been scaled by a factor of 50,000.

Comparison of the velocity time histories also suggests that we cannot use the ground motions at the absorbing boundaries for any analyses because the dampers distort the time histories. Additionally, the static displacements near the edges of the domain have limited accuracy, as a result of the lack of stiffness provided by the absorbing boundary. Hence, the simulation software provides accurate results as long as we ignore the ground motions very close to the edges of the domain.

In the above validation we use homogeneous material properties. We also want to simulate the ground

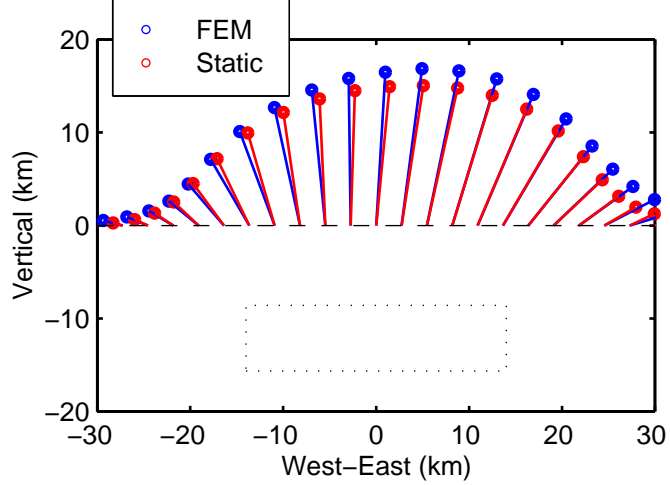


Figure 6.8: Vertical and east-west components of the final (static) displacements on the ground surface along the east-west line along the top of the fault. The dotted line indicates the projection of the fault plane onto the vertical slice. The displacements have been scaled by a factor of 50,000.

motions in heterogeneous domains with the same confidence in the accuracy of the ground motions. Because we assume homogeneous material properties within an element, varying the material properties involves simply setting the properties in each element according to some specified spatial distribution. As discussed in section 2.3, the node spacing governs the accuracy of the ground motions, so we limit the errors in the simulation by adjusting the node spacing with the material properties. In other words, in order to handle heterogeneous material properties with the same level of accuracy, all we need to do is to insure that we maintain the appropriate node spacing throughout the domain.

# Chapter 7 Sensitivity Study of Near-Source Ground Motion with Prescribed Ruptures

We now use two sets of prescribed rupture simulations to study the sensitivity of the long-period near-source ground motions to variations in the earthquake source parameters. We want to understand the variability in the near-source ground motions for changes in the seismic source and identify those parameters that most strongly influence the near-source ground motions. We systematically vary the seismic source parameters for both a strike-slip fault and a shallow dipping thrust fault. We select different hypocenter locations, maximum slip rates, rupture speeds, spatial distributions of the final slip, average slips, and the depth of the top of the fault. Additionally, we compare the ground motions from a layered half-space with those from a homogeneous half-space.

## 7.1 Strike-Slip Fault

The geometry of the strike-slip fault roughly matches the combined fault segments that ruptured in the June 1992 Landers event. We enclose the 60 km long and 15 km wide fault in a domain 100 km long, 40 km wide, and 32 km deep as shown in figure 7.1. We impose pure right-lateral slip on the vertical fault that strikes north. We offset the fault 10 km to the south from the center of the domain in anticipation of locating the hypocenters on the southern half of the fault and generating the largest displacements near the north end of the fault.

### 7.1.1 Finite-Element Model

We use two different finite-element models, one for the layered material properties case and one for the homogeneous material properties case. Table 7.1 and figure 7.2 show the mass density, shear wave speed, and dilatational wave speed as a function of depth for the layered half-space. For the homogeneous half-space we simply use the material properties that are associated with a depth of 6.0 km in the layered half-space.

We use IDEAS to create the finite-element model at coarse resolution and the 4x refinement procedure outlined in section 3.5 to create a mesh with the appropriate node spacing to model wave propagation with periods down to 2.0 sec. Table 7.2 gives the sizes of the finite-element models at coarse and fine resolution for the layered and homogeneous half-spaces. Figure 7.3 illustrates the partition of the finite-element mesh for the layered half-space among 256 processors using the inertial bisection algorithm. Each simulation took 2.8 hours using 256 processors of the Intel Paragon at the CACR.

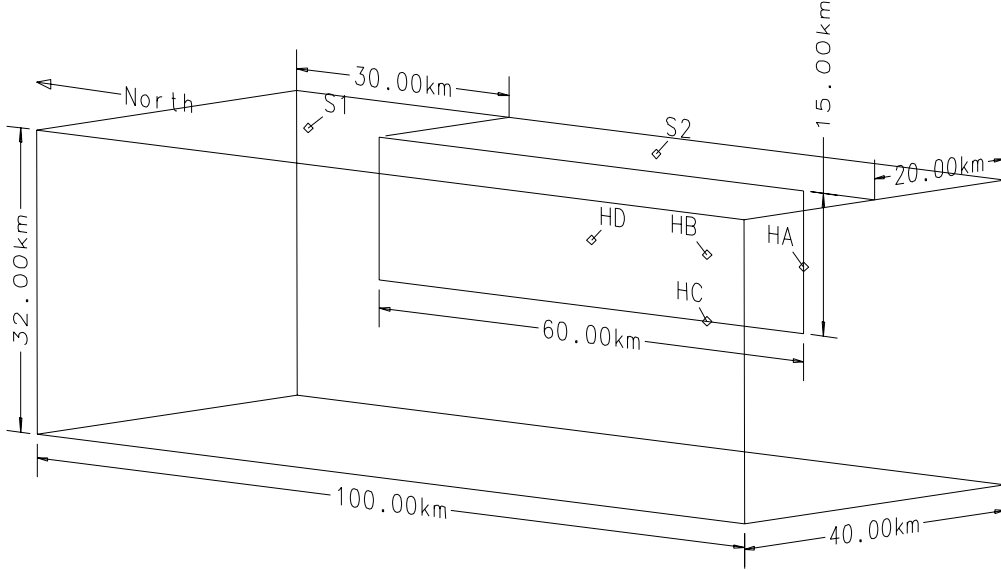


Figure 7.1: Orthographic projection of the domain geometry for the strike-slip fault for the case where the top of the fault reaches the ground surface. The labels HA through HD denote the various hypocenter locations. We will examine the waveforms at sites S1 and S2.

Depth (km)	Dilatational Wave Speed (km/sec)	Shear Wave Speed (km/sec)	Mass Density (g/cm <sup>3</sup> )
0.0	1.80	0.70	1.50
3.0	4.50	2.60	2.00
6.0	5.70	3.30	2.45
20.9	5.85	3.40	2.50
21.0	6.45	3.75	2.60
32.0	6.74	3.92	2.63

Table 7.1: Density, shear wave speed, and dilatational wave speed control elevations for the layered half-space.

	Homogeneous		Layered	
	Course	Fine	Course	Fine
# Nodes	9500	610,000	33,000	2.1 million
# Elements	48,000	3.0 million	160,000	10 million

Table 7.2: Sizes of the finite-element models of the layered and homogeneous half-spaces at coarse and fine resolution.

### 7.1.2 Earthquake Source Parameters

We vary five earthquake source parameters: the location of the hypocenter, the rupture speed, the maximum slip rate, the distribution of slip, and the fault depth. As shown in table 7.3, 15 of the simulations use the layered half-space model, while the other 2 use the homogeneous half-space model. The base case, scenario baseII, features a homogeneous slip distribution that is tapered on three edges, a rupture speed of 80% of the local shear wave speed, a maximum slip rate of 1.5 m/sec, and a hypocenter located mid-depth at the south

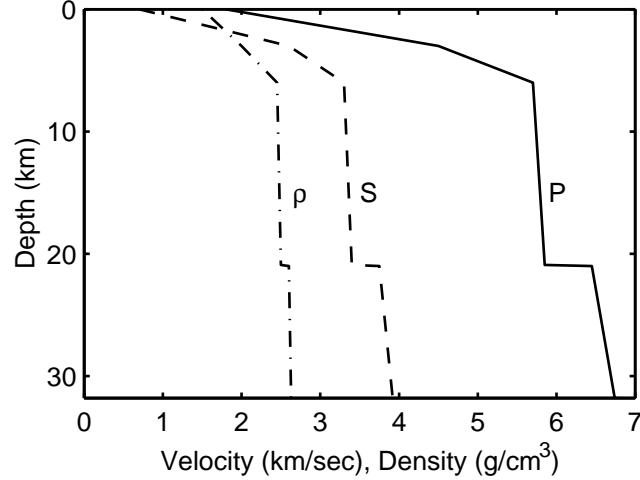


Figure 7.2: Density ( $\rho$ ), shear wave speed (S), and dilatational wave speed (P) as a function of depth for the layered half-space.

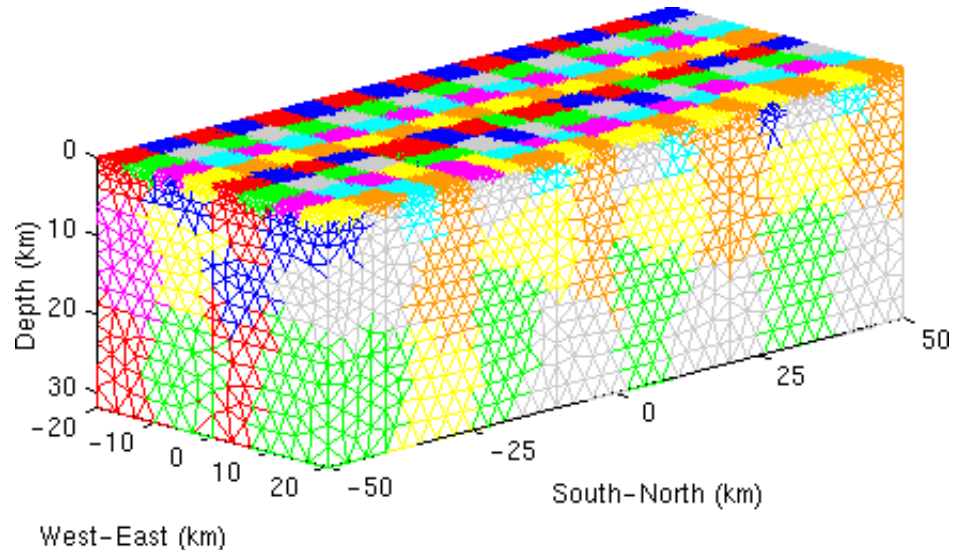


Figure 7.3: Partitioning of the coarse finite-element model among 256 processors for the layered half-space using the inertial bisection algorithm. Each color patch identifies the elements of one processor.

edge of the fault (hypocenter HA). For each parameter we generally vary the value equally about the base case, e.g., we select maximum slip rates of 2.0 m/sec and 1.0 m/sec about the base case value of 1.5 m/sec.

### Hypocenter Locations

The four hypocenter locations on the southern half of the fault are labeled HA through HD in figure 7.1, and the precise locations are given in figure 7.4. Hypocenter HA sits mid-depth at the southern edge of the fault, hypocenter HB sits mid-depth at the southern quarter point, hypocenter HC sits at the bottom of the fault at the southern quarter point, and hypocenter HD sits at the center of the fault.

Scenario	Slip Pattern	Rupture Speed % of $\beta$	Maximum Slip Rate (m/sec)	Hypocenter Location	Fault Depth (km)	Material Properties	Mom. Mag.
base	unitaper	80	1.5	HA	0.0	layered	7.0
baseII	semitaper	80	1.5	HA	0.0	layered	7.0
vr70	semitaper	70	1.5	HA	0.0	layered	7.0
vr90	semitaper	90	1.5	HA	0.0	layered	7.0
vs10	semitaper	80	1.0	HA	0.0	layered	7.0
vs20	semitaper	80	2.0	HA	0.0	layered	7.0
hymq	semitaper	80	1.5	HB	0.0	layered	7.0
hybq	semitaper	80	1.5	HC	0.0	layered	7.0
hymc	semitaper	80	1.5	HD	0.0	layered	7.0
sliptop	weakupper	80	1.5	HA	0.0	layered	7.0
slipbot	weaklower	80	1.5	HA	0.0	layered	7.0
sliphet	strongheter	80	1.5	HA	0.0	layered	7.0
slip3	semitaper3	80	1.5	HA	0.0	layered	7.1
fault4km	unitaper	80	1.5	HA	4.0	layered	7.1
fault8km	unitaper	80	1.5	HA	8.0	layered	7.1
homo	semitaper	80	1.5	HA	0.0	homo.	7.1
hvr90	semitaper	90	1.5	HA	0.0	homo.	7.1

Table 7.3: Summary of the parameters for the prescribed rupture simulations on the strike-slip fault.

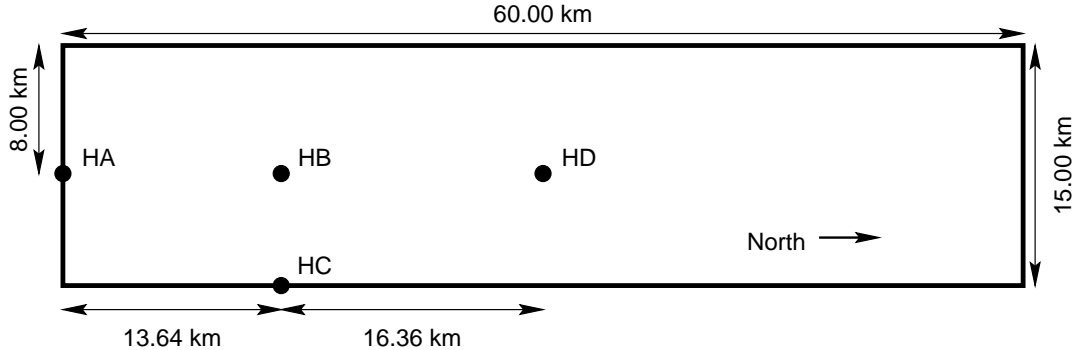


Figure 7.4: Hypocenter locations on the fault plane.

### Slip Time Histories and Rupture Speeds

We use the integral of Brune's far field time function (discussed in section 5.2) for the slip time histories. For each simulation we set a spatially uniform maximum slip rate of 1.0 m/sec, 1.5 m/sec, or 2.0 m/sec. Additionally, we independently choose a rupture speed of 70%, 80%, or 90% of the local shear wave speed. The median values of 1.5 m/sec and 80% of the shear wave speed correspond to a typical slip rate and average rupture speed found in inversions of strong ground motions (Heaton 1990). We choose to keep the maximum slip rate uniform over the fault surface, because great uncertainty still exists regarding the duration of slip for very shallow rupture. Source inversions of the Landers earthquake (Wald and Heaton 1994) and the Kobe earthquake (Wald 1996) inferred slip durations of more than four seconds for the shallow slip, but eyewitnesses reported slip durations of one second or less for the 1990 Luzon earthquake in the Phillipines

(Yomogida and Nakata 1994) and the 1983 Borah Peak earthquake (Wallace 1984).

We determine the final slip at each node on the fault based on the given spatial distribution of slip. The six slip distributions include: a homogeneous distribution that is tapered on all four edges (figure 7.5), two homogeneous distributions that are tapered on three edges (figure 7.6 and figure 7.7), two weakly heterogeneous distributions (figure 7.8 and figure 7.9), and a strongly heterogeneous distribution (figure 7.10). For the heterogeneous distributions, we start with a homogeneous slip distribution with a nominal value and add 30 asperities with uniform random distributions of radii (as given in table 7.4), heights (as given in table 7.4), strike locations between 2.0 km and 58 km, and dip locations between 0.0 km and 13 km. The weakly heterogeneous slip distributions have a bias towards larger slips on either the upper half of the fault (weakupper<sup>1</sup>) or the lower half of the fault (weaklower<sup>2</sup>). We adjust the height of all asperities that lie in the dip range of the bias by the amount given in table 7.4.

Distribution	Nominal Slip (m)	Asperity Heights (m)	Asperity Radii (km)	Bias	
				Dip (km)	Height Adj. (m)
weakupper	1.57	-0.25–1.0	5.0–10.0	2.0–7.5	+0.25
weaklower	1.52	-0.25–1.0	5.0–10.0	7.5–13.0	+0.25
strongheter	0.28	0.0–3.2	3.0–8.0	N/A	0.0

Table 7.4: Asperity parameters used in the heterogeneous slip distributions on the strike-slip fault.

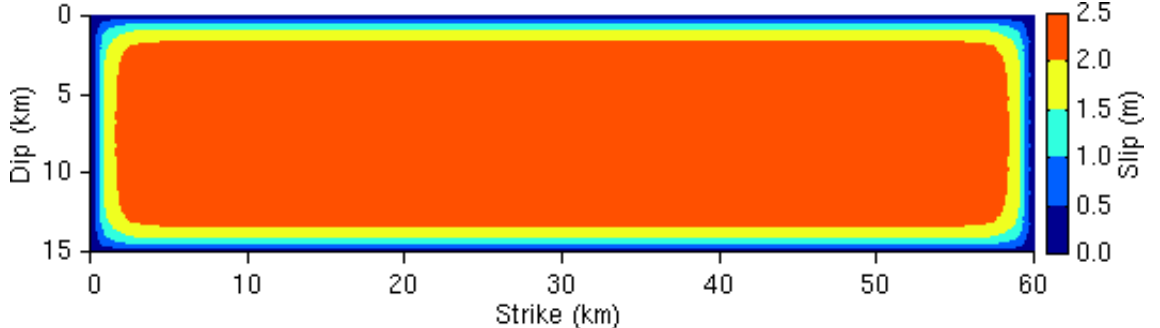


Figure 7.5: Homogeneous slip distribution unitaper which is tapered on all four edges with an average slip of 2.0 m and a maximum slip of 2.5 m.

## Fault Depth

We place the top of the fault at three different depths while maintaining the same length and width. When we bury the fault 8.0 km below the ground surface, the material properties do not vary appreciably on the fault surface. Consequently, the rupture speed is nearly uniform. When we bury the fault 4.0 km below the ground surface, the material becomes softer in the top 2.0 km of the fault surface, and the rupture slows

<sup>1</sup>Weak refers to the heterogeneity, and upper refers to the region of greater slip.

<sup>2</sup>Weak refers to the heterogeneity, and lower refers to the region of greater slip.

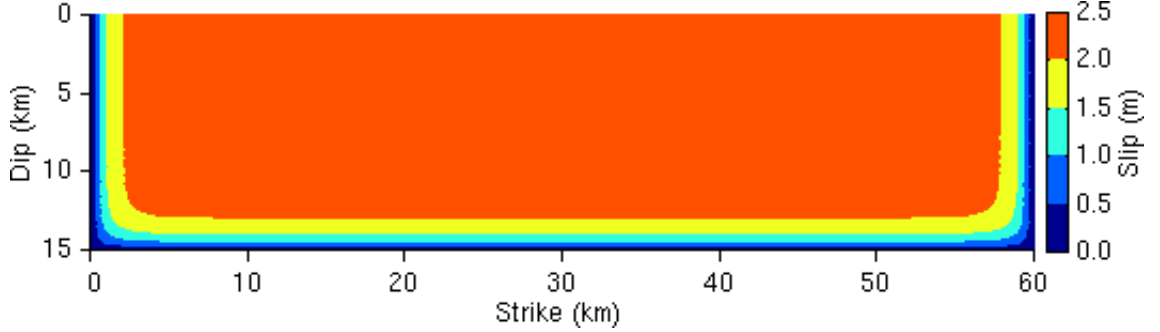


Figure 7.6: Homogeneous slip distribution semitaper which is tapered on three edges with an average slip of 2.0 m and a maximum slip of 2.3 m.

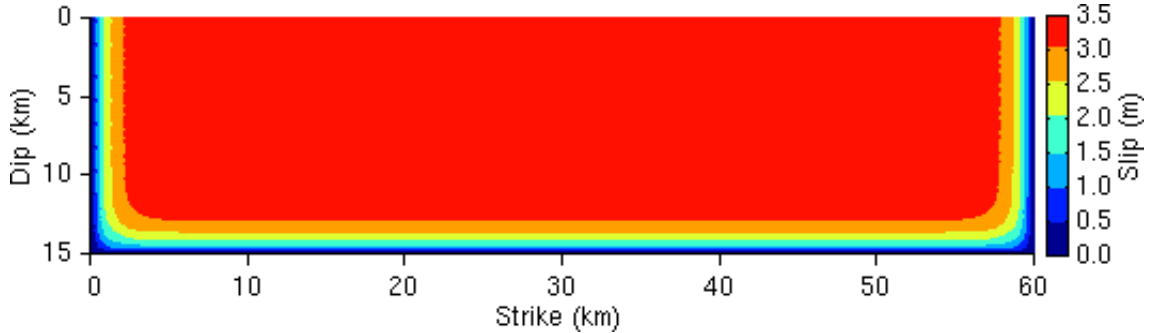


Figure 7.7: Homogeneous slip distribution semitaper3 which is tapered on three edges with an average slip of 3.0 m and a maximum slip of 3.4 m.

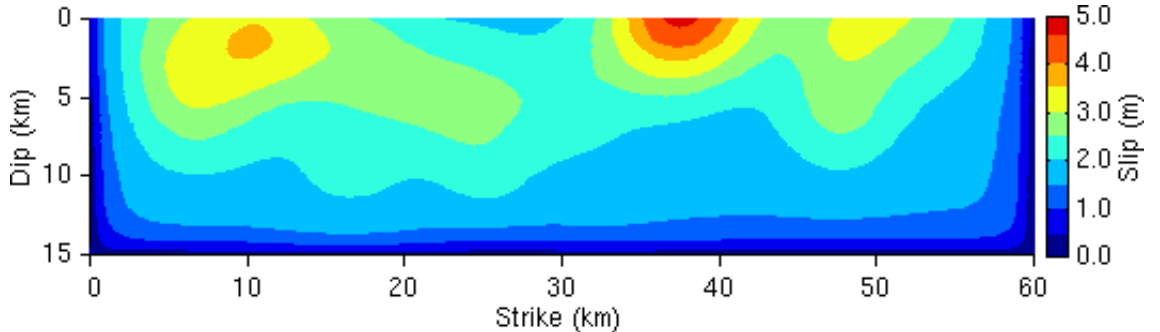


Figure 7.8: Weakly heterogeneous slip distribution weakupper which is tapered on three edges with an average slip of 2.0 m, a maximum slip of 4.7 m, and a bias towards slip near the surface.

down slightly as it runs through this region. When the fault surface reaches the ground surface, the material becomes progressively softer in the top 6.0 km. The slower rupture speed near the surface causes significant curvature in the rupture front.

### 7.1.3 Simulation Results

We will examine only the base case, scenario baseII, in detail. For the other simulations, we examine groups of scenarios in order to study the sensitivity of the ground motions to a single parameter. For all of the

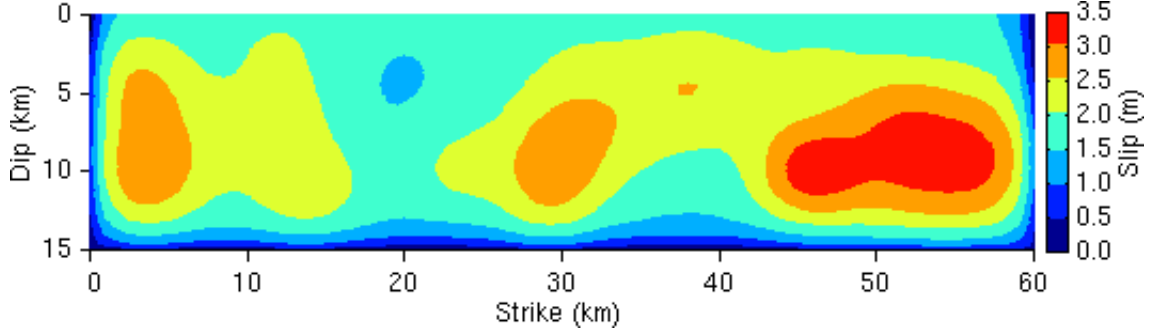


Figure 7.9: Weakly heterogeneous slip distribution which is tapered on three edges with an average slip of 2.0 m, a maximum slip of 3.4 m, and a bias towards slip at depth.

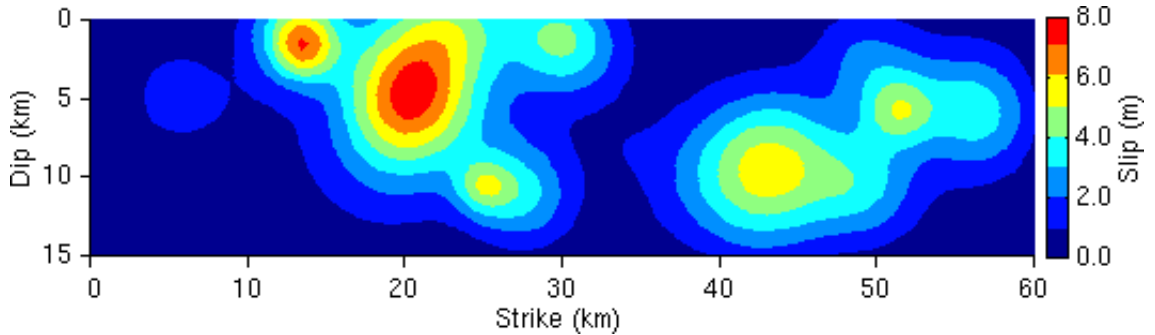


Figure 7.10: Strongly heterogeneous slip distribution which is tapered on three edges with an average slip of 2.0 m and a maximum slip of 7.8 m.

scenarios with the top of the fault at the ground surface and an average slip of 2.0 m, the earthquakes have a moment magnitude of 7.0. Thus, for these scenarios, any variability in the ground motions is independent of the moment magnitude. Each simulation took 2.8 hours using 256 processors on the Intel Paragon at the CACR.

### Base Case

We start with an examination of the slip rate on the fault as a function of time. The snapshots of slip rate, shown in figure 7.11, clearly identify the curvature of the rupture front. The rupture propagates slower in the softer material in the top 6.0 km of the domain, so that the rupture at the surface falls farther and farther behind the rupture at depth. The width of the rupture front narrows in the softer material in response to the slower rupture speed. The jaggedness of the rupture that begins at around sixteen seconds comes from propagating the rupture front with an increasing curvature through the finite elements. Furthermore, as the rupture front nears the edge of the domain, the final slips decrease while the maximum slip rate remains uniform, so the contours of slip rate in figure 7.11 no longer represent the location of the rupture front.

The velocity on the ground surface shows the propagation of the shear wave and a train of surface waves. Figure 7.12 gives snapshots in time of the magnitude of the velocity vector at each point on the ground surface. The velocities have been filtered using a fourth-order Butterworth filter with a corner frequency of

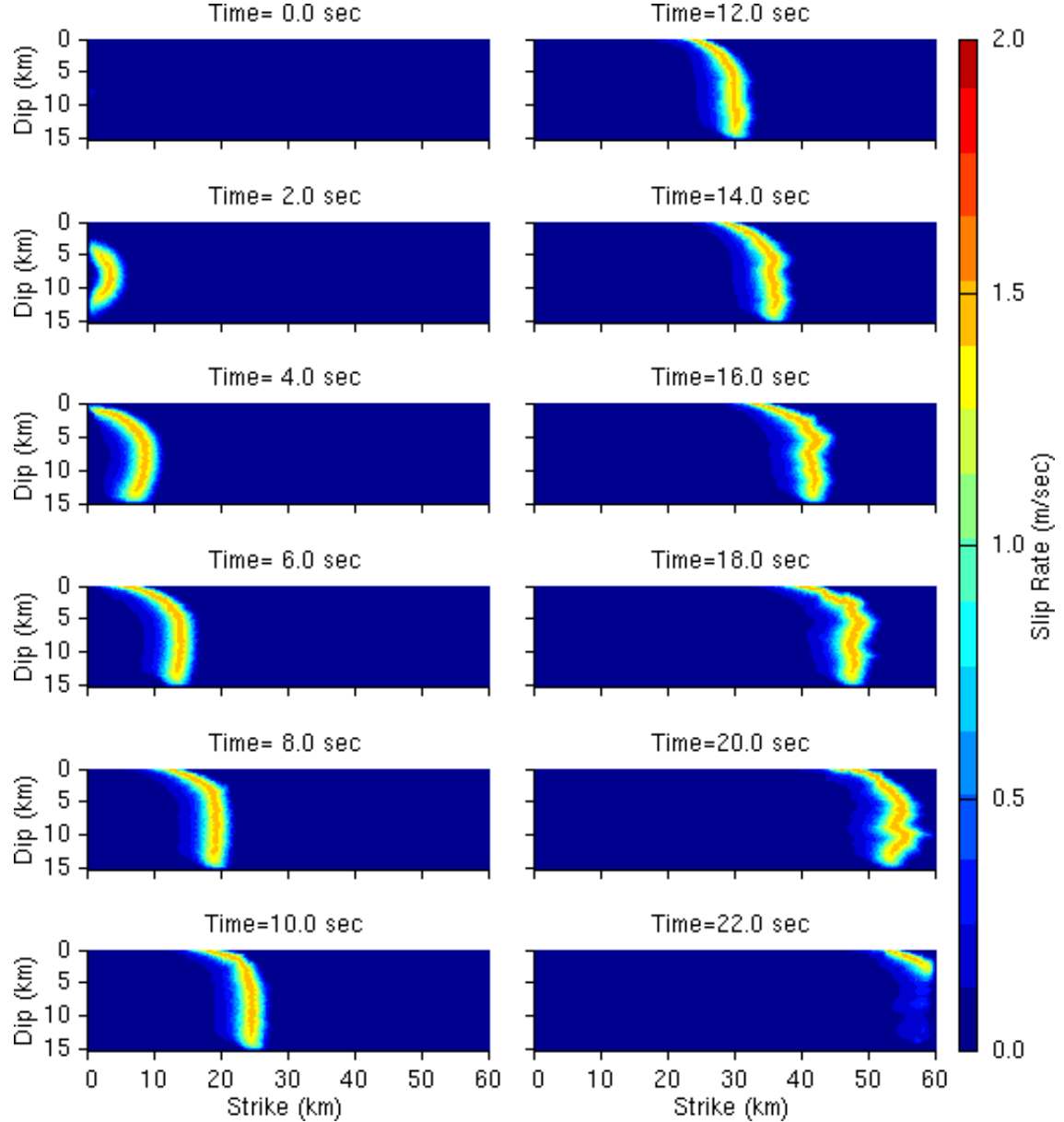


Figure 7.11: Snapshots of slip rate on the fault surface for scenario baseII.

0.5 Hz. The magnitude of the velocity near the fault increases as the rupture progresses and dies quickly after the rupture reaches the north end of the fault at about 24 sec. The most severe ground motions are concentrated close to the fault. The rupture excites trains of surface waves that propagate behind the shear wave and create a wedge-shaped interference pattern. While less than the amplitude of the shear wave, the amplitudes of some of the surface waves do exceed 1.0 m/sec starting at around thirteen seconds.

The maximum horizontal displacements and the maximum horizontal velocities on the ground surface (figure 7.13) give a clear picture of the effect of directivity on the ground motions. Both the maximum displacements and the maximum velocities are symmetric about the fault plane due to the symmetry of the

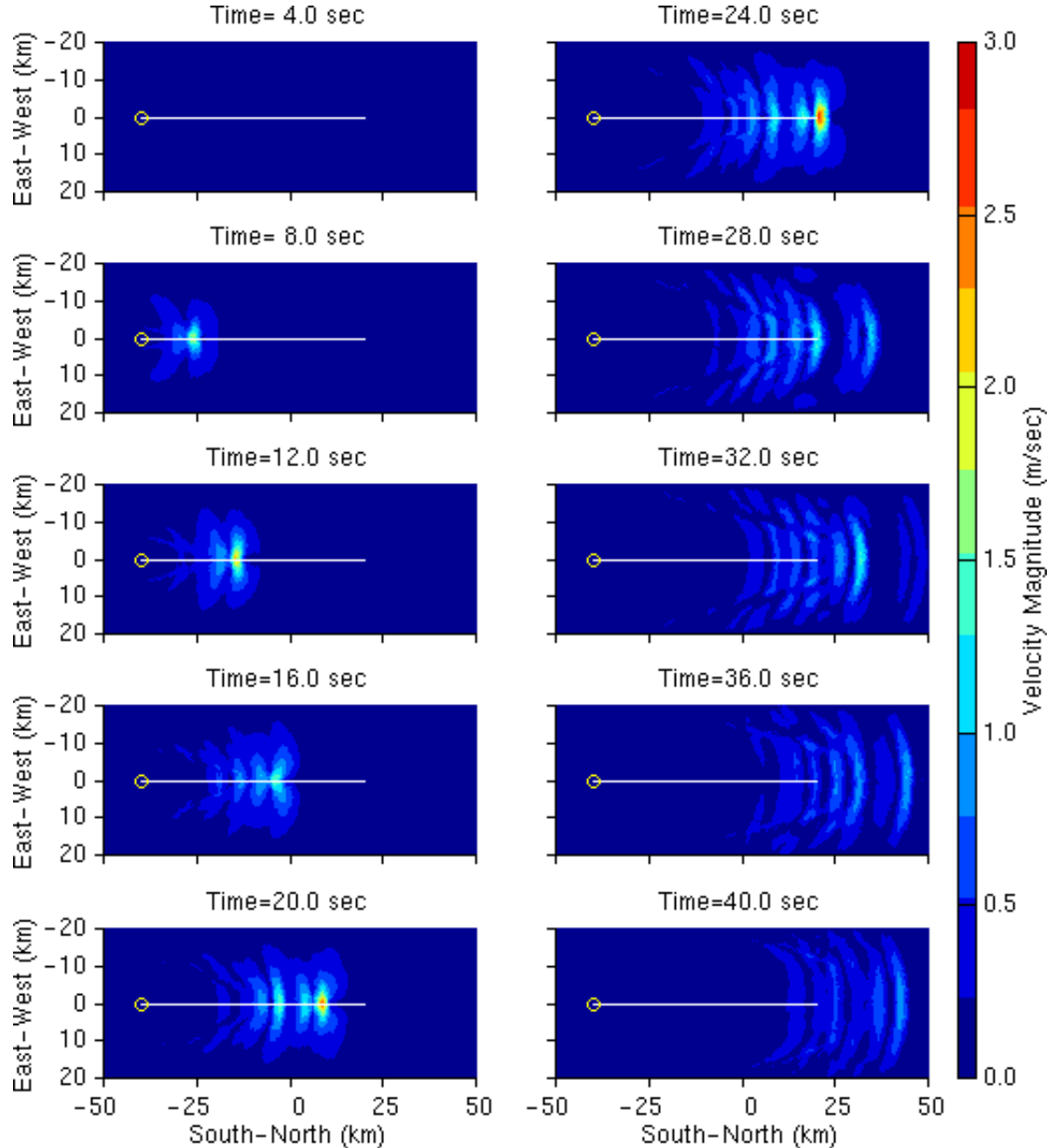


Figure 7.12: Snapshots of the magnitude of the velocity vector at each point on the ground surface for scenario baseII. The white line indicates the projection of the fault onto the ground surface, and the yellow circle identifies the epicenter.

problem. The shear wave with particle motion perpendicular to the fault plane (east-west direction) builds as the rupture propagates. This leads to a maximum horizontal displacement of 2.2 m at sites 1.7 km east or west of the north end of the fault. The maximum velocity of 2.9 m/sec occurs slightly farther south at sites located 6.7 km south and 0.5 km east or west of the north end of the fault. The maximum velocities (filtered to periods longer than 2.0 sec) exceed 1.0 m/sec over an area of 700 square kilometers. In contrast to the maximum displacements that increase along the strike of the fault, the maximum velocities increase,

decrease, and then increase again along the strike of the fault. The changing curvature of the rupture front disrupts the reinforcement of the shear wave by the propagating rupture and causes the reduction in the maximum velocities on the ground surface above the center of the fault. However, the reinforcement of the rupture front stabilizes, and the velocities build for approximately the last 25 km of the rupture.

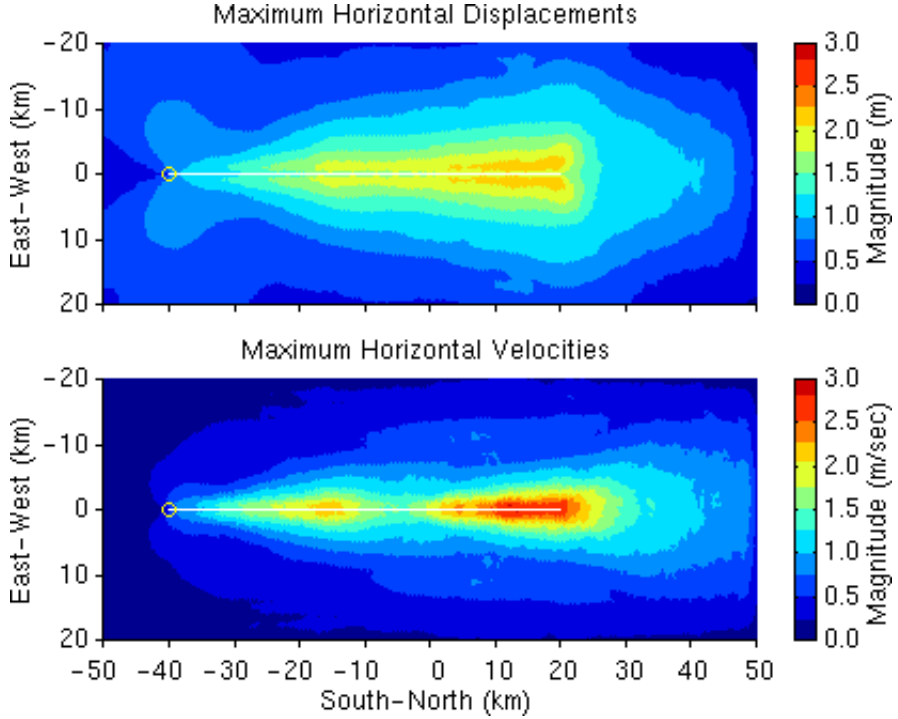


Figure 7.13: Maximum magnitudes of the horizontal displacement and velocity vectors at each point on the ground surface for scenario baseII. The white line indicates the projection of the fault plane onto the ground surface, and the yellow circle identifies the epicenter.

The directivity of the rupture causes large variations in the ground motions with changes in azimuth (angle between the projection of the slip vector onto the ground surface and the vector from the epicenter to the site). We will consider two sites located 10 km from the edge of the fault but with azimuths that differ by 90 degrees; the sites are labeled S1 and S2 in figure 7.1. Site S1 lies 10 km north of the north end of the fault (azimuth of 0 degrees) and site S2 lies 10 km east of the fault center (azimuth of 90 degrees). Figure 7.14 shows all three displacement and velocity components for the two points. Both the displacements and velocities have been filtered using a fourth-order Butterworth filter with a corner frequency of 0.5 Hz.<sup>3</sup> The north-south and vertical components are negligible at site S1 because the site falls on the north-south running line of symmetry. The vertical component at site S2 is also very small. This means that at site S1 the only surface waves we observe are Love waves, while at site S2 we observe both Love and Rayleigh waves.

The most important difference between the two sites is the fact that, while both have similar peak horizontal displacements (1.2 m at site S1 and 0.90 m at site S2), the peak horizontal velocity at site S1 is 2.6 times

---

<sup>3</sup>We use the same digital filter on all subsequent displacement and velocity time histories.

greater than the peak horizontal velocity at site S2 (1.2 m/sec at site S1 versus 0.48 m/sec at site S2). The directivity effect causes the shear wave energy from all points on the fault to arrive at nearly the same time at site S1. At site S2 the energy arrives over a longer interval of time which reduces the peak velocity. This is evident in the acceleration response spectra<sup>4</sup> in figure 7.15, where the spectrum for site S1 contains large peaks at periods of 1.9 sec and 3.1 sec, and the spectrum for site S2 contains a small, broad peak centered at around 3.0 sec.

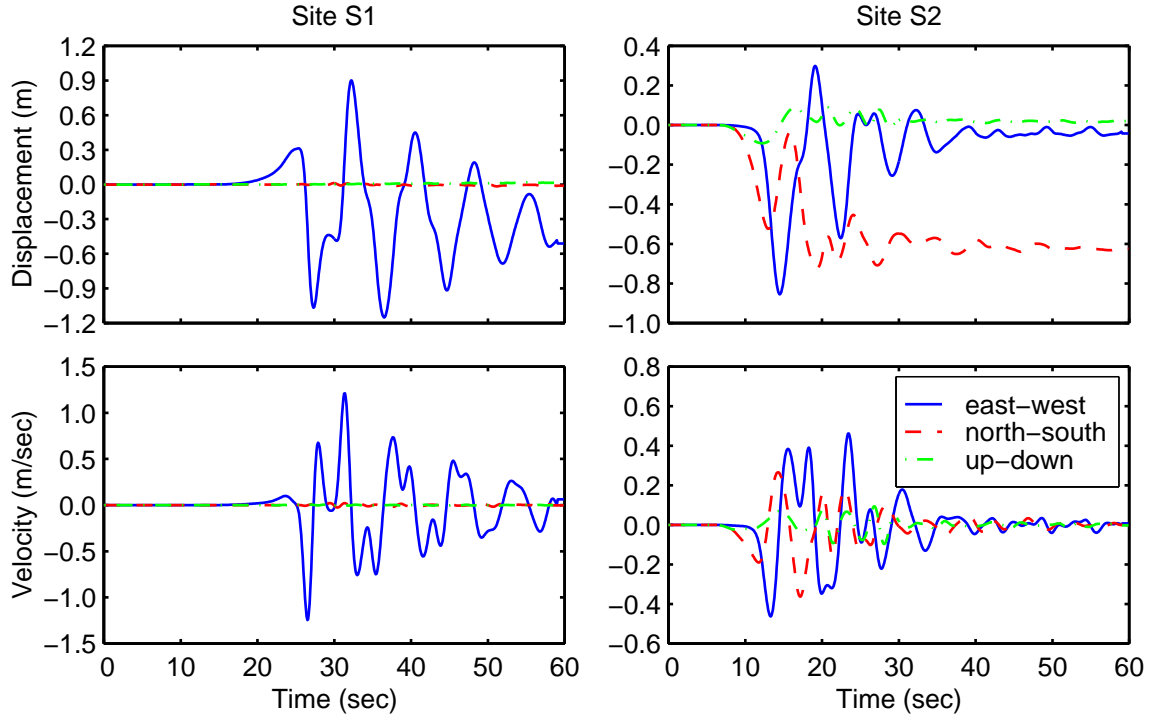


Figure 7.14: Displacement and velocity time histories at sites S1 and S2 for scenario baseII.

### Material Properties

In order to understand the effect of including softer material near the ground surface, we compare the waveforms at sites S1 and S2 from the base case, scenario baseII, where we use a layered half-space, with those from scenario homo, where we use a homogeneous half-space. The horizontal displacements (figure 7.16) at sites S1 and S2 provide a good representation of the differences in the ground motions between the two scenarios. The displacements are significantly larger in the layered half-space, and the time histories in the homogeneous case do not contain the four or five cycles of motion associated with the surface waves found in the layered half-space. At both sites the final displacements match very well as do the very long-period motions. Hence, when we prescribe the slip on the fault, the softer material near the surface has little effect

<sup>4</sup>The waveforms have been rotated into the direction with the maximum peak to peak velocity using a resolution of 2 degrees (90 degrees east of north for site S1 and 88 degrees east of north for site S2).

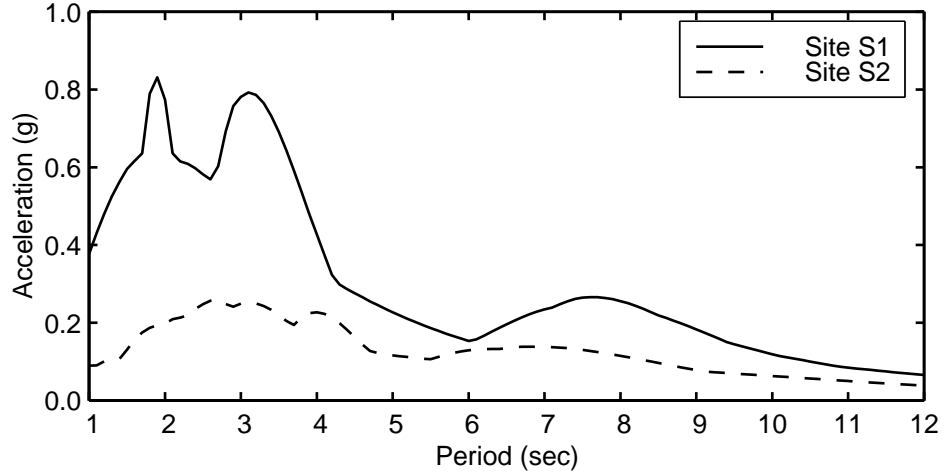


Figure 7.15: Horizontal acceleration response spectra at sites S1 and S2 for scenario baseII.

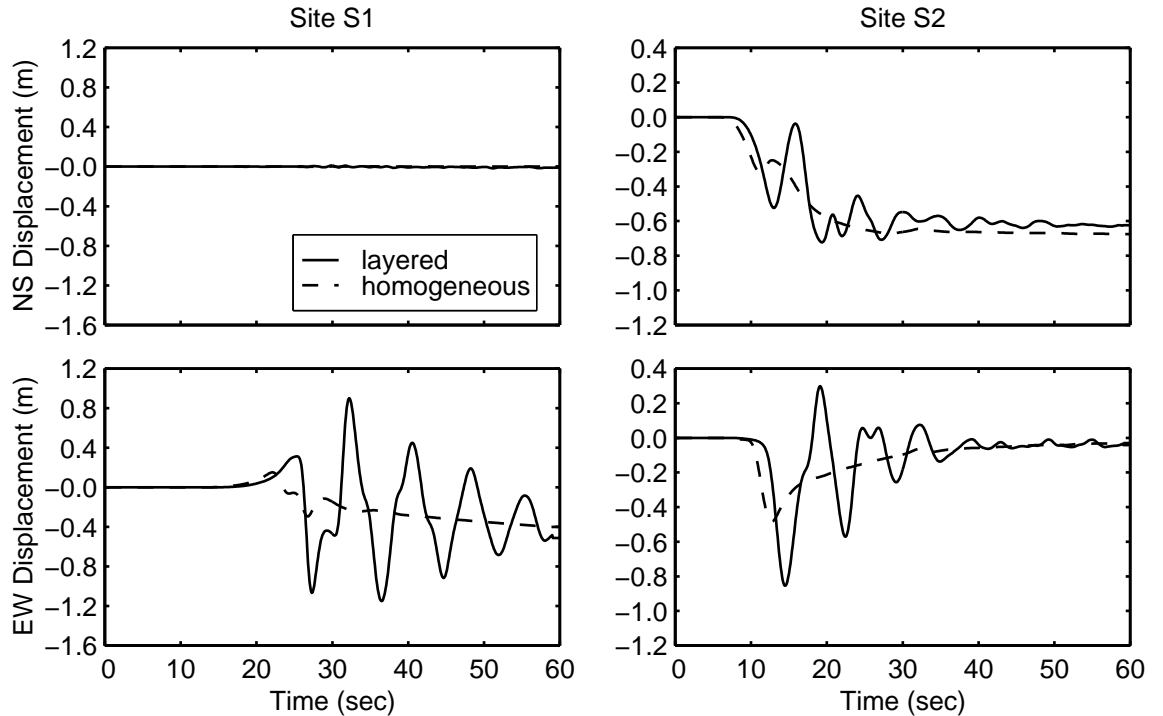


Figure 7.16: Comparison of horizontal displacement time histories at sites S1 and S2 for a layered half-space versus a homogeneous half-space.

on the very long-period progression towards the final deformation. However, the layered half-space generates much larger, short period displacements with four or five cycles compared to the single cycle in the homogeneous half-space.

### Rupture Speed

We examine the variability of the ground motions to three different rupture speeds set relative to the local shear wave speed; scenario vr70 uses a rupture speed of 70% of the local shear wave speed, scenario baseII uses a rupture speed of 80% of the local shear wave speed, and scenario vr90 uses a rupture speed of 90% of the local shear wave speed. As we increase the rupture speed towards the shear wave speed, we increase the efficiency of the reinforcement of the shear wave, because we reduce the relative distance between the shear wave and the following rupture front. If we compare the maximum horizontal velocities on the ground surface from scenario vr90 (figure 7.17) with those from scenario baseII (figure 7.13), we see that the peak horizontal velocity increases from 2.9 m/sec to 3.5 m/sec. Furthermore, the double lobe pattern disappears because the curvature of the rupture front changes more rapidly and the amplitude of the shear wave velocity quickly stabilizes. As a result, for a fixed distance from the fault, the maximum velocity in the east-west (fault normal) direction becomes nearly uniform along the northern 40 km of the fault. The maximum velocities exceed 2.5 m/sec along this northern section out to a distance of approximately two kilometers from the fault.

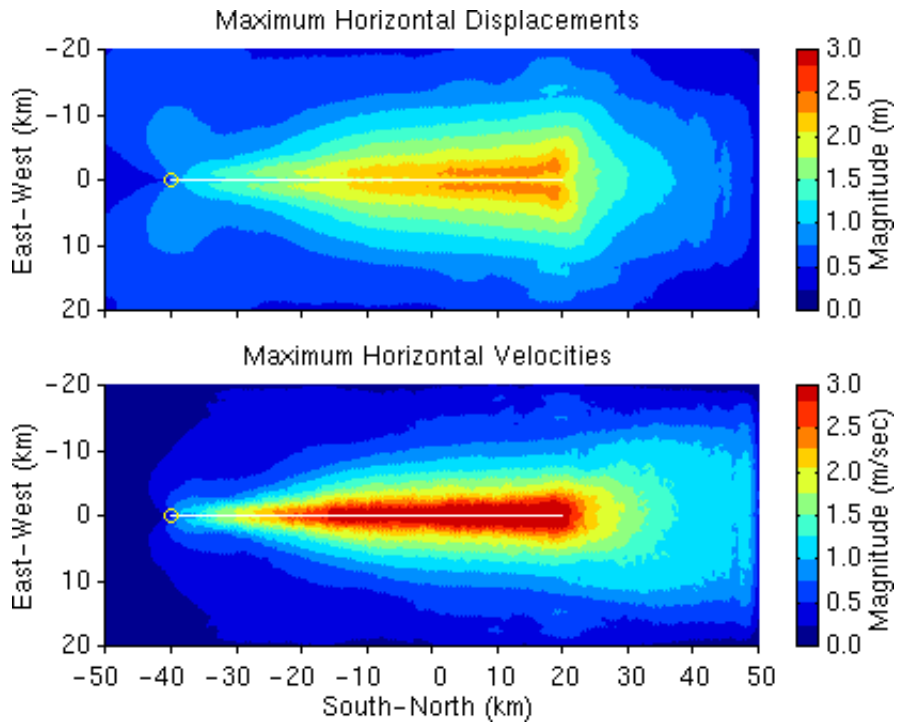


Figure 7.17: Maximum magnitudes of the horizontal displacement and velocity vectors at each point on the ground surface for scenario vr90. The white line indicates the projection of the fault plane onto the ground surface, and the yellow circle identifies the epicenter.

Comparing the horizontal velocity components at sites S1 and S2 for the three scenarios (figure 7.18), we see sharper phase arrivals as the rupture speed increases. The travel time to the hypocenter remains the same, but the energy from all parts of the fault arrives closer together in time. At sites S1 and S2 we see that this leads to a substantial increase in the amplitude of the shear wave, while the amplitudes of the surface waves

remain relatively unchanged. Besides being compressed in time, the general shapes of the ground motions remain the same.

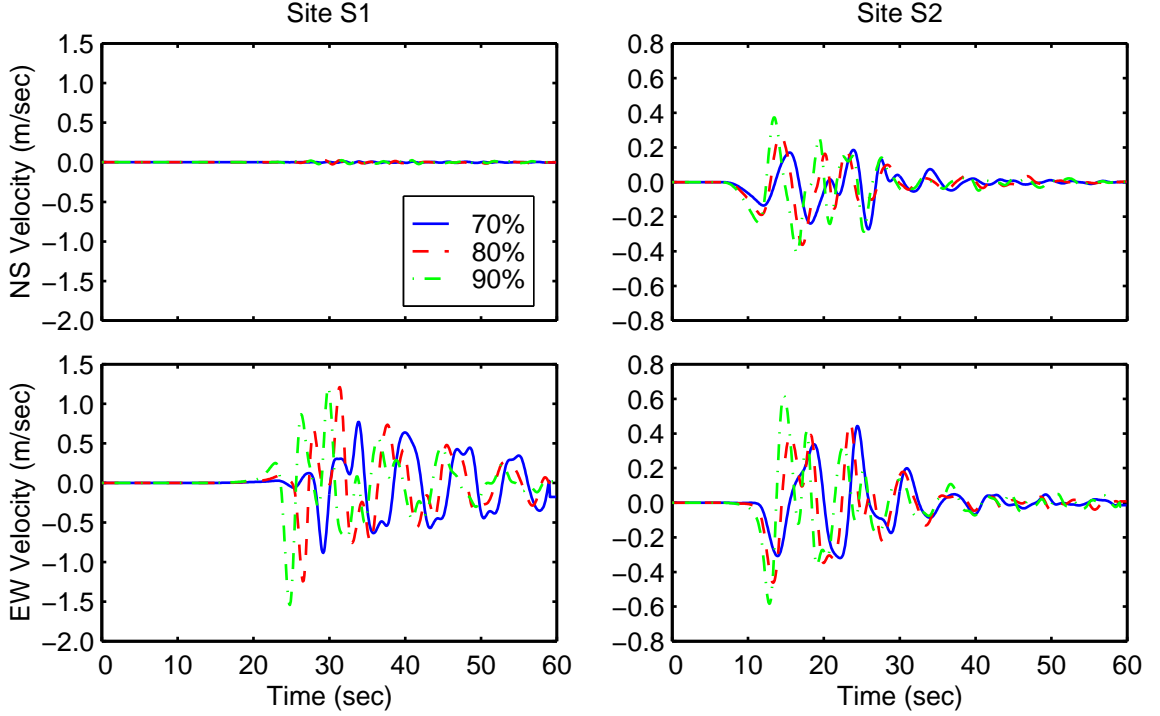


Figure 7.18: Comparison of horizontal velocity time histories at sites S1 and S2 for the three rupture speeds.

Figure 7.19 shows the maximum displacements and velocities along the east-west line that passes through the north tip of the fault for each of the three rupture speeds. As the rupture speed increases, the maximum velocities exhibit a relatively greater increase than the maximum displacements. The maximum velocities, however, decay with distance from the fault more rapidly than the maximum displacements. Figure 7.19 also includes the near-source ground motion factor,  $N_v$ , from the 1997 Uniform Building Code (UBC). The UBC uses the near-source factor to account for the greater demand placed on structures arising from earthquakes on nearby faults compared to those on faults farther away. We assume that the maximum displacements and maximum velocities correlate with the seismic demand on a structure, so that we want the shape of the near-source curve to mimic the shapes of the maximum displacements and maximum velocities. We focus on the general shape of the near-source factor and do not correlate values of the near-source factor with any specific displacements or velocities. We match the near-source factor curve with the average of the peak maximum displacements or velocities and the average of the maximum displacements or velocities at sites located 15 km from the fault. The shape of the near-source factor curve closely matches the shape of the maximum displacements. The shape of the near-source factor curve matches the shape of the maximum velocities, except the curve of the maximum velocities has a narrower peak.

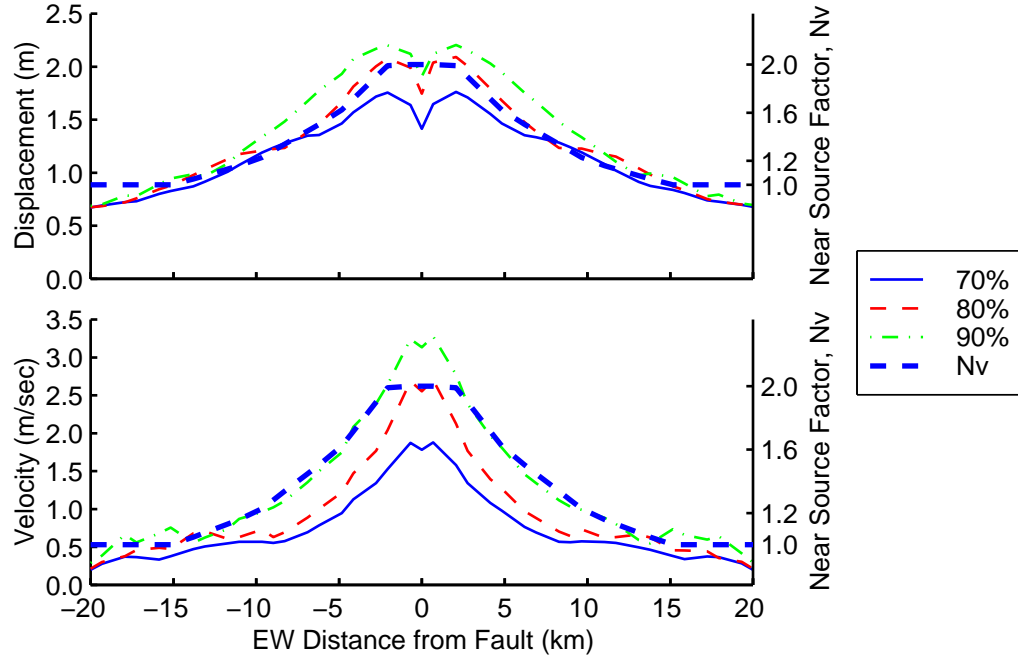


Figure 7.19: Maximum magnitudes of the horizontal displacement and velocity vectors along an east-west line running through the north tip of the fault for the three rupture speeds. The thick, dashed line indicates the near-source ground motion factor,  $N_v$ , from the 1997 Uniform Building Code.

### Maximum Slip Rate

Scenarios vs10, baseII, and vs20 allow comparison of the ground motions from simulations with maximum slip rates of 1.0 m/sec, 1.5 m/sec, and 2.0 m/sec, respectively. Figure 7.20 illustrates the sensitivity of the velocity ground motions at sites S1 and S2 to variations in the maximum slip rate. At sites S1 and S2 the velocity amplitudes exhibit a moderate increase with maximum slip rate, but the phase arrival times do not change. As the maximum slip rate increases, the slip on the fault occurs over a shorter period of time which reduces the width of the rupture front. Because the leading edge of the rupture front is controlled by the rupture speed, it remains the same distance behind the shear wave as we change the maximum slip rate. Consequently, when we increase the maximum slip rate, the center of the rupture front moves closer behind the shear wave. This leads to more efficient reinforcement of the shear wave, and hence, larger amplitude displacements and velocities.

Comparing the maximum displacements and velocities on the east-west line running through the north tip of the fault for the three slip rates (figure 7.21) with those in figure 7.19 for the three rupture speeds, we see that increasing the slip rate produces a slightly greater increase in the maximum displacements and velocities than an increase in the rupture speed. As we noted above, whereas the rupture speed strongly influences the phase arrivals, the variation in slip rates does not influence the phase arrivals. The shape of the UBC near-source factor curve matches the shapes of the maximum displacements and velocities in almost an identical fashion as it did for the scenarios with the different rupture speeds.

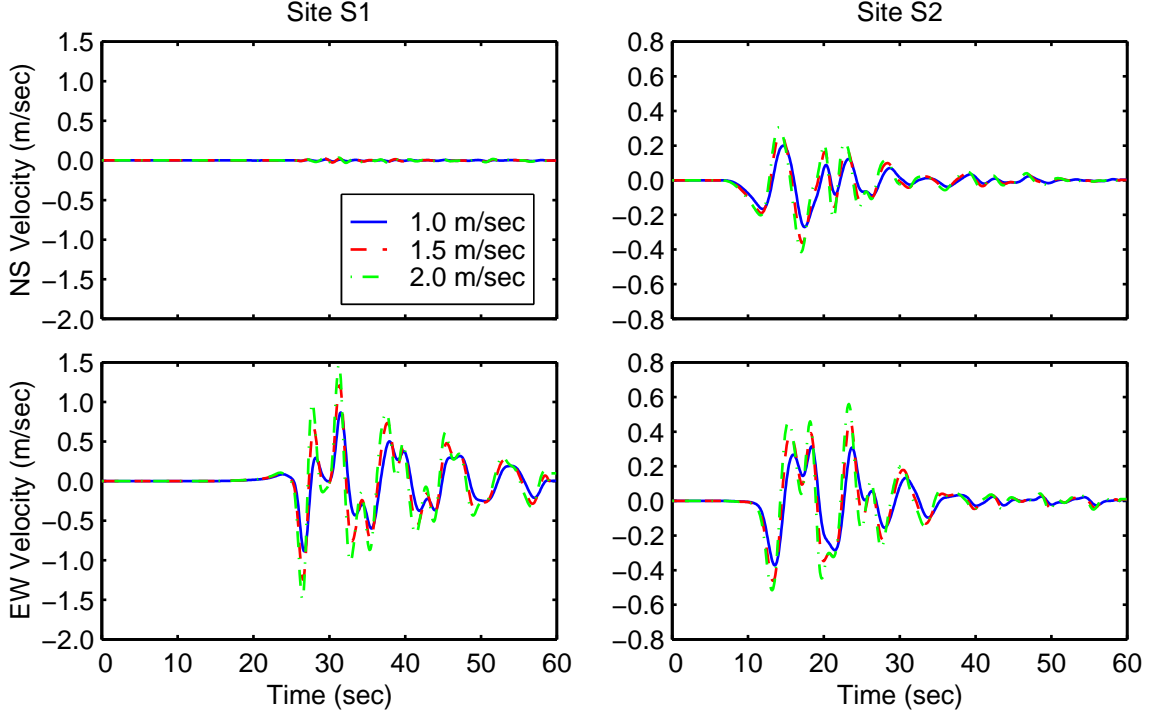


Figure 7.20: Comparison of horizontal velocity time histories at sites S1 and S2 for the three maximum slip rates.

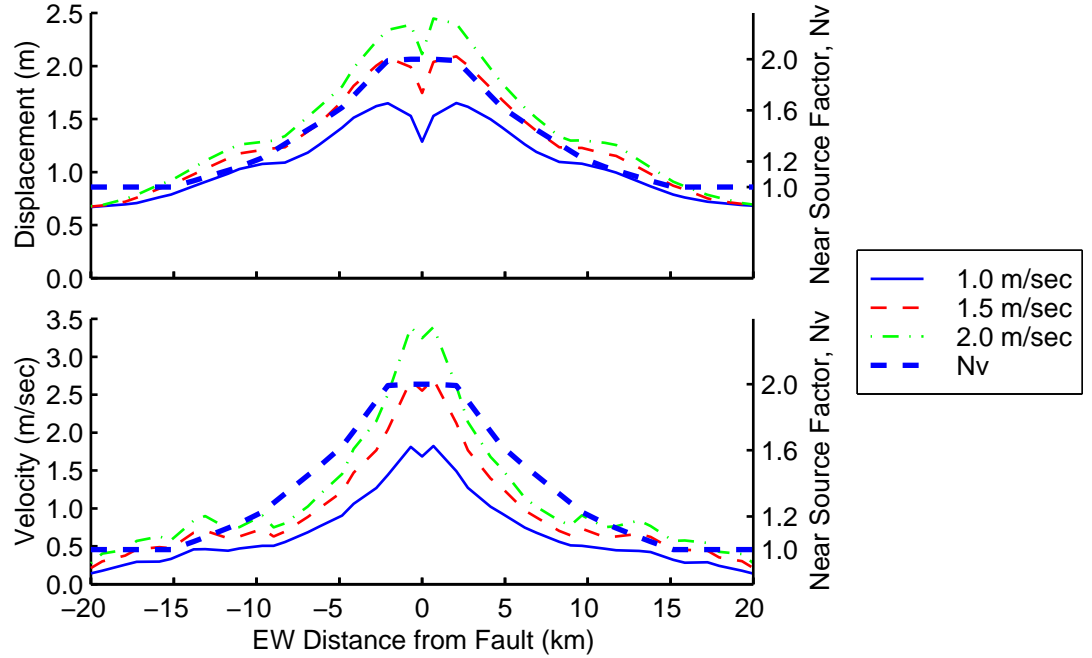


Figure 7.21: Maximum magnitudes of the horizontal displacement and velocity vectors along an east-west line running through the north tip of the fault for the three maximum slip rates. The thick, dashed line indicates the near-source ground motion factor,  $N_v$ , from the 1997 Uniform Building Code.

### Hypocenter Location

We study the sensitivity of the ground motions to the location of the hypocenter using scenario baseII (where hypocenter HA sits at the middle of the south edge of the fault as illustrated in figure 7.4), scenario hymq (where hypocenter HB sits mid-depth at the southern quarter point), scenario hybq (where hypocenter HC sits at the bottom of the fault at the southern quarter point), and scenario hymc (where hypocenter HD sits at the center of the fault). Changing the location of the hypocenter significantly alters the ground motions in some locations but has a minimal impact at other locations. If we compare the maximum horizontal displacements and velocities on the ground surface for scenario hybq (figure 7.22) to those from scenario baseII, we find the maximum displacements and velocities remain relatively unchanged at the north end of the fault. However, at the south end of the fault the spatial variation of the maximum displacements and velocities changes drastically.

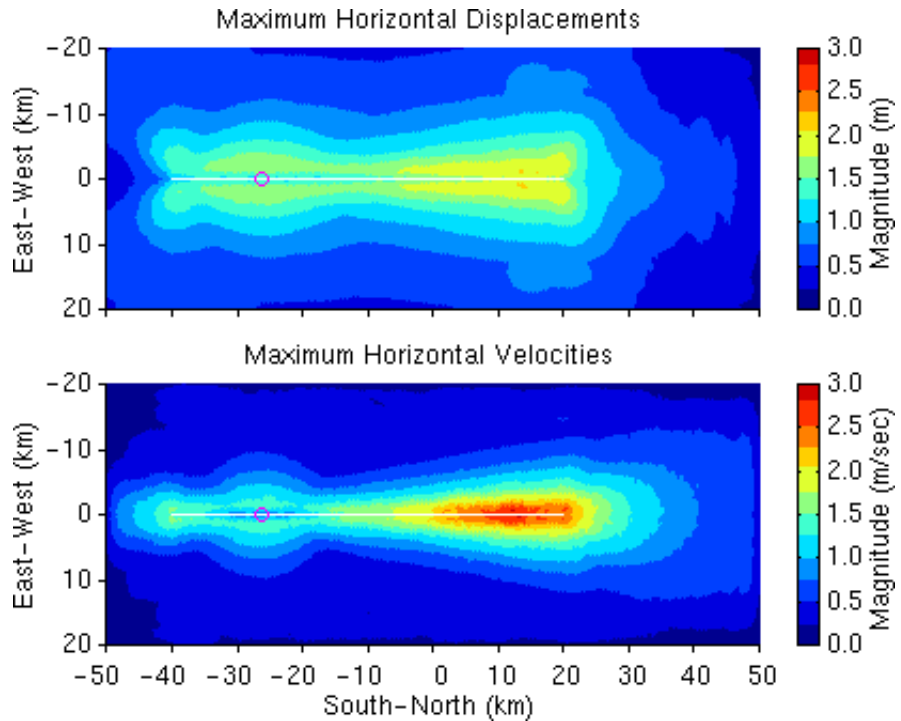


Figure 7.22: Maximum magnitudes of the horizontal displacement and velocity vectors at each point on the ground surface for scenario hybq. The white line indicates the projection of the fault plane onto the ground surface, and the purple circle identifies the epicenter.

When we place the hypocenter at the middle edge of the fault (hypocenter HA), the rupture reinforces the shear wave almost exclusively in the region north of the hypocenter. By moving the hypocenter to the bottom quarter point (hypocenter HC), the rupture reinforces the shear wave as it propagates towards the north, towards the south, and towards the ground surface. The reinforcement of the shear wave south of the epicenter occurs in the same manner as it does to the north. Consequently, the maximum displacements and velocities south of the epicenter match those the same distance to the north until we encounter the termination

of the rupture at the south end of the fault. The propagation of the rupture towards the surface reinforces the shear waves propagating normal to the fault. In the top 6.0 km of the domain, the shear waves propagating normal to the fault refract towards the surface due to the vertical variation in material properties. This creates the local peak in the maximum displacements and velocities approximately three kilometers from the fault near the epicenter.

The ground motions at site S1 exhibit minor differences with changes in the location of the hypocenter, while the ground motions at site S2 exhibit major differences. For each of the four hypocenter locations, site S1 lies along an azimuth of 0 degrees. Furthermore, site S1 lies far enough away from the hypocenter in all four cases that the amplitude of the shear wave velocity stabilizes well before it arrives at site S1. As shown in figure 7.23, the arrival times differ, but the amplitudes of the displacement time histories remain about the same. Similarly, the points along the east-west line through the north tip of the fault lie in the forward direction for all four hypocenter locations. Figure 7.24 shows there is negligible variation in the maximum horizontal displacements and velocities at these sites for the four hypocenter locations, and the shape of the UBC near-source curve continues to mimic the shapes of the maximum displacements and velocities.

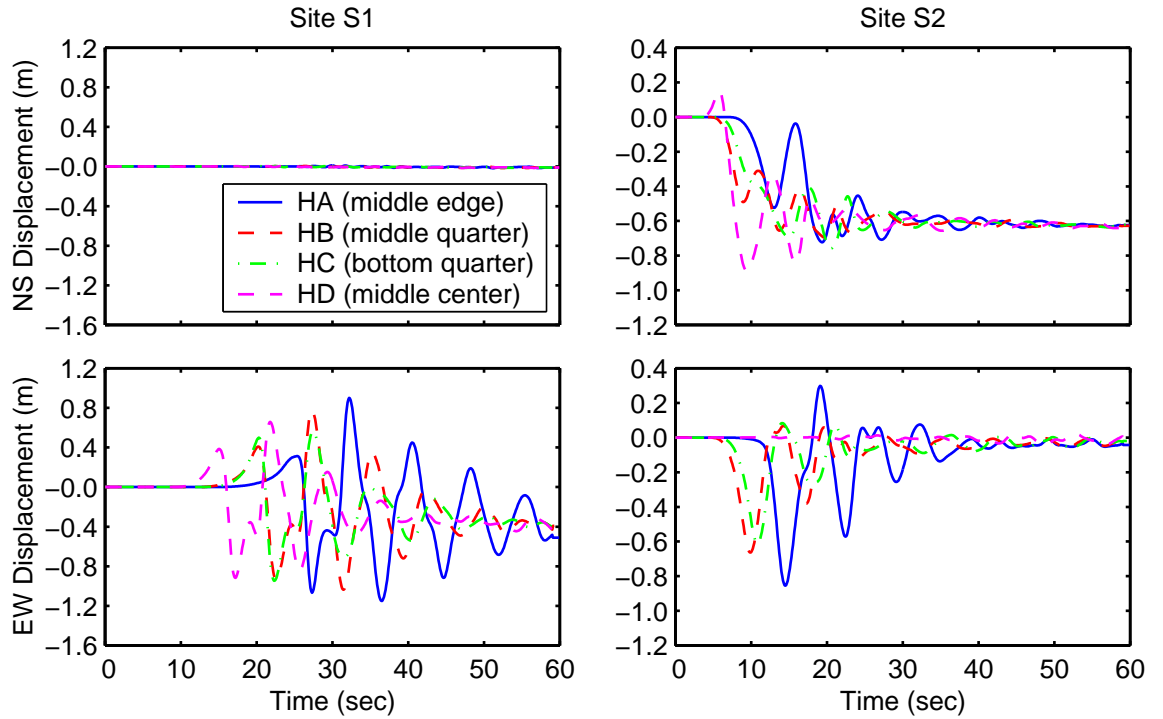


Figure 7.23: Comparison of horizontal displacement time histories at sites S1 and S2 for the four hypocenter locations.

At the other end of the spectrum, site S2 lies along three different azimuths for the four hypocenter locations. When we place the hypocenter at the center of the fault (hypocenter HD), site S2 lies on a node in the radiation pattern for displacement in the east-west and vertical directions, so it experiences motion only in the north-south direction (figure 7.23). In this case, the sharp arrival of the shear wave dominates

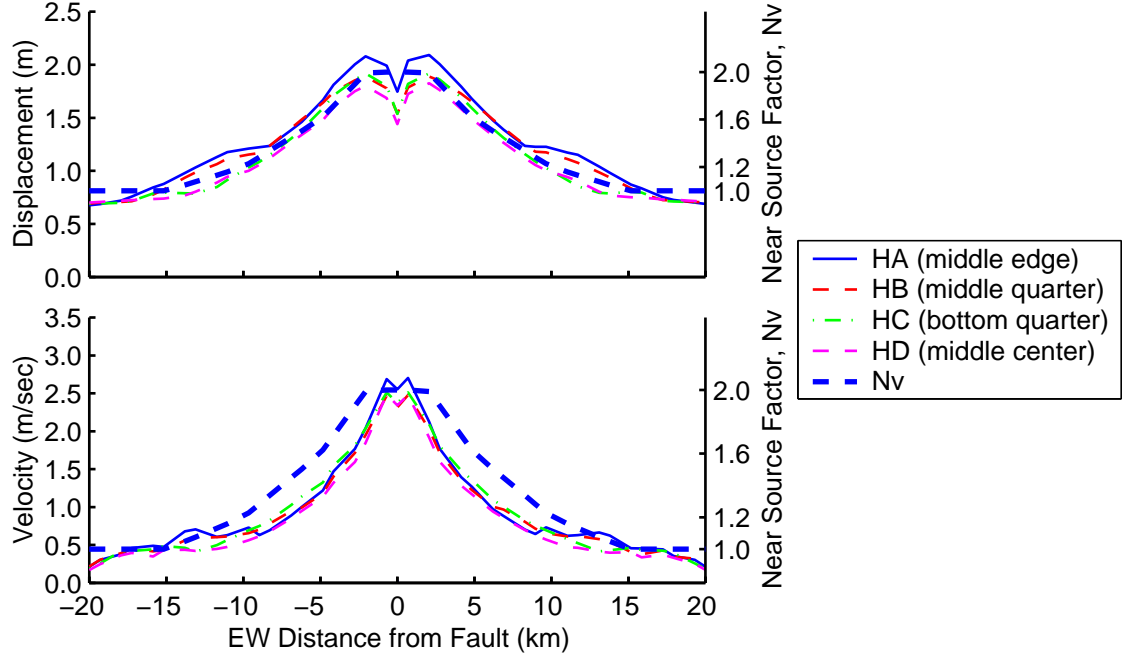


Figure 7.24: Maximum magnitudes of the horizontal displacement and velocity vectors along an east-west line running through the north tip of the fault for the four hypocenter locations. The thick, dashed line indicates the near-source ground motion factor,  $N_v$ , from the 1997 Uniform Building Code.

the motion in the north-south direction. For the three other hypocenter locations, the east-west (fault normal) displacements are greater than or equal to the north-south (fault parallel) displacements. As we might expect based on the observations at site S1, we find only minor variations in the ground motions at site S2 when we compare the ground motions from the two hypocenter locations at the southern quarter point, because site S2 remains along the same azimuth. Thus, as we move the hypocenter, site S2 experiences large fluctuations in the ground motions, particularly in the east-west direction where the motion varies from being much smaller than the north-south motion to equal to or greater than the north-south motion.

### Slip Distribution

The simulations include a homogeneous slip distribution without surface rupture in scenario base, a homogeneous slip distribution with surface rupture in scenario baseII, a weakly heterogeneous slip distribution with a bias towards slip near the surface in scenario sliptop, a weakly heterogeneous slip distribution with a bias towards slip at depth in scenario slipbot, and a strongly heterogeneous slip distribution in scenario sliphet. Small perturbations in the final distribution of slip cause negligible differences in the ground motions. Large perturbations do affect the ground motions, particularly the displacement time histories. Figure 7.25 shows the maximum displacements and velocities on the ground surface for scenario sliphet, which uses the strongly heterogeneous slip distribution shown in figure 7.10. In this case, the rupture does not continuously reinforce the shear wave; instead it reinforces the shear wave in short intervals. As a result, the maximum displacements

form a complex pattern of peaks and valleys compared to the simple pattern associated with homogeneous slip (figure 7.13).

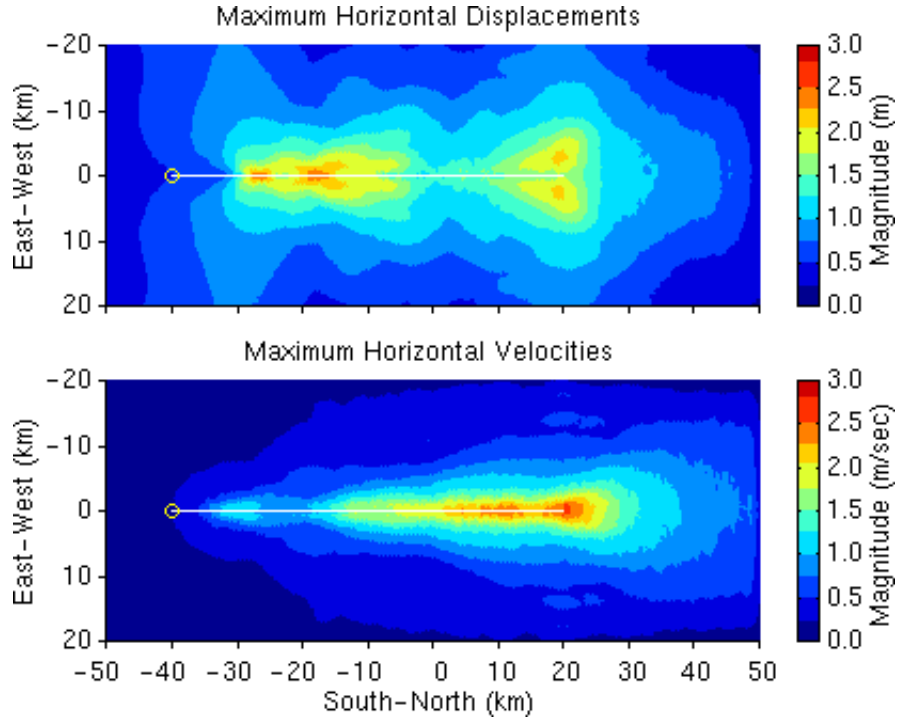


Figure 7.25: Maximum magnitudes of the horizontal displacement and velocity vectors at each point on the ground surface for scenario sliphet. The white line indicates the projection of the fault plane onto the ground surface, and the yellow circle identifies the epicenter.

The maximum velocities exhibit less sensitivity to the heterogeneity in slip, and the distribution closely resembles that of the homogeneous slip case. The maximum displacements and velocities close to the fault remain approximately the same, but away from the fault the displacements and velocities tend to be slightly smaller. At the north end of the fault, as revealed by figure 7.26, the maximum displacements and velocities do not noticeably change with the increase in heterogeneity of the final slip distribution.

Minor perturbations to the slip distribution that include tapering the slip near the surface or adding a small amount of heterogeneity result in almost no change in the displacement and velocity time histories at both sites (figure 7.27). At site S2 the strongly heterogeneous slip distribution causes significant changes to the amplitudes and alters the shape of the displacement time histories. At site S1 energy from all points on the fault arrives closer together which greatly reduces the effect caused by the discontinuity of the reinforcement of the shear wave. Consequently, the strong heterogeneity in the final slip distribution has less of an effect at site S1 than it does at site S2. Remarkably, at both sites the peak displacements remain relatively unchanged across all of the slip distributions. However, based on the maximum displacements on the entire ground surface which we discussed above, we know large perturbations in the slip distribution may significantly alter the peak displacements.

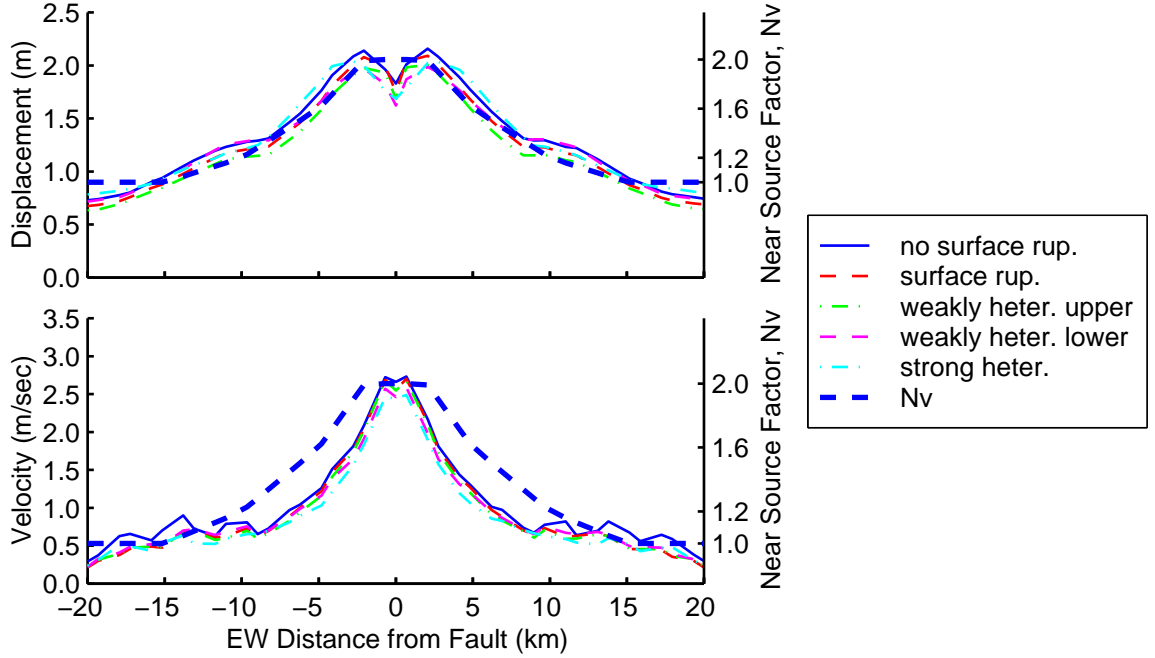


Figure 7.26: Maximum magnitudes of the horizontal displacement and velocity vectors along an east-west line running through the north tip of the fault for the five slip distributions. The thick, dashed line indicates the near-source ground motion factor,  $N_v$ , from the 1997 Uniform Building Code.

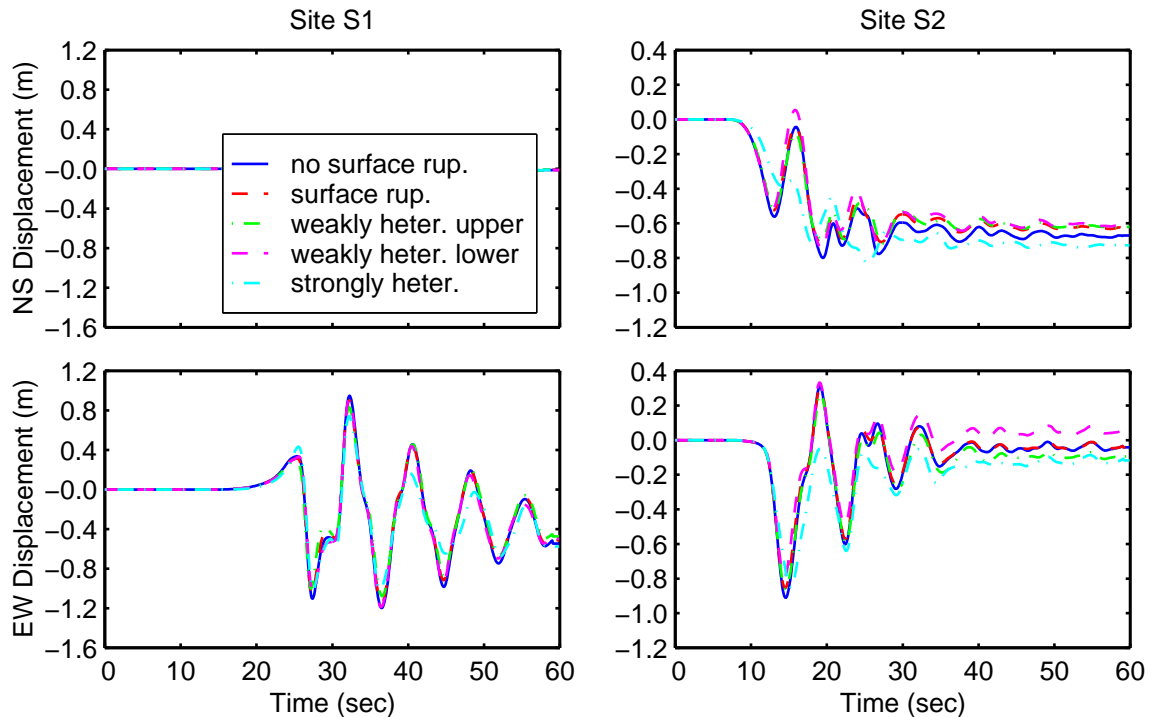


Figure 7.27: Comparison of horizontal displacement time histories at sites S1 and S2 for the five slip distributions.

### Average Slip

Increasing the average slip from 2.0 m in scenario baseII to 3.0 m in scenario slip3, while maintaining a maximum slip rate of 1.5 m/sec, increases the amplitudes of the displacements but has little effect on the amplitudes of the velocities. When we change the average slip, we also increase the moment magnitude of the earthquake from 7.0 to 7.1. The larger amplitude displacements are clearly visible in the displacement time histories at sites S1 and S2 shown in figure 7.28. Imposing the same maximum slip rate causes the maximum slip rate to occur later in the slip time history and results in a slight delay in the peak displacement amplitudes. Although not shown, we see nearly negligible variations in the amplitudes of the velocity time histories with the increase in average slip. Along the east-west line running through the north tip of the fault (figure 7.29), we also observe an increase in the peak displacements with no accompanying increase in peak velocities. With such minor differences in the ground motions, it is no surprise that the shape of the UBC near-source factor curve continues to closely follow the shapes of the maximum displacements and maximum velocities.

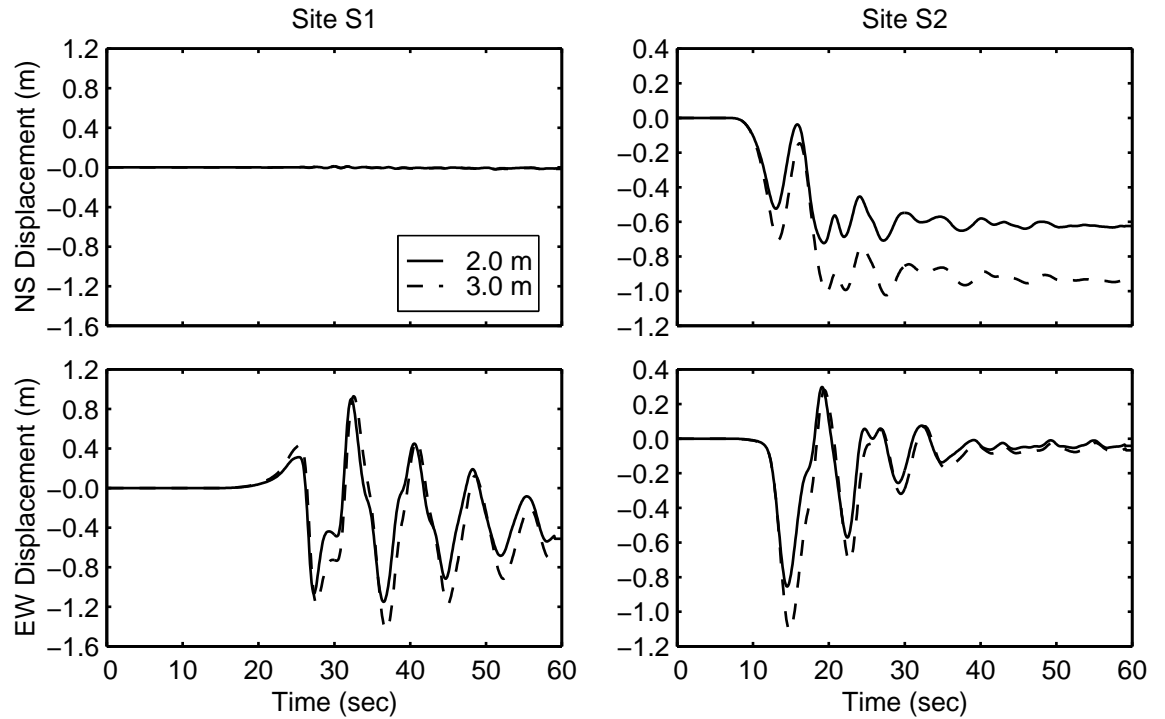


Figure 7.28: Comparison of horizontal displacement time histories at sites S1 and S2 for the two values of average slip.

### Fault Depth

We evaluate the effect of the depth of the fault using the results from scenarios baseII, fault4km, and fault8km. It is interesting to note that increasing the depth of the top of fault, while using the same slip distribution,

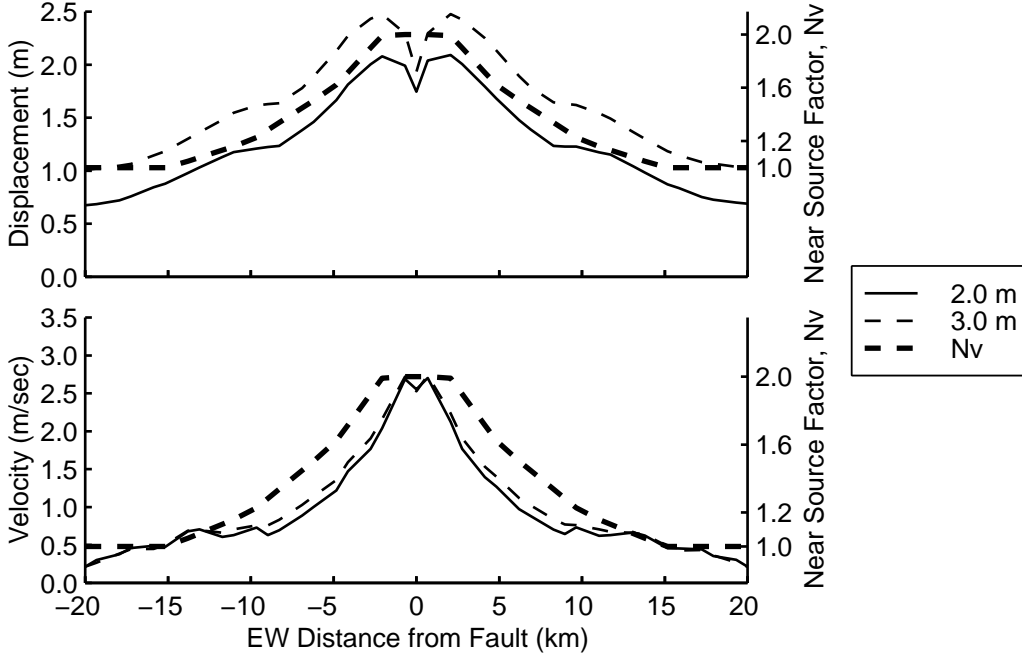


Figure 7.29: Maximum magnitudes of the horizontal displacement and velocity vectors along an east-west line running through the north tip of the fault for the two values of average slip. The thick, dashed line indicates the near-source ground motion factor,  $N_v$ , from the 1997 Uniform Building Code.

shifts the slip to a region with a larger shear modulus and leads to a slight increase in the moment magnitude of the earthquake. Lowering the top of the fault to 4.0 km below the ground surface increases the moment magnitude from 7.0 to 7.1, but lowering the fault an additional 4.0 km provides no noticeable effect on the moment magnitude, and it remains at 7.1. While dropping the fault has the same effect on the moment magnitude as increasing the average slip, the effect on the ground motions is very different.

In general, the lower the depth of the fault, the smaller the amplitude of the ground motions. Figure 7.30 shows that lowering the top of the fault to 4.0 km below the ground surface does not have as much impact as lowering the top of the fault to 8.0 km below the ground surface. As long as the top of the fault remains less than 6.0 km below the ground surface, slip occurs in the softer material at the top of the domain, and the energy tends to refract toward the ground surface. When we drop the top of the fault to 4.0 km below the ground surface, we see little reduction in the amplitude of the displacement time histories at sites S1 and S2, particularly in the north-south direction at site S2. No slip occurs in the region of softer material when the top of the fault sits 8.0 km below the ground surface. This explains why dropping the fault 8.0 km below the ground surface greatly reduces the amplitude of the displacements and velocities.

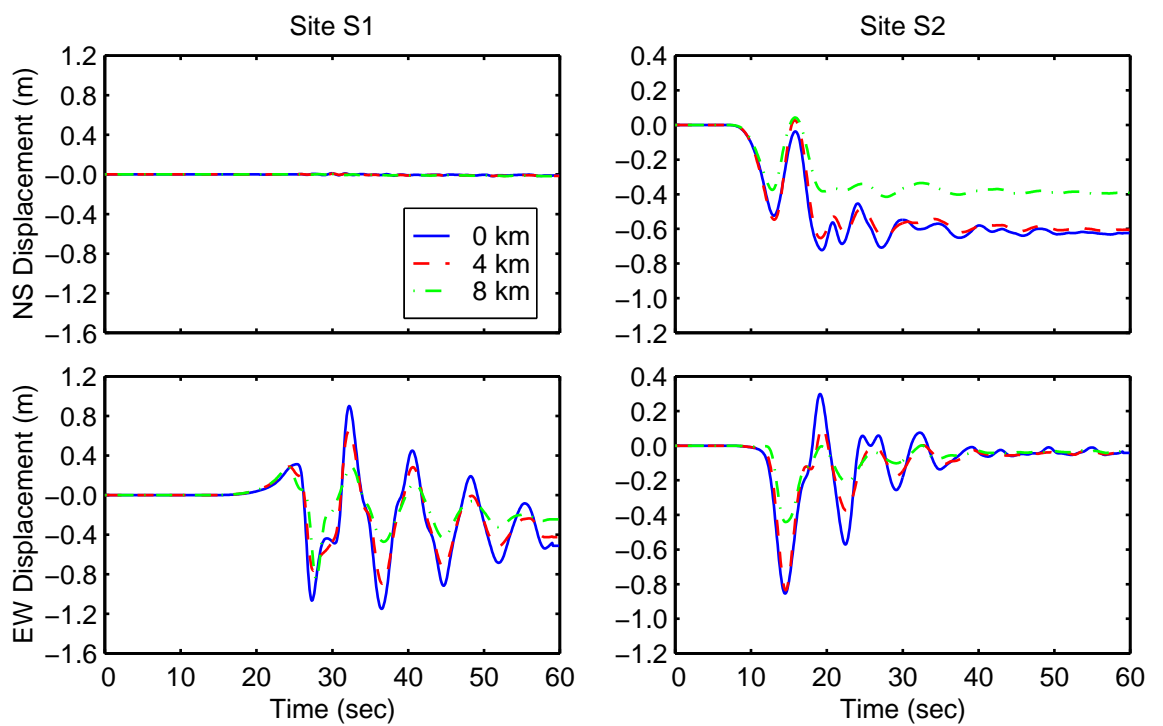


Figure 7.30: Comparison of horizontal displacement time histories at sites S1 and S2 for the three depths of the top of the fault.

## 7.2 Thrust Fault

We set up the geometry of the thrust fault so that it closely resembles that of the Elysian Park fault underneath Los Angeles as described by Hall et al. (1995). The fault measures 28 km long and 18 km wide, dips 23 degrees to the north, and projects onto the ground surface an area 28 km long by 16.6 km wide. For most of the simulations we bury the fault 8.0 km below the ground surface. We enclose the fault in a domain 60 km long by 60 km wide by 24 km deep as illustrated in figure 7.31. We impose oblique slip with a rake angle of 105 degrees from the strike to the west.

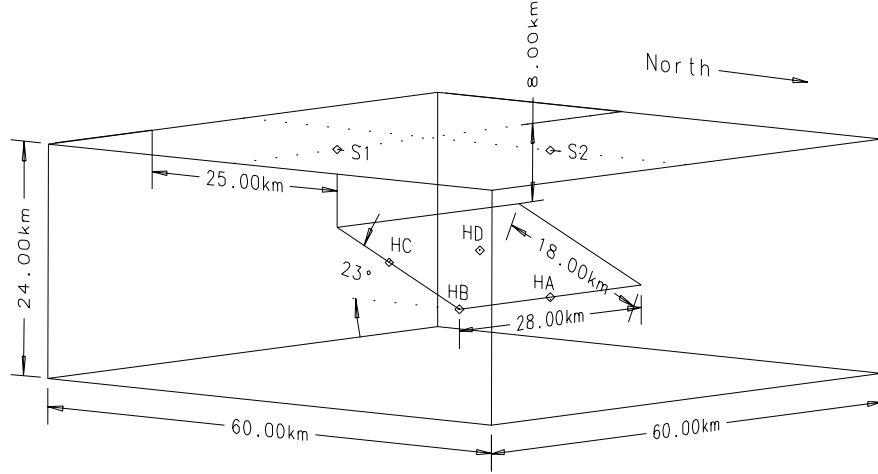


Figure 7.31: Orthographic projection of the domain geometry for the thrust fault for the case where the top of the fault lies 8.0 km below the ground surface. The labels HA through HD denote the various hypocenter locations. We will examine the waveforms at sites S1 and S2.

### 7.2.1 Finite-Element Model

We use a total of four finite-element models, one for each of the three fault depths in the layered half-space, and one for the homogeneous half-space. For the layered half-space we use the same material property variation with depth that we use for the strike-slip domain. Figure 7.32 reproduces the mass density, shear wave speed, and dilatational wave speed over the depth range of this domain for the layered half-space shown in figure 7.2. We take the material properties of the homogeneous half-space from the material properties of the layered half-space at depth of 6.0 km.

From the coarse mesh created with IDEAS, we use the 4x refinement procedure to create a mesh with the appropriate resolution for propagation of waves with periods down to 2.0 sec. Table 7.5 gives the sizes of the finite-element models at coarse and fine resolution for the layered and homogeneous half-spaces. For the layered half-space figure 7.33 illustrates the inertial bisection of the finite-element mesh among 256 processors. Each simulation took 1.2 hours using 256 processors of the Intel Paragon at the CACR.

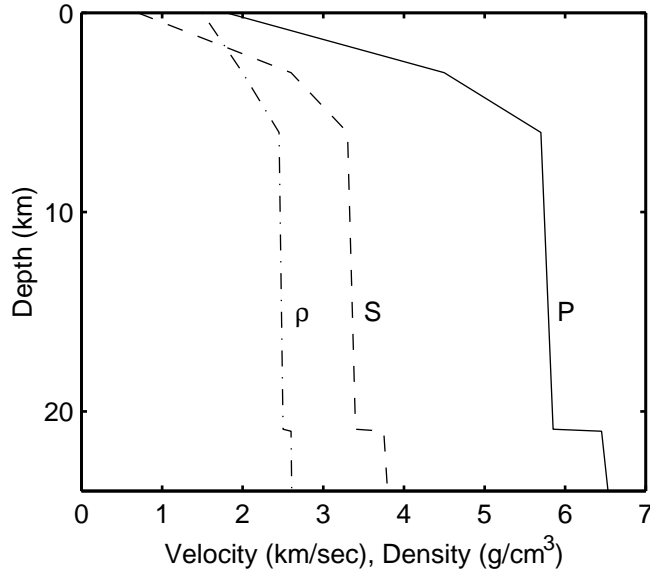


Figure 7.32: Density ( $\rho$ ), shear wave speed (S), and dilatational wave speed (P) as a function of depth for the layered half-space.

	Fault Depth	Coarse		Fine	
		# Nodes	# Elements	# Nodes	# Elements
Homogeneous	8 km	6700	33,000	420,000	2.1 million
Layered	8 km	26,000	120,000	1.7 million	7.7 million
	4 km	27,000	130,000	1.8 million	8.3 million
	0 km	26,000	120,000	1.6 million	7.6 million

Table 7.5: Sizes of the finite-element models of the layered and homogeneous half-spaces at coarse and fine resolution.

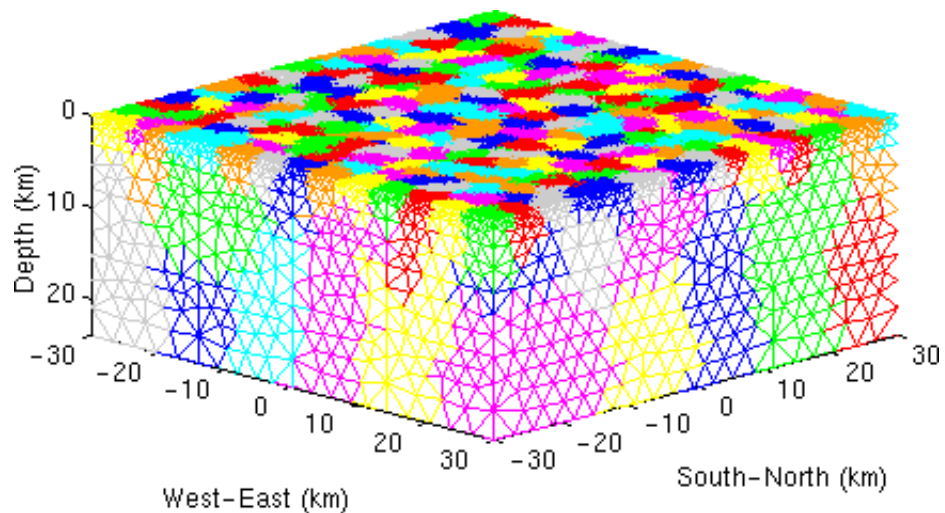


Figure 7.33: Partitioning of the coarse finite-element model among 256 processors for the layered half-space using the inertial bisection algorithm. Each color patch identifies the elements of one processor.

### 7.2.2 Earthquake Source Parameters

We follow the same procedure that we use for the strike-slip fault and systematically vary the five earthquake source parameters; these include the hypocenter location, the rupture speed, the maximum slip rate, the distribution of slip, and the fault depth. Table 7.6 summarizes the parameters for each of the 14 simulations. The base case features a fault buried 8.0 km below the ground surface, a homogeneous slip distribution tapered at the edges, a rupture speed of 80% of the local shear wave speed, a maximum slip rate of 1.5 m/sec, and a hypocenter located at the bottom center of the fault.

Scenario	Slip Pattern	Rupture Speed % of $\beta$	Maximum Slip Rate (m/sec)	Hypocenter Location	Fault Depth (km)	Material Properties	Mom. Mag.
base	unitaper	80	1.5	HA	8.0	layered	6.8
vr70	unitaper	70	1.5	HA	8.0	layered	6.8
vr90	unitaper	90	1.5	HA	8.0	layered	6.8
vs10	unitaper	80	1.0	HA	8.0	layered	6.8
vs20	unitaper	80	2.0	HA	8.0	layered	6.8
hybc	unitaper	80	1.5	HB	8.0	layered	6.8
hyme	unitaper	80	1.5	HC	8.0	layered	6.8
hymc	unitaper	80	1.5	HD	8.0	layered	6.8
slitop	weakupper	80	1.5	HA	8.0	layered	6.8
slipbot	weaklower	80	1.5	HA	8.0	layered	6.8
slip2	unitaper2	80	1.5	HA	8.0	layered	7.0
fault4km	unitaper	80	1.5	HA	4.0	layered	6.7
fault0km	unitaper	80	1.5	HA	0.0	layered	6.6
homo8km	unitaper	80	1.5	HA	8.0	homo.	6.7

Table 7.6: Summary of the parameters for the prescribed rupture simulations on the thrust fault.

### Hypocenter Locations

Figure 7.31 illustrates the general locations of the four hypocenters (labeled HA through HD) and figure 7.34 gives the precise locations of the hypocenters on the fault plane. Hypocenter HA lies at the center of the bottom edge of the fault, hypocenter HB lies at the northeast corner of the fault, hypocenter HC lies approximately mid-depth on the eastern edge of the fault, and hypocenter HD lies approximately mid-depth on the north-south running centerline.

### Slip Time Histories and Rupture Speeds

For the slip time histories we use the integral of Brune's far field time function. We also independently set the maximum slip rate to either 1.0 m/sec, 1.5 m/sec, or 2.0 m/sec and the rupture speed to either 70%, 80%, or 90% of the local shear wave speed. The spatial distributions of final slip include two homogeneous distributions that are tapered on all four edges (figure 7.35 and figure 7.36) and two weakly heterogeneous distributions (figure 7.37 and figure 7.38). The heterogeneous slip distributions each have a nominal slip to

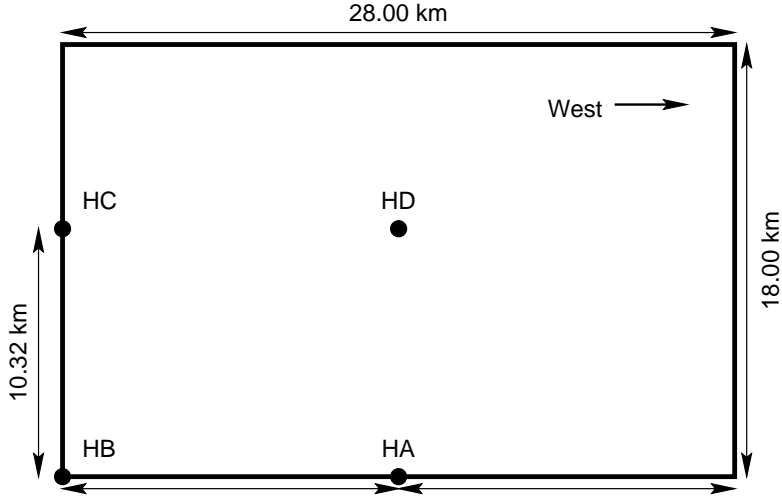


Figure 7.34: Hypocenter locations on the fault plane.

which we add 20 asperities with uniform random distributions of radii (as given in table 7.7), heights (as given in table 7.7), strike locations between 2.0 km and 26 km, and dip locations between 2.0 km and 16 km. The weakly heterogeneous slip distributions have a bias towards slip on either the upper (weakupper<sup>5</sup>) or the lower (weaklower<sup>6</sup>) half of the fault surface. We adjust the height of the asperities that lie in the dip range of the bias by the amount given in table 7.7.

Distribution	Nominal Slip (m)	Asperity Heights (m)	Asperity Radii (km)	Bias	
				Dip (km)	Height Adj. (m)
weakupper	0.66	-0.25–0.50	5.0–8.0	2.0–8.0	+0.50
weaklower	0.68	-0.25–0.50	5.0–8.0	8.0–16.0	+0.50

Table 7.7: Asperity parameters used in heterogeneous slip distributions on the thrust fault.

### Fault Depth

In order to be able to study the sensitivity of the ground motions to fault depth, we place the top of the fault at depths of 8.0 km, 4.0 km, and 0.0 km while maintaining the same length, width, and dip. When we bury the top of the fault 8.0 km below the ground surface, the bottom of the fault sits 15.0 km below the ground surface.

### 7.2.3 Simulation Results

We will follow the same procedure that we use to study the strike-slip simulations: we examine the base case in detail and analyze the other simulations in groups based on the variation of one of the parameters. When

<sup>5</sup>Weak refers to the heterogeneity, and upper refers to the region of greater slip.

<sup>6</sup>Weak refers to the heterogeneity, and lower refers to the region of greater slip.

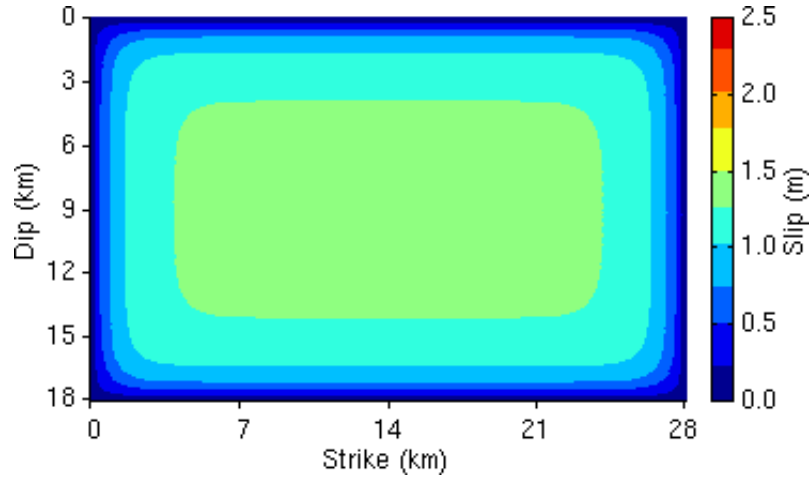


Figure 7.35: Homogeneous slip distribution unitaper which is tapered on all four edges with an average slip of 1.0 m and a maximum slip of 1.3 m.

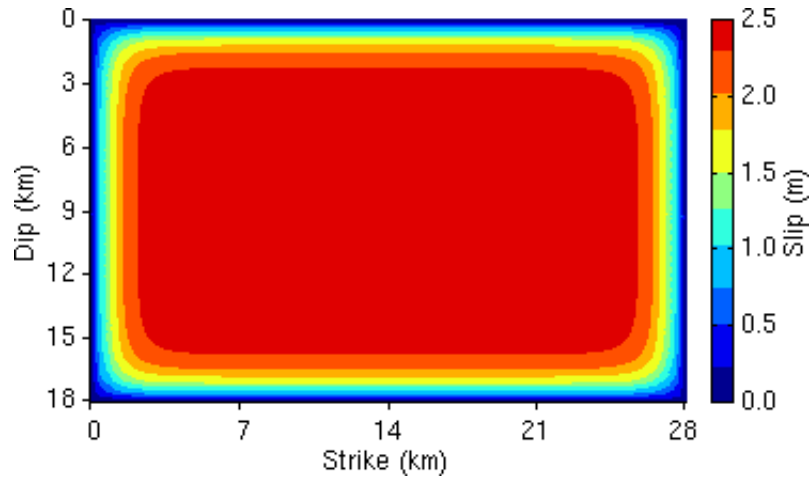


Figure 7.36: Homogeneous slip distribution unitaper2 which is tapered on all four edges with an average slip of 2.0 m and a maximum slip of 2.6 m.

we bury the top of the fault 8.0 km below the ground surface and prescribe an average final slip of 1.0 m, the earthquakes have a moment magnitude of 6.8. The simulations took 1.2 hours using 256 processors on the Intel Paragon at the CACR.

### Base Case

We begin by analyzing the ground motions on a north-south vertical slice through the center of the fault. Figure 7.39 shows the magnitude of the velocity vectors at each point on the slice. We allow the scale to saturate at 0.5 m/sec in order to illustrate the ground motions at depth more clearly. As the rupture propagates up the fault, the largest velocities are confined to a narrow region near the fault. Once the seismic waves reach the softer material in the top 6.0 km of the domain, the velocities increase and saturate the scale. Beginning at 9.0 sec the most severe motions are confined to the ground surface and are propagating to the south. In

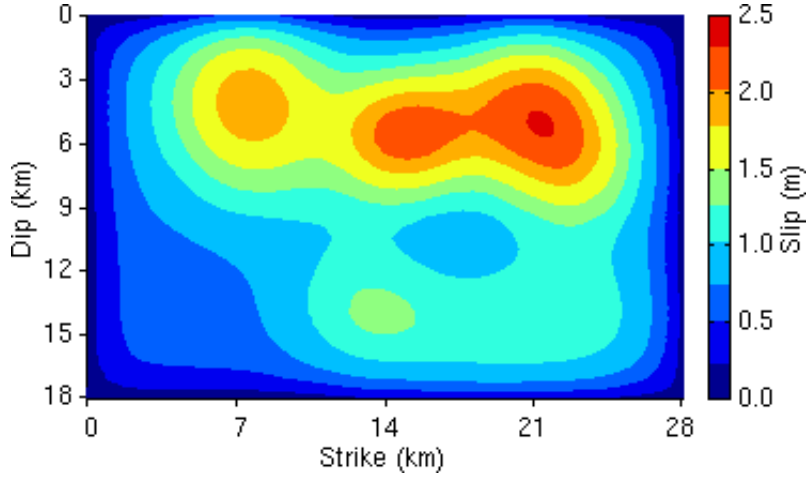


Figure 7.37: Weakly heterogeneous slip distribution weakupper which is tapered on three edges with an average slip of 1.0 m, a maximum slip of 2.3 m, and a bias towards slip near the surface.

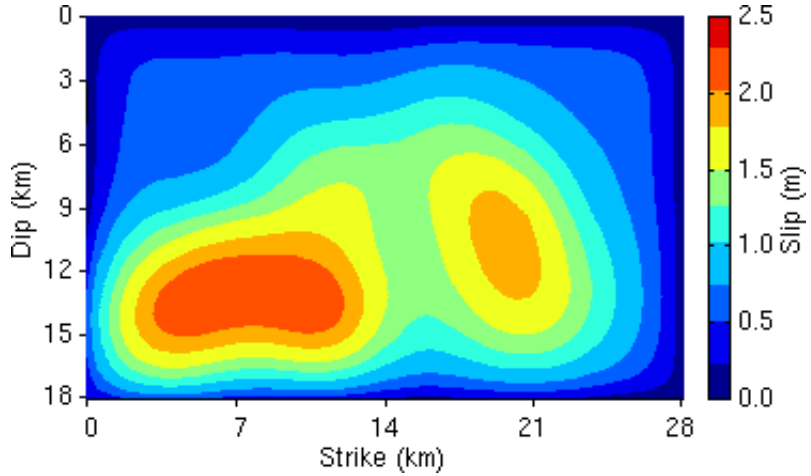


Figure 7.38: Weakly heterogeneous slip distribution weaklower tapered on three edges with an average slip of 1.0 m, a maximum slip of 2.2 m, and a bias towards slip at depth.

contrast to the area south of the epicenter, over the entire region to the north of the epicenter, we observe ground motions with velocities less than 0.15 m/sec.

The seismic waves reach the ground surface approximately five seconds after the rupture begins. Figure 7.40 displays the magnitude of the velocity vectors at each point on the ground surface beginning at 6.0 sec. As we noted above, the most severe shaking occurs in the region extending from above the top of the fault to near the south edge of the domain. The snapshot of the velocity at 10.0 sec clearly shows a double velocity pulse associated with the out and back motion of the ground with peaks in both the positive and negative directions exceeding 0.8 m/sec. The peak velocities develop in the second pulse at around twelve seconds, after which the amplitudes decay due to geometric spreading as the waves continue to propagate to the south. The shear wave with the double pulse is followed by Love and Rayleigh waves with amplitudes much smaller than the shear wave.

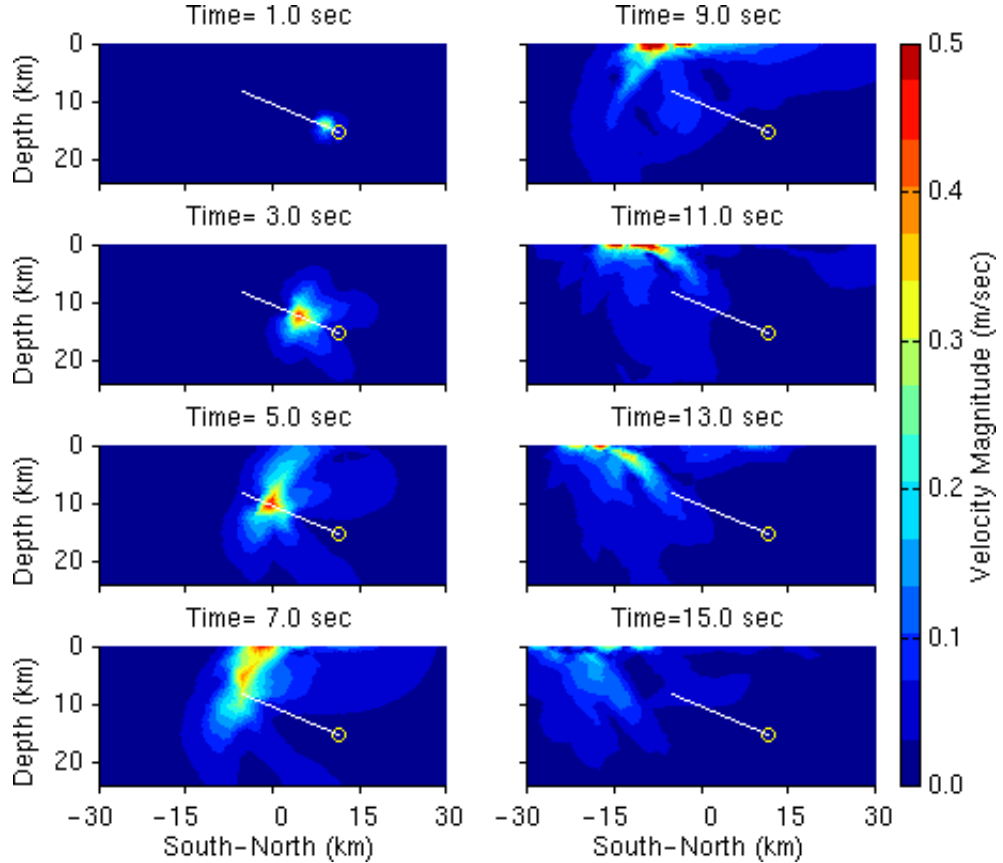


Figure 7.39: Snapshots of the magnitude of the velocity vector on a north-south vertical slice through the center of the fault for scenario base. The white line indicates the projection of the fault onto the slice, and the yellow circle identifies the hypocenter.

The maximum displacements (figure 7.41) and velocities (figure 7.42) occur five kilometers south of the top of the fault. The slip direction with a rake angle of 105 degrees skews the maximum displacements and maximum velocities slightly towards the east. The particle motion of the shear waves becomes more horizontal as the shear wave propagates through the softer material. This causes a maximum horizontal displacement 1.5 times the maximum vertical displacement (1.1 m versus 0.75 m). The velocities exhibit an even greater disparity with the maximum horizontal velocity 3.0 times the maximum vertical velocity (1.2 m/sec versus 0.40 m/sec). The maximum, filtered horizontal velocities exceed 1.0 m/sec over an area of 100 square kilometers. The final deformation at the ground surface (not shown) involves both horizontal and vertical components which tends to more evenly distribute the displacement among the two directions.

The displacements and velocities at sites S1 and S2 given in figure 7.43 exemplify the disparity between the motion in the forward direction (south of the fault) and the motion in the backwards direction (north of the fault). As shown in figure 7.31, site S1 lies above the southeast corner of the fault, and site S2 lies above the center of the northern edge of the fault, which in this case coincides with the epicenter. At site S1 the shear wave arrival consisting of a single pulse in displacement and a corresponding double pulse in

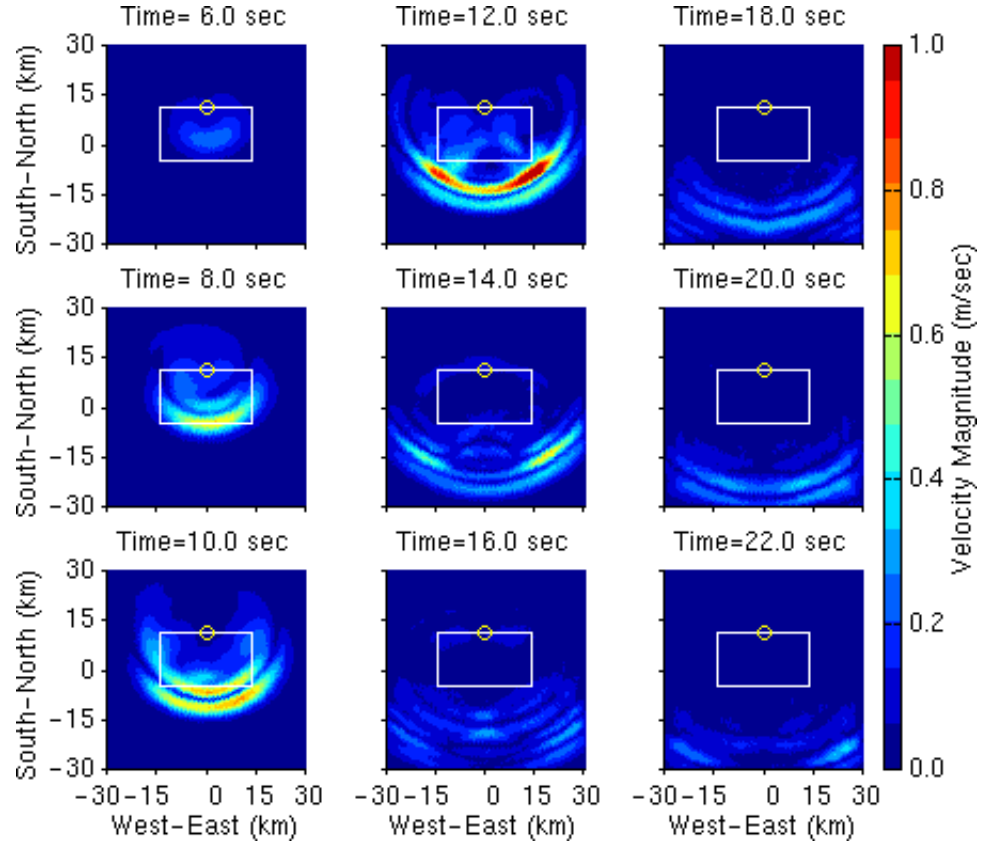


Figure 7.40: Snapshots of the magnitude of the velocity vector at each point on the ground surface for scenario base. The white line indicates the projection of the fault onto the ground surface, and the yellow circle identifies the epicenter.

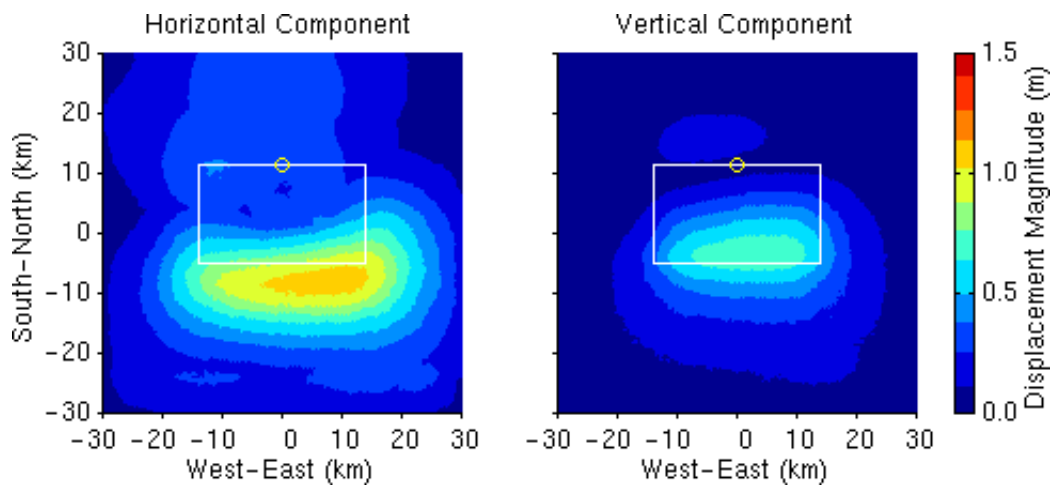


Figure 7.41: Maximum magnitudes of the horizontal and vertical displacement vectors at each point on the ground surface for scenario base. The white line indicates the projection of the fault plane onto the ground surface, and the yellow circle identifies the epicenter.

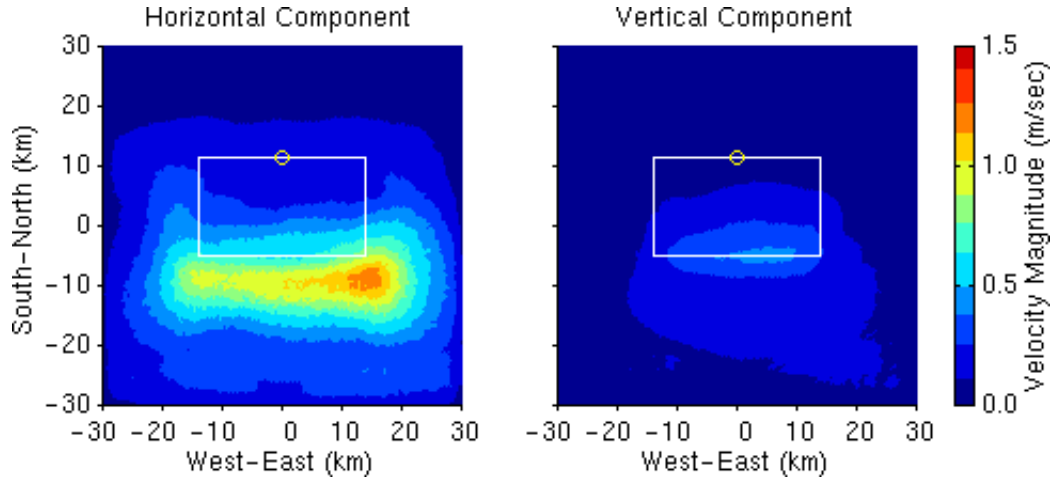


Figure 7.42: Maximum magnitudes of the horizontal and vertical velocity vectors at each point on the ground surface for scenario base. The white line indicates the projection of the fault plane onto the ground surface, and the yellow circle identifies the epicenter.

velocity dominates the motion on all three components. The horizontal motion occurs almost exclusively in the southeast direction and is skewed to the east of the slip direction. As we noted above, the peak horizontal displacement exceeds the peak vertical displacement by approximately 40%. The arrival of the shear wave is followed by the arrival of Love and Rayleigh waves but with almost negligible amplitudes compared to the shear wave. Site S2 receives far less shear wave energy, and the energy arrives over a longer interval of time. As a result, the amplitude of the shear wave blends in with the small amplitude surface waves.

We compute the response spectra at both sites following the same procedure that we use for the strike-slip fault outlined in section 7.1.3. In this case we rotate the ground motions at sites S1 and S2 to 140 degrees east of north and 170 degrees east of north, respectively. The horizontal acceleration response spectra shown in figure 7.44 vividly illustrate the severity of the ground motion at site S1 compared to the rather benign ground motion at site S2. The response spectrum for site S1 displays a broad peak of 40% g centered around a period 2.6 sec. The response spectrum for site S2, in contrast, is nearly flat with a level below 5% g.

### Material Properties

We study the effect of allowing variation in the material properties with depth by comparing the waveforms at sites S1 and S2 from scenario base, which uses a layered half-space, with those from scenario homo, which uses a homogeneous half-space. Figure 7.45 gives the north-south and vertical components of the velocity time histories at the two sites. In both cases site S1 undergoes much more severe shaking than site S2. In addition to the obvious increase in amplitude of the velocity with the layered half-space, in the homogeneous half-space the north-south and vertical components are nearly equal, while in the layered half-space the horizontal components dominate the motion as we noted in our discussion of the base case. The softer material near the ground surface does not appear to affect the vertical ground motion; however, we

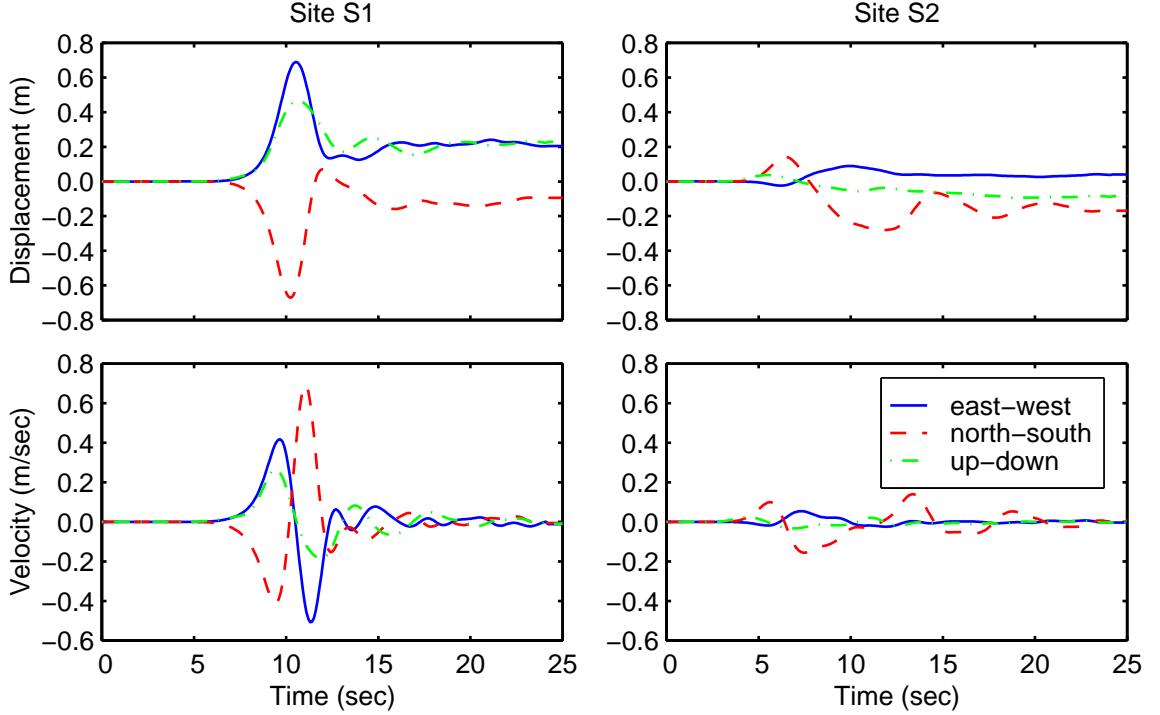


Figure 7.43: Displacement and velocity time histories at sites S1 and S2 for scenario base.

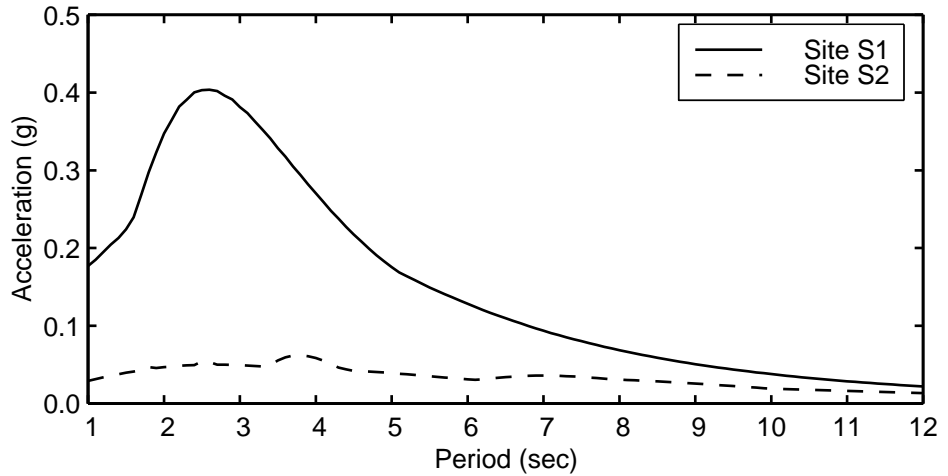


Figure 7.44: Horizontal acceleration response spectra at sites S1 and S2 for scenario base.

know that the particle motion rotates towards the horizontal as the shear wave refracts while propagating through the softer material. This causes an increase in the horizontal motion with a corresponding decrease in the vertical motion, so it is purely coincidental the vertical motion remains relatively unchanged.

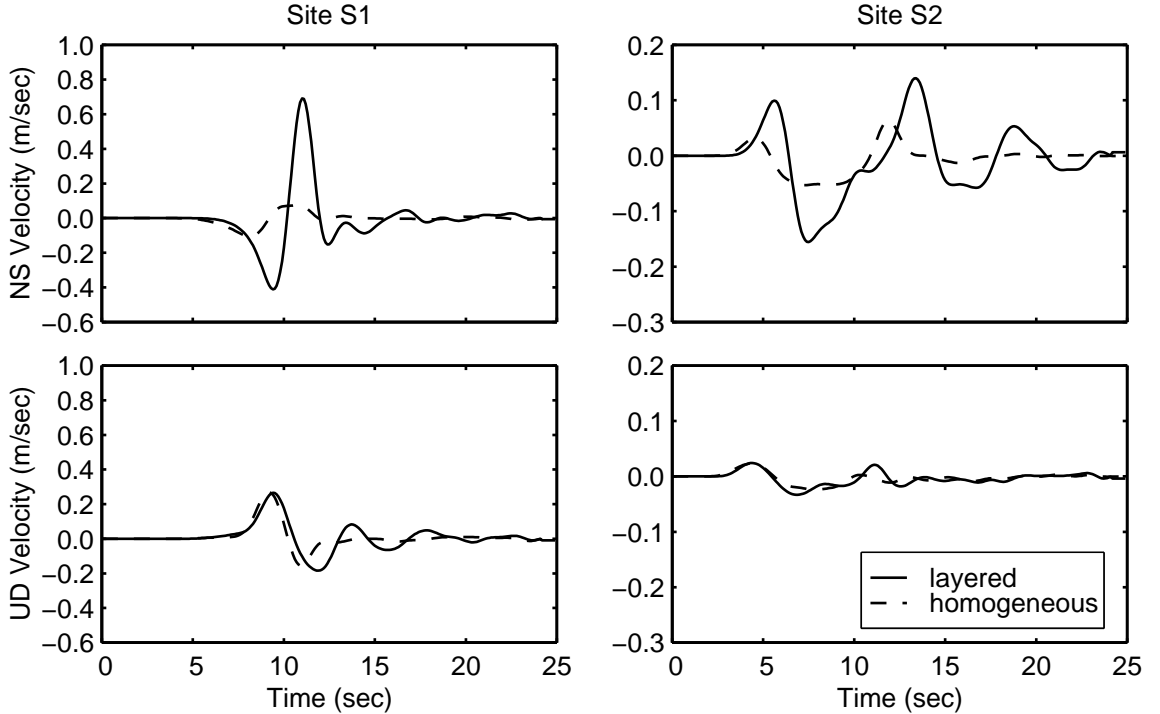


Figure 7.45: Comparison of north-south and vertical velocity time histories at sites S1 and S2 for a layered half-space versus a homogeneous half-space.

### Rupture Speed

We study the sensitivity of the ground motions to the rupture speed using scenario vr70 with a rupture speed of 70% of the local shear wave speed, scenario base with a rupture speed of 80% of the local shear wave speed, and scenario vr90 with a rupture speed of 90% of the local shear wave speed. In figure 7.46 we see that increasing the rupture speed leads to a significant increase in the amplitude of the velocity in the north-south direction at both sites S1 and S2. The vertical components show no corresponding increase. As we found in the strike-slip fault simulations (section 7.1.3), increasing the rupture speed causes the shear waves from all portions of the fault to arrive in a shorter time interval which leads to sharper phase arrivals. As a result, the width of the double pulse in velocity at site S1 decreases as the rupture speed increases.

If we examine the maximum horizontal displacements and velocities on the ground surface along the north-south line running through the center of the domain given in figure 7.47, we see that the maximum displacements and velocities increase as we increment the rupture speed from 70% to 90% of the local shear wave speed. The rupture speed does not affect the shapes of the curves. We again overlay the near-source ground motion factor,  $N_v$ , from the 1997 UBC even though the California Division of Mines and Geology does not include blind thrust faults on the maps used to determine the near-source factor (California Department of Conservation, Division of Mines and Geology 1998). With the fault dipping 23 degrees and buried 8.0 km below the ground surface, the fault lies within 10 km of the surface along a 5.1 km section of the north-south

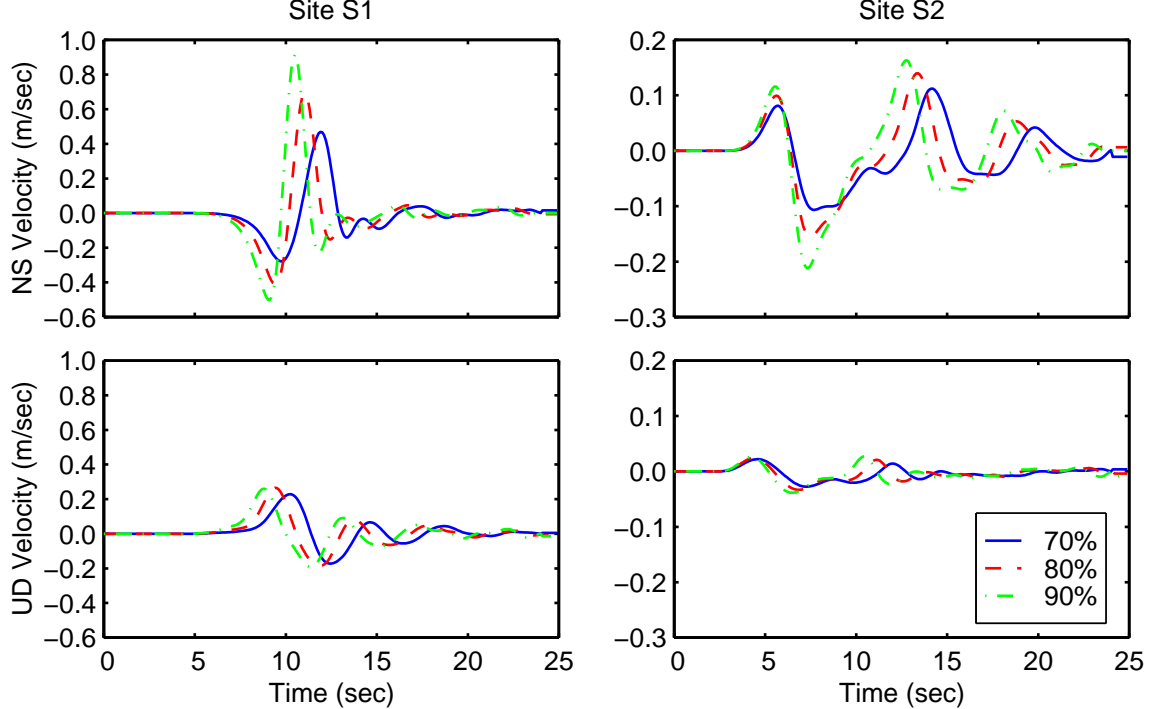


Figure 7.46: Comparison of north-south and vertical horizontal velocity time histories at sites S1 and S2 for the three rupture speeds.

line. Consequently, we set the near-source factor to 2.0 over this section and the adjacent 2.0 km on either side. The maximum displacements and velocities fall outside of this region where we set the near-source factor to 2.0. The shallow dip of the fault causes the shear wave to reach the surface 5.0 km from the top of the fault, which lies 3.0 km outside the region where the near-source factor reaches its maximum value. Additionally, the maximum displacements and velocities decay rapidly north of their peak values, while the near-source factor remains constant for several kilometers before decaying. Thus, the shape of the near-source factor does not appear to correlate with the distribution of the shaking.

### Maximum Slip Rate

Scenarios vs10, base, and vs20 with maximum slip rates of 1.0 m/sec, 1.5 m/sec, and 2.0 m/sec, respectively, illustrate the limited sensitivity of the ground motions to changes in the maximum slip rate. The maximum slip rate influences the amplitude of motion in the north-south direction at sites S1 and S2, as shown in figure 7.48, but not the shape of the waveforms. Increasing the slip rate from 1.0 m/sec to 1.5 m/sec has a more significant impact than increasing the slip rate from 1.5 m/sec to 2.0 m/sec, whereas in the case of the strike-slip fault, each increment in the maximum slip rate yields roughly the same changes in the amplitudes of the time histories. The vertical component remains relatively unchanged as we vary the maximum slip rate.

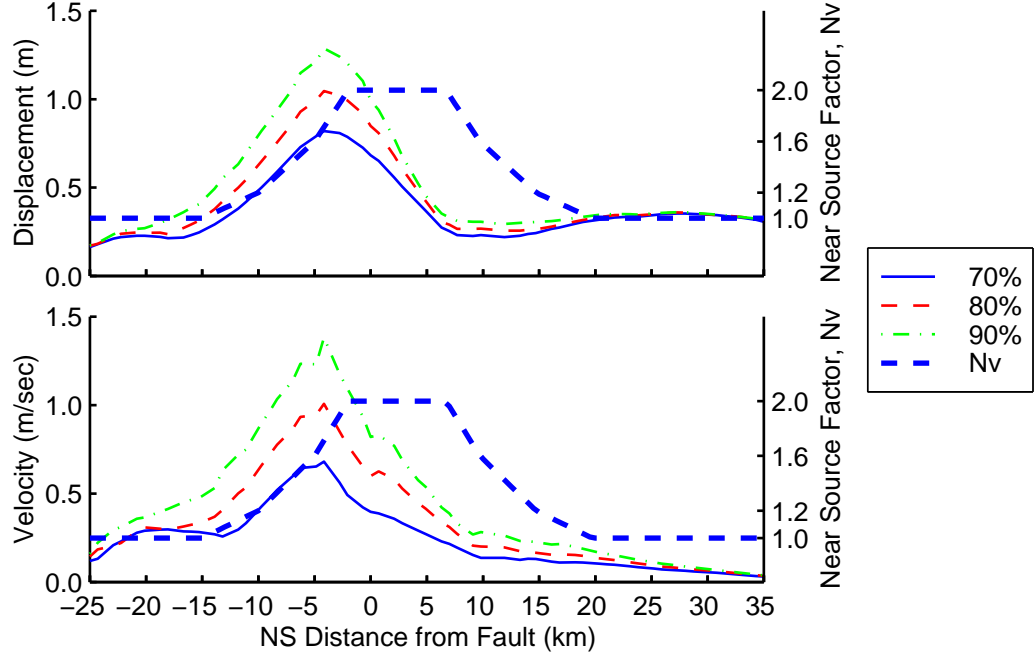


Figure 7.47: Maximum magnitudes of the horizontal displacement and velocity vectors along a north-south line running over the center of the fault for the three rupture speeds. The thick, dashed line indicates the near-source ground motion factor,  $N_v$ , from the 1997 Uniform Building Code.

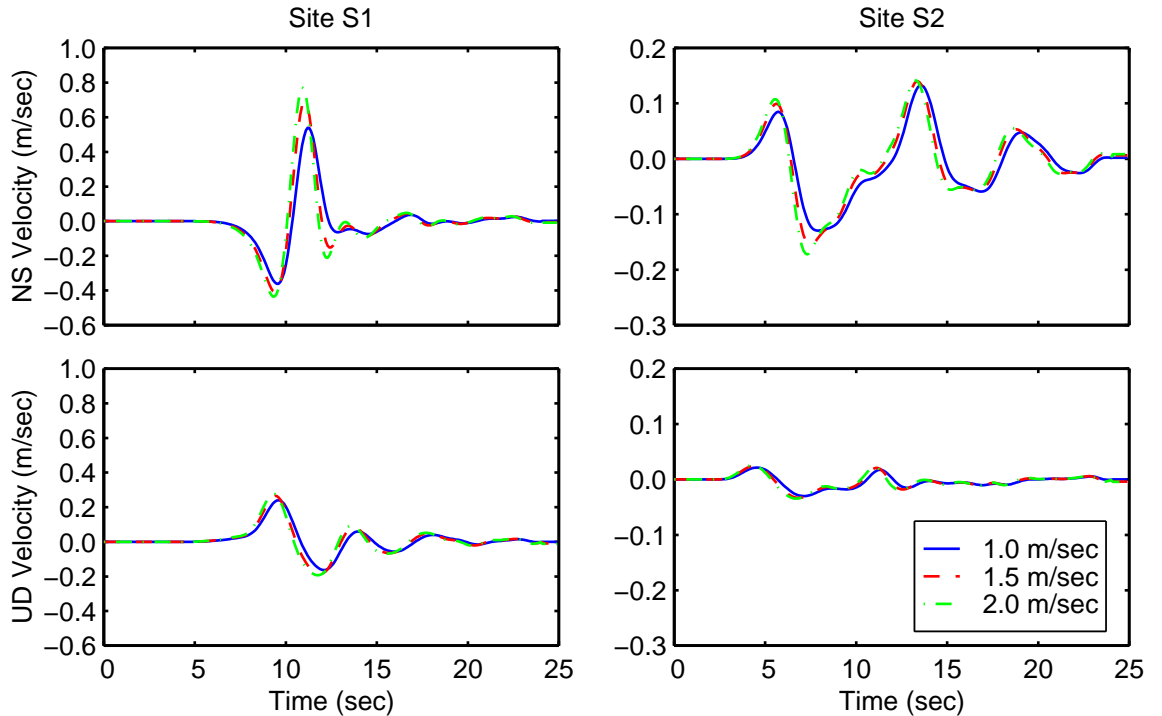


Figure 7.48: Comparison of north-south and vertical velocity time histories at sites S1 and S2 for the three maximum slip rates.

Figure 7.49 shows that the maximum horizontal displacements and velocities on the ground surface along the north-south running centerline also display a markedly greater sensitivity to increasing the maximum slip rate from 1.0 m/sec to 1.5 m/sec than to increasing the maximum slip rate from 1.5 m/sec to 2.0 m/sec. The shapes of the curves of the maximum displacements and velocities closely match those in figure 7.47 for the three rupture speeds and continue to peak approximately three kilometers south of end of the region where the near-source factor is 2.0.

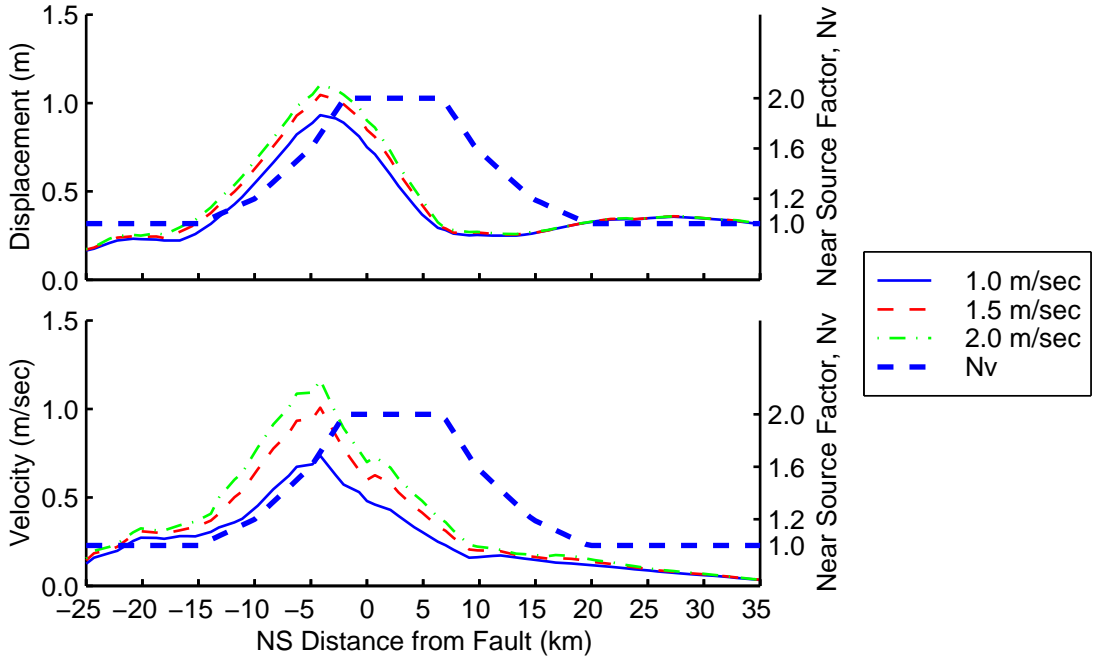


Figure 7.49: Maximum magnitudes of the horizontal displacement vectors and velocity vectors along a north-south line running over the center of the fault for the three maximum slip rates. The thick, dashed line indicates the near-source ground motion factor,  $N_v$ , from the 1997 Uniform Building Code.

### Hypocenter Location

We examine the variability of the ground motions with changes in the location of the hypocenter using scenario base (where hypocenter HA sits at the center of the bottom edge of the fault), scenario hybc (where hypocenter HB sits at the northeast corner of the fault), scenario hymc (where hypocenter HC sits near the middle of the east edge of the fault), and scenario hymc (where hypocenter HD sits near the fault center). Figure 7.34 gives the precise hypocenter locations. Figure 7.50 shows the maximum horizontal and vertical velocities on the ground when we place the hypocenter at the middle edge (hypocenter HC) for scenario hymc. By comparing the maximum velocities from scenario base (figure 7.42) with those from scenario hymc (figure 7.50), we see that moving the hypocenter location from the bottom center (hypocenter HA) to the middle edge (hypocenter HC) causes a dramatic shift in the spatial variation of the maximum velocities. The peak velocity remains near the top of the fault, but the velocities above the west edge of the fault increase

relative to the rest of the domain. Additionally, the peak horizontal velocity decreases from 1.2 m/sec to 0.55 m/sec.

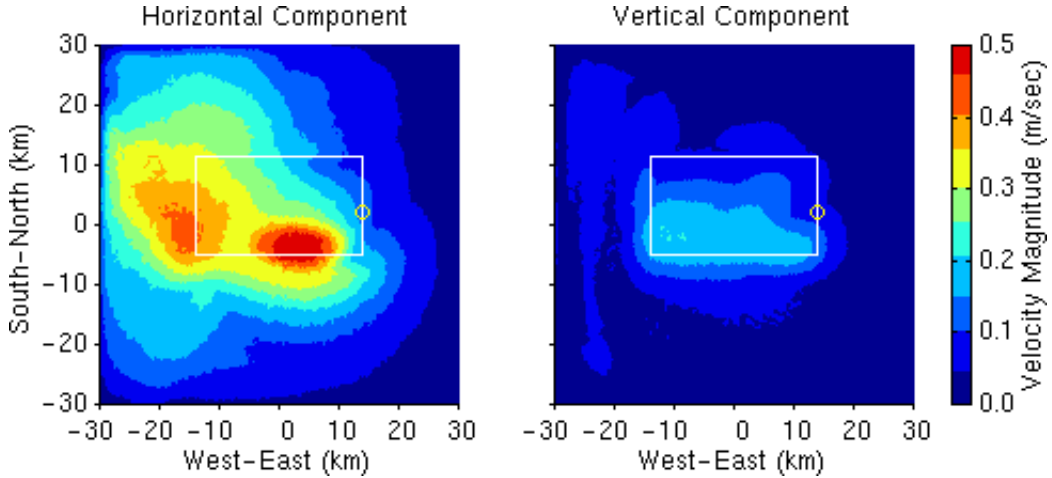


Figure 7.50: Maximum magnitudes of the horizontal and vertical velocity vectors at each point on the ground surface for scenario hymc. The white line indicates the projection of the fault plane onto the ground surface, and the yellow circle identifies the epicenter.

Site S1 lies along a different azimuth for each hypocenter location, while site S2 lies along three different azimuths for the four hypocenter locations. As we might expect from our observations of the ground motions from the strike-slip fault, at both sites S1 and S2 the displacement time histories for the different hypocenter locations given in figure 7.51 differ considerably when the sites lie along substantially different azimuths, but match reasonably well when the sites lie along similar azimuths. In general, the displacement amplitudes increase as we increase the distance the fault ruptures toward the site and place the site closer to an azimuth of zero degrees. For example, at site S1 moving the hypocenter from the middle center (hypocenter HD) to the bottom center (hypocenter HA) increases the distance the rupture propagates towards the site and places site S1 closer to an azimuth of zero degrees. As a result, the peak north-south displacement increases by 86% (from 0.36 m to 0.67 m). Similarly, shifting the hypocenter from the bottom corner (hypocenter HB) to the bottom center (hypocenter HA) increases the distance the rupture propagates towards the site, and the peak north-south displacement increases by 76% (from 0.38 m to 0.67 m). At site S2 we find that placing the hypocenter at either location at the bottom of the fault or at either location at mid-depth results in displacement time histories with similar shapes. As we expect from using the same final slip distribution, the final displacements remain the same as we change the location of the hypocenter.

We again turn our attention to the maximum horizontal displacements and velocities along the north-south line running over the center of the fault. We see only a minor shift in the shape of the maximum displacements in figure 7.52 as we move the hypocenter. The shape of the maximum velocities exhibits a more dramatic shift with fluctuations in the hypocenter location. The curve of the maximum velocities for scenario hymc contains two peaks, while the curves for the other scenarios contain only one. For scenario hymc the peak

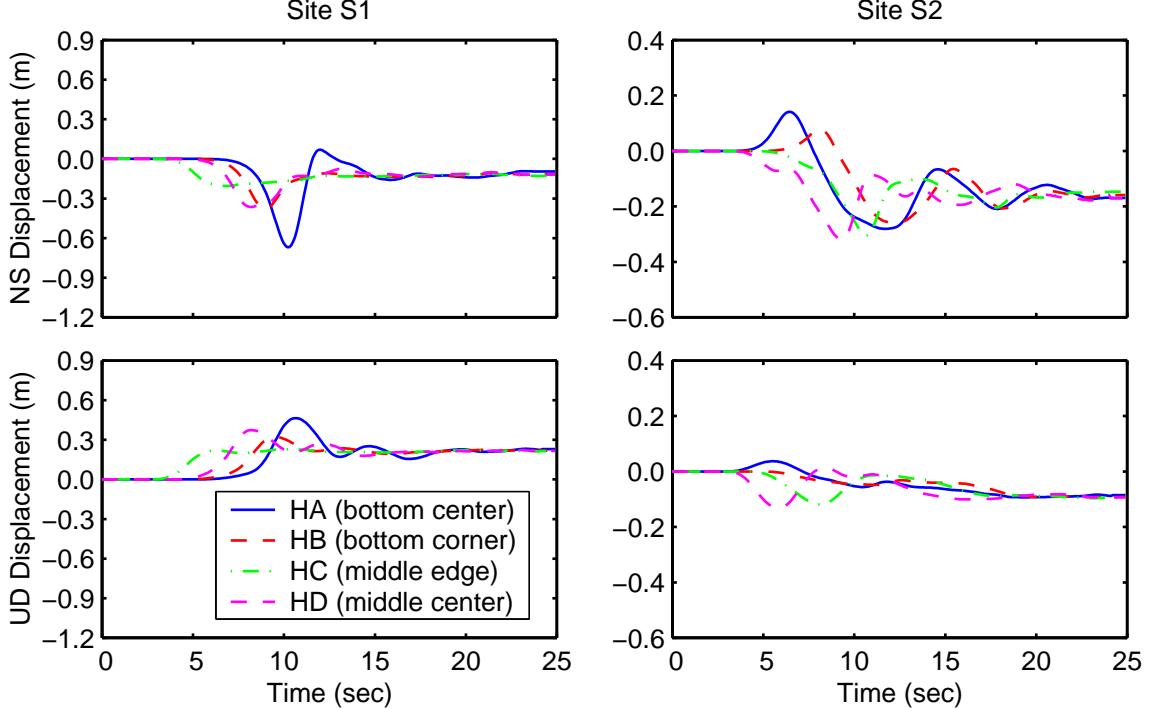


Figure 7.51: Comparison of north-south and vertical displacement time histories at sites S1 and S2 for the four hypocenter locations.

of the curve of maximum velocities falls near the middle of the region where the near-source factor is at its maximum value, whereas for the other scenarios the peak of the curve falls near the southern edge of the region where the near-source factor is at its maximum value.

### Slip Distribution

The simulations use a homogeneous slip distribution in scenario base, a weakly heterogeneous slip distribution with a bias towards slip on the upper half of the fault plane in scenario sliptop, and a weakly heterogeneous slip distribution with a bias towards slip on the lower half of the fault plane in scenario slipbot. Figure 7.53 shows that the maximum velocities on the ground surface become more symmetric about the north-south centerline when we use the slip distribution with a bias towards slip at the surface. This slip distribution contains a large asperity near the southwest corner of the fault and increases the velocities at the surrounding locations. Hence, while the slip direction tends to increase the velocities above the southeast corner of the fault, the large asperity near the southwest corner of the fault tends to increase the velocities above the southwest corner of the fault. Consequently, the spatial variation of the maximum velocities becomes more symmetric and contains one peak approximately five kilometers south of each corner at the top of the fault.

Upon examining the displacement time history at site S1 in figure 7.54, we see small variations in the

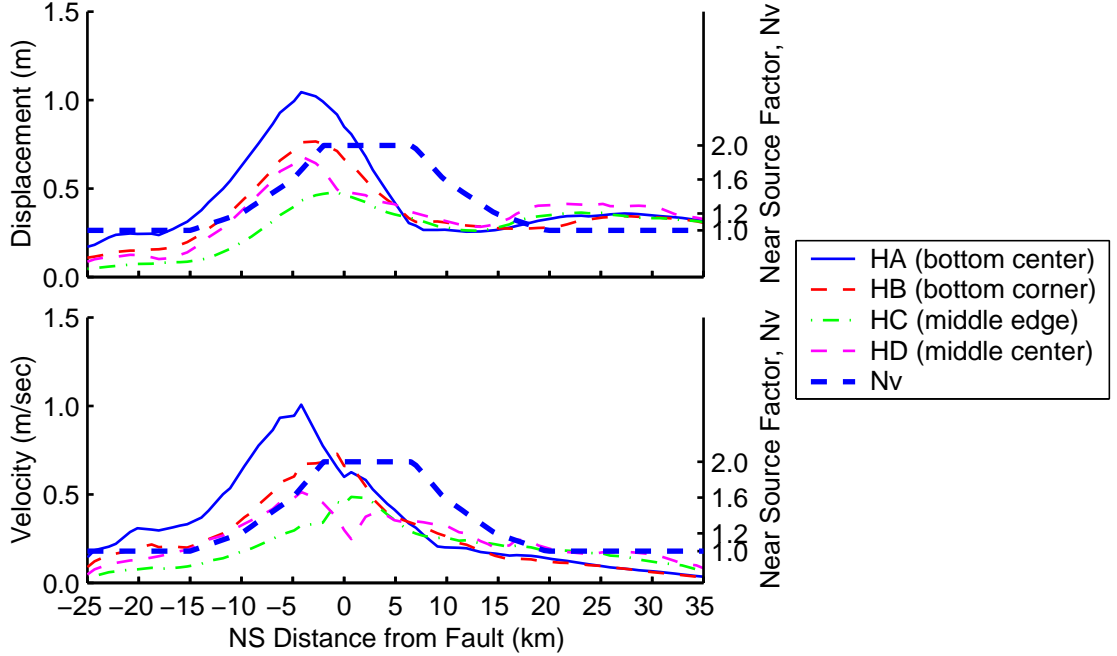


Figure 7.52: Maximum magnitudes of the horizontal displacement vectors and velocity vectors along a north-south line running over the center of the fault for the four hypocenter locations. The thick, dashed line indicates the near-source ground motion factor,  $N_v$ , from the 1997 Uniform Building Code.

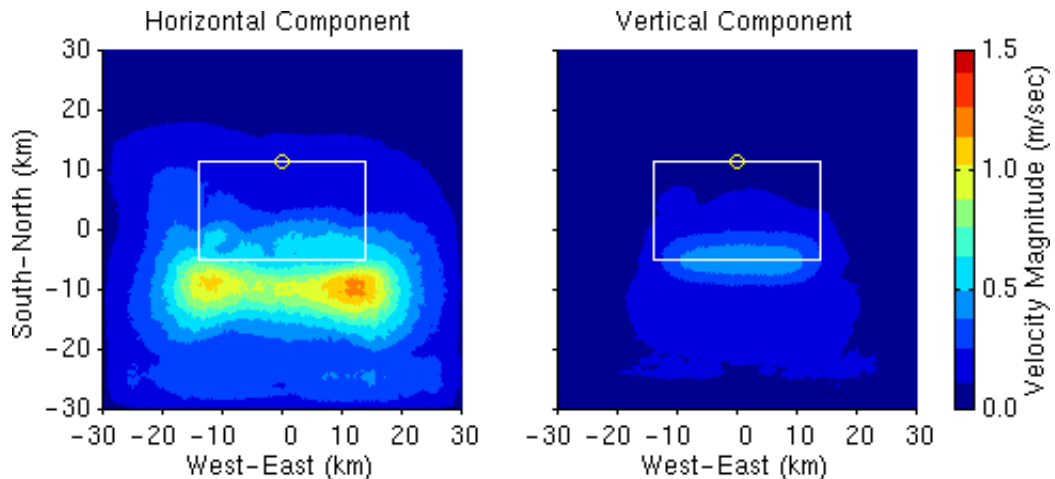


Figure 7.53: Maximum magnitudes of the horizontal and vertical velocity vectors at each point on the ground surface for scenario slip. The white line indicates the projection of the fault plane onto the ground surface, and the yellow circle identifies the epicenter.

amplitude of the displacement pulse associated with the shear wave arrival, but the remainder of the displacement time history appears unaffected by the weak heterogeneity in the slip distributions. At site S2 the ground motion displays no noticeable variation until nearly ten seconds, after which the ground motion in the north-south direction remains noticeably different for the remainder of the record. In other words, the surface waves radiating towards the north appear more sensitive to the spatial distribution of slip than the shear

waves. As we move the bias in slip from the lower half towards the upper half (considering homogeneous slip to have a bias in the center), the amplitudes of the surface waves increase because slip near the ground surface excites the surface waves more efficiently.

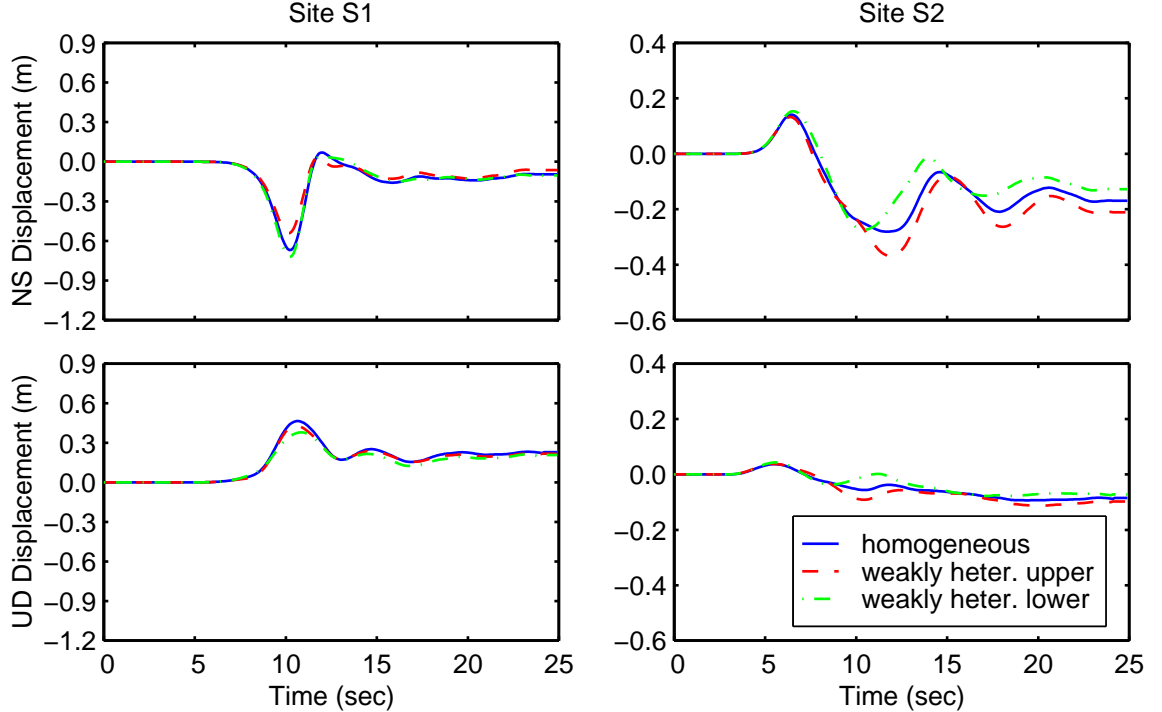


Figure 7.54: Comparison of north-south and vertical displacement time histories at sites S1 and S2 for the three slip distributions.

The maximum horizontal displacements and velocities along the north-south centerline given in figure 7.55 display only minor variations when we add heterogeneity to the slip distributions. We find two distinct trends in the curve of the maximum displacements; these include a shift in the peak of the curve towards the north when we use the slip distribution with a bias towards slip at depth, and an increase in the maximum displacements above the north end of the fault when we use the slip distribution with a bias towards slip near the surface. As we noted in our discussion of the waveforms at sites S1 and S2, the increase in the displacement amplitudes towards the north is associated with larger amplitude surface waves that are excited more efficiently by the increase in slip at shallower depths.

The only noticeable trend in the curve of the maximum velocities is the slight variation in the peak maximum velocity. This variability arises from shifts in the locations of the slip asperities. With only minor variations in the shapes of the curves of the maximum horizontal displacements and velocities, it is no surprise that the shape of the curve for the UBC near-source factor again fails to capture the shape of either the maximum displacements or the maximum velocities.

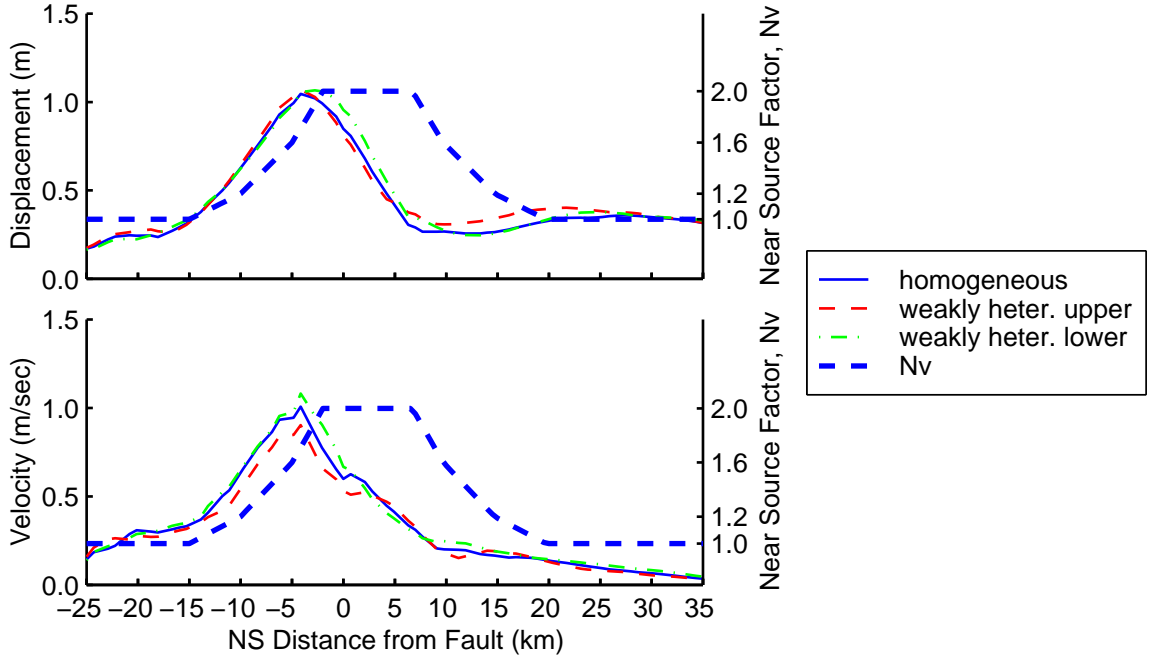


Figure 7.55: Maximum magnitudes of the horizontal displacement vectors and velocity vectors along a north-south line running over the center of the fault for the three slip distributions. The thick, dashed line indicates the near-source ground motion factor,  $N_v$ , from the 1997 Uniform Building Code.

### Average Slip

Increasing the average slip from 1.0 m in scenario base to 2.0 m in scenario slip2 causes a dramatic increase in the displacement amplitudes, but only a small increase in the velocity amplitudes. This doubling of the average slip changes the moment magnitude from 6.8 to 7.0. In figure 7.56 we find at sites S1 and S2 that varying the average slip affects both the north-south and vertical displacement components. We observe that the final displacements double as do the amplitude of the displacement pulse at site S1 and the amplitudes of the surface waves at site S2. Maintaining the same maximum slip rate of 1.5 m/sec causes the peak slip rates to occur later in the slip time history and leads to a slight delay in the peak amplitudes for an average slip of 3.0 m compared to an average slip of 2.0 m.

The maximum horizontal displacements and velocities on the north-south centerline in figure 7.57 reflect the relatively larger impact that changing the average slip has on the displacements compared to the velocities. The maximum displacements exhibit a nearly uniform increase by a factor of two consistent with our observations at sites S1 and S2. The maximum velocities, on the other hand, show only a minor increase towards the south with little variation near the peak values. The peaks of the maximum displacements and maximum velocities remain approximately three kilometers to the south of the region where we set the near-source factor to a value of 2.0.

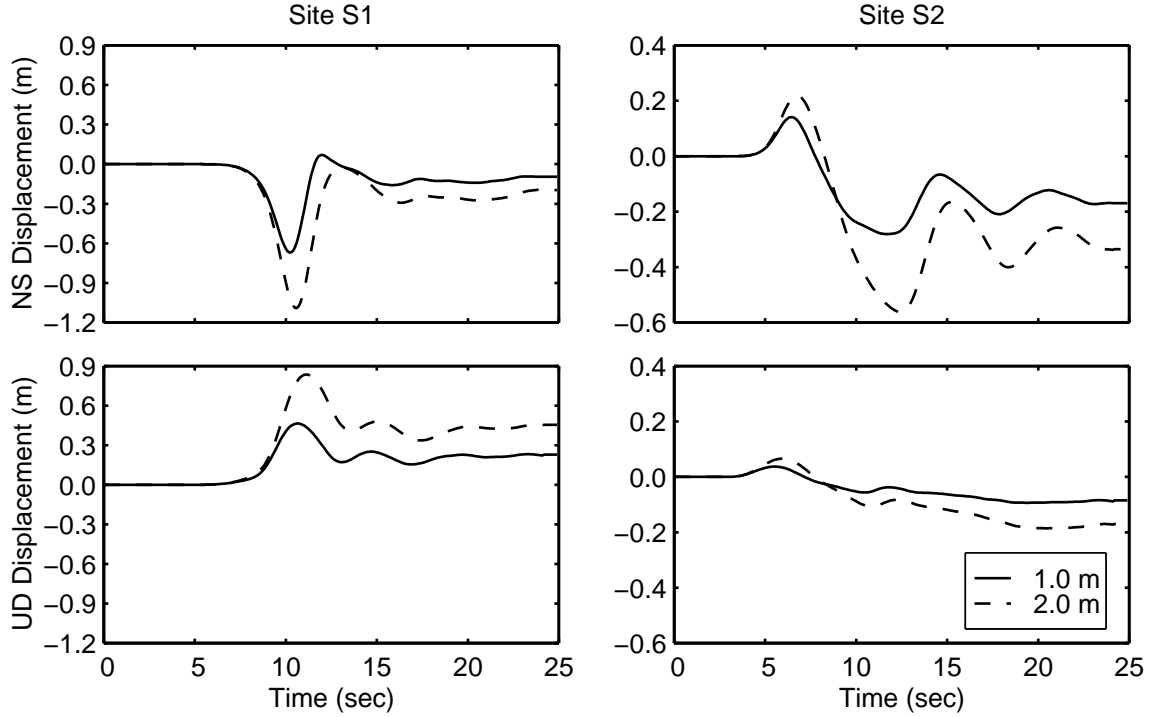


Figure 7.56: Comparison of north-south and vertical displacement time histories at sites S1 and S2 for the two values of average slip.

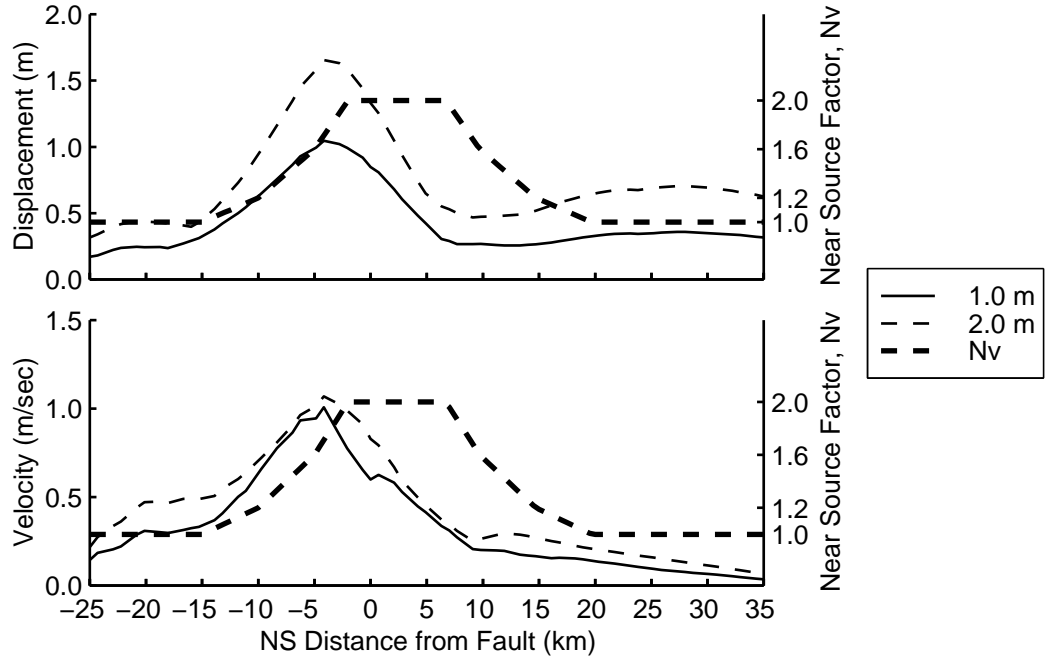


Figure 7.57: Maximum magnitudes of the horizontal displacement vectors and velocity vectors along a north-south line running over the center of the fault for the two values of average slip. The thick, dashed line indicates the near-source ground motion factor,  $N_v$ , from the 1997 Uniform Building Code.

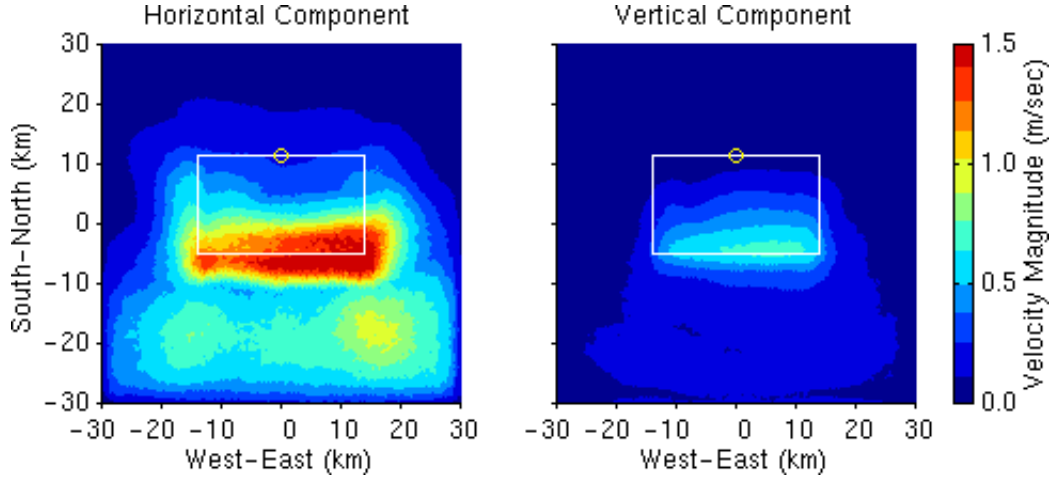


Figure 7.58: Maximum magnitudes of the horizontal and vertical velocity vectors at each point on the ground surface for scenario fault4km. The white line indicates the projection of the fault plane onto the ground surface, and the yellow circle identifies the epicenter.

### Fault Depth

We study the effect that changing the depth of the fault has on the ground motions using scenario base where the top of fault sits at a depth of 8.0 km, scenario fault4km where the top of the fault sits at a depth of 4.0 km, and fault0km where the top of the fault sits at the ground surface. As we raise the top of the fault, the slip occurs in softer material which reduces the moment magnitude from 6.8 (8.0 km depth) to 6.7 (4.0 km depth) and 6.6 (0.0 km depth). While the moment magnitude decreases, the ground motions become much more severe, particularly directly above the top of the fault. Figure 7.58 illustrates the increase in the maximum velocities above the top of the fault and the shift in the peak values in the horizontal direction from 5.0 km south of the top of the fault to directly above the top of the fault. The peak maximum horizontal velocity increases by 50%, and the area subjected to maximum velocities exceeding 1.1 m/sec jumps from roughly 20 square kilometers to more than 200 square kilometers.

As evident in figure 7.59, raising the top of the fault from 8.0 km to 4.0 km causes a substantial increase in the amplitude of the displacement pulse at site S1. Raising the top of the fault an additional 4.0 km, so that the top of the fault reaches the ground surface, leads to a velocity pulse of about the same size, but with three peaks; this implies the single pulse in displacement becomes a double pulse, or in other words, the rebound in displacement overshoots the final value. Additionally, raising the top of the fault to the surface causes a delay in the arrival of the shear wave at site S1, because the rupture is completely contained in the softer material near the surface; to reach site S1 the shear waves must traverse a more horizontal path with a greater distance through the softer material where the shear wave speed is slower. In contrast to site S1, as we raise the fault, the shear waves continue a near vertical propagation path to site S2, and the reduction in propagation distance needed to reach the site leads to earlier arrivals of the shear waves. Furthermore, the increased motion of the hanging wall contributes to a more pulse like motion in the horizontal direction at site S2. The motion in the

vertical direction is less sensitive to the changes in the depth of the fault.

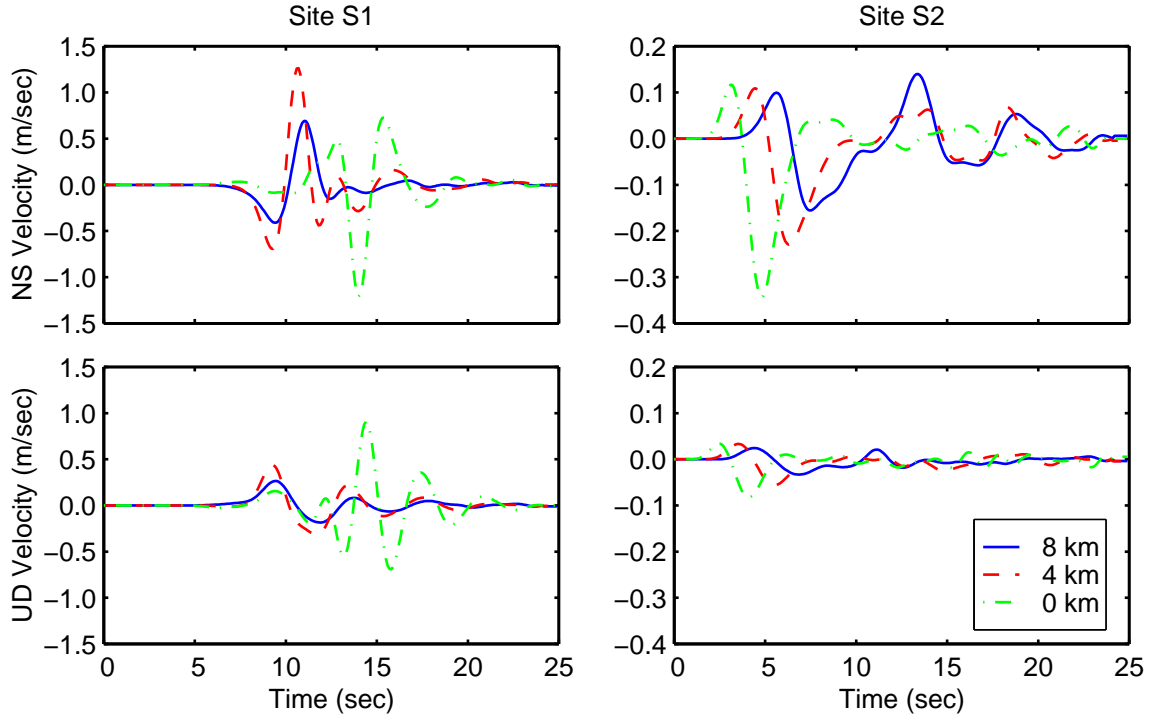


Figure 7.59: Comparison of north-south and vertical velocity time histories at sites S1 and S2 for the three depths of the top of the fault.

Figure 7.60 displays the maximum horizontal displacements and velocities along the north-south centerline. As we previously noted, for the base case with a fault depth of 8.0 km, the curve for the maximum displacements and the curve for the maximum velocities peak 5.0 km south of the top of the fault. When the top of the fault sits 4.0 km below the surface, the maximum displacements and velocities contain two peaks. The first peak is associated with the maximum amplitude of the shear wave, while the second peak is associated with the maximum amplitude of the surface waves. Note that the second peak falls in a region where the near-source factor has decayed to near its minimum value. When the top of the fault lies at the ground surface, the maximum displacements directly above the fault exhibit a greater increase than those up-dip from the fault, and the peak displacements fall near the center of the region where the near-source factor is a maximum. The curve of the maximum velocities becomes complicated due to shear waves reflecting off the surface and interacting constructively and destructively with shear waves generated at other locations on the fault. Thus, we find the shape of the curve for the near-source factor better fits the general shape of the curve of the maximum velocities when the fault lies close to the surface. This comes as no surprise since the California Division of Mines and Geology includes only strike-slip faults and thrust faults with surface rupture in the maps used to determine the near-source factor.

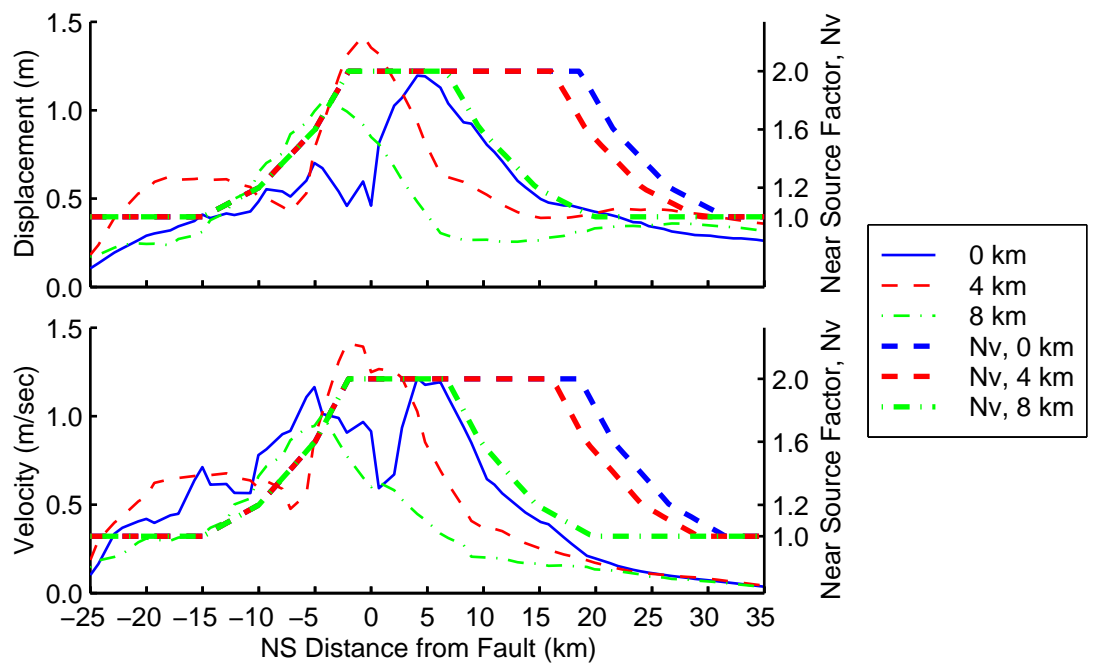


Figure 7.60: Maximum magnitudes of the horizontal displacement vectors and velocity vectors along a north-south line running over the center of the fault for the three depths of the top of the fault. The thick, dashed lines indicate the near-source ground motion factor,  $N_v$ , from the 1997 Uniform Building Code for three fault depths.

## 7.3 Discussion

### 7.3.1 Ground Motion Characteristics

The earthquake simulations on the strike-slip fault share several distinct characteristics. When slip occurs in the softer material in the top six kilometers of the domain, the rupture slows considerably in this region causing the curvature of the rupture front to progressively increase. As a result, the reinforcement of the shear wave by the rupture stabilizes and the peak velocities become uniform along the strike of the fault for a significant portion of the fault length. Due to positive reinforcement by the rupture, the peak displacements tend to increase along the strike of the fault away from the epicenter until the end of the fault where they decay rapidly with distance. A typical ground motion contains a large amplitude shear wave followed by a train of surface waves with nearly the same amplitude. The most severe ground motion occurs in the direction normal to the fault.

We also find several common features for the simulations where the top of the thrust fault lies 8.0 km below the ground surface. The shallow dip of the fault to the north causes the maximum displacements and velocities to occur approximately five kilometers south of the top of the fault. The rake angle of 105 degrees directs the largest displacements and velocities towards the southeast. A large, single pulse in displacement and a corresponding large, double pulse in velocity characterize the ground motions towards the south (the forward direction). The ground motions towards the north (the backward direction) are much less severe. As we raise the top of the fault towards the ground surface, the motion above the fault becomes more severe, and a pulse-like shear wave arrival appears in the displacements above the north end of the fault.

### 7.3.2 Sensitivity of Ground Motions to Variations in Parameters

Based on the strike-slip and thrust fault simulations we assess the sensitivity of the ground motions to our systematic variation of the simulation parameters.

#### Material Properties

The ground motions exhibit a strong sensitivity to vertical variation of the material properties (homogeneous half-space versus layered half-space). Softening the material near the surface leads to a substantial increase in the displacement and velocity amplitudes. In the strike-slip simulations when we place the top of the fault at the ground surface, we observe large amplitude Love and Rayleigh waves in the layered half-space, but not in the homogeneous half-space. In the thrust fault simulations when we bury the fault beneath the ground surface, the horizontal component dominates the motion in the layered half-space, while the horizontal and vertical components are much smaller and roughly the same in the homogeneous half-space.

### Rupture Speed

Increasing the rupture speed compresses the time histories in duration, and we observe a corresponding narrowing of the ground motion pulses. Additionally, the reinforcement of the shear wave by the rupture becomes more efficient as the rupture speed increases, because the rupture follows more closely behind the shear wave. This leads to larger amplitudes in both the displacement and velocity time histories in the strike-slip and thrust simulations as we increase the rupture speed from 70% to 90% of the local shear wave speed. However, in the thrust fault simulations this increase is predominantly confined to the horizontal components. The ground motions appear moderately sensitive to variations in the rupture speed.

### Maximum Slip Rate

The ground motions display slightly less sensitivity to the changes in the maximum slip rate than they do to the changes in the rupture speed. Increasing the maximum slip rate narrows the rupture front which positions the center of the rupture front closer behind the shear wave. As a result, the efficiency of the reinforcement of the shear wave improves, as it does when we increase the rupture speed, and we observe similar increases in the amplitudes of the ground motions. However, on both faults the phase arrivals remain relative unchanged. Hence, the maximum slip rate influences the amplitude of the motion but not the shapes of the waveforms.

### Hypocenter Location

At a given site the sensitivity of the ground motions to the location of the hypocenter depends on the relative changes in azimuth. In the strike-slip simulations the azimuth of the sites in the forward direction remains nearly constant and we observe very small variations in the motions when we move the hypocenter location. On both faults when the azimuth changes significantly as we move the hypocenter, we find large variations in the ground motions. In some cases the site may move off of or onto a nodal line, and the ground motions increase or decrease by very large amounts.

### Slip Distribution

The ground motions exhibit little sensitivity to the addition of weak heterogeneity into the distribution of final slip, particularly in the forward direction. However, we expect the high frequency portion of the ground motions, which we do not include in the simulations, to exhibit a greater sensitivity to heterogeneity in the final slip. In the thrust fault simulations the dip location of the heterogeneity affects the amplitude of the surface waves at sites towards the north (backward direction). In the strike-slip simulations we use a strongly heterogeneous slip distribution which does reduce the displacement amplitudes for a considerable portion of the time histories. As in the thrust fault simulations with weak heterogeneity, the ground motions in the backward direction show a greater sensitivity to the strong heterogeneity in the final slip. In the forward

direction we do observe some minor changes in the waveforms, but the peak displacements and velocities remain relatively unchanged.

Graves (1998) also found near-source ground motions relatively insensitive to weakly heterogeneous slip distributions; however, he found large reductions in the peak velocities with a strongly heterogeneous distribution of slip. In contrast to our simulations, he lengthened the slip duration on the shallow portion of the fault based on the kinematic source model of the 1992 Landers earthquake from Wald and Heaton (1994). This significantly disrupts the efficiency of the reinforcement of the shear wave by the rupture and leads to a decrease in the amplitude of the motion. As we noted in our discussion of our choice of the slip rates and rupture speeds in section 7.1, considerable uncertainty still exists regarding the duration of slip for very shallow rupture, and lengthening of the duration of slip near the surface may or may not be realistic.

### Average Slip

Because the displacement solution is linear in slip, when we increase the average slip on the fault, the displacement amplitudes increase about the same relative amount as the increase in average slip. Maintaining the same rupture speed and maximum slip rate prevents a similar increase in the velocities; the amplitudes of the velocity time histories show only a minor increase. Additionally, by keeping the maximum slip rate the same, the larger slip leads to a longer rise time. Consequently, we observe a slight delay in the peak displacement and velocity amplitudes as we increase the average slip. Thus, the displacements exhibit a strong sensitivity to different values of average slip, while the velocities exhibit a weak sensitivity.

### Fault Depth

In our simulations the ground motions are most severe when the slip occurs near the surface. With shallow slip we observe large amplitude surface waves with several cycles of deformation. We often do not observe these features in the real earth, because dissipation and lateral heterogeneity in the material properties tend to disrupt the generation of surface waves. Raising the top of the thrust fault causes an increase in the motion directly above the fault and shifts the largest motion from south of the top of the fault to directly above the top of the fault. On both the strike-slip fault and the thrust fault, the ground motions display a strong sensitivity to the depth of the fault.

### 7.3.3 Implications for Earthquake Engineering

This sensitivity study shows that in order to accurately model ground motion, in particular ground motion for engineering design, we must carefully select the values for those parameters that cause the most variability in the resulting ground motion. Thus, for a given site we must know the material properties of the surrounding region and the location and geometry of all nearby faults. To simulate the most severe cases of ground motion, the hypocenter should be placed such that the rupture propagates as far as possible towards the site

under study, and that the site lies close to an azimuth of zero. Additionally, we must select reasonable values of rupture speed, maximum slip rate, and average slip; if the amplitudes of the displacement time histories are particularly important, we need to pay special attention to the average slip. As long as the site sits in the forward direction, the spatial distribution of slip on the fault has little influence on the long-period ground motions, so we need not model it with as great of care.

We consider the distribution of the ground motions on the ground surface for the base cases in the sensitivity study (scenario baseII for the strike-slip fault and scenario base for the thrust fault). Figure 7.61 displays the area on the ground surface where the maximum horizontal displacements and velocities exceed a given value. The areas where the maximum values exceed 0 m and 0 m/sec correspond to the total areas of the ground surfaces in the two domains. The entire ground surfaces in the domains experience at least small displacements and velocities, so the curves are relatively flat for small levels of shaking. The shapes of the curves corresponding to the maximum horizontal displacements for the strike-slip and thrust faults closely agree, as do the shapes of the curves corresponding to the maximum horizontal velocities for the two types of faults. The area subjected to a given maximum displacement or velocity decreases rapidly as we approach the peak maximum displacements and velocities. This is associated with the rapid increase in the maximum displacements and velocities as we approach the fault.

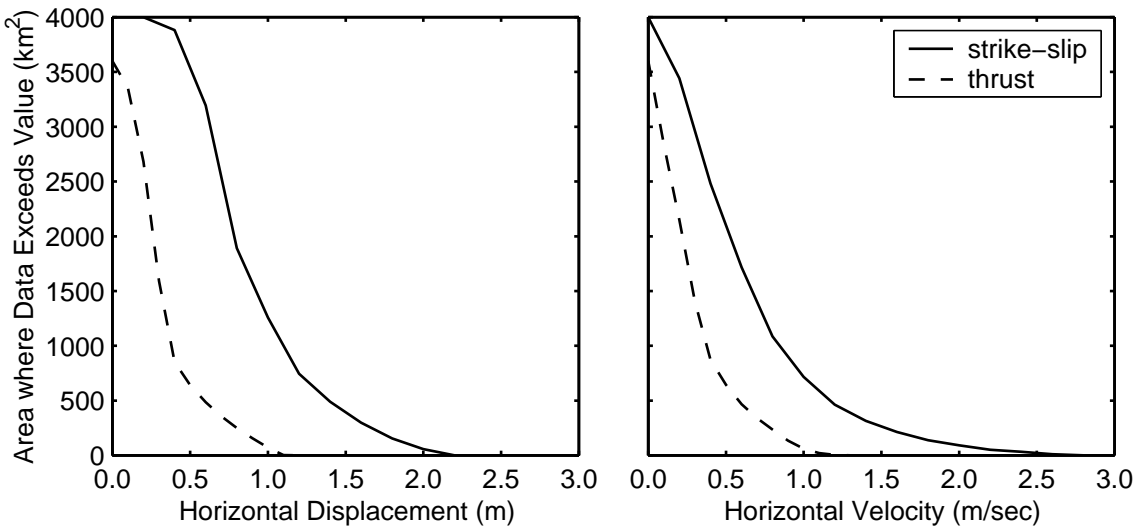


Figure 7.61: Areas on the ground surface in the strike-slip and thrust fault domains where the maximum horizontal displacements and velocities exceed a given value.

Near the middle of the curves the area subjected to a given level of ground motion increases very rapidly for small changes in the level of ground motion. This means that if a region contains many structures that experience damage for these moderate levels of ground motion (relative to the severe ground motion near the fault), then only minor improvements in the structural capacity may drastically reduce the area of the region where damage occurs. Alternatively, small degradations in the structural capacity of these structures lead to a substantial increase in the area where damage occurs. We illustrate the former of these two cases

with an example. If a given type of structure generally suffers severe damage when the maximum horizontal velocity exceeds 0.40 m/sec, then the strike-slip earthquake in scenario base would cause severe damage in these structures over an area of 2400 square kilometers. If we retrofit these structures so that similar damage occurs at 0.60 m/sec instead of 0.40 m/sec, then the same earthquake would cause the same level of damage over an area of only 1600 square kilometers. This is a 33% reduction in the area where severe damage occurs. The same strategy applied at higher velocities generates similar percentage reductions, but the sizes of the areas are much smaller.

The difference in the average slip between the base case for strike-slip fault (2.0 m) and the base case for the thrust fault (1.0 m) creates the shift in the areas subjected to maximum displacements exceeding a given value. We cannot attribute the difference in the areas for the maximum velocities to the difference in average slip between the base cases for the strike-slip fault and thrust fault, because in the sensitivity studies we find the maximum velocities relatively insensitive to the average slip. Instead, we attribute the increase in the area subjected to a given maximum velocity to the differences in the fault geometries. For the thrust fault the shallow dip angle of 23 degrees and the 28 km fault length leads to the velocity pulse sweeping across a large area, but the 18 km fault width limits the distance over which the rupture reinforces the shear wave. For the strike-slip fault the vertical dip of the fault tends to confine the velocities pulses to the region close to the fault (small area), but the 60 km fault length allows the rupture to reinforce the shear wave over a much greater distance compared to the thrust fault. The longer fault length of the strike-slip fault has a greater impact than the shallow dip angle of the thrust fault, so that the area on the ground surface subjected to a given velocity level is larger for the strike-slip fault than for the thrust fault.

The simulations also reveal some information regarding ground motions and moment magnitude. As we might expect and the simulations confirm, we find variability in the ground motions for a given moment magnitude for different sites and scenarios with different rupture speeds, slip rates, and hypocenter locations. However, we generally expect the severity of the ground motion to increase with the moment magnitude.

For the strike-slip fault and the thrust fault, table 7.8 gives the maximum displacements and velocities for the base case and those scenarios with different moment magnitudes. We see that increasing the average slip increases the moment magnitude, and it is accompanied by the expected increase in maximum displacement with little change in the maximum velocity. We also see that raising or lowering the depth of the fault causes an equal or greater change in moment magnitude accompanied by larger variations in maximum displacement and velocity, but the motions are more severe as the moment magnitude decreases. The moment magnitude depends on the shear modulus which is smaller in the softer material near the surface, so that the moment magnitude decreases as we raise the fault closer to the ground surface. Thus, the moment magnitude provides a poor measure of the severity of the ground motion with variations in the depth of the fault. The seismic potency, which is defined as the product of the average slip and fault area, provides a slightly better measure of the severity of shaking by removing the dependence on the shear modulus.

For each group of simulations in the sensitivities studies with the strike-slip fault and the thrust fault,

Fault Type	Scenario	Moment Magnitude	Seismic Potency (m <sup>3</sup> )	Average Slip (m)	Maximum Horizontal Displacement (m)	Maximum Horizontal Velocity (m/sec)
Strike-Slip	baseII	7.0	$1.8 \times 10^9$	2.0	2.2	2.9
	slip3	7.1	$2.7 \times 10^9$	3.0	2.5	2.8
	fault4km	7.1	$1.8 \times 10^9$	2.0	1.2	1.7
	fault8km	7.1	$1.8 \times 10^9$	2.0	0.95	1.0
Thrust	base	6.8	$5.0 \times 10^8$	1.0	1.1	1.2
	slip2	7.0	$1.0 \times 10^9$	2.0	1.8	1.4
	fault4km	6.7	$5.0 \times 10^8$	1.0	1.6	1.8
	fault0km	6.6	$5.0 \times 10^8$	1.0	1.3	1.5

Table 7.8: Variations in the peak maximum displacements and velocities with moment magnitude.

we compared the shapes of the curves of the maximum displacements and maximum velocities along a line running normal to the strike of the fault with the shape of the curve of the Uniform Building Code near-source factor,  $N_v$ . If we assume that the maximum displacements and velocities correlate with the seismic demand imposed on a building, then we want the shape of the near-source factor curve to match the general shapes of the maximum displacements and the maximum velocities; we do not correlate the maximum displacements or velocities with specific values of the near-source factor. For the strike-slip fault we find that the near-source factor accurately captures the location of the peak motion and the decay with distance from the fault.

We apply the formula for the near-source factor from the 1997 Uniform Building Code to all three depths of the thrust fault. The California Division of Mines and Geology, on the other hand, does not include blind thrust faults on the maps used to determine the near-source factor (California Department of Conservation, Division of Mines and Geology 1998). For the thrust fault the near-source factor reaches a maximum value where the fault lies within 10 km of the surface and 2.0 km on either side. When we place the fault close to the ground surface, this region does receive the more severe ground motion. However, the peak motion falls outside this region when we bury the fault 8.0 km below the ground surface. The near-source factor remains at a maximum value for only 2.0 km on the up-dip side of the fault regardless of the depth of the fault. In order for the shape of the near-source factor to more closely follow the shapes of the maximum displacements and velocities for buried thrust faults, it must be either shifted towards the up-dip side of the fault or extended in that direction.

We now consider a modification in the formulation of the near-source factor curve to account for blind thrust faults. We adopt the conservative approach of increasing the near-source factor in the up-dip direction rather than shifting the entire curve. Instead of using the top of the fault as the reference point in determining the distance from the fault in the region up-dip from the fault, we use the up-dip projection of the fault plane to determine the distance from the fault. Consequently, the modified near-source factor remains at its maximum value over the region where the extension of the fault plane lies within 10 km of the ground surface and 2.0 km

on either side as illustrated in figure 7.62. Our modification includes variations in both the location of the top of the fault and the angle of dip of the fault plane; however, we can test only the application to various fault depths, because we do not vary the dip angle in the simulations. We reproduce figure 7.60 in figure 7.63 with the modified near-source factor. For all three depths of the fault, the peak maximum horizontal displacements and velocities generally lie in the center of the region where we set the modified near-source factor to its maximum value. The conservative nature of the modification is apparent by the narrow peaks in the curves of the maximum displacements and velocities compared to the peaks in the modified near-source factor. This alteration of the near-source factor remains consistent with 1997 UBC near-source factor as it applies to strike-slip faults and thrust faults with surface rupture. Thus, the shape of the modified near-source factor provides a much better fit to the pattern of strong shaking than the near-source factor,  $N_v$ , in the 1997 UBC.

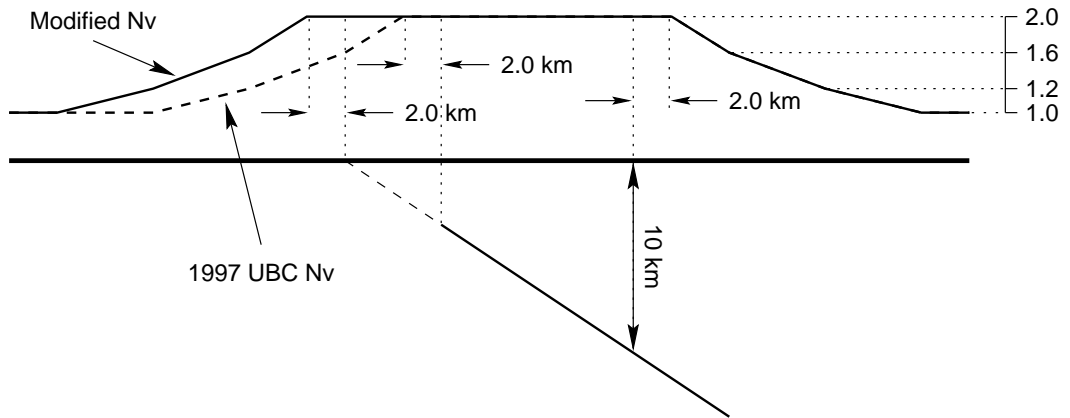


Figure 7.62: Modified version of the 1997 UBC near-source. The upper portion shows the modified near-source factor and the 1997 UBC near-source factor,  $N_v$ . The lower portion of the figure shows the location of the fault plane and the up-dip projection.

### 7.3.4 Geophysical Implications

As discussed in the preceding section, the moment magnitude often, but not always, correlates with the severity of the ground motion. Hanks and Kanamori defined the moment magnitude so that it is proportional to the radiated energy and it is compatible with the empirical energy-magnitude relation developed by Gutenberg and Richter (Heaton et al. 1986). Figure 7.64 displays the radiated energy as a function of moment magnitude for all of the strike-slip and thrust fault simulations along with the energy-magnitude relation of Gutenberg and Richter given by equation (7.1) (Lay and Wallace 1995). The Gutenberg-Richter energy-magnitude relation gives the radiated energy in ergs in terms of the surface wave magnitude,  $M_s$ . Using the expressions for the surface wave magnitude and moment magnitude as a function of the seismic moment, we manipulate the energy-magnitude relation to give the radiated energy in terms of the moment magnitude.

$$\log E = 11.75 + 1.5M_W \quad (7.1)$$

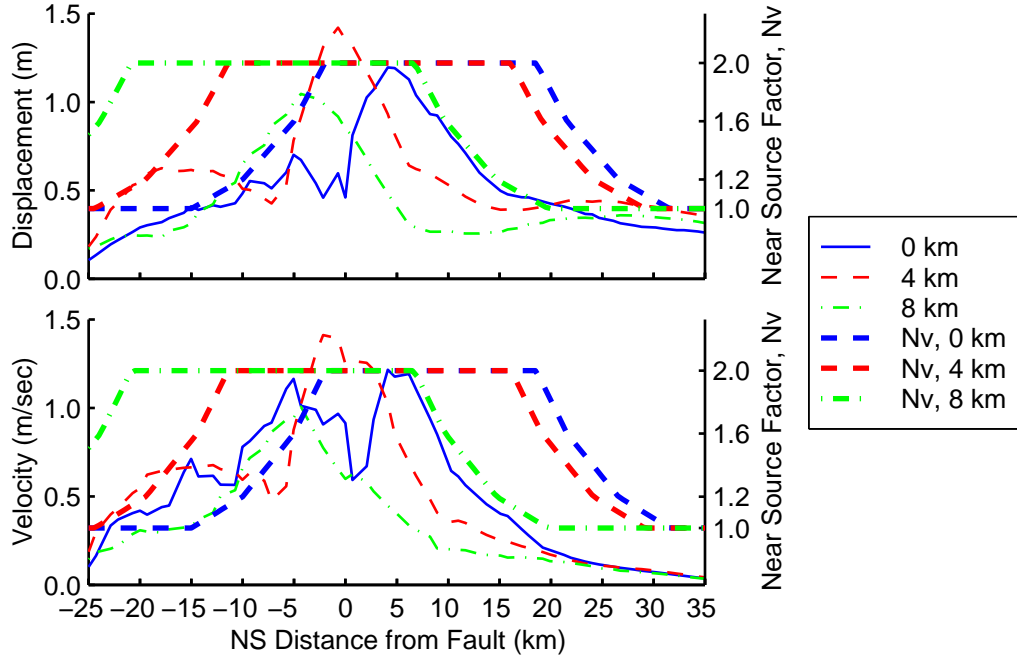


Figure 7.63: Maximum magnitudes of the horizontal displacement vectors and velocity vectors along a north-south line running over the center of the fault for the three depths of the top of the fault. The thick, dashed lines indicate the modified near-source ground motion factor for the three fault depths.

We compute the radiated energy during the simulation before low-pass filtering the velocities. Hence, the radiated energy reflects the energy emitted at all wavelengths from the prescribed rupture, although we construct the rupture to generate predominantly long-period motion as discussed in section 5.2.

We see that the radiated energies from the simulations agree with the Gutenberg-Richter relationship. The relative scatter for each of the faults depends on whether we plot the radiated energy using a linear scale or a log scale. As the rupture speed approaches intrinsic wave speeds, directivity effects cause displacement pulses with short durations and large amplitudes. Consequently, changing the duration of slip via the maximum slip rate or changing the rupture speed causes changes in the particle velocities. These changes cause fluctuations in the radiated energy and lead to the scatter in the radiated energy at a given moment magnitude. Because our simulations include only the long-period ground motions, we expect the radiated energies from the simulations to be smaller than those predicted by the Gutenberg-Richter relationship. The radiated energies for the thrust fault simulations display this trend, but the radiated energies for the strike-slip fault tend to be larger than those predicted by the Gutenberg-Richter relationship. However, the radiated energies from the strike-slip simulations probably lie well within the scatter of the events used to generate the Gutenberg-Richter relationship. Because larger earthquakes tend to radiate energy at longer periods, we do expect relatively larger radiated energies from the strike-slip fault simulations, which have larger moment magnitudes, than the thrust fault simulations. Relative to the Gutenberg-Richter relationship, our radiated energies do display this trend.

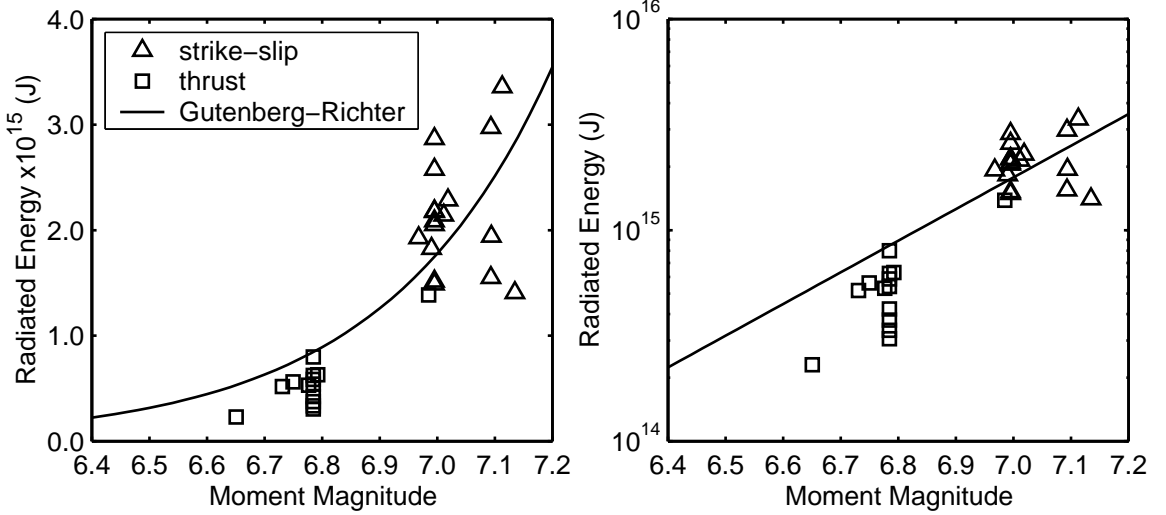


Figure 7.64: Radiated energy as a function of moment magnitude for all of the strike-slip and thrust earthquake simulations. The plot on the left uses a linear scale for the radiated energy, and the plot on the right uses a log scale for the radiated energy.

When we use prescribed ruptures, we ignore the dynamics of the rupture process and set the rupture speed independent of the maximum slip rate. This means that we may choose a rupture speed that is incompatible with our choice of slip rate. Moreover, while the slip time history may meet our spectral content needs related to the discretization size, the shape may not conform to those found in nature. This is not a problem when we want to simulate recent events where these parameters are well known. However, for hypothetical events it is difficult to select physically realistic parameters without an understanding of the dynamics of the rupture process.

# Chapter 8 Dynamic Failure

We incorporate the frictional sliding on the fault surface into the earthquake source with the goals of creating more physically realistic ruptures and better understanding the physics of the rupture process. We specify the friction model and the initial tractions on the fault, and the dynamic behavior of the rupture controls the slip on the fault as a function of time.

## 8.1 Earthquake Source

We need to make only a few, simple modifications to the model of the earthquake source to add the ability to simulate the earthquakes using dynamic failure. Instead of specifying the displacements at the slip degrees of freedom, we use the friction model to specify the forces acting on the slip degrees of freedom. We must also include the stresses from the surrounding region that act on the fault, which we call the tectonic stresses because a significant portion comes from plate tectonics.

We assume that the coefficient of friction is a function of slip distance and slip rate, and possibly, a number of state variables. We use the usual definition of slip rate, i.e., the magnitude of slip velocity. When sliding occurs on a plane, the definition of slip distance depends on the length scale of the surface asperities (surface roughness) that create the friction. If the asperities are large compared to the distance over which slip occurs, then an appropriate definition of slip distance is the magnitude of the distance a point slides from its original position. This definition allows the slip distance to remain constant if sliding occurs along the circumference of any circle centered at the point where sliding begins. On the other hand, if the asperities are small compared to the distance over which sliding occurs, then the slip distance should increase independently of the slip path, and an appropriate definition of slip distance is the total distance over which sliding has occurred. We will assume that the asperities are small compared to the slip distance and use the total sliding distance as the slip distance. Regardless of how we choose to define the slip distance, the friction force always acts in the opposite direction of the sliding.

### 8.1.1 Governing Equations with Friction

We replace the force vector in the governing equation, equation (2.2), with the difference between the friction force vector,  $\{F_f\}$ , and the vector of tectonic forces,  $\{F_t\}$ , as shown in equation (8.1).

$$[M]\{\ddot{u}(t)\} + [C]\{\dot{u}(t)\} + [K]\{u(t)\} = \{F_t(t)\} - \{F_f(D(t), \dot{D}(t))\} \quad (8.1)$$

The minus sign in front of the friction force vector indicates that we choose to explicitly include the dissipative nature of the friction force in the governing equation, so that the vector  $\{F_f\}$  acts in the direction of sliding. We will discuss the formulation of the vector of tectonic forces in section 8.1.2. Following the same procedure that we used for the prescribed ruptures discussed in section 2.2, we integrate the differential equation using the central-difference scheme. The expression for the displacement at time  $t + \Delta t$  is

$$\begin{aligned} \left( \frac{1}{\Delta t^2} [M] + \frac{1}{2\Delta t} [C] \right) \{u(t + \Delta t)\} &= \{F_t(t)\} - \{F_f(D(t), \dot{D}(t))\} \\ &\quad + \left( \frac{2}{\Delta t^2} [M] - [K] \right) \{u(t)\} \\ &\quad - \left( \frac{1}{\Delta t^2} [M] - \frac{1}{2\Delta t} [C] \right) \{u(t - \Delta t)\}. \end{aligned} \quad (8.2)$$

We compute the friction at time  $t$  assuming that we know the slip rate at time  $t$ . In the central-difference scheme the velocity at time  $t$  depends on the displacement at time  $t + \Delta t$ , so that computing the slip rate at time  $t$  requires knowing the slip at time  $t + \Delta t$ , which we do not know. To remedy this difficulty, we assume that the time step is small enough so that the slip rate does not change significantly in a single time step. This approximation may cause problems if the slip rate exhibits a strong influence on the coefficient of friction. Fortunately, we do not use friction models with this feature. Thus, we use the slip rate at time  $t - \Delta t$ , instead of the slip rate at time  $t$ , to compute the friction force at time  $t$ . Equation (8.3) gives the amended version of the expression for the displacement at time  $t + \Delta t$ .

$$\begin{aligned} \left( \frac{1}{\Delta t^2} [M] + \frac{1}{2\Delta t} [C] \right) \{u(t + \Delta t)\} &= \{F_t(t)\} - \{F_f(D(t), \dot{D}(t - \Delta t))\} \\ &\quad + \left( \frac{2}{\Delta t^2} [M] - [K] \right) \{u(t)\} \\ &\quad - \left( \frac{1}{\Delta t^2} [M] - \frac{1}{2\Delta t} [C] \right) \{u(t - \Delta t)\} \end{aligned} \quad (8.3)$$

### 8.1.2 Forces on Slip Degrees of Freedom

We must transform the initial tractions applied on the fault surface into forces acting on the slip degrees of freedom. We specify the initial tractions on the fault surface using the spatial interpolation procedure described in section 2.5. At each node on the fault, we interpolate from the given initial tractions and convert the tractions to forces using the node's tributary area on the fault plane. We assume that the fault is in equilibrium and apply the forces equally to both sides of the fault. We transform the forces into the slip coordinate frame using the transformation matrix  $[T_{slip}]$  given by equation (2.19). Equation (8.4) shows the simplified expression for the force vector applied at the degrees of freedom for a node on the fault with tributary area  $A$ . Following the conventions used in section 2.4.1,  $(p, q, r)$  denotes the coordinates on the fault plane, the subscript 1 denotes the degrees of freedom associated with the movement of the hanging wall, and

the subscript 2 denotes the degrees of freedom associated with the movement of the footwall.

$$\begin{Bmatrix} F_{p_1-p_2} \\ F_{q_1-q_2} \\ F_{r_1-r_2} \\ F_{p_1+p_2} \\ F_{q_1+q_2} \\ F_{r_1+r_2} \end{Bmatrix} = A\sqrt{2} \begin{Bmatrix} T_p \\ T_q \\ T_r \\ 0 \\ 0 \\ 0 \end{Bmatrix} \quad (8.4)$$

The initial tractions do not contribute any forces to the average degrees of freedom, which we associate with movement of both sides of the fault in the same direction, because we assume that the fault surface is in equilibrium.

The friction force does not require any transformation; the product of the coefficient of friction and the force acting on the relative normal degree of freedom gives the magnitude of the friction force vector acting on the slip degree of freedom. The dynamic deformation in the domain may cause variations in the normal forces acting on the fault. We compute the dynamic normal force at the slip degrees of freedom as part of the formulation of the right-hand side of the time stepping equation (equation (8.3)). By checking that the normal force remains compressive, we confirm that clamping the relative normal displacement across the fault remains valid. In other words, because tensile tractions imply opening of the fault, which we do not allow, we want the normal tractions to remain compressive.

The appearance of the difference between the tectonic force vector and the friction force vector in the equation of motion implies that we may create the same sliding behavior from an infinite combination of tectonic and friction forces by keeping the difference between them the same. In other words, given the sliding behavior and the values of the tectonic forces and friction forces, if we are given different tectonic forces, we may adjust the friction model to maintain the same sliding behavior.

### 8.1.3 Initiation of Sliding

To initiate sliding at a point on the fault, the friction force must be less than the sum of the other forces acting on that point. We start the earthquakes by increasing the tectonic forces in order to overcome the friction. During the first 0.5 sec of the simulation, we increase the friction force above the level given by the friction model in order to create gradual failure and prevent sudden initiation of the rupture. At each point on the fault where failure occurs, we transition the friction force from the critical force necessary to prevent slip at time  $t = 0$  to the force given by the friction model at time  $t = 0.5$  sec. Equation (8.5) gives the expression for the transition of the artificially adjusted friction force,  $F_f^{adj}$ , from the critical force required to prevent slip,

$F_{cr}$ , to the force given by the friction model.

$$F_f^{adj} = \left(1 - \frac{t}{t_h}\right)F_{cr} + \frac{t}{t_h}F_f \quad (8.5)$$

### 8.1.4 Condition for Termination of Sliding

Once a point on the fault starts sliding, it continues sliding until the slip rate decreases and the friction force is large enough to “lock” the fault. In more mathematical terms, the sliding stops when the friction force becomes larger than the sum of all of the other forces. Because sliding occurs on a plane, we must consider the vectors for the forces acting on each node on the fault. Following the conventions of section 2.4.1, we consider the  $p_1 - p_2$  and  $q_1 - q_2$  sliding degrees of freedom at each node on the fault. Using equation (8.3) with diagonal mass and damping matrices, the magnitude of the critical friction force for the  $i$ th degree of freedom is

$$F_{cr_i}(D_i(t), \dot{D}_i(t - \Delta t)) = \left| F_{t_i} - \frac{1}{\Delta t^2} M_i(u_i(t + \Delta t) - 2u_i(t) + u_i(t - \Delta t)) - \frac{1}{2\Delta t} C_i(u_i(t + \Delta t) - u_i(t - \Delta t)) - K_{ij}u_j(t) \right|. \quad (8.6)$$

We do not know the value of  $u_i(t + \Delta t)$  since that is what we want to find; however, when sliding stops,  $u_i(t + \Delta t) = u_i(t)$ , and the critical friction force for the  $i$ th degree of freedom becomes

$$F_{cr_i}(D(t), \dot{D}(t - \Delta t)) = \left| F_{t_i} + \frac{1}{\Delta t^2} M_i(u_i(t) - u_i(t - \Delta t)) - \frac{1}{2\Delta t} C_i(u_i(t) - u_i(t - \Delta t)) - K_{ij}u_j(t) \right|. \quad (8.7)$$

When sliding stops, the friction force may act in any direction. This implies we do not need to account for the current sliding direction in our criterion for terminating the sliding. In other words, we only need to determine if the magnitude of the friction force meets or exceeds the magnitude of the force required to terminate the sliding. Denoting the friction force at a node on the fault by  $F_f$ , equation (8.8) gives the expression for the condition used to determine if sliding stops at a node on the fault with sliding degrees of freedom  $p_1 - p_2$  and  $q_1 - q_2$ .

$$F_f(D, \dot{D}) \geq \sqrt{F_{cr_{p_1-p_2}}^2 + F_{cr_{q_1-q_2}}^2} \quad (8.8)$$

### 8.1.5 Average Stress Drop

Seismologists often use the average stress drop to characterize earthquakes. Modeling the friction on the fault allows explicit computation of the stress drop at every point. Equation (8.9) indicates how we compute the average stress drop,  $\Delta\bar{\sigma}$ , from the slip degrees of freedom by finding the drop in friction force at each node

and dividing by the fault area, where  $N$  is the number of nodes where slip occurred and  $A_i$  is the fault tributary area for node  $i$ . We follow the same convention that we use for stress and denote the friction forces before and after by  $F_0$  and  $F_1$ . A positive stress drop signifies a reduction in the stress on the fault.

$$\Delta\bar{\sigma} = \frac{\sum_{i=1}^N F_{0i} - F_{1i}}{\sum_{i=1}^N A_i} \quad (8.9)$$

## 8.2 Initial Tensions on Fault

The seismic waves generated by the rupturing fault create dynamic stresses in the surrounding volume. We assume that the other stresses present, such as those due to gravity and plate tectonics, do not change on the time scale of the earthquake, so we consider them to be constant. As in the prescribed ruptures, we do not need to know the initial stresses throughout the domain to model the seismic wave propagation. However, in order to simulate the dynamic failure of the fault, we must know the initial stresses acting on the fault surface. These stresses may be found in a number of ways, including solution of a static problem, solution of a viscoelastic problem, extrapolated from data, or assumed from intuition. Regardless of their source, we resolve the stresses into shear and normal tractions acting on the fault surface. Thus, off the fault surface we consider only the dynamic stresses, while on the fault surface we consider both the initial and dynamic stresses.

### 8.2.1 Effective Normal Tensions

We will consider gravity and plate tectonics as sources of normal stresses acting on the fault surface. In a self-gravitating, spherical earth with only radial variations in material properties, the weight of the material generates lithostatic stresses (total stress due to gravity) with no shear stresses and equal axial stresses (Mohr's circle degenerates into a point). For homogeneous material properties, the lithostatic stresses increase linearly with depth. In addition to shear stresses, plate tectonics also creates normal stresses on the fault surface, especially in the case of inclined faults. The presence of water in the interstices of the grains generates pore pressures that decrease the effective normal stresses. The three definitive cases include: when the interstices contain no water, when the interstices are saturated with water at hydrostatic pressure, and when the interstices contain water at pressures greater than hydrostatic pressure.

If little or no water sits in the interstices, the pore pressures are negligible and the effective normal stresses equal the normal stresses. For homogeneous material properties and much larger lithostatic stresses than tectonic normal stresses, the effective normal stresses increase approximately linearly with depth. If the interstices are saturated with water, then the pore pressures equal the hydrostatic pressures, and the effective normal stresses are the difference between the normal stresses and the hydrostatic pressures. Under the assumptions of homogeneous material properties and greater lithostatic normal stresses than tectonic normal stresses, the effective normal stresses again increase approximately linearly with depth, but at a slower rate

due to the presence of hydrostatic pore pressures. Finally, if the confining pressures reach high enough levels, the pore pressures may approach the normal stresses causing the effective normal stresses to become negligible. In this third case the material essentially “floats.” The existence of topography and density variations implies large shear stresses at depth that require large normal stresses to prevent failure. Consequently, except in localized areas, we expect the pore pressures to be no greater than the hydrostatic pressures. We also expect the normal stresses on the fault from gravity to be much greater than the stresses from plate tectonics, so that the effective normal stresses closely resemble the normal stresses from gravity. Researchers often use uniform effective normal stresses for simplicity (Olsen et al. 1997; Ben-Zion and Andrews 1998; Madariaga et al. 1998) without acknowledging that assuming uniform effective normal stresses with depth implies very large confining pressures. We will examine the rupture behavior for all three cases of pore pressure in chapter 9.

### 8.2.2 Shear Traction

Shear tractions on the fault generate the forces that cause slip on the fault surface. As discussed above in section 8.1.2, we convert the shear tractions to forces acting on the slip degrees of freedom. We apply the shear tractions in the direction of the desired slip and use an asperity (usually circular in shape) with a shear stress greater than the failure stress to start the rupture. Many factors, such as discretization size, failure stress, and dynamic stress drop, influence the size of the asperity necessary to initiate a propagating rupture (Madariaga et al. 1998).

### 8.2.3 Effect of Gravity

In general gravity affects both the normal and shear stresses acting on the fault surface. For a self-gravitating, spherically symmetric earth with only radial variations in material properties, gravity does not cause shear stresses on any planes. However, the earth is not spherically symmetric and contains lateral density variations. As a result, the stress field due to gravity generally contains both shear and normal stresses. We will use the analogy shown in figure 8.1 between a block on an incline plane and a thrust fault to demonstrate the typical effect gravity has on a thrust fault. The tectonic forces push the mountain higher and the block up the incline, while gravity resists the motion.

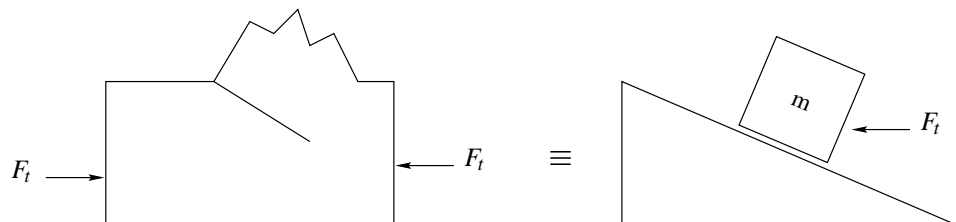


Figure 8.1: Analogy between a mountain created by a thrust fault and a block on an incline plane.

First, we consider the block without gravitational forces present as shown in figure 8.2(a). For the block

to move up the incline, the shear component of the tectonic force must be greater than the friction force,

$$F_t \cos \theta > F_f. \quad (8.10)$$

After substituting in the coefficient of friction,  $\mu_f$ , and simplifying, we find

$$\mu_f < \cot \theta. \quad (8.11)$$

This result does not depend on the tectonic force, which implies that for a small enough coefficient of friction, we can move the block up the incline with an infinitesimal amount of force.

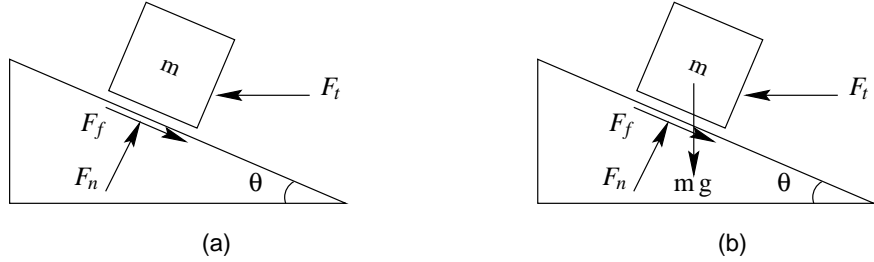


Figure 8.2: Block on an incline plane subjected to a horizontal tectonic force,  $F_t$ . We denote the normal and friction forces acting on the block by  $F_n$  and  $F_f$ . (a) Neglecting gravitational forces. (b) Including gravitational forces.

Now we consider the same block on an incline under the force of gravity as shown in figure 8.2(b). In order to move the block up the incline, the shear component of the tectonic force must overcome both the friction force and the shear force caused by gravity,

$$F_t \cos \theta > F_f + mg \sin \theta, \quad (8.12)$$

where  $m$  is the mass of the block and  $g$  is the acceleration of gravity. Substituting in the coefficient of friction and simplifying yields

$$F_t > mg \frac{\mu_f \cos \theta + \sin \theta}{\cos \theta - \mu_f \sin \theta}. \quad (8.13)$$

In this case a minimum tectonic force exists for sliding to occur. Including gravity increases the tectonic force required to move the block, because gravity increases the shear force acting down the incline and increases the friction force through an increase in the normal force. Thus, the existence of gravity requires larger tectonic stresses to create slip on a thrust fault. Because the seismic wave propagation does not require knowing the stresses due to gravity, we do not explicitly include the contribution of gravity in the stresses on the fault; however, we do include them in the initial shear and normal tractions on the fault surface.

### 8.2.4 Spatial Distribution of Parameters for Dynamic Failure

We specify the initial tractions and parameters of the friction model using the spatial interpolation procedure outlined in section 2.5. This means that we may apply the same techniques we use to create the data points that specify the final distribution of slip on the fault (described in section 5.3) to specify the initial tractions and friction model parameters on the fault. This includes both the exponential function to taper the shear tractions at the edges of the fault (equation (5.1)) and the circular asperities (equation (5.2)) to generate heterogeneity in the shear tractions or parameters of the friction model. Tapering the shear tractions at the edges of the fault terminates or nearly terminates the propagation of the rupture as it approaches the edge of the fault surface. We start the rupture using a circular asperity with a height that corresponds to shear tractions one or two percent greater than the failure stress. The one or two percent over the failure stress effectively gives the rupture a small kick to start propagating. As we noted in section 8.2.2, many factors influence the size of the asperity needed to initiate a propagating rupture. For this reason no relationships have yet been found that give the size of the asperity required to initiate a rupture (Madariaga et al. 1998).

The normal tractions usually follow one of the three definitive cases described in section 8.2.1. When the material properties depend only on depth, we can find closed form solutions for the stresses in a self-gravitating, spherical earth as a function of depth. Of course, under simple initial conditions, such as uniform effective normal stresses, specifying the effective normal stress is trivial. For lithostatic normal stresses with negligible pore pressures, equation (8.14) gives the normal stresses (Mohr's circle degenerates into a point) as a function of depth when the mass density varies piecewise linearly with depth. Figure 8.3 shows the set of  $N$  control points that define the variation of the mass density with depth.

$$\begin{aligned} \sigma_l(z) = & \frac{g}{2} \frac{\rho_j}{z_{j-1} - z_j} (2z_{j-1}z - z^2 - z_{j-1}^2) + \frac{g}{2} \frac{\rho_{j-1}}{z_{j-1} - z_j} (z^2 - 2zz_j - z_{j-1}^2 + 2z_jz_{j-1}) \\ & + \sum_{i=1}^{j-1} \frac{g}{2} (\rho_i + \rho_{i-1})(z_i - z_{i-1}) \quad (8.14) \end{aligned}$$

Equation (8.14) does not account for non-zero pore pressures. For hydrostatic pore pressures, we simply replace the mass density at each point in equation (8.14) with the difference between the mass density and the mass density of water.

## 8.3 Overview of Rupture Dynamics

The friction model enables us to examine some of the basic relationships surrounding the dynamics of the rupture. We study the rupture dynamics by focusing, first, on the friction stress and, second, on the energy.

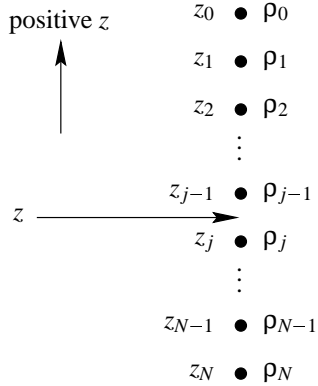


Figure 8.3: Control points that define the piecewise linear variation of the mass density with depth. We compute the normal stresses at the location denoted by the open circle with coordinate  $z$ .

### 8.3.1 Stress and Rupture Dynamics

We examine the anatomy of the shear stress on the fault near the rupture front shown in figure 8.4 to find the relationship between its features and the dynamics of the rupture. From fracture mechanics,<sup>1</sup> we know that ahead of the rupture front the shear stresses increase and becomes nearly singular just ahead of the leading edge of the rupture. At the leading edge of the rupture where slip begins, the shear stresses decrease dramatically, and then, depending on the friction model, may or may not recover as the slip rate decreases. Of course, in the earth and our finite-element models failure occurs at a finite value which prevents the formation of a true singularity.

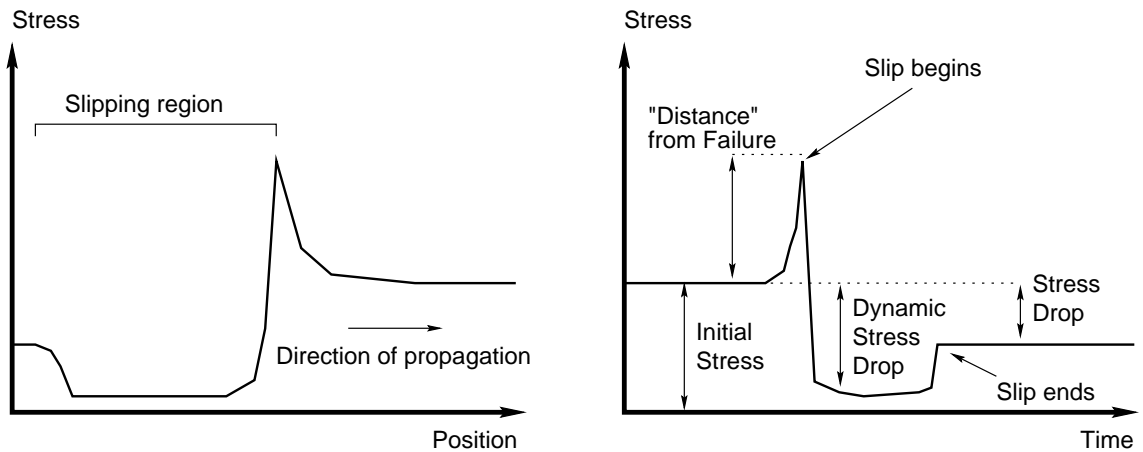


Figure 8.4: Diagrams of the concentration of shear stress near the rupture front as a function of space (left diagram) and as a function of time (right diagram).

The friction model controls the decrease in friction stress as slip progresses, and therefore, the dynamic stress drop. The rate of the dynamic stress drop governs the slip rate with faster decreases in shear stress leading to faster increases in slip. The dynamic stress drop and the distance from failure (the difference

<sup>1</sup>See Freund (1990) for an extensive discussion on the stress field associated with dynamic fracture.

between the failure stress and the initial shear stress) determine the nature of the concentration of stress ahead of the leading edge of the rupture. A larger distance from failure magnifies the stress concentration, and a larger dynamic stress drop increases the rate of the decay of the stress concentration. The increase in shear stress associated with the stress concentration dictates when slip occurs at each point and, as a result, the rupture speed. Thus, the slip rate and rupture speed are related through the dynamic stress drop.

### 8.3.2 Energy and Rupture Dynamics

We may also study the dynamics of the rupture using energy. The increase in shear stress on the fault ahead of the rupture implies storage of strain energy in the surrounding region. As the rupture propagates, the rupture front consumes energy through sliding. We associate two forms of energy with the sliding. We call the energy dissipated during the decrease in the friction during sliding the fracture energy, because it corresponds to the fracture energy in crack models. We associate the energy dissipated through sliding at a relatively constant friction stress with the change in thermal energy. The sliding also generates the energy radiated in the seismic waves. As we increase the fracture energy, the rupture consumes more energy leaving less available for sliding. In such cases the slip rates and rupture speed decrease (Fukuyama and Madariaga 1998). Likewise, when we decrease the fracture energy, more energy is available for sliding, and the slip rates and rupture speed increase. If the rupture dissipates more energy than the energy released, then the rupture slows and eventually stops.

The fracture energy involves both the failure stress and the rate of change of the friction stress with slip. For an increment of slip,  $dD$ , the increment in fracture energy per unit area,  $dG$ , is

$$dG = \sigma_f dD, \quad (8.15)$$

where  $\sigma_f$  is the friction stress. Expanding the friction stress about the failure stress ( $\sigma_{fail}$ ) to first order in  $dD$  and substituting yields

$$dG = \sigma_{fail} dD + \frac{1}{2} \frac{d\sigma_f}{dD} |_{\sigma_{fail}} dD^2. \quad (8.16)$$

This expression shows that the failure stress does not uniquely determine the fracture energy. We may adjust the slope of the friction model to change the fracture energy. For example, if we lower the failure stress, we may maintain the same fracture energy by reducing the rate at which the friction stress decreases with slip.

This technique plays a critical role in manipulating the dynamics of the rupture in the finite-element simulations. We want the wave propagation to govern the local element sizes. However, accurately capturing the stress concentration in shear stress near the leading edge of the rupture requires much smaller elements than those necessary to model the wave propagation (Madariaga et al. 1998). With extremely high resolution meshes, the failure stress will develop only over a very localized region. We want to capture the general

behavior of such failure without modeling such localized behavior. As we increase the element size, the concentration in shear stress decreases for a given dynamic stress drop. In other words, the buildup of stress becomes distributed over a longer length, which reduces the stress concentration. Consequently, we must reduce the failure stress for the rupture to propagate. Thus, the ability of a continuous medium to generate nearly singular stresses near the leading edge of the rupture front means the fracture energy, not the precise level of the stress at failure, governs the propagation of the rupture. On the other hand, in a discrete model, such as our finite-element models, the failure stress becomes a length-scale dependent parameter, but the fracture energy continues to control the behavior of the rupture. Luckily, we may manipulate the friction model as demonstrated in figure 8.5 to maintain the same fracture energy as we change the failure stress. This means that we may use larger elements than those required to accurately capture the stress concentration and may allow the wave propagation to control the discretization size without altering the behavior of the rupture.

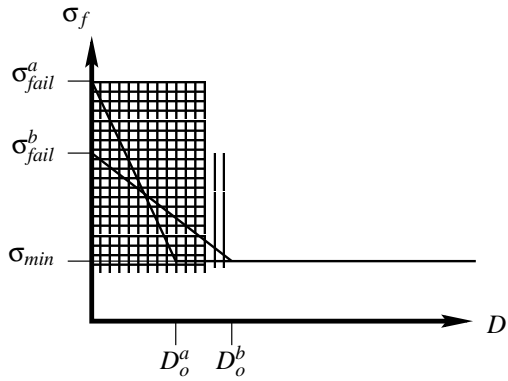


Figure 8.5: Illustration of two sets of parameters for the slip-weakening friction model (denoted by the superscripts  $a$  and  $b$ ) that have the same fracture energy with different failures stresses ( $\sigma_{fail}^a$  and  $\sigma_{fail}^b$ ) and characteristic slip distances ( $D_o^a$  and  $D_o^b$ ).

## 8.4 Friction Models

The simulation software implements eight models of sliding friction. All of the models define a functional form of the coefficient of friction, and we compute the friction force from the product of the normal force and the coefficient of friction. We do not implement the state-rate friction models advocated by several researchers, including Scholz (1998) and Dieterich (1992), because they are based upon viscoelastic creep behavior (Persson 1997). Slip during earthquakes occurs at rates on the order of meters per second (Heaton 1990). These slip rates lie well outside the range of the creep slip rates of millimeters per year used in the laboratory experiments to develop the state-rate friction models. Thus, we choose to use simple, *ad hoc* friction models with characteristics, such as weakening with the progression of slip and re-strengthening with the decline of slip rate, that produce realistic rupture behavior and capture the general features of more

complicated models.

We focus on capturing the macroscopic characteristics of the sliding. We lump small-scale effects into the friction model, because several possible mechanisms have been suggested to explain the reduction in friction during sliding. These include fluid pressurization (Sleep 1997), contrasts in material properties (Ben-Zion and Andrews 1998), acoustic fluidization (Melosh 1996), and normal vibrations (Tworzydlo and Hamzeh 1997). In other words, we do not model any particular mechanism that reduces the friction stress; instead, we incorporate these effects into the model of the coefficient of friction and do not account for the reduction in the friction stress by modifying the normal stresses. We will discuss the dynamics of the rupture process for several of these *ad hoc* friction models in chapter 9 and chapter 10. Table 8.1 provides descriptions of the parameters used in the functional forms of the coefficient of friction.

Variable	Dimensions	Description
$\mu_f$	dimensionless	coefficient of friction
$\mu_{max}$	dimensionless	maximum coefficient of friction
$\mu_{min}$	dimensionless	minimum coefficient of friction
$D$	length	slip distance
$V, \dot{D}$	length/time	slip rate
$D_o$	length	characteristic slip distance
$V_o$	length/time	characteristic slip rate
$s$	dimensionless	state variable in shear melting-freezing model
$\tau_o$	time	characteristic time

Table 8.1: Description of the variables involved in the friction models.

### 8.4.1 Constant

The coefficient of friction remains constant during sliding. This is the simplest friction model possible.

$$\mu_f = \mu_{max} \quad (8.17)$$

### 8.4.2 Two-Phase

The coefficient of friction takes a value of  $\mu_{min}$  when sliding occurs and  $\mu_{max}$  otherwise. This is the simplest friction model that with constant normal tractions leads to the stick-slip behavior associated with earthquakes. The instantaneous drop in the coefficient of friction implies no energy is required for fracture. This model corresponds to the slip-weakening I friction model with  $D_o = 0$ .

$$\mu_f(\dot{D}(t)) = \begin{cases} \mu_{max} & \dot{D}(t) = 0 \\ \mu_{min} & \dot{D}(t) \neq 0 \end{cases} \quad (8.18)$$

### 8.4.3 Slip-Weakening I

We modify the two-phase friction model by decreasing the coefficient of friction over a slip distance of  $D_o$ . This includes the latent heat (fracture energy) generated by fracture in the friction model. We assume instantaneous recovery of the coefficient of friction upon the termination of sliding, so that as soon as sliding stops, the coefficient of friction increases to  $\mu_{max}$ . We will refer to this model as slip-weakening friction, because the material exhibits a weakening in shear strength as slip occurs. Figure 8.6 illustrates how the coefficient of friction decreases from  $\mu_{max}$  (labeled  $u_{max}$  in the figure) to  $\mu_{min}$  (labeled  $u_{min}$  in the figure) over a characteristic slip distance of  $D_o$ .

$$\mu_f(D(t)) = \begin{cases} \mu_{min} & D(t) > D_o \\ \mu_{max} - (\mu_{max} - \mu_{min}) \frac{D(t)}{D_o} & D(t) \leq D_o \end{cases} \quad (8.19)$$

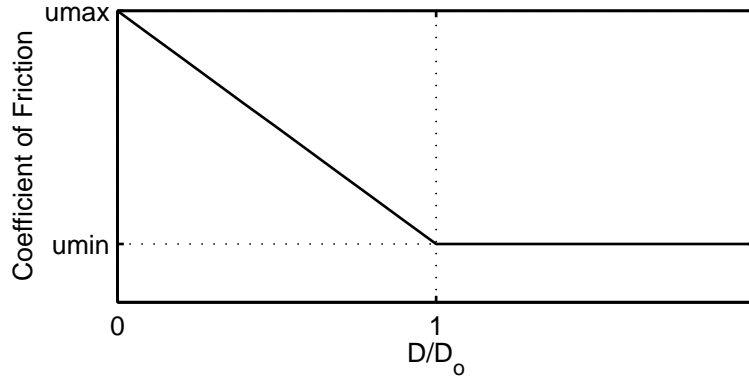


Figure 8.6: Slip-weakening I friction model.

### 8.4.4 Slip-Weakening II

In this case, instead of a linear decrease in the coefficient of friction with slip distance, we decrease the coefficient of friction inversely with slip distance as shown in figure 8.7.

$$\mu_f(D(t)) = \mu_{min} + (\mu_{max} - \mu_{min}) \frac{D_o}{D(t) + D_o} \quad (8.20)$$

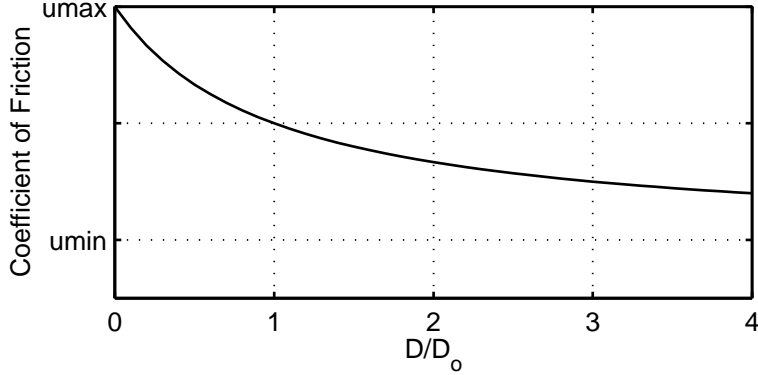


Figure 8.7: Slip-weakening II friction model.

### 8.4.5 Rate-Weakening I

This model is analogous to the slip-weakening I friction model with the decay as a function of slip distance replaced by a decay as a function of slip rate.

$$\mu_f(\dot{D}(t)) = \begin{cases} \mu_{min} & \dot{D}(t) > V_o \\ \mu_{max} - (\mu_{max} - \mu_{min}) \frac{\dot{D}(t)}{V_o} & \dot{D}(t) \leq V_o \end{cases} \quad (8.21)$$

### 8.4.6 Rate-Weakening II

This model is analogous to the slip-weakening II friction model with the decay as a function of slip distance replaced by a decay as a function of slip rate.

$$\mu_f(\dot{D}(t)) = \mu_{min} + (\mu_{max} - \mu_{min}) \frac{V_o}{\dot{D}(t) + V_o} \quad (8.22)$$

### 8.4.7 Slip- and Rate-Weakening

Following Madariaga et al. (1998) we create a friction model that depends on slip distance and slip rate by taking the greater of the two coefficients of friction determined from the slip-weakening I and rate-weakening I friction models. We will often refer to this model as slip- and rate-weakening. We replace  $\mu_{max}$  in the rate-weakening I friction model with  $\mu_{post}$  to allow different shear strengths before and after slip. Figure 8.8 illustrates the variation of the coefficient of friction with both slip distance and slip rate; we also show a typical path of the coefficient of friction during sliding.

### 8.4.8 Shear Melting-Refreezing

This model comes from Persson (1997) and contains several of the same general features of the slip- and rate-weakening model. However, the coefficient of friction depends on the history of the slip rate. Figure 8.9 displays a typical trajectory of the coefficient of friction during a slip event.

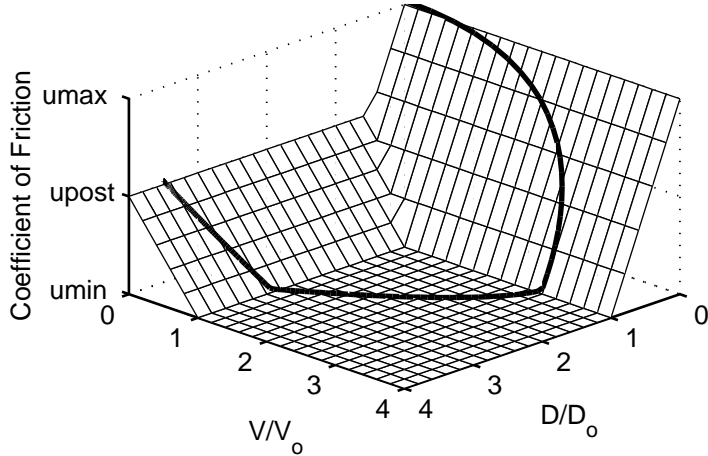


Figure 8.8: Slip- and rate-weakening friction model. The thick line indicates a typical trajectory of the coefficient of friction.

We denote the state of the sliding surface by the state variable  $s$ . When  $s = 1$  the surface is in a “solid” state with a high coefficient of friction, and when  $s = 0$  the surface is in a “fluid” state with a low coefficient of friction. Although Persson derives the friction model associating the low level of friction with a fluid state and the high level of friction with a solid state, the physics of the friction model do not explicitly involve melting and refreezing; the friction model involves transitions between two states with two different coefficients of friction. In this friction model the characteristic slip distance refers to the sliding distance over which “melting” occurs, and the characteristic time varies inversely with the rate at which areas “refreeze.”

$$\mu_f(\dot{D}(t), s(t)) = \mu_{min} + (\mu_{max} - \mu_{min})s(t) \quad (8.23)$$

$$\dot{s}(t) = \frac{1}{\tau_o}(1 - s(t))(-\ln(1 - s(t)))^{\frac{2}{3}} - \frac{s(t)\dot{D}(t)}{D_o} \quad (8.24)$$

When no sliding occurs, we have two equilibrium states where the coefficient of friction does not change with time:  $\mu_f = \mu_{min}$  when  $s = 0$  and  $\mu_f = \mu_{max}$  when  $s = 1$ . If the system is not in equilibrium and not sliding,  $\dot{s} = \frac{1}{\tau_o}s(1 - s) > 0$  because  $0 < s < 1$ , and the surface refreezes ( $s \rightarrow 1$ ). We integrate the state equation using the forward difference scheme to obtain the value of the state variable at time  $t + \Delta t$ .

$$s(t + \Delta t) = s(t) + \frac{\Delta t}{\tau_o}(1 - s(t))(-\ln(1 - s(t)))^{\frac{2}{3}} - \Delta t \frac{s(t)\dot{D}(t)}{D_o} \quad (8.25)$$

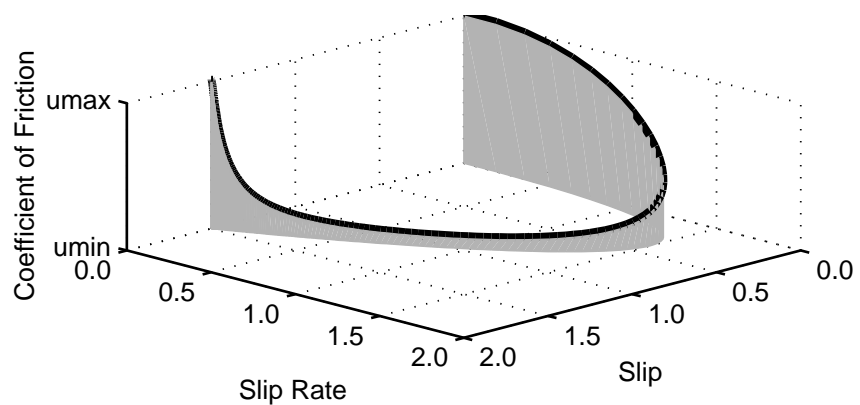


Figure 8.9: Shear melting-refreezing friction model. The thick line indicates a typical trajectory of the coefficient of friction.

# Chapter 9 Dynamic Failure in a Homogeneous Half-Space

We begin our examination of dynamic failure with simulations in a homogeneous half-space. We study the behavior of the rupture, including the role of fracture energy, the effects of the free surface on the rupture, and the effects of the various friction models on the ground motions. We also consider different variations in the effective normal stresses with depth and their implications on the parameters of the friction model.

We will use some of the basic features of ruptures observed in nature to judge the behavior of the simulated ruptures. Heaton (1990) examined the rupture behavior of seven earthquakes and found no systematic variations in the slip distributions with depth. On the other hand, we do expect some systematic variations in the slip distribution for theoretical, constant stress drop earthquakes (Heaton and Heaton 1989). When the fault reaches the free surface, for a uniform stress drop the largest slip occurs along the free surface due to the reduction in stiffness. Likewise, when we bury the fault, the largest slips occur near the center of the fault. Although difficult to resolve, Heaton (1990) did not find any clear variations in the duration of slip with depth. Consequently, we want relatively uniform maximum slip rates. We will also assume that the nominal tectonic tractions may be derived from application of relatively uniform stresses or uniform strains (the two are equivalent in homogeneous half-spaces).

## 9.1 Finite-Element Models

We focus on the general characteristics of the rupture behavior for these simulations. Consequently, where possible, we consider only the volume immediately surrounding the fault to reduce the computation effort and storage requirements. This allows these simulations to run on a Sun workstation. When we need to examine dynamic failure in a homogeneous half-space with a larger fault, we use the finite-element model for the homogeneous half-space from section 7.1.

### 9.1.1 Strike-Slip Fault

We enclose the 16 km long and 9.9 km wide fault in a domain 30 km long, 14 km wide, and 16 km deep as shown in figure 9.1. The top of the fault sits at the ground surface. We impose horizontal shear stresses to generate left-lateral slip on the north striking, vertical fault.

We use IDEAS to create the finite-element model at coarse resolution and the 2x refinement procedure to generate a nominal node spacing of 660 m. We again model wave propagation down to periods of 2.0 sec with

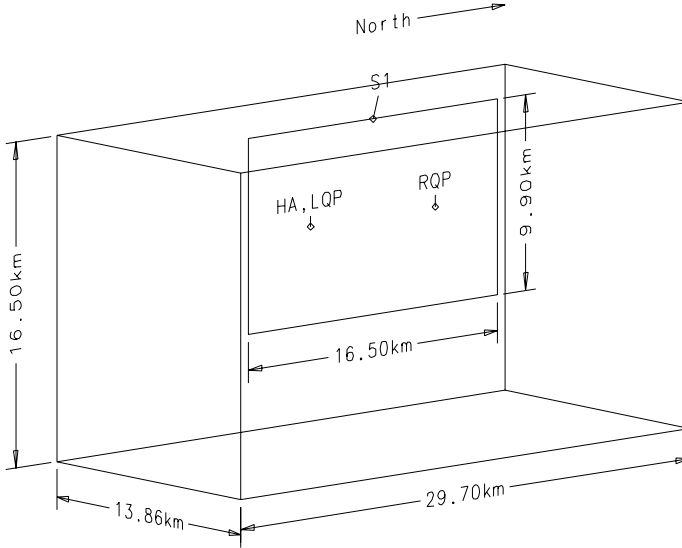


Figure 9.1: Orthographic projection of the domain geometry for the strike-slip fault. The label HA denotes the location of the hypocenter. We will examine the waveforms at site S1.

the same material properties as the homogeneous half-spaces with prescribed ruptures in chapter 7. Using the 4x refinement procedure reduces the period by an additional factor of two, but increases the number of elements by a factor of eight as illustrated in table 9.1.

Resolution	# Nodes	# Elements
Coarse	4200	21,000
2x refinement	34,000	160,000
4x refinement	270,000	1.3 million

Table 9.1: Sizes of the finite-element models at various resolutions for the domain containing the strike-slip fault.

### 9.1.2 Thrust Fault

The domain with dimensions shown in figure 9.2 contains a 9.9 km long and 11.2 km wide thrust fault that dips 35 degrees to the south. We bury the fault 5.3 km below the ground surface, and impose shear stresses on the fault surface 105 degrees from the strike to the east. Table 9.2 gives the sizes of the finite-element model created at coarse refinement using IDEAS and after 2x refinement.

Resolution	# Nodes	# Elements
Coarse	4900	24,000
2x refinement	39,000	190,000

Table 9.2: Sizes of the finite-element models at various resolutions for the domain containing the thrust fault.

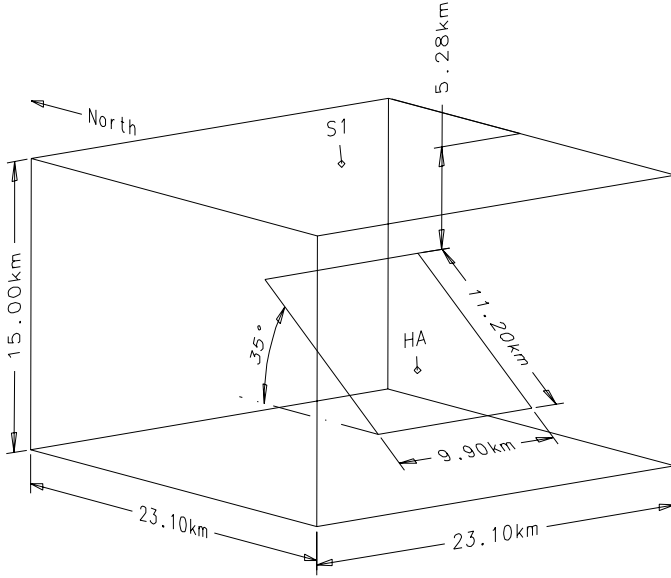


Figure 9.2: Orthographic projection of the domain geometry for the thrust fault. The label HA denotes the location of the hypocenter. We will examine the waveforms at site S1.

## 9.2 General Features of Dynamic Rupture

We consider rupture on the strike-slip fault in the homogeneous half-space described in section 9.1.1. We follow the lead of some of the other researchers who simulate earthquakes using dynamic failure, such as Madariaga et al. (1998) and Ben-Zion and Andrews (1998), and begin by assuming uniform effective normal stresses. Recall from section 8.2.1 that this variation in the effective normal stress is generally used for simplicity.

### 9.2.1 Base Case: Scenario ssbase

From the subsurface rupture length and average slip relationship from Wells and Coppersmith (1994) we expect an average slip of 0.5 m on a strike-slip fault this size. The average stress drop on a rectangular, vertical, strike-slip fault in a homogeneous Poissonian half-space generally follows equation (9.1) where  $l$  and  $w$  denote the length and width of the fault (Heaton et al. 1986).

$$\Delta\bar{\sigma} = C\mu \frac{\bar{D}}{w} \quad (9.1)$$

where

$$C \approx \begin{cases} C_D & w = l \\ C_D + 0.9(1 - \frac{l}{w}) & w < l < 2w \\ C_D - 0.9 & l > 2w \end{cases}$$

$$C_D \approx \begin{cases} 1.6 & \text{surface rupture} \\ 2.1 & \text{deeply buried faults} \end{cases}$$

Substituting in for the shear modulus and fault width, we find that we expect an average stress drop of 1.3 MPa. The recovery of the coefficient of friction upon termination of the sliding means that the average stress drop will be less than the maximum dynamic stress drop. As a result, we must use a dynamic stress drop that is larger than the expected average stress drop to generate comparable slip. Consequently, based on a trial simulation we impose a maximum dynamic stress drop of 2.0 MPa to produce approximately 0.5 m of slip.

### Initial Conditions

We will assume that the earthquake does not completely relieve the initial stress and apply uniform initial shear tractions of 4.0 MPa. We still need to determine a value for the failure stress. We expect the initial stresses to lie somewhere between the minimum sliding shear stresses and the shear stresses at failure. A small distance from failure (the difference between the failure stress and the initial shear stress) implies that the fault is close to failure and the rupture will propagate very fast. At the other extreme, a large distance from failure inhibits propagation of the rupture. Thus, we want to avoid the extreme cases and expect the initial shear stresses to be about midway between the minimum sliding shear stresses and the shear stresses at failure. In this case and in nearly all other cases, we select the distance from failure to match the maximum dynamic stress drop. As a result, the initial shear stresses lie halfway between the minimum sliding shear stresses and the failure stresses.

Matching the distance from failure with the maximum dynamic stress drop gives a failure stress of 6.0 MPa. Assuming a typical value of 0.6 for the coefficient of friction at failure (Persson 1997) yields a normal traction of 10 MPa. We need to keep in mind that at seismogenic depths in the earth we find effective normal stresses as high as 500 MPa. We want to produce a smooth slip distribution, so we choose a uniform dynamic stress drop. This implies a minimum coefficient of friction of 0.2. Table 9.3 summarizes the friction model parameters and initial tractions, and figure 9.3 displays the shear and normal tractions on the fault surface. We initiate the rupture with a circular asperity with a radius of 1.8 km whose center sits 5.0 km below the ground surface and 5.0 km north of the south end of the fault.

Friction Model	Slip-Weakening I
$\mu_{max}$	0.6
$\mu_{min}$	0.2
$D_o$	0.15 m
Normal Traction	-10 MPa
Shear Traction	6.0 MPa

Table 9.3: Friction model parameters and initial tractions for scenario ssbase.

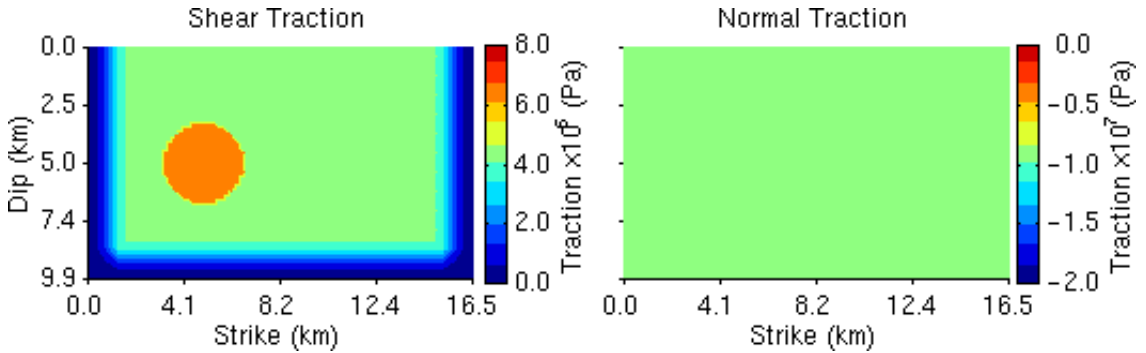


Figure 9.3: Shear and normal tractions on the strike-slip fault for the base case which features uniform effective normal stresses and no variations of the coefficient of friction parameters with depth.

### Characteristics of Earthquake

The general features of the rupture conform to what we expect in an earthquake. As shown in figure 9.4, the rupture initiates in the asperity and propagates across the fault. The rupture expands as an ellipse with a faster rupture speed in the direction of slip compared to the direction perpendicular to slip. This differs from the prescribed ruptures where we use a uniform rupture speed, but it does make sense physically. In the direction of slip, the rupture displays mode-II crack behavior (shearing), and in the direction perpendicular to slip, the rupture displays mode-III crack behavior (tearing).

When the fracture energy is small, the stress intensities in the anti-plane (mode-III) direction exceed those in the in-plane (mode-II) direction (Madariaga et al. 1998). As a result, we would expect ruptures to propagate faster in the direction perpendicular to slip (anti-plane direction). However, Madariaga et al. found that ruptures with this limited amount of fracture energy are numerically controlled, so that the numerical solution fails to model the rupture front accurately. As the fracture energy increases, the rupture speed in the direction of slip tends to exceed the speed in the direction perpendicular to slip due to the asymmetry in the shear wave radiation pattern (Madariaga et al. 1998). We observe precisely this type of behavior; in the direction parallel to the slip we observe a rupture speed of 1.7 km/sec (compared to a shear wave speed of 3.3 km/sec), and in the direction perpendicular to the slip we observe a rupture speed of 1.4 km/sec. These values correspond to rupture speeds of roughly 50% and 40% of the shear wave speed. We may increase this slow rupture speed to a more realistic value by decreasing the fracture energy without changing the fundamental behavior of the rupture.

An eight kilometer long portion of the rupture front encounters the free surface almost simultaneously,

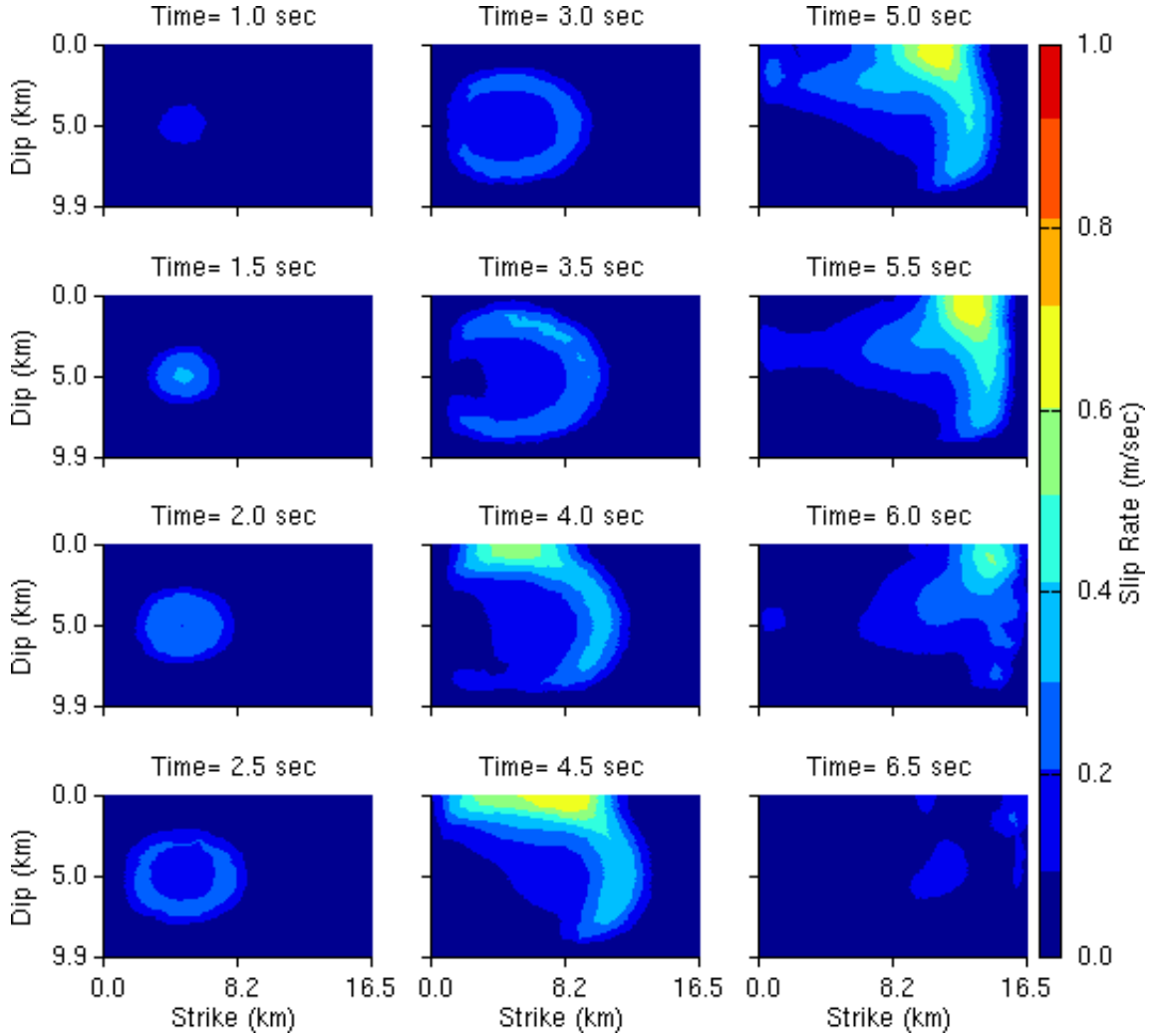


Figure 9.4: Snapshots of slip rate on the strike-slip fault for the base case.

which dramatically reduces the resistance to sliding near the center of this portion of the rupture front. This creates rapid slip near the surface with a high apparent velocity along the ground surface at 4.0 sec. The reduced resistance to slip generates a small reflection in slip off the free surface that is barely visible at 5.0 sec near the back of the main rupture front. The larger slip rates near the ground surface allow the rupture to continue propagating along the ground surface at a faster rupture speed (compared to the true speed that the rupture has when it hits the ground surface with a high apparent velocity). This fast portion of the rupture catches up to the rupture at depth just before the rupture reaches the end of the fault. The width of the rupture front, i.e., the region where the slip rates are nonzero, stretches across a large portion of the fault; however, the larger slip rates (where most of the slip occurs) are confined to a small portion located close to the leading edge of the rupture.

Figure 9.5 gives the distributions of final slip and maximum slip rate on the fault. The final slip resembles that of a uniform stress drop earthquake, as it should based on the use of a uniform dynamic stress drop and

a slip-weakening friction model. The average slip of 0.51 m closely matches our target value of 0.5 m and corresponds to a moment magnitude of 6.2. Additionally, the average stress drop of 1.2 MPa generally agrees with the value of 1.3 MPa from equation (9.1). As we noted in our discussion of the rupture propagation, the maximum slip rates occur along the free surface. The maximum slip rates away from the ground surface display a tendency to increase as the rupture propagates.

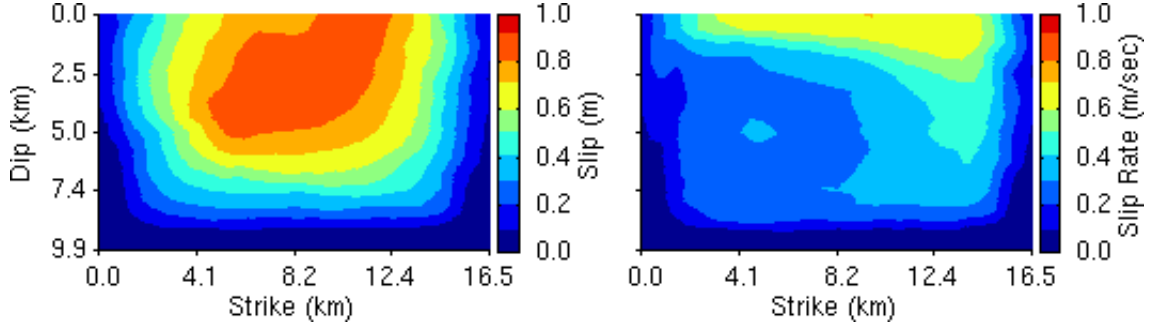


Figure 9.5: Distributions of final slip and maximum slip rate at each point on the strike-slip fault for the base case.

### 9.2.2 Role of Fracture Energy

We switch the friction model from the slip-weakening friction model to the two-phase friction model, while applying the same initial tractions. This coincides with decreasing the characteristic slip distance to zero in the slip-weakening friction model. However, the discrete nature of the finite-element model does provide some inherent or effective fracture energy. Upon initiation of sliding the coefficient of friction immediately drops to its minimum value, and no energy is required for fracture. Figure 9.6 shows the slip time histories at a depth of 8.0 km at the left and right quarter points of the fault (labeled LQP and RQP in figure 9.1); the left quarter point lies at the center of the asperity used to initiate the rupture. As expected with the instantaneous drop in friction, the slip quickly accelerates inside the asperity. With no fracture energy, the rupture propagates with an approximate rupture speed in the direction of slip of 4.9 km/sec compared to the shear wave speed of 3.3 km/sec, or nearly three times faster than the rupture with slip-weakening friction. At the right quarter point, the slip rate exhibits only a minor increase when we remove the fracture energy. At both locations, slip occurs in closely spaced, multiple events due to the introduction of numerical noise associated with the sharp initiation of slip and the inability of the model to accurately handle frequencies above 0.5 Hz. Thus, we confirm our intuition outlined in the discussion of the fracture energy and rupture speed in section 8.3.2; the fracture energy displays a strong influence on the speed of the rupture.

### 9.2.3 Effect of Discretization Size

We examine the effects of the discretization size by using the same parameters as the base case, i.e., the same initial tractions on the fault surface and the same slip-weakening friction model, but replace the 2x

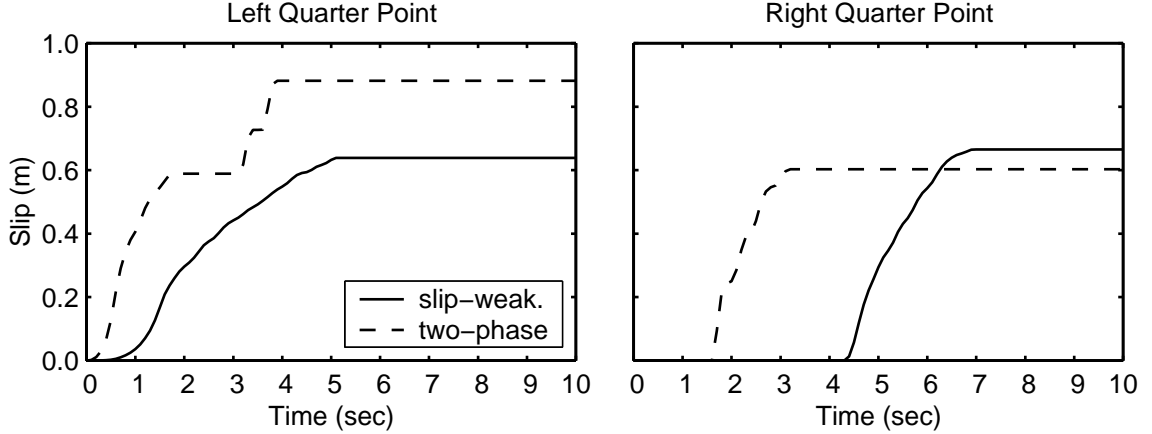


Figure 9.6: Comparison of slip time histories at the left and right quarter points on the strike-slip fault at a depth of 8.0 km for ruptures with fracture energy (slip-weakening friction model) and without fracture energy (two-phase friction model).

refinement procedure with the 4x refinement procedure. This reduces the nominal node spacing from 660 m to 330 m. Figure 9.7 shows the horizontal displacement time histories at site S1, which is located on the ground surface above the center of the fault. The earlier initiation of slip in the finer mesh indicates that the rupture propagates 11% faster (1.9 km/sec compared to 1.7 km/sec). The larger displacement in the north-south (fault parallel) component for the finer resolution reflects the increase in average slip from 0.51 m to 0.55 m. On both components the velocities exhibit little change. Thus, reducing the discretization size leads to only small changes in the rupture speed and slip time histories with no fundamental differences in the rupture dynamics. We conclude that with the appropriate fracture energy we may use the node spacing criterion from the wave propagation for the simulations with dynamic failure.

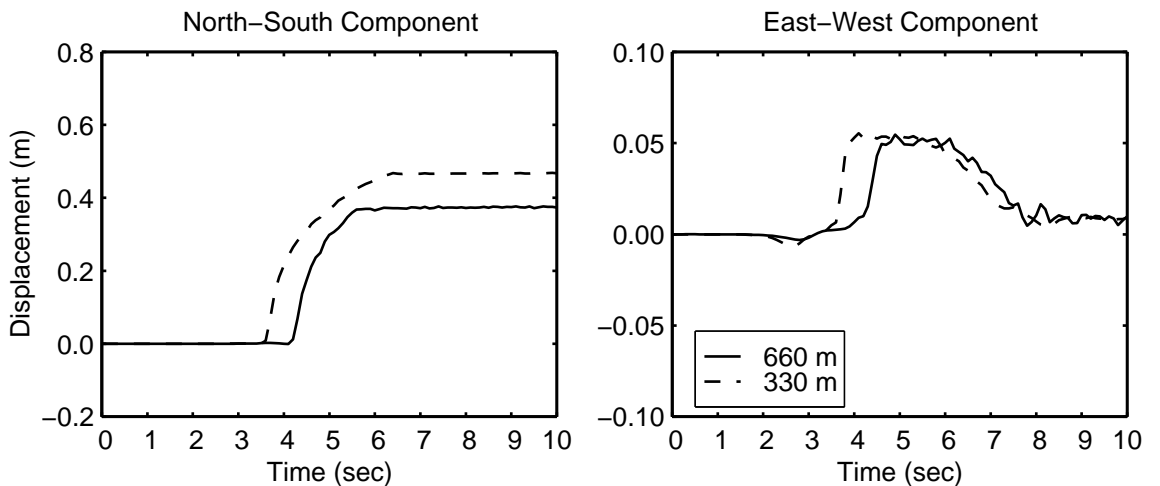


Figure 9.7: Comparison of horizontal displacement time histories at site S1 for the two spatial resolutions of the strike-slip domain.

## 9.3 Effective Normal Stresses

We want to determine how the changes in the variations of the effective normal stresses with depth affect the dynamics of the rupture on the strike-slip fault. Furthermore, when the characteristics of the rupture do not lead to realistic events, we will adjust the friction model to create realistic ruptures. We return to the three definitive cases of pore pressures described in section 8.2.1 to create three different variations of the normal tractions with depth, including uniform effective normal tractions, lithostatic effective normal tractions, and lithostatic effective normal tractions reduced by hydrostatic pore pressures.

### 9.3.1 Uniform Stresses with a Uniform Friction Model:

#### Scenario ssbase

We already discussed scenario ssbase (the base case) which features uniform effective normal stresses. Figure 9.8 displays the uniform tractions with depth. While we do not *a priori* know the change in the shear tractions, the uniform dynamic stress drop suggests the approximate values of the change in shear tractions. We illustrate the final shear tractions using the initial shear tractions and the change in the shear tractions. In scenario ssbase we found realistic rupture dynamics, i.e., the rupture propagates along the fault at a relatively constant speed and generates a smooth uniform slip distribution consistent with a uniform stress drop.

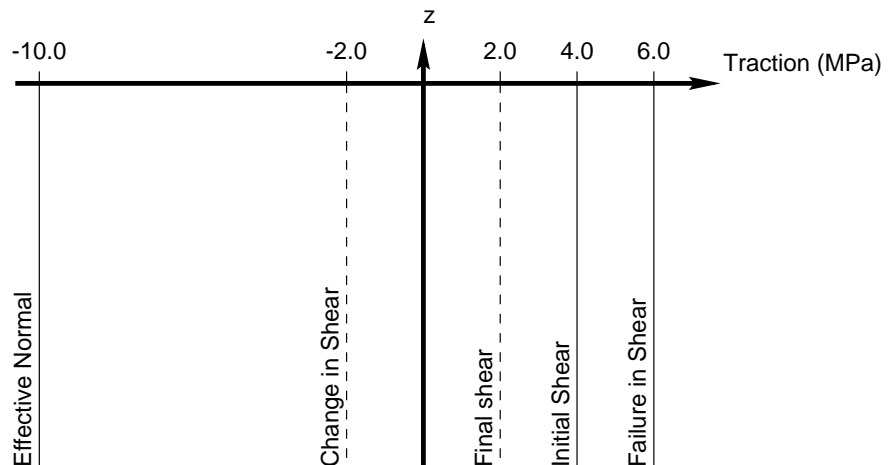


Figure 9.8: Variations of the tractions with depth on the strike-slip fault for the case of uniform effective normal stresses and no variations of the coefficient of friction parameters with depth. The dashed lines give an estimation of those tractions whose precise values depend on the results of the simulation.

### 9.3.2 Lithostatic Stresses with a Uniform Friction Model:

#### Scenario sslithouni

In this case we assume that little or no water resides in the interstices of the grains, so that the pore pressures are negligible, and the effective normal stresses are lithostatic. We use the same slip-weakening friction

model that we use in the base case. The parameters in the friction model do not vary with depth.

### Initial Conditions

With negligible pore pressures the effective normal stresses equal the lithostatic stresses. In the case of our homogeneous half-space, the effective normal stresses increase linearly with depth. The shear tractions at failure increase linearly with depth, because they come from the product of the normal tractions, which increase linearly with depth, and the maximum coefficient of friction ( $\mu_{max}$ ), which is uniform with depth. To create a propagating rupture with a uniform speed, we employ a uniform distance from failure. This implies that the initial shear tractions should increase linearly with depth. Maintaining a uniform distance from failure over the entire depth of the fault would require negative initial shear tractions near the ground surface, so we limit the shear tractions to positive values and taper the distance from failure near the ground surface. Because the effective normal tractions increase with depth, the change in the shear tractions will be larger at depth. Figure 9.9 summarizes the variations of these tractions with depth. We do not know the final shear stresses on the fault surface, but we expect the final shear stresses to generally follow the variations of the minimum sliding shear stresses. Figure 9.10 shows the initial shear and normal tractions applied to the fault surface. The asperity used to start the rupture requires only small relative increases in the shear tractions, so unlike the base case, it blends in with the surrounding shear tractions. Due to the large increase in the shear tractions with depth, we choose not to taper the shear tractions along the lateral edges and bottom of the fault.

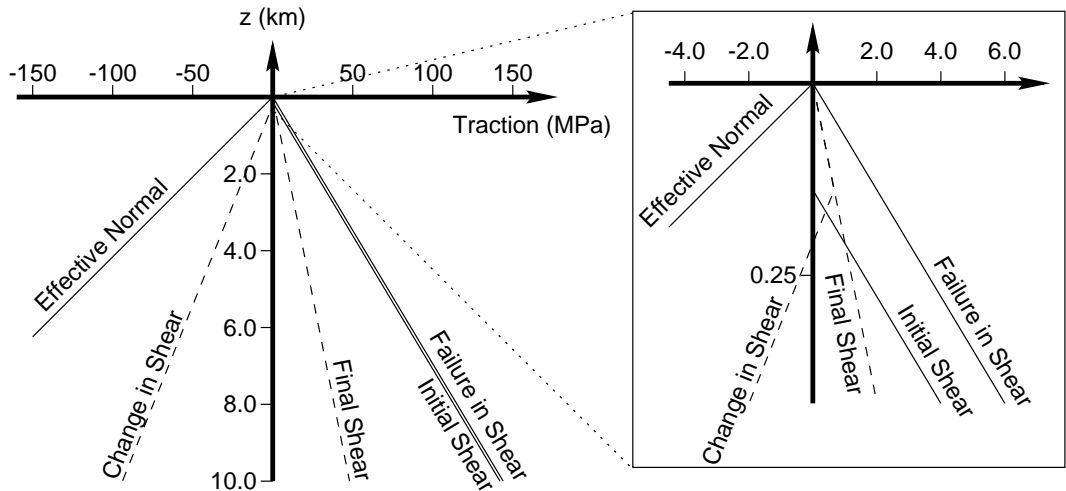


Figure 9.9: Variations of the tractions with depth on the strike-slip fault for the case of lithostatic effective normal stresses and no variations of the coefficient of friction parameters with depth. The dashed lines give an estimation of those tractions whose precise values depend on the results of the simulation.

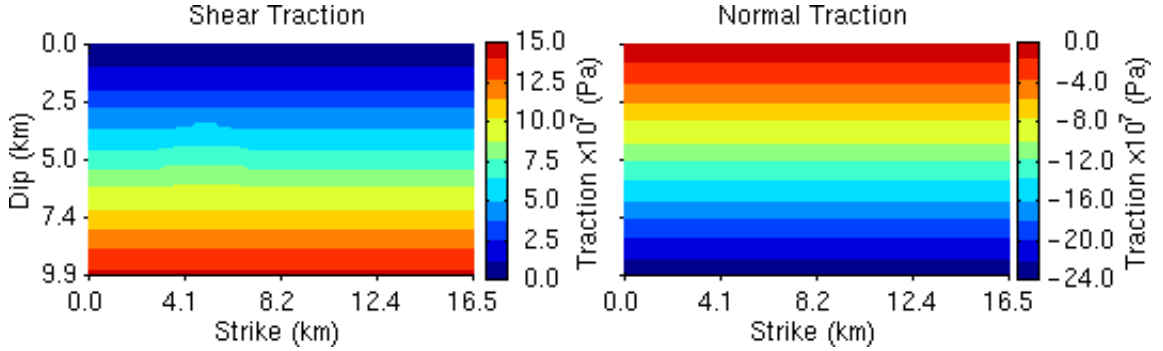


Figure 9.10: Initial shear and normal tractions on the strike-slip fault for scenario sslihouni.

### Characteristics of the Earthquake

The rupture propagates rapidly across the bottom of the fault in response to the increase in the dynamic stress drop with depth. Recall from section 8.3.1 that the size of the dynamic stress drop influences the rupture speed. Figure 9.11 shows the distributions of final slip and maximum slip rate on the fault. In contrast to scenario ssbase, both the final slip and maximum slip rate show a clear trend with depth with extraordinarily large values near the bottom of the fault. We see that a dynamic stress drop that increases with depth leads to unreasonable behavior, and, in particular, the final slips and maximum slip rates increase with depth.

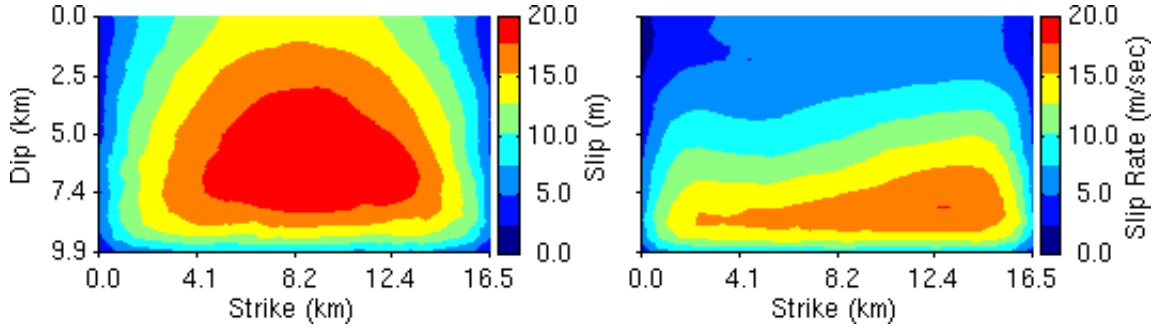


Figure 9.11: Distributions of final slip and maximum slip rate at each point on the strike-slip fault for scenario sslihouni.

We may scale the initial tractions to create reasonable values of final slip and slip rate near the bottom of the fault, but we cannot change the trend with depth as long as the parameters in the friction model remain uniform with depth. Similarly, if the pore pressures remain well below the lithostatic pressures, increasing the pore pressures will only reduce the rate at which the slip and slip rate increase with depth; it cannot change the trend. Additionally, any other friction model with uniform parameters with depth will produce the same trends with depth. This suggests that either the effective normal stresses are uniform with depth or the friction model parameters vary with depth. As we noted in section 8.2.1, the existence of topography and density variations imply the pore pressures do not generally approach the lithostatic normal stresses. Consequently, we will attempt to adjust the parameters in the friction model to compensate for effective

normal stresses that increase with depth.

### 9.3.3 Lithostatic Stresses with a Variable Friction Model:

#### Scenario `sslithovar`

We continue to assume negligible pore pressures so that the effective normal stresses increase linearly with depth in the homogeneous half-space. We adjust the coefficient of friction parameters,  $\mu_{max}$  and  $\mu_{min}$ , in the slip-weakening friction model to create a uniform dynamic stress drop. We start with the expressions for the effective normal stress ( $\sigma_n$ ), the shear stress at failure ( $\sigma_{fail}$ ), and the stress drop ( $\Delta\sigma$ ):

$$\sigma_n = \rho g z \quad (9.2)$$

$$\sigma_{fail} = -\mu_{max}\sigma_n \quad (9.3)$$

$$\Delta\sigma = \sigma_0 - \sigma_1. \quad (9.4)$$

We follow the convention that  $z$  is positive upwards so  $z < 0$  below the ground surface. We define the initial shear stress relative to the failure stress using the distance from failure,  $\sigma_{dff}$ ,

$$\sigma_0 = \sigma_{fail} - \sigma_{dff}, \quad (9.5)$$

and assume that the final shear stress equals the minimum sliding shear stress,

$$\sigma_1 = -\mu_{min}\sigma_n. \quad (9.6)$$

Substituting into the expression for the stress drop and solving for the minimum coefficient of friction yields

$$\mu_{min} = \mu_{max} + \frac{\Delta\sigma + \sigma_{dff}}{\rho g z}. \quad (9.7)$$

The distance from failure may or may not change with depth. Assuming a distance from failure proportional to depth implies that the minimum and maximum coefficients of friction remain relatively uniform with depth. In order to maintain a uniform rupture speed with a distance from failure that increases with depth, the stress concentration ahead of the rupture must increase with depth. As we discussed in section 8.3.2, in continuous media propagating ruptures generate nearly singular shear stresses near the rupture front. Such shear stresses can cause failure over the depth of the fault when the distance from failure increases with depth. In the finite-element model the dependence of the failure stress on the discretization size coupled with our basing the discretization size on the wave propagation necessitates using a uniform distance from failure. As a result, we focus on accurately modeling the fracture energy and the shear stresses during sliding as opposed to the shear stresses at failure.

Returning to our expression for the change in the minimum coefficient of friction, a uniform distance from failure means that the absolute difference between the maximum and minimum values of the coefficient of friction decreases with depth, i.e.,  $\mu_{max} - \mu_{min} \rightarrow 0$  as  $z \rightarrow -\infty$ . We may accomplish this task in three general ways.

1. We use a uniform value for the coefficient of friction at failure ( $\mu_{max}$ ) and decrease the relative change in the coefficient of friction during sliding by adjusting  $\mu_{min}$  using

$$\mu_{min} = \mu_{max} + \frac{\Delta\sigma + \sigma_{diff}}{\rho g z}. \quad (9.8)$$

The uniform coefficient of friction at failure and a uniform distance from failure means that the initial shear stresses must increase linearly with depth. Consequently, the tectonic stresses must increase linearly with depth. In other words, the tectonic stresses cannot be derived from application of uniform stresses or uniform strains in the homogeneous half-space, which seems unrealistic. Furthermore, the sliding stresses increase with depth which implies huge changes in temperature during sliding. For example, assuming a coefficient of friction at failure of 0.6, a density of  $2450 \text{ kg/m}^3$ , a distance from failure of 2 MPa, at a depth of 10 km we find a sliding stress of 140 MPa. If the heat is confined to a region 5 mm wide and the heat capacity is  $1000 \text{ J/(kg}\cdot\text{^\circ K)}$  (Kanamori et al. 1998), the change in temperature for every meter of slip is 11,000 degrees Kelvin. Such a large change in temperature would induce melting and would lead to a decrease in the sliding stress. With larger effective normal stresses with depth, the degree of melting would increase with depth. Assuming that the sliding stresses decrease significantly with melting implies that the sliding stresses do not increase with depth. This contradicts our original assumption. Thus, the coefficient of friction at failure must decrease with depth.

2. We use a uniform value for the minimum coefficient of friction during sliding ( $\mu_{min}$ ). We decrease the relative change in the coefficient of friction by altering the coefficient of friction at failure using

$$\mu_{max} = \mu_{min} - \frac{\Delta\sigma + \sigma_{diff}}{\rho g z}. \quad (9.9)$$

The failure stress approaches a uniform value as the depth increases, which in conjunction with the uniform distance from failure implies larger initial shear stresses near the surface. As in the previous case, we find this unrealistic because the tectonic tractions cannot be derived from application of uniform stresses or uniform strains.

3. We decrease the coefficient of friction with depth by adjusting both the coefficient of friction at failure ( $\mu_{max}$ ) and the coefficient of friction during sliding ( $\mu_{min}$ ) in the same manner. As slip progresses, the absolute change of the coefficient of friction decreases with depth, but the relative change does not. This leads to uniform failure and sliding stresses with depth and resembles the case of uniform

effective normal stresses. In this case, we may generate the tectonic shear and normal stresses from uniform stresses or uniform strains with depth.

We choose the third alternative because the initial and sliding shear stresses seem most realistic. Additionally, the uniform relative change in the coefficient of friction appears reasonable, yet remarkably simple.

### Initial Conditions

The two parameters,  $\mu_{max}$  and  $\mu_{min}$ , in the slip-weakening friction model vary with the inverse of depth as shown in figure 9.12. Equation (9.10) gives the function form of the friction model. It seems unreasonable to let the coefficient of friction approach infinity at the surface, so we clip its value above a depth of 250 m.

$$\begin{aligned}\mu_{max} &= \begin{cases} -\frac{250\text{m}}{z} & z < -250\text{m} \\ 1.00 & z > -250\text{m} \end{cases} \\ \mu_{min} &= \begin{cases} -\frac{83.3\text{m}}{z} & z < -250\text{m} \\ 0.333 & z > -250\text{m} \end{cases}\end{aligned}\quad D_o = 0.150\text{m} \quad (9.10)$$

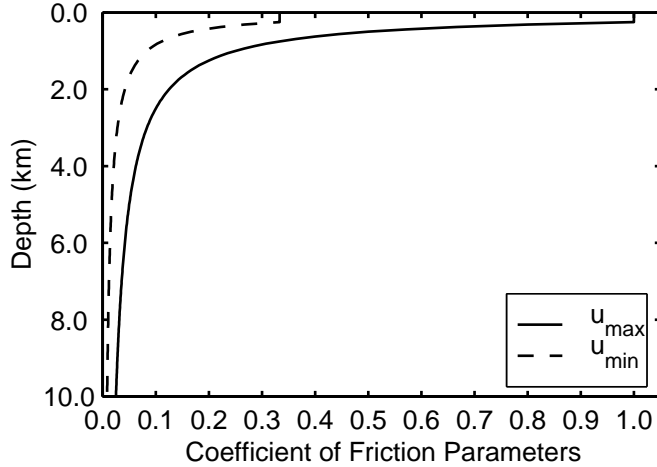


Figure 9.12: Depth variations of the coefficient of friction parameters,  $\mu_{max}$  and  $\mu_{min}$ , in the slip-weakening friction model.

Our *ad hoc* adjustment of the friction model parameters creates large variations in the coefficient of friction with depth. Researchers observe reduced values of the coefficient of friction when the temperature increases (Scholz 1990). Rice and Ben-Zion (1996) vary the parameters in their friction model with depth based on temperature; however, their parameters exhibit only small variations with depth. Thus, some decrease in the coefficient of friction with depth based on the increase in temperature seems reasonable. We do

not know how the coefficient of friction varies with depth, so our large variation in the coefficient of friction with depth may or may not be realistic. We reduce the coefficient of friction with depth in order to create low sliding shear stresses that do not imply melting, to allow a uniform stress or strain field to generate the nominal initial shear stresses on the fault, and to maintain a uniform distance from failure. We choose a uniform distance from failure based on our desire not to increase the resolution of the finite-element model with depth and our focus on the shear stresses during sliding as opposed to the shear stresses at failure. Moreover, the variation of the coefficient of friction remains relatively unconstrained by seismological data.

Figure 9.13 illustrates that the shear tractions at failure along with the initial and final shear tractions do not vary with depth except near the ground surface. Above the depth where we clip the coefficient of friction at failure (labeled “Taper Depth” in figure 9.13), the tractions taper towards a value of zero at the ground surface. Figure 9.14 shows the effective normal tractions and initial shear tractions that we apply to the fault surface. The effective normal tractions match those from the previous case (figure 9.10), and the initial shear tractions match those from the case of uniform effective normal stresses (figure 9.3), except in the top 250 m where we taper the shear tractions.

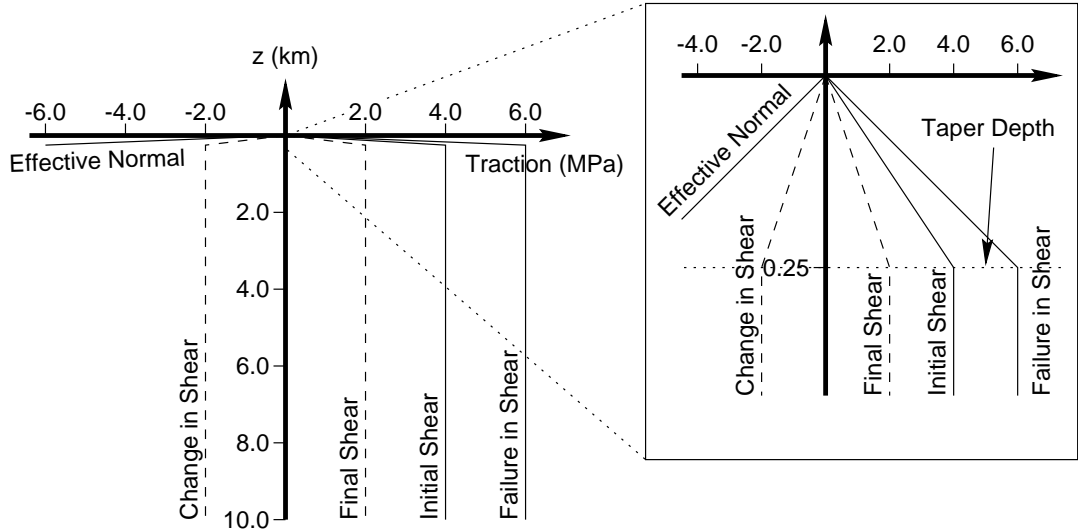


Figure 9.13: Variations of the tractions with depth on the strike-slip fault for the case of lithostatic effective normal stresses and variations of the coefficient of friction parameters with depth. The dashed lines give an estimation of those tractions whose precise values depend on the results of the simulation.

### Characteristics of the Earthquake

Our manipulation of the friction model parameters yields the desired results. The rupture exhibits nearly identical behavior to the one in scenario ssbase. The rupture propagates at the same speed (1.7 km/sec) and produces the distributions of final slip and maximum slip rate given in figure 9.15. Comparing the distributions to those from scenario ssbase (figure 9.5), we find only small deviations between the two. The tapering of the tractions near the ground surface causes the more noticeable differences, including the reduction of the

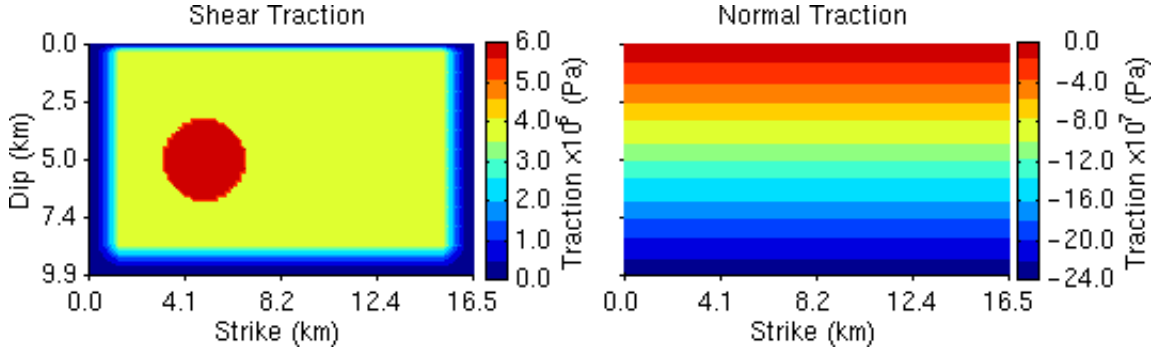


Figure 9.14: Shear and normal tractions on the strike-slip fault for scenario ss lithovar.

maximum slip rate along the ground surface.

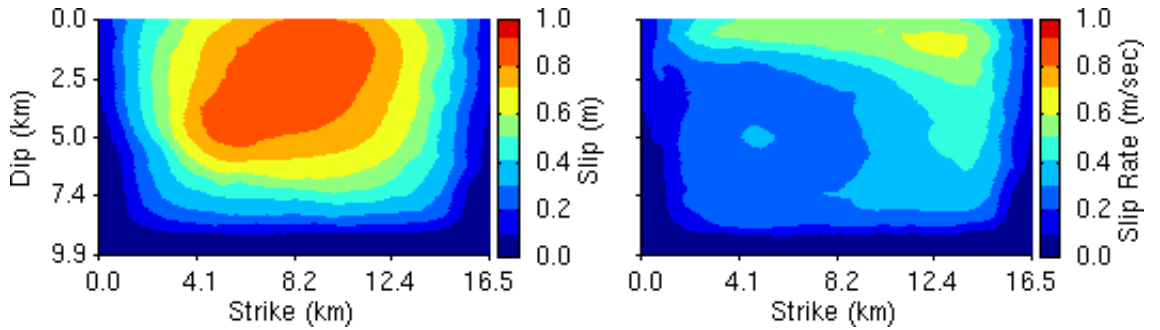


Figure 9.15: Distributions of final slip and maximum slip rate at each point on the strike-slip fault for scenario ss lithovar.

The horizontal velocities at site S1 reflect these minor differences. In figure 9.16 we see a smaller peak velocity in the north-south (fault parallel) direction for scenario ss lithovar compared to scenario ss base. This coincides with the reduced maximum slip rates along the ground surface. The east-west component of velocity shows negligible differences.

### 9.3.4 Lithostatic-Hydrostatic Stresses with a Variable Friction Model:

#### Scenario ss lithohydro

We now consider the case of saturated material where the pore pressure equals the hydrostatic pressure. Several researchers, such as Rice and Ben-Zion (1996), Sleep (1997), and Tullis (1996), use this distribution of the effective normal stresses with depth. Compared to the case of lithostatic effective normal stresses, the saturation of the material with water reduces the effective normal stresses by the hydrostatic pressures. We maintain the same failure stress at every point with a 70% increase in the coefficient of friction. Equation (9.11) gives the functional forms of the parameters in the slip-weakening friction model. Consequently, we apply the same initial shear tractions that we use for scenario ss lithovar. Figure 9.16 shows that the waveforms remain the same, i.e., the rupture behavior and the resulting ground motions do not change. Thus, the

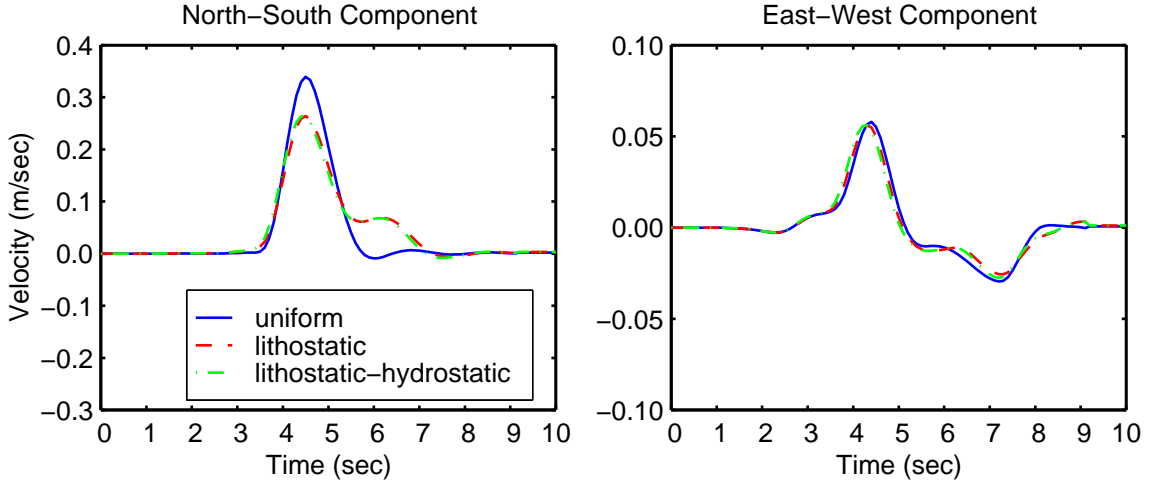


Figure 9.16: Comparison of horizontal velocity time histories at site S1 for the three cases of effective normal stresses on the strike-slip fault.

variations of the parameters in the friction model works equally well for both negligible and hydrostatic pore pressures.

$$\mu_{max} = \begin{cases} -\frac{422}{z} & z < -250 \text{ m} \\ 1.69 & z > -250 \text{ m} \end{cases}$$

$$\mu_{min} = \begin{cases} -\frac{141}{z} & z < -250 \text{ m} \\ 0.563 & z > -250 \text{ m} \end{cases}$$

$$D_o = 0.150 \text{ m} \quad (9.11)$$

## 9.4 Thrust Fault

In this section we demonstrate that these same issues regarding the effective normal stresses also apply to inclined faults by considering a thrust fault with a dip angle of 35 degrees (see section 9.1.2 for a description of the domain). We impose shear tractions on the fault surface at an angle of 105 degrees from the strike. Additionally, we create the same dynamic stress drop and distance from failure as in scenario ssbase. In contrast to vertical faults, such as the strike-slip fault that we use above, on dipping faults the shear and normal tractions are coupled during application of horizontal axial stresses. The ground surface remains traction free, and we must apply shear and normal stresses acting in the horizontal direction to generate the shear tractions on the fault plane with the appropriate rake angle.

### 9.4.1 Uniform Stresses with a Uniform Friction Model: Scenario thbase

As with the strike-slip fault, we begin with uniform effective normal stresses and use a friction model with parameters that do not vary with depth. Researchers, such as Magistrale and Day (1999) and Oglesby et al. (1998), typically select these uniform distributions for simplicity.

#### Initial Conditions

We create the 4.0 MPa shear tractions through application of axial stresses in the north-south direction and horizontal shear stresses that mimic the stresses generated through plate tectonics. The shear stresses give the shear traction vectors the appropriate rake angle on the fault plane. This also generates effective normal stresses on the fault surface of 2.7 MPa that are much less than the 10 MPa effective normal stresses that we impose on the strike-slip fault. The shallow dip causes the effective normal tractions to be much less than the shear tractions, and we must use a coefficient of friction greater than 1.0. Table 9.4 gives the parameters for the slip-weakening friction model; we increase the coefficient of friction by a factor of 3.7 compared to the strike-slip case (scenario ssbase).

Parameters	Value
$\mu_{max}$	2.2
$\mu_{min}$	0.74
$D_o$	0.15 m

Table 9.4: Parameters of the slip-weakening I friction model for scenario thbase.

Figure 9.17 shows the initial shear and normal tractions that we apply to the fault surface. We taper the shear tractions on all four edges to smother the rupture as it approaches the edges of the fault. We place the asperity used to initiate the rupture along the north-south running centerline 4.0 km from the bottom of the fault. The diameter of the asperity matches the one used in the strike-slip cases.

#### Characteristics of the Earthquake

As demonstrated in figure 9.18, the rupture propagates with the same elliptic shape that we observe in the simulations on the strike-slip fault. The slip follows the direction of the applied shear tractions, so the slip direction has a rake angle of 105 degrees. As a result, the rupture propagates at a speed of 1.8 km/sec up the fault but skewed slightly to the west. Compared to the strike-slip case, the smaller fault and lack of a free surface reduces the width of the rupture front. The portion of the rupture front that contains large slip rates (where most of the slip occurs) remains about the same.

Figure 9.19 shows the distribution of final slip and maximum slip rate on the fault surface. As we expect, the final slip resembles that of a uniform stress drop earthquake with an average slip of 0.25 m and a moment magnitude of 5.8. We find a nearly uniform maximum slip rate over the area where slip occurred. The

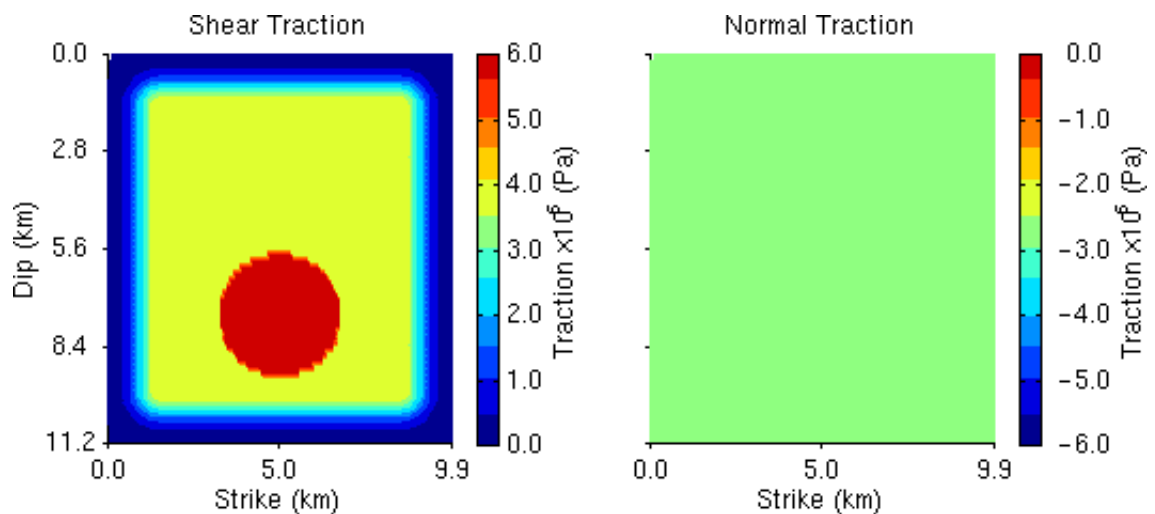


Figure 9.17: Shear and normal tractions on the thrust fault for scenario thbase.

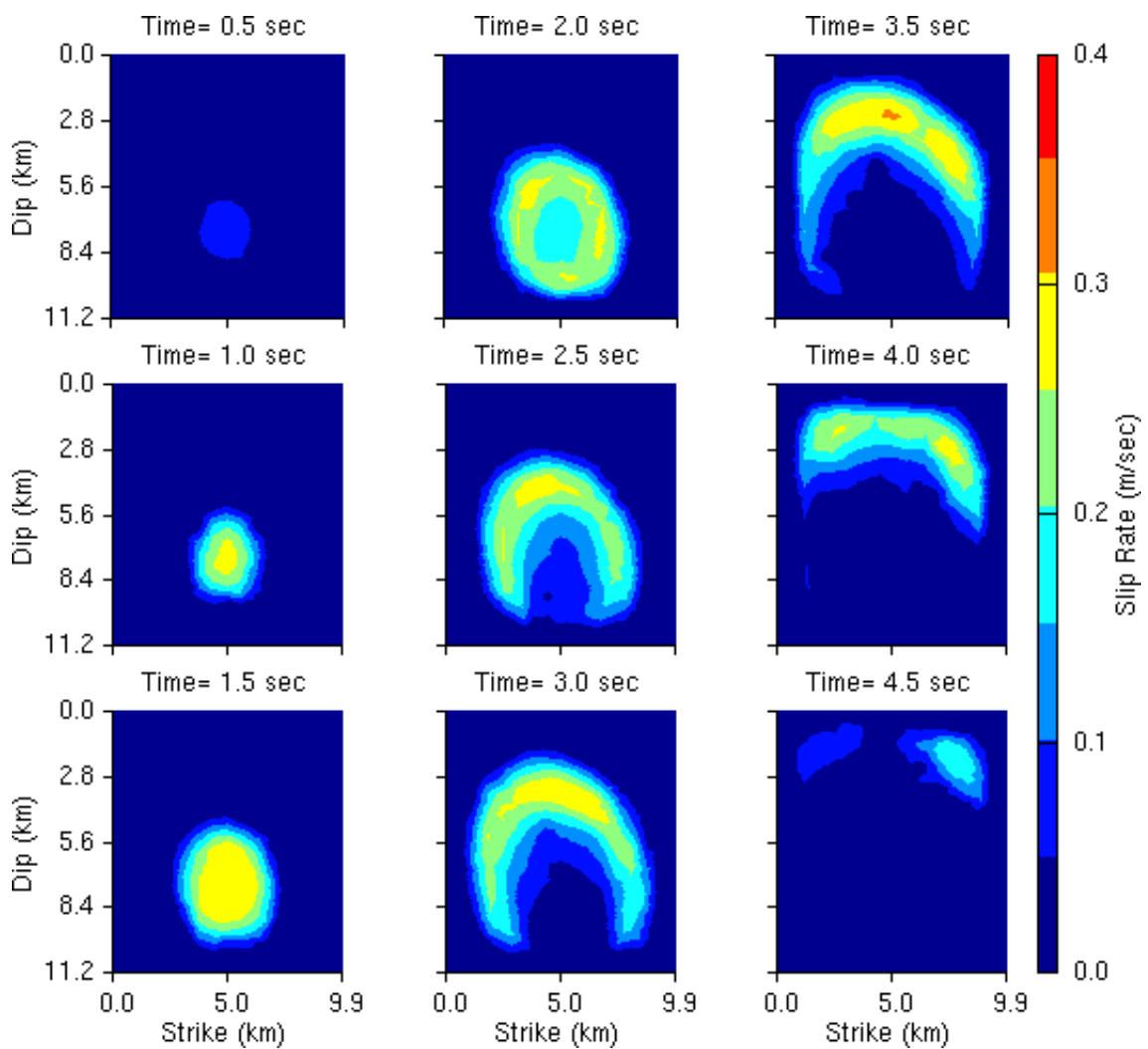


Figure 9.18: Snapshots of slip rate on the thrust fault for scenario thbase.

negligible maximum slip rates along the edges of the fault illustrate that the tapering of the initial shear traction at the edges of the fault smothers the rupture. Despite the elliptic shape of the rupture front, the final slip and maximum slip rate are nearly symmetric about the fault centerlines. We examine velocity time histories in section 9.4.2 below.

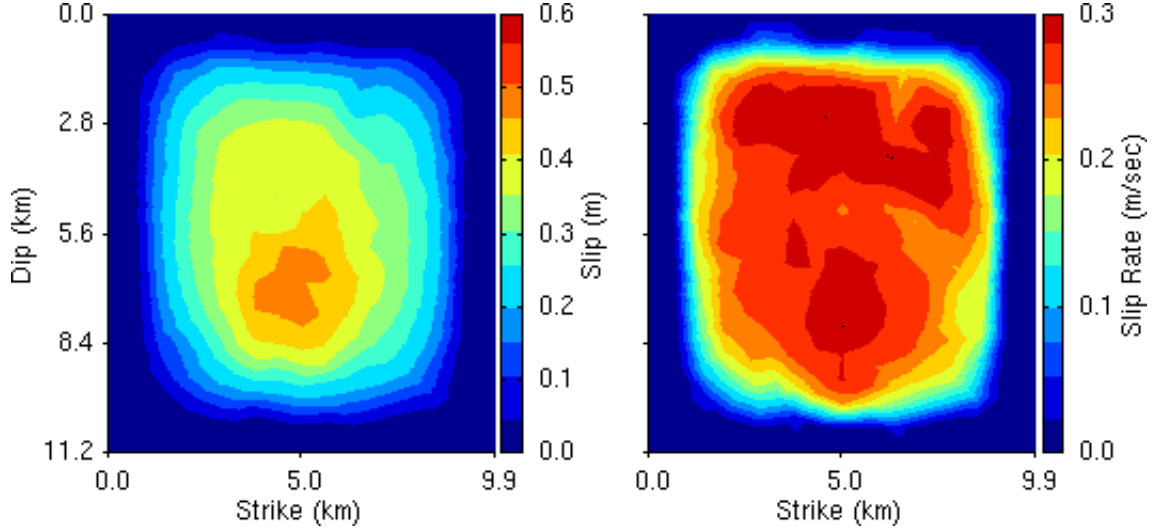


Figure 9.19: Distributions of final slip and maximum slip rate at each point on the thrust fault for scenario thbase.

#### 9.4.2 Lithostatic Stresses with a Variable Friction Model: Scenario tlithovar

We now consider the case of lithostatic effective normal stresses with variations of the parameters of the coefficient of friction with depth. Because we use the same homogeneous material properties as in the strike-slip case, gravity generates the same effective normal stresses. With negligible pore pressures the stresses due to gravity dominate the normal stresses due to the tectonic loading applied as horizontal axial stresses, and the effective normal stresses closely match those on the strike-slip fault in scenario sslithovar. Thus, it makes sense to use the parameters of the friction model from scenario sslithovar.

##### Initial Conditions

Figure 9.20 illustrates the effective normal stresses created from the superposition of the lithostatic stresses due to gravity and the normal tractions due to plate tectonics. Gravity does not contribute to the shear tractions, so the shear tractions do not change from scenario thbase. We find much larger effective normal stresses at the top of the thrust fault than at the top of the strike-slip fault, because we bury the thrust fault 5.3 km below the ground surface.

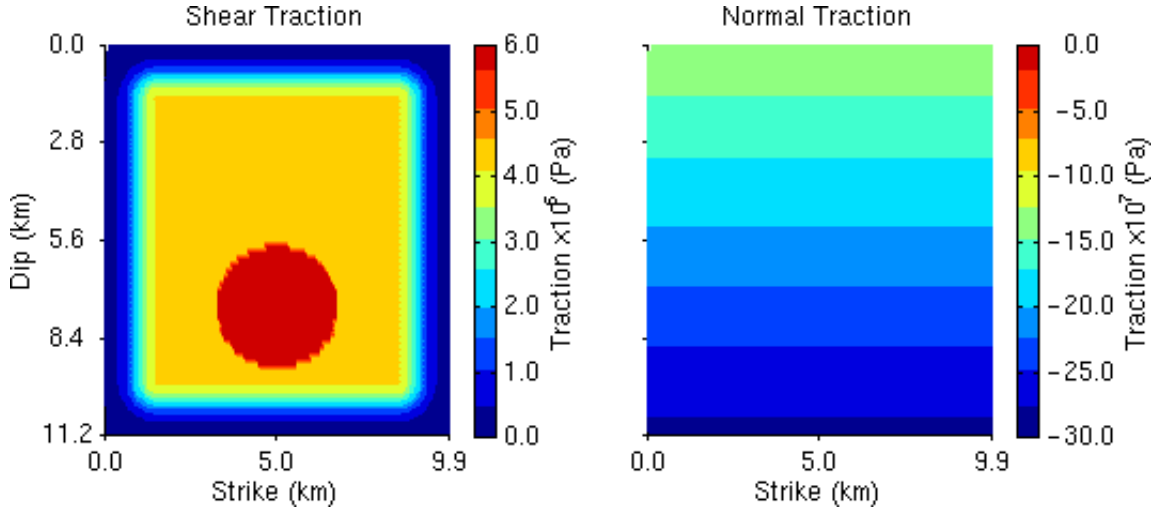


Figure 9.20: Shear and normal tractions on the thrust fault for scenario tlithovar.

### Characteristics of the Earthquake

As in the case of the strike-slip fault, we find only minor differences in the behavior of the rupture between the case of uniform effective normal stresses with a uniform coefficient of friction and the case of lithostatic effective normal stresses with a variable coefficient of friction. The average slip increases from 0.25 m (scenario thbase) to 0.30 m (scenario tlithovar), but the moment magnitude remains 5.8. Comparing the final slip distribution for this scenario (figure 9.21) with the one from scenario thbase (figure 9.19), we notice that the slip increases in the center of the fault with almost no change near the edges. We also find just a small, general increase in the maximum slip rate.

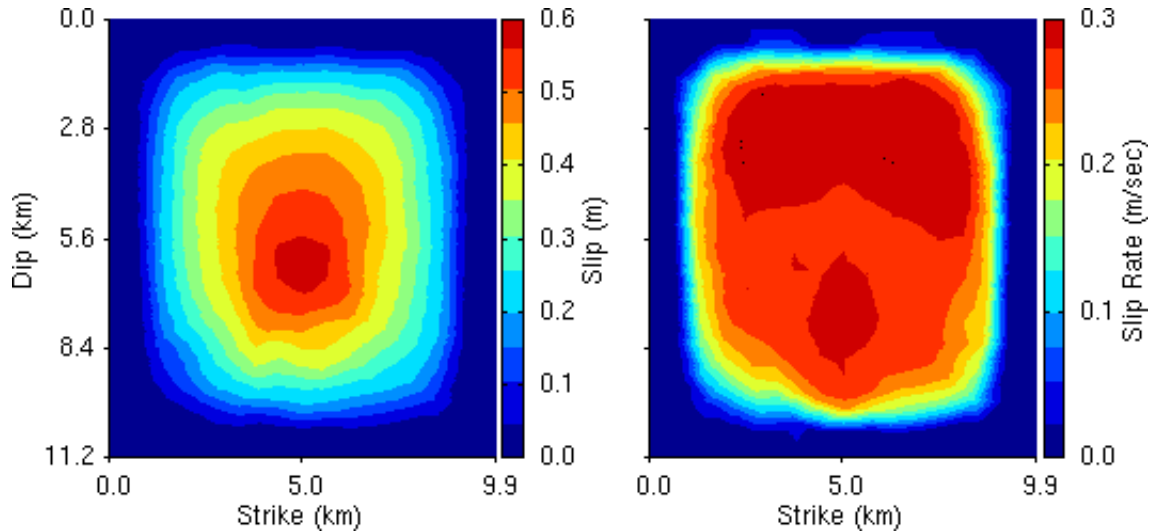


Figure 9.21: Distributions of final slip and maximum slip rate at each point on the thrust fault for scenario tlithovar.

We examine the time histories at site S1, which sits above the center of the top edge of the fault. The

north-south and vertical components of the velocity time histories shown in figure 9.22 exhibit similar characteristics. We observe a slightly later initiation of slip corresponding to the difference in the rupture speeds (1.7 km/sec for scenario sslithovar compared to 1.8 km/sec for scenario thbase). In both the north-south and vertical components the amplitudes of the velocity increase slightly, but the shapes of the pulses do not change.

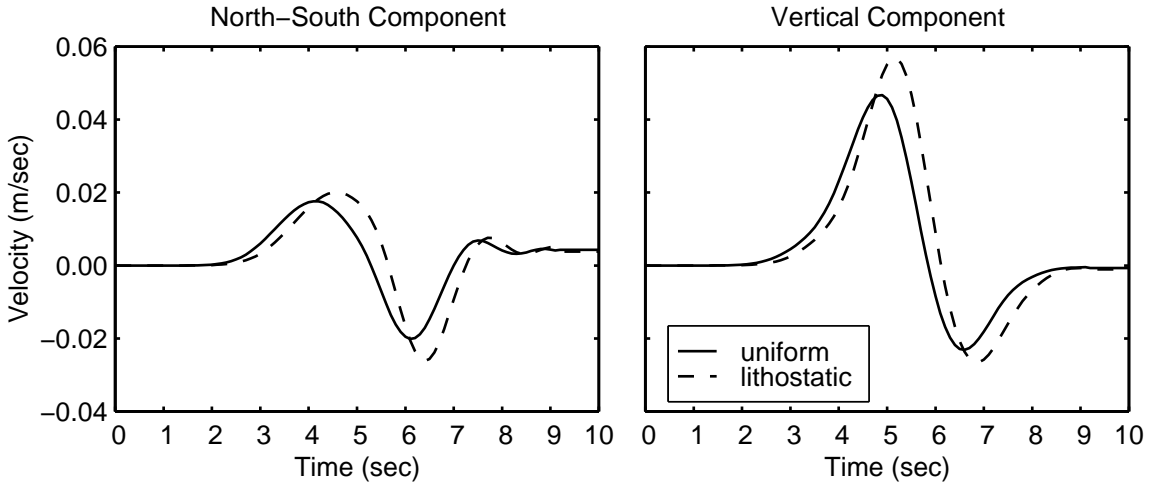


Figure 9.22: Comparison of north-south and vertical velocity time histories at site S1 for the two cases of effective normal stresses on the thrust fault.

## 9.5 Rupture Behavior with Different Friction Models

We study the changes in the behavior of the rupture on the strike-slip fault to variations in the friction model by replacing the slip-weakening I friction model with the slip- and rate-weakening model and the melting-refreezing model. In both cases we apply normal tractions equal to the lithostatic pressures and vary the coefficient of friction parameters with depth. We adjust the parameters in the friction models to create earthquakes with average slips that closely match the 0.52 m average slip of scenario sslithovar.

### 9.5.1 Slip- and Rate-Weakening Friction Model: Scenario sscombo

With slip- and rate-weakening friction, the friction stress initially decreases as slip progresses, but returns close to its original level as the slip rate decreases (see figure 8.8). With the re-strengthening as the slip rate drops, slip will terminate sooner than when we use the friction models with only slip-weakening and the same sliding stress. Consequently, we select a new value for the dynamic stress drop, but we maintain the same initial rate of decrease of the coefficient of friction with slip distance as in the base case (scenario ssbase) in order to generate a similar rupture. We use a post-seismic coefficient of friction that is 83% of the coefficient of friction at failure. Equation (9.12) gives the parameters of the friction model that yield an average slip

of 0.55 m, which is close to our target value of 0.52 m. With no change in the effective normal tractions and initial shear tractions from those in scenario sslithovar, we use the same maximum coefficient of friction ( $\mu_{max}$ ). In order to enlarge the dynamic stress drop, we reduce the minimum coefficient of friction ( $\mu_{min}$ ). Additionally, maintaining the same initial rate of decrease of the coefficient of friction with slip distance involves adjusting the characteristic slip distance.

$$\begin{aligned}\mu_{max} &= \begin{cases} -\frac{250\text{m}}{z} & z < -250\text{m} \\ 1.00 & z > -250\text{m} \end{cases} \\ \mu_{min} &= \begin{cases} -\frac{41.7\text{m}}{z} & z < -250\text{m} \\ 0.167 & z > -250\text{m} \end{cases} \\ \mu_{post} &= \begin{cases} -\frac{208\text{m}}{z} & z < -250\text{m} \\ 0.833 & z > -250\text{m} \end{cases} \\ D_o &= 0.188\text{ m} \\ V_o &= 0.133\text{ m/sec} \end{aligned} \tag{9.12}$$

### Characteristics of the Earthquake

The rupture propagates with nearly the same speed as in scenario sslithovar (1.9 km/sec compared to 1.7 km/sec), but the maximum slip rates increase significantly. Comparing figure 9.23 with figure 9.15, we see that the maximum slip rates exhibit a nearly uniform increase of approximately 0.2 m/sec. Because we attempt to match the average slip with scenario sslithovar, we expect a similar final slip distribution. Indeed, we find a small, nearly uniform increase in the final slip that corresponds to the difference in the average slips.

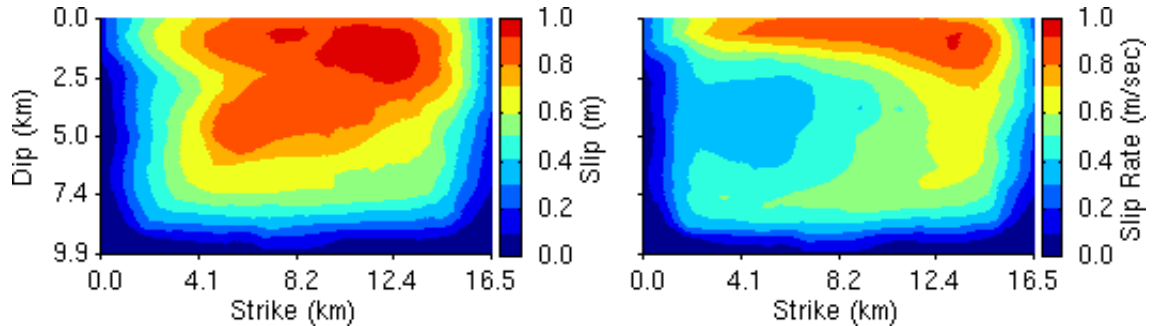


Figure 9.23: Distributions of final slip and maximum slip rate at each point on the strike-slip fault for scenario sscombo.

Figure 9.24 shows the velocity time histories at site S1 for both scenario sslithovar and scenario sscombo. The north-south (fault parallel) velocity time histories confirm the increase in rupture speed with earlier motion in scenario sscombo than in scenario sslithovar. The termination of sliding occurs more abruptly in scenario sscombo in response to the shear re-strengthening. The shear wave continues to dominate the

east-west (fault normal) velocity time histories. The reflection of the rupture off the free surface generates a second slip event in the central portion of the fault and causes the noticeably different shape in the east-west component towards the end of the time history.

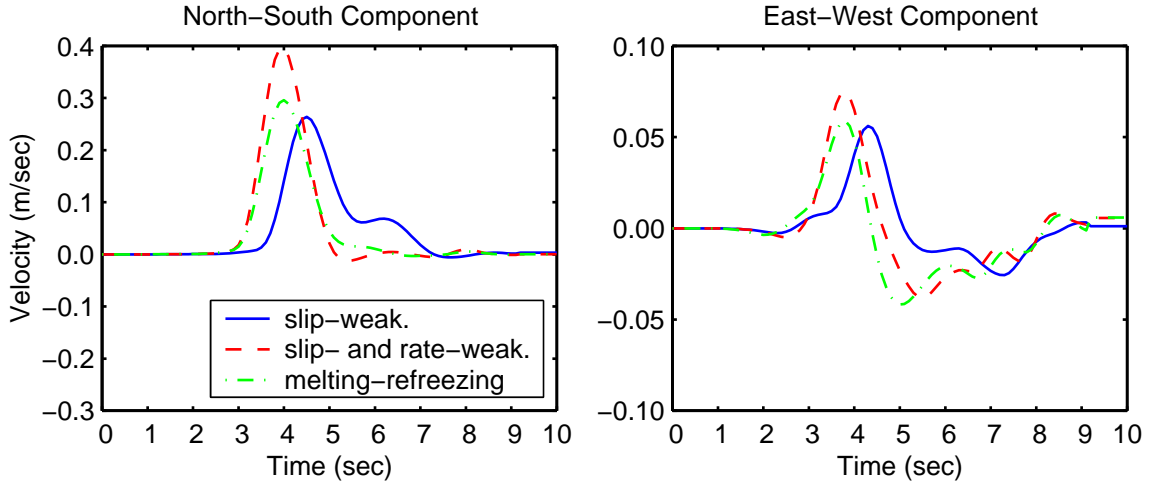


Figure 9.24: Comparison of north-south and vertical velocity time histories at site S1 for the three friction models on the strike-slip fault.

### 9.5.2 Shear Melting-Refreezing Friction Model:

#### Scenario ssmelt

The shear melting-refreezing model produces the same general behavior as the slip- and rate-weakening friction model (see figure 8.9 for a typical trajectory of the coefficient of friction in terms of slip distance and slip rate). We again select the parameters to closely match the average slip of scenario sslithovar (0.52 m). We apply the effective normal tractions and initial shear tractions from scenario sslithovar. We use the friction model parameters given by equation (9.13) to produce an average slip of 0.51 m.

$$\mu_{max} = \begin{cases} -\frac{250 \text{ m}}{z} & z < -250 \text{ m} \\ 1.00 & z > -250 \text{ m} \end{cases}$$

$$\mu_{min} = \begin{cases} -\frac{45.8 \text{ m}}{z} & z < -250 \text{ m} \\ 0.183 & z > -250 \text{ m} \end{cases}$$

$$D_o = 0.0800 \text{ m}$$

$$T_o = 0.650 \text{ sec} \quad (9.13)$$

### Characteristics of the Earthquake

Based on the similarity of the friction models and the dynamic stress drop, we expect to find about the same increase in the maximum slip rates for this scenario and scenario sscombo compared to scenario sslithovar, where we use a slip-weakening friction model. The maximum slip rates shown in figure 9.25 exhibit approximately a 0.1 m/sec increase compared to the 0.2 m/sec increase for scenario sscombo. If we compare the final slip distribution from this scenario with that from scenario sslithovar, we find that the slip distribution shifts slightly towards the north. In the shear melting-refreezing friction model the rate of decrease of the coefficient of friction depends on the history of the slip rate. This creates a tendency for relatively larger values of slip to occur in regions with larger values of maximum slip rate.

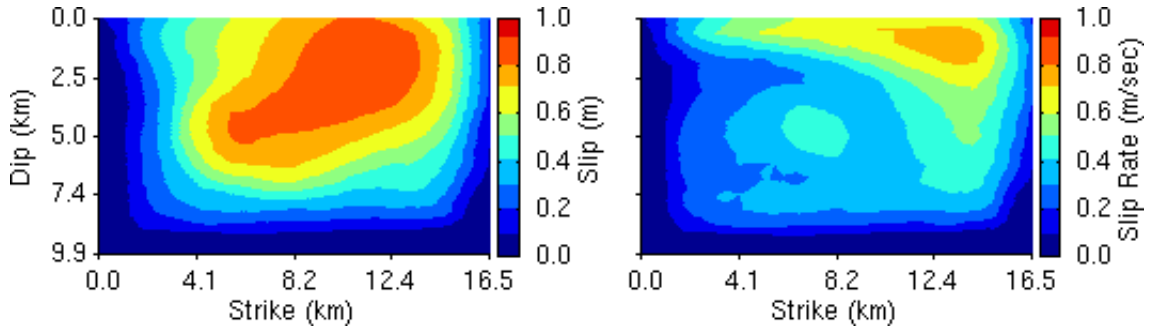


Figure 9.25: Distributions of final slip and maximum slip rate at each point on the strike-slip fault for scenario ss melt.

If we return to figure 9.24, we observe similar velocity time histories at site S1 for the scenarios with the slip- and rate-weakening friction model (scenario sscombo) and the shear melting-refreezing friction model (scenario ss melt). The peak velocities differ in proportion to the difference in maximum slip rates, which we noted above. The reflection of slip off the ground surface generates a second slip event in the central portion of the fault as it did in scenario sscombo, so we find that the east-west (fault normal) components match very well towards the end of the time history.

## 9.6 Effect of the Free Surface

On the strike-slip faults the slip rates increase in the vicinity of the free surface. This causes the rupture to propagate faster along the free surface. We illustrate the nature of this behavior by studying the effects of ruptures with different curvatures encountering the free surface. Additionally, we subject a much larger strike-slip fault to similar initial conditions and examine the behavior of the rupture.

### 9.6.1 Slip Rate and Hypocenter Location

In section 9.2.1 we claim that the combination of the large slip rates and the initial high apparent velocity of the rupture along the free surface allows the rupture to continue propagating at a faster speed along the ground

surface compared to the other portions of the rupture. We now demonstrate this phenomenon by changing the depth of the hypocenter (asperity) in order to vary the apparent velocity of the rupture as it hits the free surface. We consider three asperity locations by using the results from scenario sslithovar and selecting two new asperity locations.

### Initial Conditions

We maintain the same initial conditions and parameters from scenario sslithovar, and change the depth of the asperity as shown in figure 9.26. The parameters of the friction model follow the same depth variations, and we apply the same initial effective normal and shear tractions on the fault surface (see section 9.3.3 for the details).

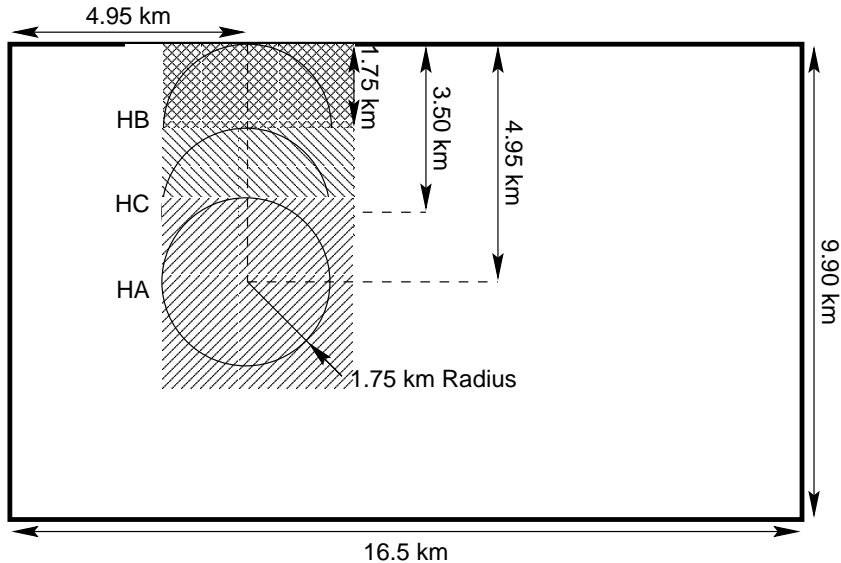


Figure 9.26: Diagram of starting asperity locations on the strike-slip fault. The asperity HA corresponds to the hypocenter location in figure 9.1.

### Characteristics of the Earthquakes

Placing the top of the asperity at the top of the fault (hypocenter HB) effectively eliminates the high apparent velocity along the free surface. As shown in figure 9.27, the maximum slip rates become nearly uniform with a slight tendency to increase as the rupture progresses; the large slip rates near the free surface disappear. The absence of the large slip rates near the surface prevents the rupture from propagating faster along the free surface, and the rupture propagates at a uniform speed of 1.9 km/sec. The average slip of 0.48 m closely matches that of scenario sslithovar, and we see some small variations in the distribution of final slip caused by the shift in the hypocenter.

Hypocenter location HC sits roughly halfway between hypocenter locations HA and HB. This creates a slower apparent rupture velocity along the ground surface when the rupture hits the ground surface compared

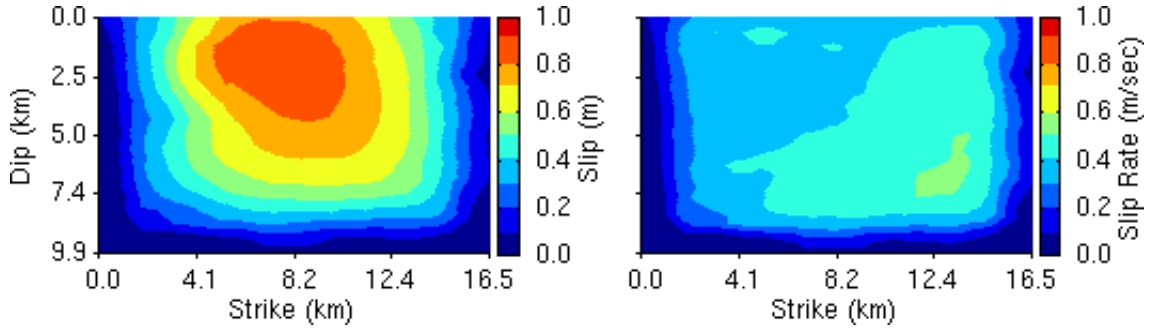


Figure 9.27: Distributions of final slip and maximum slip rate at each point on the strike-slip fault for the case with hypocenter location HB.

to scenario sslithovar. Figure 9.28 illustrates that we find a slight variation in the slip rates with depth. While the general shape of the distribution matches that of scenario sslithovar where the rupture speed and slip rates do vary with depth, the peak maximum slip rates remain near the level that we observe with hypocenter HB. As we expect based on the larger slip rates near the surface, the rupture propagates marginally faster near the free surface. Thus, as we increase the apparent velocity of the rupture along the free surface, the slip rates near the ground surface increase. This allows the portion of the rupture near the free surface to propagate faster than the portion of the rupture at depth.

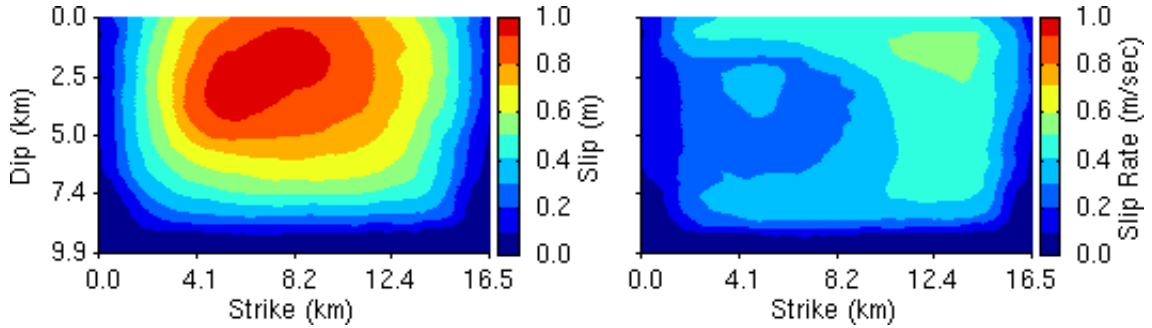


Figure 9.28: Distributions of final slip and maximum slip rate at each point on the strike-slip for the case with hypocenter location HC.

### 9.6.2 Bifurcation of the Rupture on a Long Fault

As noted in the previous sections, the variation of the slip rates with depth creates a similar variation in the rupture speed with depth. In section 9.2.1 we found that the rupture near the surface appears ready to overtake the rupture at depth just as the tapering in the initial shear tractions at the edge of the fault smothers the rupture. We use the homogeneous half-space model from the strike-slip fault in section 7.1 to discover how the rupture behaves when we allow the propagation to continue.

### Initial Conditions

We use the same homogeneous material properties and apply lithostatic effective normal tractions. Following the same procedure as in scenario `sslithovar`, we impose nominal shear tractions of 4.0 MPa and taper the shear tractions at the edges of the fault. In this case, we place the asperity used to initiate the rupture at a depth of 8.0 km. Figure 9.29 gives the distributions of the normal and shear tractions on the fault surface. The friction model corresponds to the one in scenario `sslithovar`.

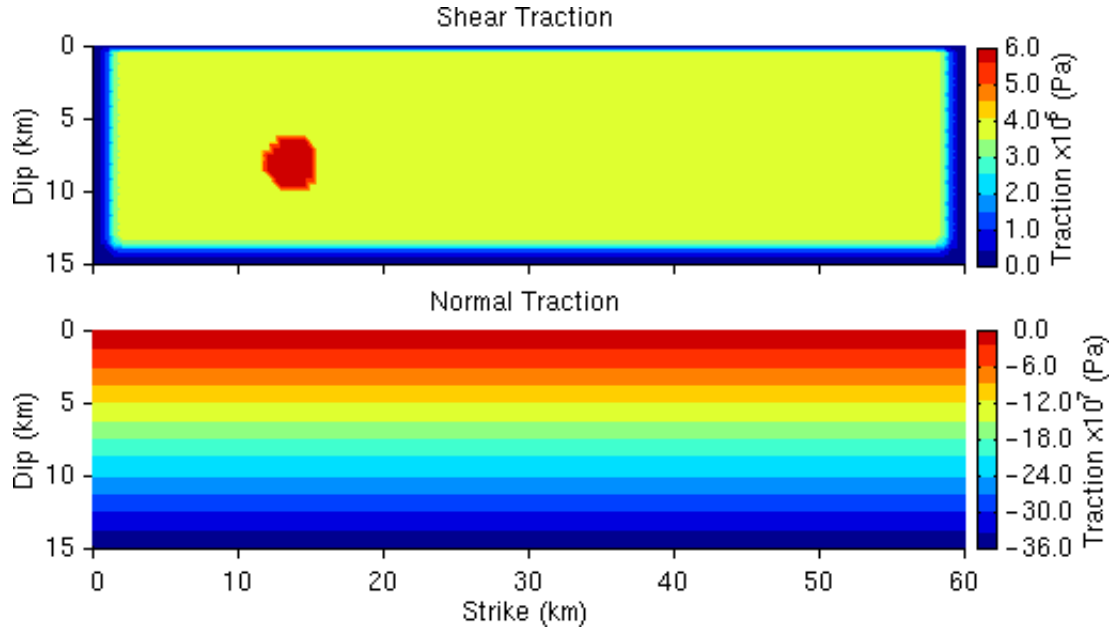


Figure 9.29: Shear and normal tractions on the fault surface of the large homogeneous half-space.

### Characteristics of the Earthquake

The snapshots of slip rate in figure 9.30 show that the rupture bifurcates as the rupture near the free surface passes the rupture at depth. The white ellipses identify the leading edge of the rupture that propagates at 2.2 km/sec (67% of the shear wave speed of 3.3 km/sec). When the rupture reflects off the free surface, we add a second white ellipse at 5.5 sec to coincide with the reflected portion of the rupture. We also add a purple ellipse at the leading edge of the portion of the rupture that propagates along the free surface at a speed of 4.4 km/sec. This speed lies between the shear wave speed of 3.3 km/sec and the dilatational wave speed of 5.7 km/sec. The rupture at the free surface begins to separate at 8.5 sec, and at 10 sec we see two distinct slip events at the free surface. We observe substantially larger slip rates where the two portions of the rupture constructively interfere (identified by the intersection of the white and purple ellipses). In general the portion of the rupture traveling near the dilatational wave speed generates larger slip rates than the portion traveling near the shear wave speed. Furthermore, as the two portions interact, the speed of the portion of the rupture that propagates near the shear wave speed increases to around 3.0 km/sec. The white ellipses we overlay on

the slip rate reflect this change in rupture speed.

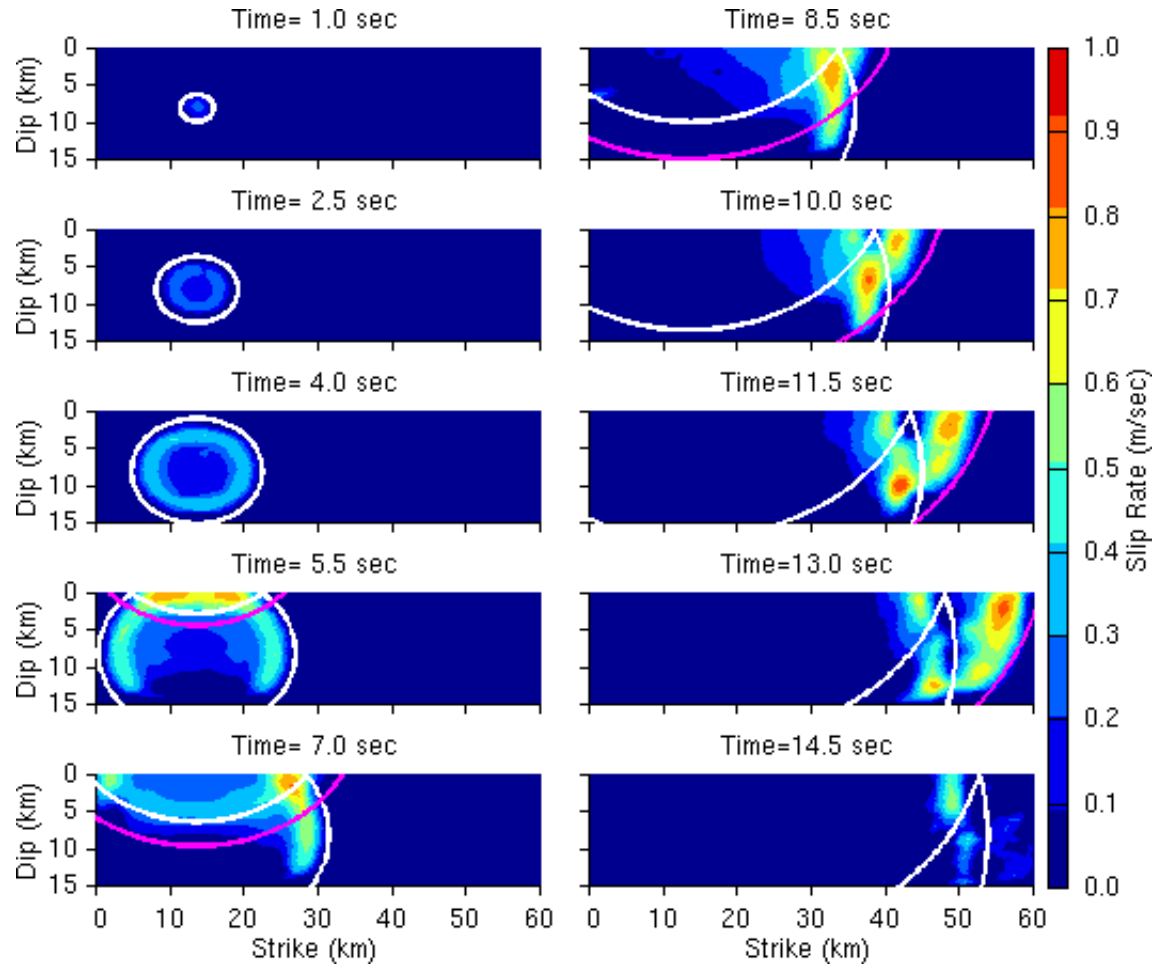


Figure 9.30: Snapshots of slip rate on the fault surface of the large homogeneous half-space. The white and purple ellipses indicate the leading edges of the ruptures propagating near the shear and dilatational wave speeds.

This complex rupture creates the smooth distribution of final slip shown in figure 9.31. The shape of the distribution roughly matches the one on the small strike-slip fault from scenario `sslithovar`. In contrast to the final slip, the maximum slip rate at each point on the fault surface reflects the complex nature of the rupture. The path of constructive interference between the two portions of the rupture is clearly visible with slip rates roughly 0.2 m/sec greater than the surrounding region. We also see large slip rates near the top of the fault at the north end that come from the faster portion of the rupture.

The faster portion of the rupture propagates at a speed between the shear wave speed and the dilatational wave speed, while the slower portion propagates at a speed slower than the shear wave speed. In earthquakes we observe ruptures propagating slower than the shear wave speed (Heaton 1990). However, using a Dugdale model of mode-II crack propagation, Burridge et al. (1979) found steady solutions for propagation at speeds both slower than the Rayleigh wave speed and between the shear speed and the dilatational wave speed. Based

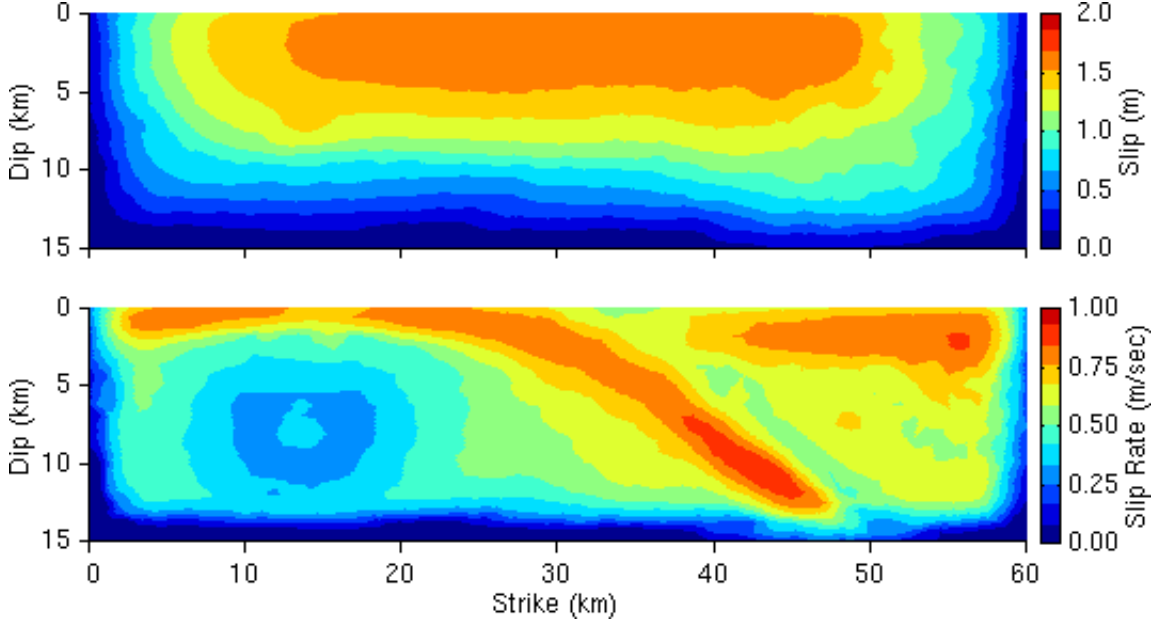


Figure 9.31: Distributions of final slip and maximum slip rate at each point on the fault surface for the large homogeneous half-space.

on the variation of the force with the propagation speed, they concluded that stable propagation occurred for mode-II cracks with speeds between  $\sqrt{2}$  times the shear wave speed and the dilatational wave speed. Furthermore, Rosakis et al. (1999) observed cracks propagating at  $\sqrt{2}$  times the shear wave speed in a brittle polyester resin under far-field loading. In our simulation the faster portion of the rupture propagates at approximately 1.3 times the shear wave speed, or within 6% of  $\sqrt{2}$  times the shear wave speed. We will examine the dynamic shear strain from a double couple to illustrate why shear ruptures may propagate both near the shear wave and the dilatational wave speeds.

We consider a vertically oriented double couple (an azimuth of 0 degrees, a dip angle of 90 degrees, and a rake angle of 0 degrees) in a whole-space as shown in figure 9.32. Note that in this particular case and this case only, we follow the convention used by Heaton (1979), and  $x_3$  is positive downwards. We want to compute the shear strain corresponding to pure lateral slip, i.e.,  $\varepsilon_{r\phi}$  using the spherical coordinates given in figure 9.32. Equation (9.14) (Heaton 1979) displays the pertinent displacements in spherical coordinates as a function of space and time.

$$u_r = \begin{cases} \frac{\beta^2 R_R}{4\pi\alpha^3} \left( \frac{\delta(t-\frac{R}{\alpha})}{R} - \frac{\alpha}{2R^2} + \frac{9\alpha^3 t^2}{2R^4} \right) & \frac{R}{\alpha} < t < \frac{R}{\beta} \\ \frac{1}{8\pi} \frac{3\lambda+5\lambda}{\lambda+2\mu} \frac{R_R}{R^2} & t > \frac{R}{\beta} \end{cases} \quad (9.14)$$

$$u_\phi = \begin{cases} \frac{\beta^2 R_\phi}{4\pi\alpha^2} \left( \frac{1}{R^2} + \frac{3\alpha^2 t^2}{R^4} \right) & \frac{R}{\alpha} < t < \frac{R}{\beta} \\ \frac{1}{4\pi} \left( \frac{\mu}{\lambda+2\mu} \frac{R_\phi}{R^2} + \frac{R_\phi \delta(t-\frac{R}{\beta})}{\beta R} \right) & t > \frac{R}{\beta} \end{cases} \quad (9.15)$$

where

$$\begin{aligned} R_R &= \sin^2 \theta \sin 2\phi \\ R_\theta &= \frac{1}{2} \sin 2\theta \sin 2\phi \\ R_\phi &= \sin \theta \cos 2\phi \end{aligned} \quad (9.16)$$

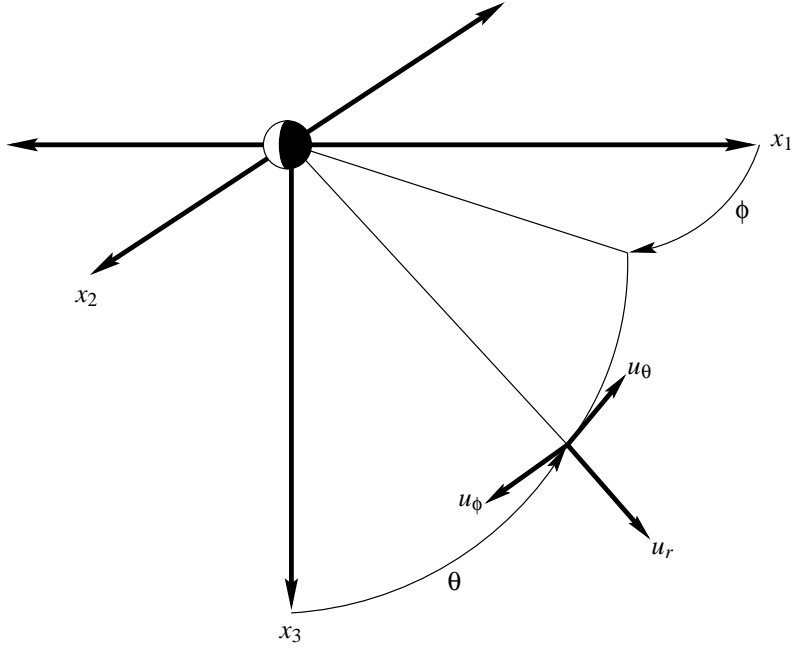


Figure 9.32: Orientation of spherical coordinates relative to a vertical double couple in a whole-space.

We want to compute the shear strain along the  $x_1$  axis, which for a vertical strike-slip fault lies on the fault in the direction of propagation. Using the definition of  $\varepsilon_{r\phi}$  in spherical coordinates,

$$\varepsilon_{r\phi} = \frac{1}{2} \left( \frac{1}{R \sin \theta} \frac{\partial u_r}{\partial \phi} + \frac{\partial u_\phi}{\partial R} - \frac{\partial u_\phi}{\partial R} \right), \quad (9.17)$$

and restricting the domain to the  $x_1$  axis where  $\theta = \frac{\pi}{2}$  and  $\phi = 0$ , we find that equation (9.18) gives the lateral shear strain as a function of space and time, where  $\delta'$  denotes the derivative of the Dirac delta function.

$$\varepsilon_{r\phi} = \begin{cases} \frac{\beta^2}{4\pi\alpha^3 R^2} \left( \delta(t - \frac{R}{\alpha}) - \frac{2\alpha}{R} - \frac{3\alpha^3 t^2}{R^3} \right) & \frac{R}{\alpha} < t < \frac{R}{\beta} \\ \frac{1}{8\pi R^3} \left( \frac{3\lambda+2\mu}{\lambda+2\mu} \right) - \frac{1}{4\pi\beta R^2} \delta(t - \frac{R}{\beta}) + \frac{1}{8\pi\beta^2 R} \delta'(t - \frac{R}{\beta}) & t > \frac{R}{\beta} \end{cases} \quad (9.18)$$

We find Dirac delta functions in the shear strain propagating at both the dilatational and shear wave speeds. This implies the shear strain may cause a dislocation to propagate near the dilatational and shear wave speeds in the direction of slip on a vertical strike-slip fault.

## 9.7 Discussion

### 9.7.1 Modeling of Dynamic Failure

Including the frictional sliding on the fault surface in the simulation allows the dynamics of the rupture to determine the speed of the rupture and the slip distribution. This prevents combining physically unrealistic combinations of slip rate and rupture speed, which is possible when we use prescribed ruptures. The dynamic ruptures also illustrate the dependence of the rupture speed on the direction of propagation. Including this effect in prescribed ruptures on strike-slip faults will lead to minimal changes in behavior, but the effect becomes more dramatic on thrust faults, which we will demonstrate in chapter 10. Additionally, the use of the slip degrees of freedom to model the dislocation across the fault surface allows simulating earthquakes with dynamic failure on any arbitrarily oriented fault plane. We find only small differences in the rupture behavior when we use the slip-weakening friction model and increase the resolution of the mesh by a factor of two from the size based on the wave propagation. Therefore, with appropriate selection of the failure stress and fracture energy, we may base the discretization size on accurate modeling of the wave propagation.

### 9.7.2 Effective Normal Stresses

In order to create realistic ruptures with effective normal stresses that increase with depth, the absolute change in the coefficient of friction during slip must decrease with depth. We assume a nearly uniform minimum sliding stress with depth, which implies a uniform relative variation of the coefficient of friction with depth. This generates ruptures with behaviors that closely match those produced by assuming uniform effective normal stresses and no variations in the friction model parameters with depth. In other words, with realistic initial conditions (effective normal stresses that increase with depth) we can produce ruptures with behaviors similar to those with unrealistic initial conditions (uniform effective normal stresses). This may explain why researchers, such as Olsen et al. (1997) and Ben-Zion and Andrews (1998), who use uniform effective normal stresses are able to create ruptures with realistic behavior.

The strongest support for the increase in the effective normal stress with depth comes from the examination of inclined faults. The tectonic stresses generate both shear and normal stresses on the fault surface. If we assume pore pressures near the lithostatic stresses, then the dominant contribution of the effective normal stresses comes from the tectonic stresses. For our thrust fault with a dip angle of 35 degrees, this implies the effective normal stresses are less than 3 MPa. Furthermore, as we decrease the dip angle of the fault from 90 degrees and keep the shear tractions constant, the effective normal stresses go to zero. To maintain the same failure stresses we must scale the coefficient of friction parameters accordingly. For example, in order to use the friction model from the strike-slip fault on the thrust fault, we scale the coefficient of friction by a factor of 3.7.

On the other hand, assuming negligible pore pressures (the argument applies equally well for hydrostatic

pore pressures) generates effective normal stresses that increase with depth and dominate the normal stresses created by the tectonic stresses. Consequently, changing the dip angle of the fault while keeping the shear tractions constant causes almost no variations in the effective normal stresses. We do not need to alter the parameters in the friction model to keep the failure stresses the same. Hence, we may use the same friction model on both strike-slip and the thrust faults. It seems much more realistic to be able to apply a friction model to any arbitrarily oriented fault plane, than to have to scale the parameters for every change in the dip angle of the fault. Thus, the simulations on the strike-slip fault and thrust fault confirm that it is more realistic to assume that the effective normal stresses increase with depth than remain uniform.

### 9.7.3 Friction Models

The fracture energy plays a critical role in the behavior of the rupture. We control the fracture energy through the rate of decrease in the coefficient of friction at the onset of sliding. When we allow the coefficient of friction to decrease instantaneously from the static value to a dynamic value in the two-phase friction model, the rupture propagates near the dilatational wave speed. The sharp initiation of slip also introduces high frequencies in the solution and the mesh resolution is too coarse to accurately capture the behavior. We adjust the fracture energy to manipulate the maximum slip rate and rupture speed. As we increase the fracture energy, the maximum slip rates and rupture speed decrease; continuing to increase the fracture energy ultimately leads to ruptures that fail to propagate.

The ruptures exhibit the same general behavior for the slip-weakening, slip- and rate-weakening, and shear melting-refreezing friction models. The slip-weakening friction model does not allow the re-strengthening of the shear stress on the fault as the slip rates decrease that we find in the slip- and rate-weakening and the shear melting-refreezing friction models. For ruptures with the same average slip, we must use larger dynamic stress drops with the slip- and rate-weakening and shear melting-refreezing friction models to generate the same slip. Consequently, the maximum slip rates increase slightly compared to when we use the slip-weakening friction model. The coefficient of friction in the shear melting-refreezing model depends on the history of the slip rate, while both the slip-weakening and slip- and rate-weakening models are path independent. At locations on the fault with relatively larger slip rates, this creates larger slips in the simulation with the shear melting-refreezing model than in the simulation with the slip- and rate-weakening friction model. For comparable average slip distributions the ground motions associated with the friction models with shear re-strengthening show excellent agreement and exhibit slightly greater maximum velocities than those associated with the slip-weakening friction model.

### 9.7.4 Effect of Free Surface

When the rupture hits the free surface, it encounters a reduced resistance to slip. In many cases the rupture will reflect off the free surface and generate additional slip on the portion of the fault below the free surface.

As we move the hypocenter to greater depths, the rupture hits the ground surface with less curvature. This causes a longer portion of the rupture front to arrive at the free surface in a shorter period of time and creates a high apparent velocity along the ground surface. Consequently, the slip rates increase and the rupture may sustain a super-shear propagation speed along the surface. On a long fault this leads to bifurcation of the rupture into a portion propagating near the dilatational wave speed and a portion propagating near the shear wave speed. While the portion propagating near the dilatational wave speed appears feasible, we do not observe such phenomenon for real earthquakes. The real earth includes variations in the material properties with depth which these models do not. This could explain why we do not observe ruptures propagating faster than the shear wave speed in the real earth.

## Chapter 10 Dynamic Failure in a Layered Half-Space

Armed with our knowledge of how to create relatively realistic ruptures with dynamic failure on faults in a homogeneous half-space, we study dynamic failure on faults in a layered half-space. We use the finite-element models of the strike-slip and thrust fault domains from the prescribed rupture simulations discussed in chapter 7. We focus on creating ruptures in the layered half-space that generally match the prescribed ruptures. Additionally, we examine the sensitivity of the ground motion to variations in the initial tractions and the friction models and identify the characteristics of the dynamic ruptures that differ from our prescribed ruptures.

### 10.1 Strike-Slip Fault

Section 7.1 gives a complete description of the geometry of the domain and the strike-slip fault. Instead of using the inertial bisection method to partition the meshes, for improved performance we switch to the METIS library (see section 3.2 for a discussion of both methods). The improved load balancing among the processors reduces the execution time without altering the solutions. Figure 10.1 illustrates the partitioning of the coarse mesh among 16 processors. Each simulation took 5.6 hours using 16 processors of the Hewlett Packard Exemplar at the CACR.

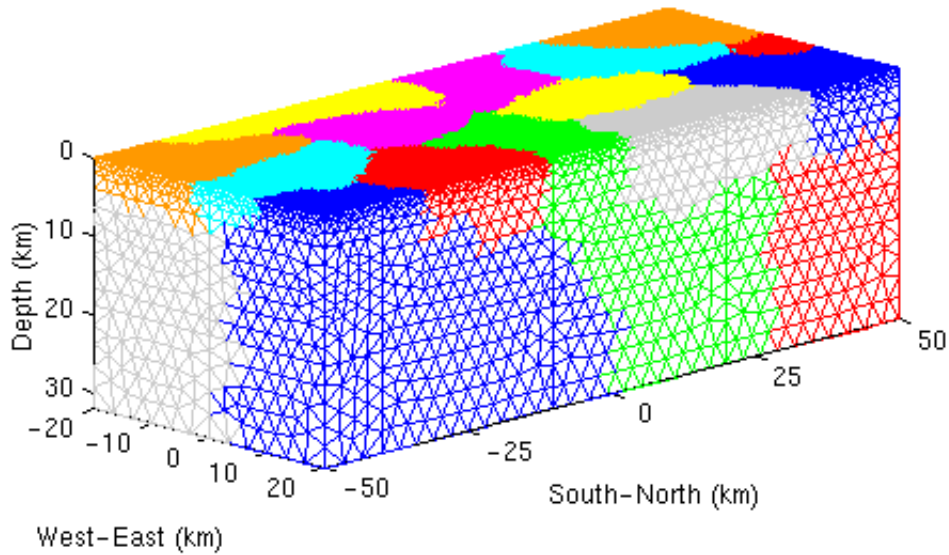


Figure 10.1: Partitioning of the coarse finite-element model among sixteen processors for the layered half-space using the METIS library. Each color patch identifies the elements of one processor.

### 10.1.1 Earthquake Source Parameters

We follow the same procedures that we use for the dynamic failure simulations in the homogeneous half-space (see section 9.3.3) to determine the initial shear and normal tractions on the fault surface. For each scenario we assume that the pore pressures are negligible and apply lithostatic effective normal tractions. We want to compare the ground motions from these simulations, which use dynamic failure, to the ones in chapter 7, which use prescribed ruptures, so we aim for an average slip of 2.0 m. The distribution of the initial shear tractions with depth depends on whether we assume uniform tectonic stresses or uniform tectonic strains. Additionally, using the slip- and rate-weakening friction model or the melting-refreezing friction model, as opposed to the slip-weakening friction model, requires a larger dynamic stress drop to generate the same average slip. Thus, we will discuss the details of the shear tractions on the fault surface on a case by case basis.

### 10.1.2 Uniform Stress Versus Uniform Strain

We continue to generate the initial stress distribution on the fault based on intuition and some degree of trial and error. With the variations in the material properties with depth in the layered half-space, uniform tectonic stresses create a substantially different distribution of shear tractions on the fault than uniform tectonic strains. We evaluate both cases to determine which generates a more realistic rupture.

#### Uniform Stress: Scenario unistress

We need to determine the nominal initial shear tractions on the fault surface. Equation (9.1) gives the approximate average stress drop for a strike-slip fault in a homogeneous Poissonian half-space. Below a depth of 6.0 km, the material properties on the fault surface are nearly uniform, so we use the shear modulus from a depth of 6.0 km in equation (9.1). Applying this equation with an average slip of 2.0 m and our fault dimensions yields an average stress drop of 2.5 MPa. The recovery of the coefficient of friction upon termination of sliding means that the dynamic stress drop will exceed the average stress drop. Consequently, based on a test simulation with the homogeneous half-space, we impose a maximum dynamic stress drop of 4.5 MPa. We assume that some residual shear stresses remain on the fault after the earthquake, so we impose an initial shear stress of 6.0 MPa. At the lateral edges of the fault, we taper the initial shear tractions to smother the rupture. Figure 10.2 gives the initial shear and normal tractions that we apply to the fault surface. For this scenario the asperity that initiates the rupture has a radius of 1.8 km and sits 8.0 km below the ground surface and 14 km north of the south end of the fault. In order to prevent the effective normal stress from vanishing at the ground surface, we apply uniform axial stresses of 2.0 MPa in the east-west direction.

We set the parameters of the slip-weakening friction model based on our knowledge of creating realistic ruptures in a homogeneous half-space. We assume that the relative change in the coefficient of friction as a function of slip, i.e., the relative difference between  $\mu_{max}$  and  $\mu_{min}$ , does not vary with depth. In the strike-slip

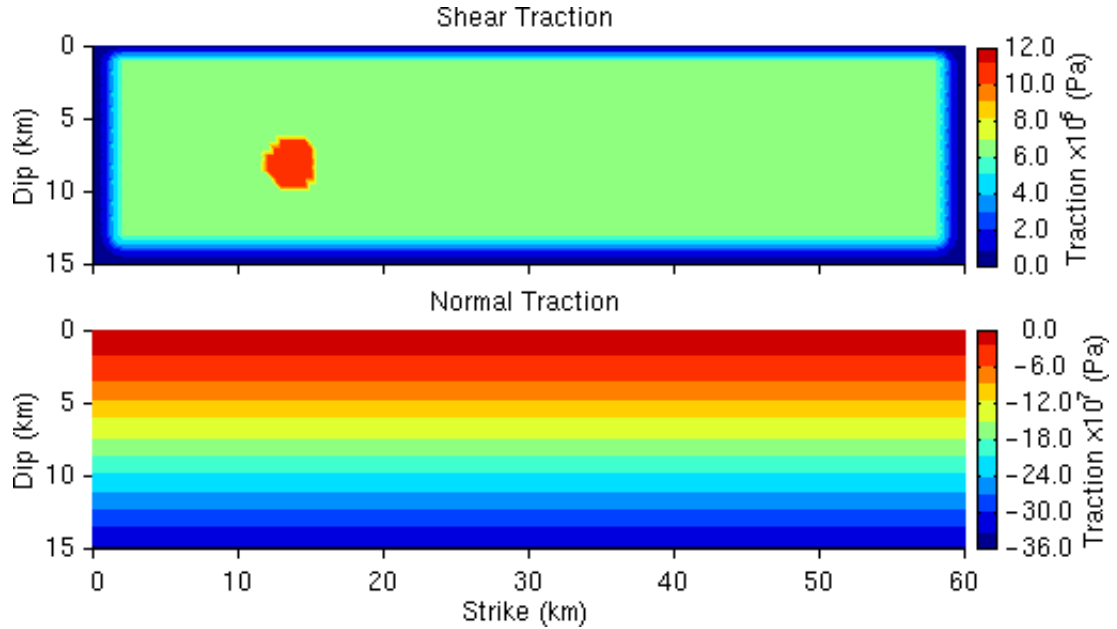


Figure 10.2: Shear and normal tractions on the strike-slip fault for scenario unistress.

simulations with the homogeneous half-space, outside the asperity that starts the rupture, we use a distance from failure equal to the maximum dynamic stress drop (see section 9.2.1). Applying the same strategy here gives nominal failure stresses of 10.5 MPa.

With the variations of the material properties with depth, we cannot match the distance from failure over the entire depth of the fault. As a result, we choose to match (in an average sense) the distance from failure over the depth range of 6.0 km to 15.0 km, where the material properties remain relatively uniform. We determine the parameters in the friction model based on our selections of the maximum dynamic stress drop and the distance from failure. Equation (10.1) gives the functional forms of the parameters in the friction model and figure 10.3 shows the parameters of the slip-weakening friction model as a function of depth. We clip the values above a depth of 1.0 km to prevent the values from approaching infinity at the ground surface. In order for the fracture energy to remain nearly uniform, we modify the characteristic slip distance in the softer material near the ground surface from its uniform value at depth. We denote this friction model by the label litholayeruf.

$$\begin{aligned}
\mu_{max} &= \begin{cases} 0.499 & z > -1.0 \text{ km} \\ -\frac{0.499m}{z} & z < -1.0 \text{ km} \end{cases} \\
\mu_{min} &= \begin{cases} 0.0713 & z > -1.0 \text{ km} \\ -\frac{0.0713m}{z} & z < -1.0 \text{ km} \end{cases} \\
D_o &= \begin{cases} 0.227m + 1.86 \times 10^{-5}z & z > -6.0 \text{ km} \\ 0.338m & z < -6.0 \text{ km} \end{cases}
\end{aligned} \tag{10.1}$$

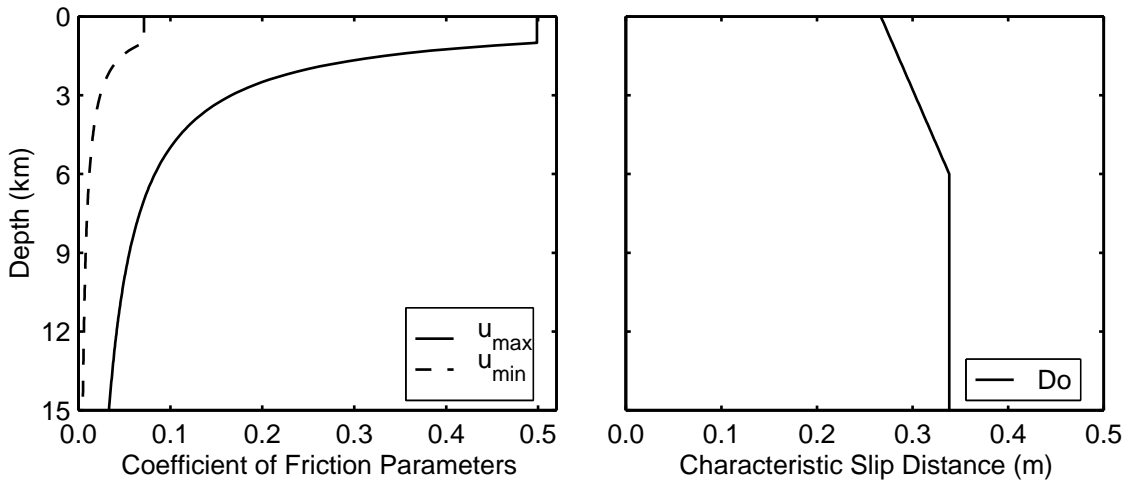


Figure 10.3: Parameters of the slip-weakening I friction model, litholayeruf, as a function of depth.

Figure 10.4 gives the initial shear stresses, the shear stresses at failure, and the minimum sliding stresses as a function of dip on the fault. The minimum sliding stresses exhibit very little variation with depth except in the top 1.0 km where we clip the parameters in the friction model. The figure displays the initial shear stresses through the center of the asperity that initiates the rupture. Outside the asperity and away from the edges of the fault, we apply uniform initial shear stresses. The decrease in density near the ground surface causes the effective normal stresses to decrease rapidly approaching the ground surface. Consequently, the failure stresses decrease as does the distance from failure.

The reduced distance from failure in the softer material in the top 6.0 km of the domain allows the rupture to propagate at 4.9 km/sec. The rupture bifurcates towards the end of the rupture, but not to the same degree that we found in the homogeneous half-space (see section 9.6.2). Additionally, the reduced distance from failure leads to final slips (figure 10.5) exceeding 6.0 m over much of the top five kilometers of the fault with a maximum final slip of over 11 m. We also find maximum slip rates greater than 3.0 m/sec in the top two to three kilometers of the fault with a peak maximum slip rate of 11 m/sec. The distribution of the maximum slip rate in figure 10.5 displays relatively larger values along the path of constructive interference of the two portions of the rupture. We find this same interference in the large homogeneous half-space (see figure 9.31).

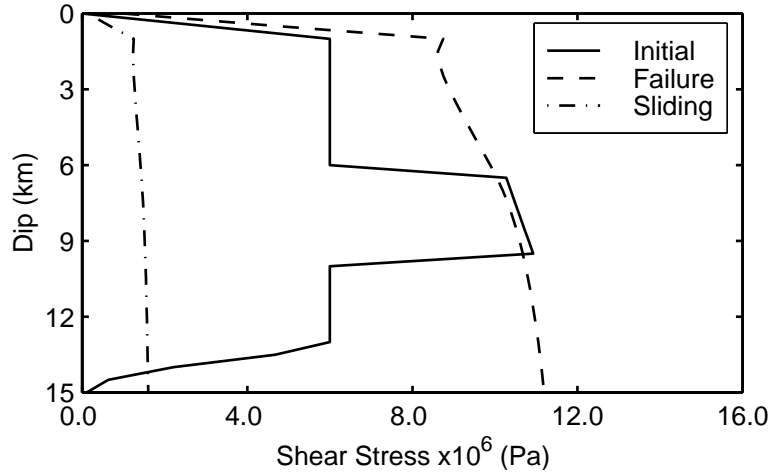


Figure 10.4: Initial, failure, and minimum sliding shear stresses through the center of the asperity on the strike-slip fault as a function of dip for scenario unistress.

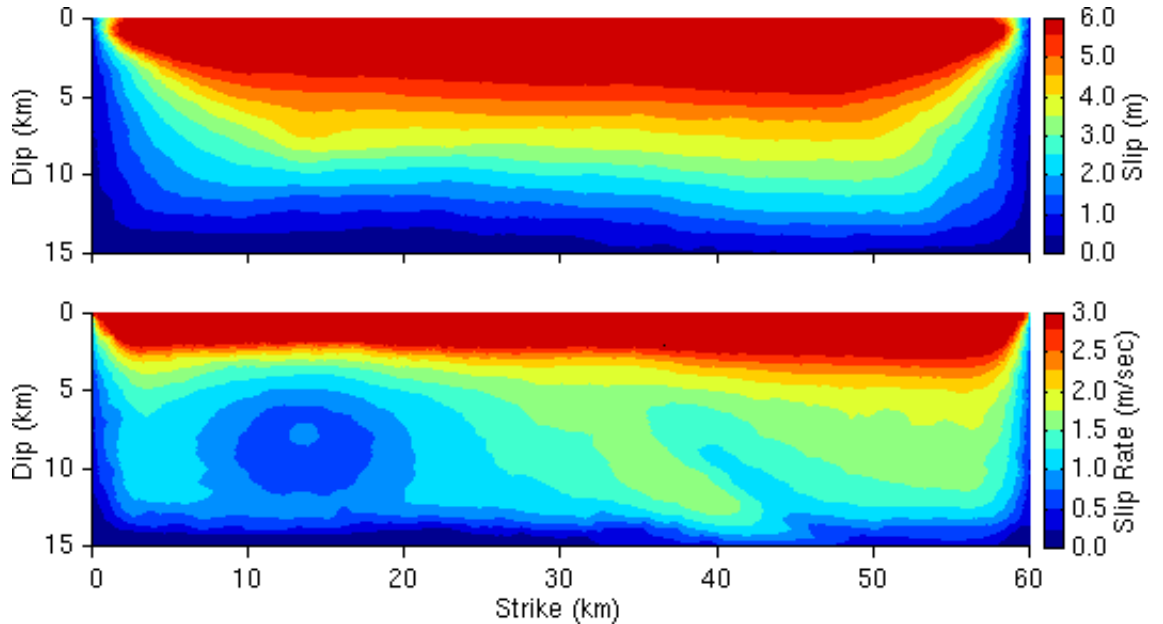


Figure 10.5: Distributions of final slip and maximum slip rate at each point on the strike-slip fault for scenario unistress.

### Uniform Strain: Scenario unistrain

In scenario unistrain we determine the nominal initial shear tractions on the fault surface based on application of uniform tectonic shear strains. We select shear strains that produce the desired shear tractions of approximately 6.0 MPa below a depth of 6.0 km where the material properties are nearly uniform. In order to prevent the effective normal stress from vanishing at the ground surface, we also apply uniform axial strains in the east-west direction. Equation (10.2) gives the strain field used to generate the shear and normal tractions that we apply on the fault surface (figure 10.6).

$$\begin{aligned}
\epsilon_{xx} &= -2.93 \times 10^{-5} \\
\epsilon_{yy} = \epsilon_{zz} &= 7.25 \times 10^{-6} \\
\epsilon_{xy} &= 1.10 \times 10^{-4} \\
\epsilon_{yz} = \epsilon_{xz} &= 0
\end{aligned} \tag{10.2}$$

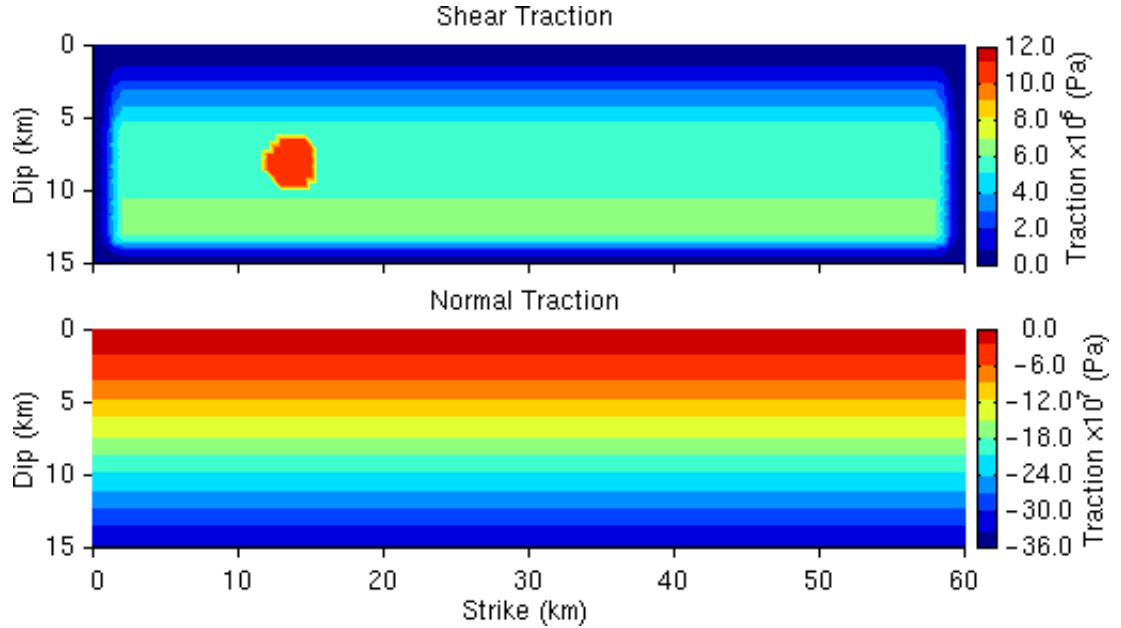


Figure 10.6: Shear and normal tractions on the strike-slip fault for scenario unistrain.

We continue to use the litholayeruf friction model from scenario unistress. Figure 10.7 shows that this leads to the same relatively uniform distribution of sliding stresses with depth as those in scenario unistress. The initial shear stresses reflect the decrease in the shear modulus in the softer material in the top 6.0 km of the domain. In contrast to the variations of the shear stresses at failure in scenario unistress, the shear stresses at failure in scenario unistrain decrease gradually from the bottom of the fault up to a depth of 1.0 km, where we clip the coefficient of friction parameters. Two of the undesirable features of scenario unistress (figure 10.4) that we successfully eliminate in scenario unistrain (figure 10.7) include: the uniform maximum dynamic stress drop and the decrease in the distance from failure in the softer material near the top of the fault.

The rupture propagates across the fault with a nearly uniform speed of 2.9 km/sec. The distribution of the final slip in figure 10.8 exhibits little variation; we find the usual tapering at the edges of the fault and only a small peak located where the asperity initiated the rupture. The maximum slip rate shows a slight tendency to increase as the rupture propagates, which allows the rupture to penetrate into progressively shallower depths. The large distance from failure at shallow depths prevents the rupture from reaching the top of the fault.

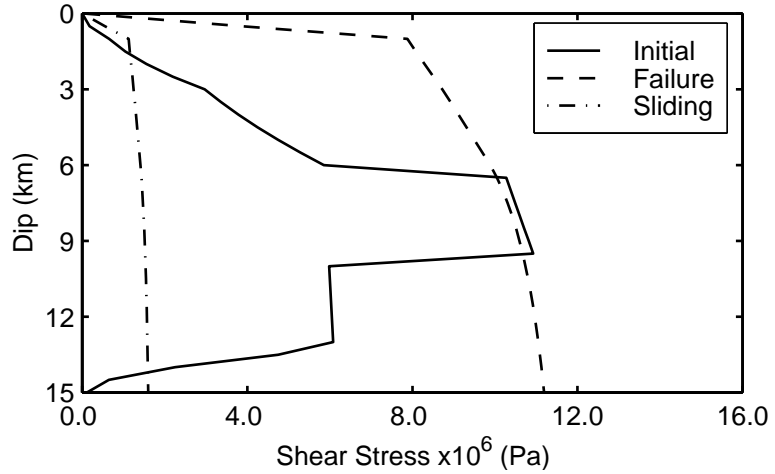


Figure 10.7: Initial, failure, and minimum sliding shear stresses through the center of the asperity on the strike-slip fault as a function of dip for scenario unistrain.

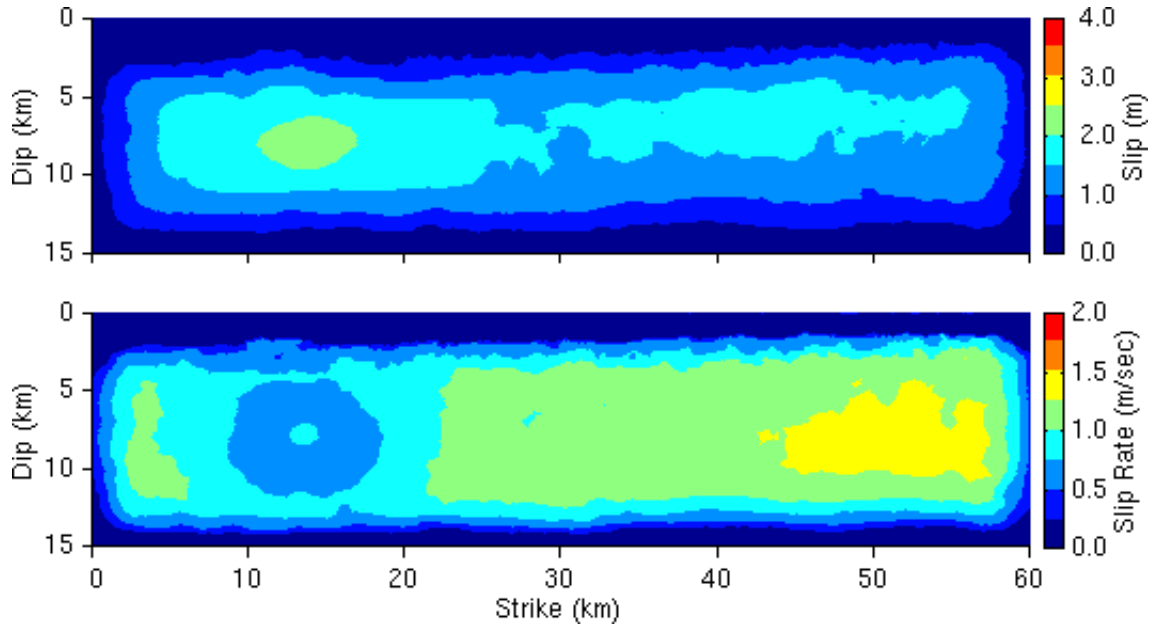


Figure 10.8: Distributions of final slip and maximum slip rate at each point on the strike-slip fault for scenario unistrain.

Comparing the characteristics of this scenario (unistrain) with those from scenario unistress, where we apply a uniform stress, we find that this rupture appears more realistic. The excessive final slip and maximum slip rates near the surface disappear, creating relatively uniform distributions of final slip and maximum slip rate. Additionally, the rupture propagates at 88% of the local shear wave speed. The rupture does not propagate to the ground surface, and we consider this the only prominent feature of the scenario that seems unrealistic.

### 10.1.3 Variation of Friction Parameters with Material Properties

The parameters in the litholayer friction model do not change with the variations in the material properties; they change only with depth. Based on the inability of the rupture to reach the ground surface in scenario unistain, it seems logical to make the parameters in the friction model a function of the material properties as well as depth. We want to create a relatively uniform slip distribution with depth where the material properties change with depth, and the effective normal stresses increase with depth.

The change in stress at a point on the fault varies proportionally with the shear modulus and the slip,

$$\Delta\sigma = C_1\mu D. \quad (10.3)$$

The change in stress is also the difference between the initial shear stress,  $\sigma_0$ , and the final shear stress,  $\sigma_1$ . We assume that we derive the initial shear stress from a uniform strain field, which gives

$$\sigma_0 = C_2\mu. \quad (10.4)$$

For the final shear stress, we use the minimum sliding shear stress,

$$\sigma_1 = \mu_{min}\sigma_n. \quad (10.5)$$

Combining these equations, substituting in the expression for the shear modulus ( $\mu = \rho\beta^2$ ), and solving for the minimum coefficient yields

$$\mu_{min} = \frac{(C_1D - C_2)\rho\beta^2}{\sigma_n}. \quad (10.6)$$

We now consider four cases of how the mass density, shear wave speed, and normal stress vary with depth.

1. If the mass density, shear wave speed, and normal stress are all uniform with depth, then for uniform slip we want a uniform minimum coefficient of friction. This coincides with the simplistic case of uniform normal stress in the homogeneous half-space that we examined in chapter 9.
2. If the mass density and shear wave speed are uniform with depth, and the normal stress varies linearly with depth (due to the overburden pressure), then we want a minimum coefficient of friction that varies inversely with depth. This matches the reasoning that we use to derive the depth dependence of the coefficient of friction for the homogeneous half-space in chapter 9.
3. If the mass density is uniform, and the shear wave speed and normal stress increase linearly with depth, then we want a minimum coefficient of friction that varies linearly with depth. This corresponds to a layered half-space where the shear wave speed is proportional to the depth, but the mass density is

relatively uniform with depth.

4. If the mass density and shear wave speed vary linearly with depth, and the normal stress varies with the depth squared, then we again want the minimum coefficient of friction to vary linearly with the depth. This corresponds to a layered half-space where both the shear wave speed and the mass density are proportional to the depth.

Our layered half-space follows neither of the last two cases. Near the surface it roughly matches the last case, but the material properties become relatively uniform below a depth of 6.0 km. Because the mass density and shear wave speed do not vanish at the ground surface, they actually vary slower than that predicted by a simple proportionality. As a result, we find that we achieve a desirable distribution of slip (as predicted from equation (10.6)) by making the coefficient of friction proportional to either the ratio of the square root of the shear modulus to the depth or the ratio of the shear wave speed to the depth.

Figure 10.9 gives the normalized slip distribution predicted by equation (10.7) for three different variations of the coefficient of friction: the coefficient of friction depends on the inverse of the depth, the coefficient of friction depends on the ratio of the square root of the shear modulus to the depth, and the coefficient of friction depends on the ratio of the shear wave speed to the depth. We use the effective normal stresses from scenario unistrain and select values of  $C_1$  and  $C_2$  to create normalized slips between approximately -1 and 1.

$$D = \frac{1}{C_1} \left( C_2 + \frac{\mu_{min}\sigma_n}{\mu} \right) \quad (10.7)$$

The negative slip values indicate that slip at that depth leads to a local increase in the shear stress on the fault. Smaller normalized slips indicate a reduced preference for slip to occur. We see that varying the coefficient of friction inversely with the depth tends to retard slip near the surface, which matches our observations from scenario unistrain. Adding dependence on the square root of the shear modulus or the shear wave speed shifts the preference in slip towards a more uniform distribution with depth.

We choose to vary the coefficient of friction with the quotient of the square root of the shear modulus and the depth, because based on equation (10.7) it gives the most uniform distribution of normalized slip with depth. We apply the dependence on the square root of the shear modulus to the characteristic slip distance to create a relatively uniform fracture energy. Equation (10.8) gives the functional forms of the parameters in the friction model, and figure 10.10 displays the variations of the parameters in the friction model with depth in the layered half-space. We denote this friction model by the label litholayeruf2.

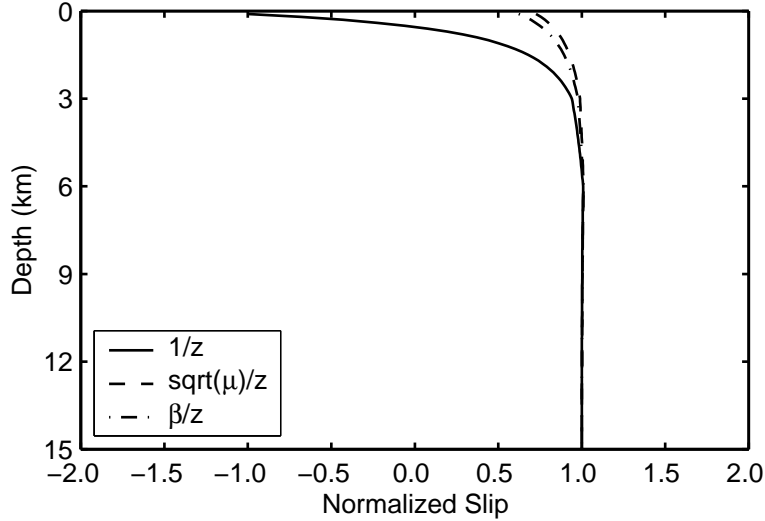


Figure 10.9: Normalized slip with depth for three different variations of the coefficient of friction with depth and material properties.

$$\begin{aligned}
 \mu_{max} &= \begin{cases} 0.164 & z > -1.0 \text{ km} \\ -3.02 \times 10^{-3} \left( \frac{\text{m}^3 \text{sec}^2}{\text{kg}} \right)^{\frac{1}{2}} \frac{\sqrt{\mu}}{z} & z < -1.0 \text{ km} \end{cases} \\
 \mu_{min} &= \begin{cases} 0.0235 & z > -1.0 \text{ km} \\ -4.31 \times 10^{-4} \left( \frac{\text{m}^3 \text{sec}^2}{\text{kg}} \right)^{\frac{1}{2}} \frac{\sqrt{\mu}}{z} & z < -1.0 \text{ km} \end{cases} \\
 D_o &= \begin{cases} 0.111 \text{ m} & z > -1.0 \text{ km} \\ -2.04 \times 10^{-6} \left( \frac{\text{m}^3 \text{sec}^2}{\text{kg}} \right)^{\frac{1}{2}} \sqrt{\mu} & z < -1.0 \text{ km} \end{cases} \quad (10.8)
 \end{aligned}$$

We apply the initial shear and normal tractions from scenario unistrain. This gives the distributions of the initial, failure, and sliding stresses shown in figure 10.11 on the vertical line through the center of the asperity. The shapes of the shear stresses at failure and the minimum sliding stresses more closely match the shapes of the initial shear stresses compared to those from scenarios unistress and unistrain. At each depth the maximum dynamic stress drop generally matches the distance from failure. Our homogeneous half-space simulations with dynamic failure that produce realistic ruptures contain this precise feature. Additionally, the dynamic stress drop closely follows the variations of the shear modulus that increases linearly in the top 6.0 km and is nearly uniform below 6.0 km.

The snapshots of slip rate on the fault surface in figure 10.12 show that the rupture propagates all the way to the ground surface. Before the rupture hits the ground surface, the rupture propagates at about 2.5 km/sec, and after hitting the ground surface the rupture maintains a speed of 3.0 km/sec at a depth of 6.0 km. We attribute the change in the rupture speed to the increase in the maximum slip rates as the rupture approaches

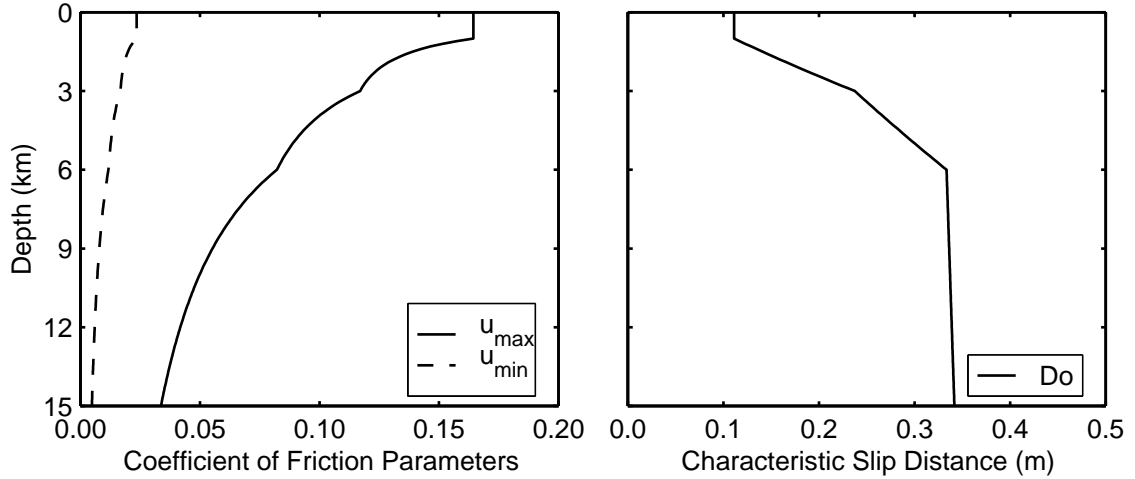


Figure 10.10: Parameters of the slip-weakening I friction model, litholayeruf2, as a function of depth in the layered half-space.

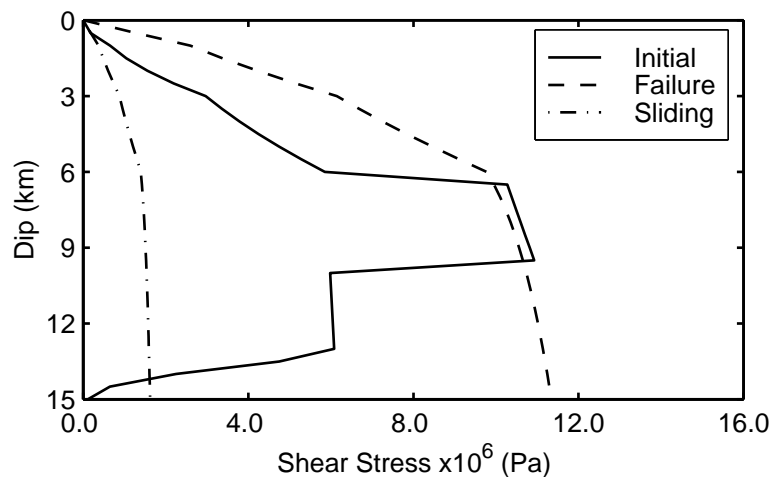


Figure 10.11: Initial, failure, and minimum sliding shear stresses through the center of the asperity on the strike-slip fault as a function of dip for scenario unistrain2.

the ground surface and encounters a reduction in the stiffness. The rupture reflects off the ground surface, but this second slip event soon disappears. As in scenario unistrain, the rupture does not bifurcate and propagates slower than the local shear wave speed. The average slip of 1.9 m nearly matches our target value of 2.0 m from the prescribed ruptures. The moment magnitude of the event is 6.9. We compute an average stress drop of 1.4 MPa which falls short of the 2.5 MPa average stress drop predicted by equation (9.1). The presence of the softer material in the top 6.0 km of the domain reduces the average stress drop relative to the same average slip in a homogeneous half-space. This causes a deviation in the relationship between the average stress drop and the product of the shear modulus and the average slip from the one given by equation (9.1), which applies to homogeneous Poissonian half-spaces.

Figure 10.13 shows the distributions of the final slip and maximum slip rate on the fault surface. The

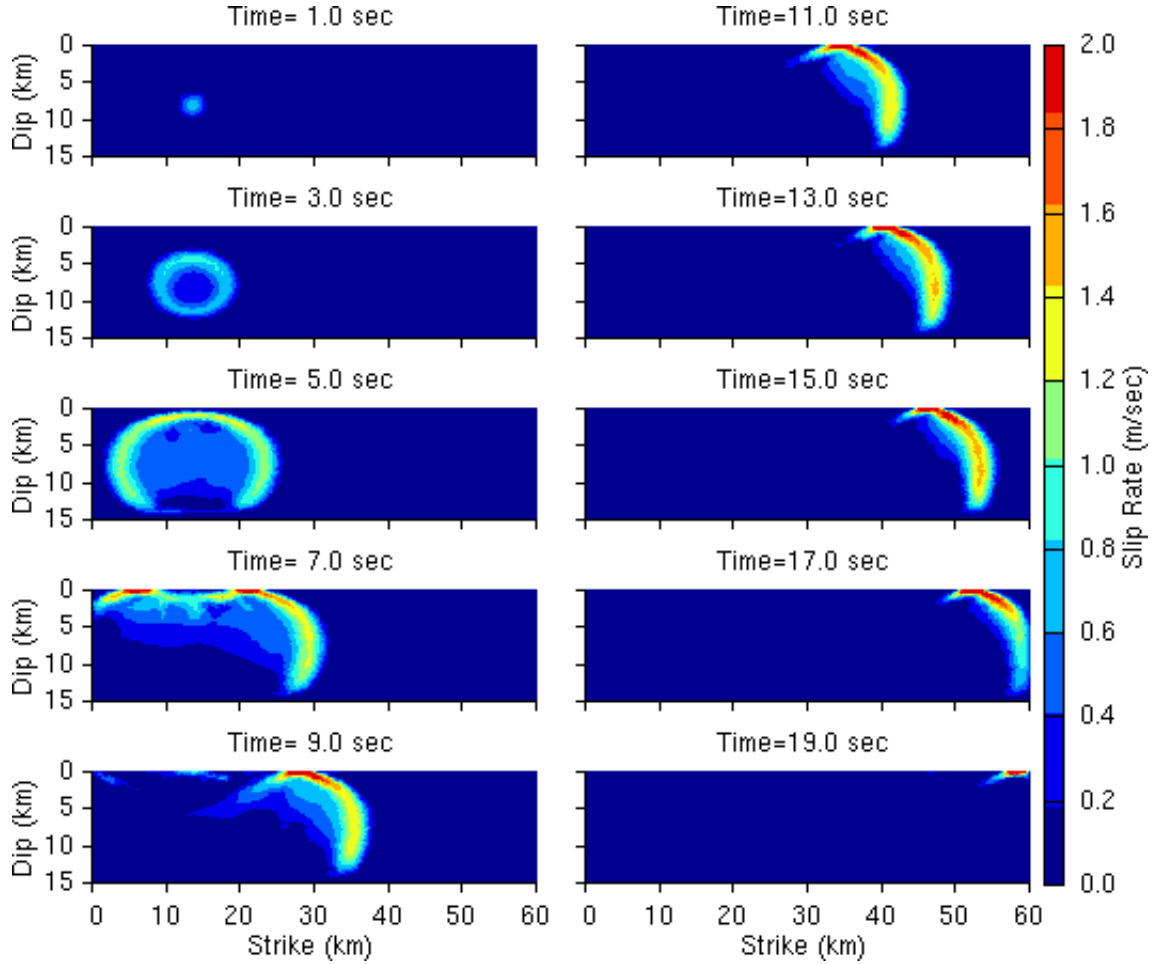


Figure 10.12: Snapshots of slip rate on the strike-slip fault for scenario unistrain2.

region where the final slip exceeds 3.0 m coincides with the locations that are subjected to the second slip event associated with the reflection of the rupture off the ground surface. This appears to distort the final slip from a more uniform distribution. The distribution of the maximum slip rate displays the features that we expect based on the snapshots of slip rate. We find the maximum slip rates near the surface are about 0.5 m/sec greater than the maximum slip rates at depth. The tendency for the maximum slip rate to increase as the rupture propagates causes this region of larger slip rates at the surface to progressively increase in size. The increases in the slip rates are small, and the maximum slip rates increase by less than 0.25 m/sec over a distance of 25 km.

We now evaluate the level of the shear stresses on the fault during sliding. Recall that by appropriate scaling of the initial, failure, and sliding shear stresses (see section 8.1.2), we may change the sliding stresses without any changes in the rupture behavior. This means the observed rupture behavior and ground motions do not constrain the sliding stresses. However, using equation (4.10) we may compute the change in temperature at each point on the fault. Few faults contain glassy material that would indicate frictional melting

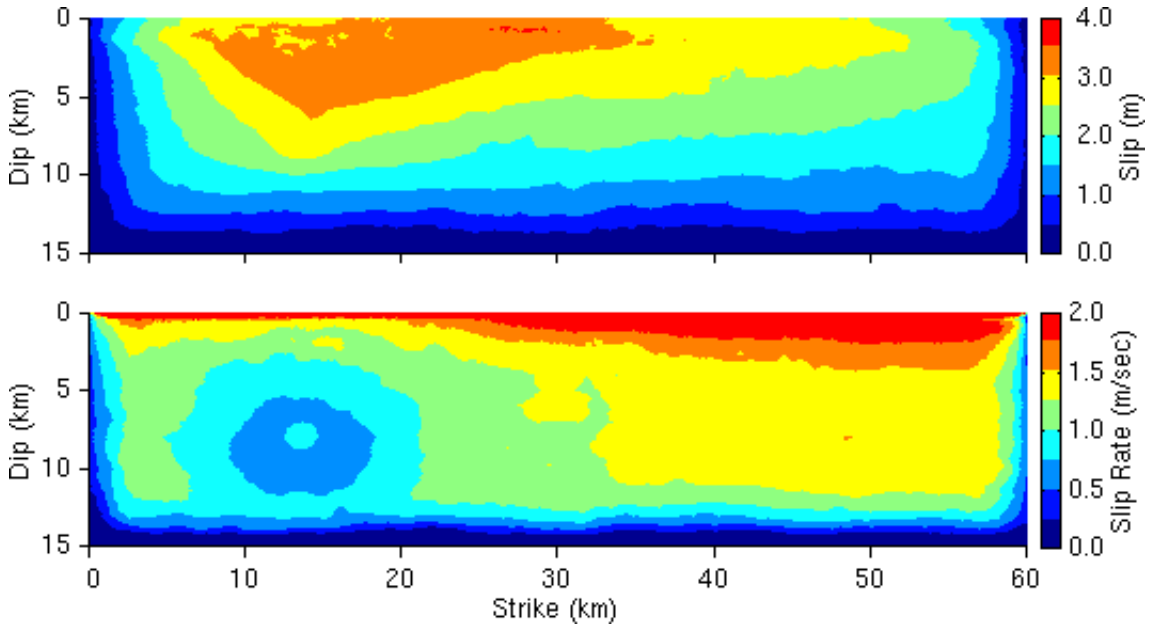


Figure 10.13: Distributions of final slip and maximum slip rate at each point on the strike-slip fault for scenario unistrain2.

(Kanamori et al. 1998). This implies that the change in temperature on the fault during sliding remains below the level that would cause melting. If we assume that changes in temperature on the order of 1000 degrees Kelvin cause melting, then we want our sliding stresses to yield estimated temperature changes less than 1000 degrees Kelvin.

Following Kanamori et al. (1998) we assume a heat capacity per unit mass of  $1000 \text{ J/(kg}\cdot\text{K)}$  and confinement of the heat to a region that extends 5.0 mm perpendicular to the fault. If the slip occurs across an infinitesimally thin zone, then the heat is confined to the thermal penetration depth given by  $d = \sqrt{k\tau_d}$ , where  $k$  is the thermal diffusivity and  $\tau_d$  is the time scale of the slip. Assuming that  $k = 1.35 \times 10^{-6} \text{ m/sec}^2$  and choosing  $\tau_d = 5 \text{ sec}$  gives  $d = 2.6 \text{ mm}$ . If the slip is distributed over a wider zone, then  $d$  may be larger. Consequently, we moderate the value of  $d$  given by the thermal penetration depth and choose a value of  $d = 5.0 \text{ mm}$ . As shown in figure 10.14, at most locations the temperature increases 300–400 degrees Kelvin. We observe smaller changes in temperature near the top of the fault because the minimum sliding stresses are smaller. Below a depth of 6.0 km the sliding stresses vary little, so below that depth the change in temperature closely resembles the distribution of final slip. Thus, our sliding stresses seem consistent with the lack of melting observed in fault zone materials.

The distributions of the maximum horizontal displacements and velocities clearly show the effect of directivity that we observe in the prescribed ruptures. In figure 10.15 both the maximum horizontal displacements and velocities increase along the strike of the fault away from the epicenter until the end of the fault where they begin to decay. The maximum displacements exceed 1.0 m over an area of approximately 1200 square kilometers with a peak value of 3.0 m. The maximum velocities exceed 1.0 m/sec over an area of

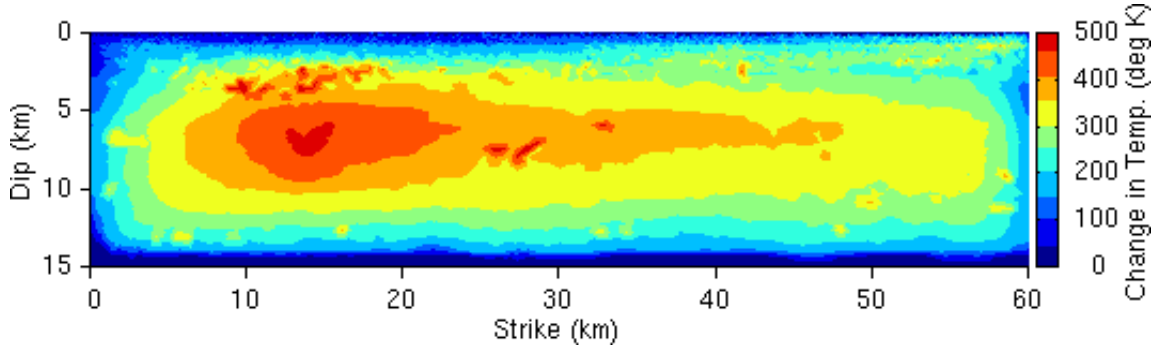


Figure 10.14: Final change in temperature at each point on the strike-slip fault for scenario unistrain2.

approximately 550 square kilometers with a peak value of 3.5 m/sec. The maximum displacements exhibit the gradual decay away from the fault that we found in the prescribed ruptures, while the distribution of the maximum velocities fits the familiar teardrop shape, but with a more rapid decay.

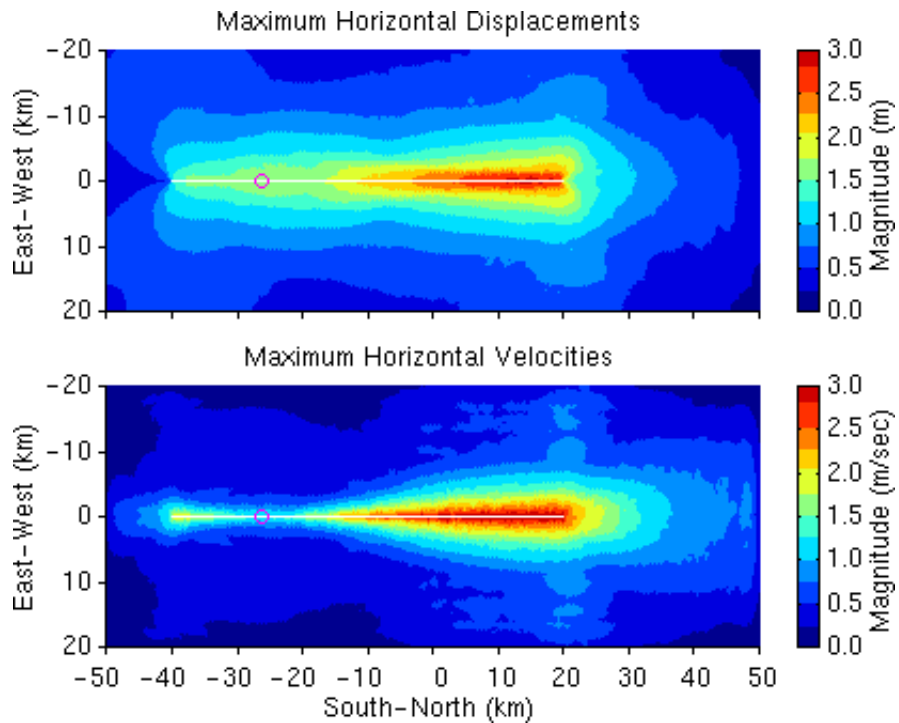


Figure 10.15: Maximum magnitudes of the horizontal displacement and velocity vectors at each point on the ground surface for scenario unistrain2. The white line indicates the projection of the fault plane onto the ground surface, and the purple circle identifies the epicenter.

We now examine the displacement and velocity time histories<sup>1</sup> at site S1, which is located on the ground surface 10 km north of the north tip of the fault, and at site S2, which is located on the ground surface 10 km east of the center of the fault (see figure 7.1 for a diagram of the locations of the two sites). Site S1 lies on the

<sup>1</sup>As in chapter 7, we low-pass filter all displacement and velocity time histories using a fourth-order Butterworth filter with a corner frequency of 0.5 Hz.

nodal line for motion in both the north-south and vertical directions, so we observe motion only in the east-west (fault normal) direction in figure 10.16. We see a sharp arrival of the shear wave with a peak velocity of 1.3 m/sec followed by a train of surface waves with progressively smaller amplitudes. At site S2 the peak displacement in the north-south (fault parallel) direction exceeds the peak displacement in the east-west (fault normal) direction by 34%, but the peak velocities in the two directions are nearly equal (0.26 m/sec compared to 0.25 m/sec). These general features are consistent with the ground motions from the prescribed ruptures.

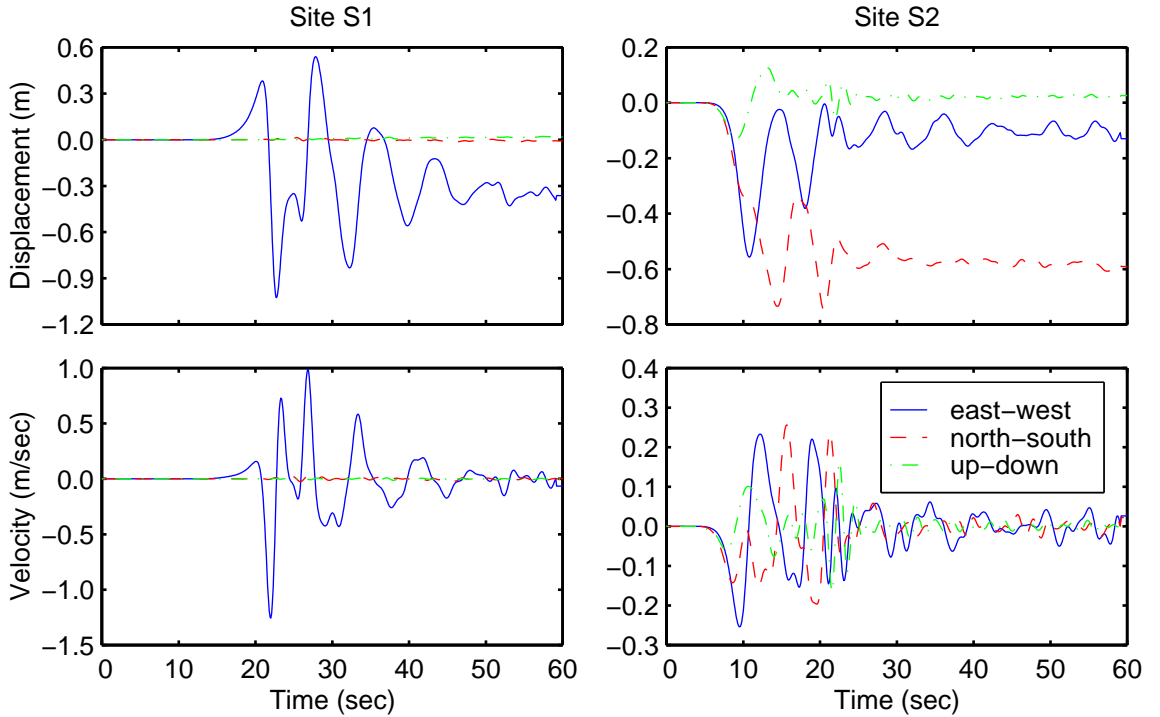


Figure 10.16: Displacement and velocity time histories at sites S1 and S2 for scenario unistrain2.

We find that uniform tectonic strains and a friction model with parameters that vary as a function of both depth and shear modulus produce a realistic rupture. We observe reasonable values for the rupture speed and the maximum slip rate, and the ground motions exhibit the directivity that we expect. The horizontal velocities near the north end of the fault that exceed 3.0 m/sec appear excessive and may be attributed to the rapid slip rates near the surface. However, these excessive values are isolated to the sites within one kilometer of the fault. Using a uniform characteristic slip distance of 0.338 m in the friction model (scenario unichardist) produces negligible changes in the behavior of the rupture and the ground motions. Moreover, changing the dependence of the coefficient of friction from the square root of the shear modulus to the shear wave speed (scenario shearspeed) also yields nearly identical behavior. Because scenarios unistrain2 and unichardist generate realistic rupture behavior and ground motions, we will use these two scenarios as base cases for a sensitivity study.

### 10.1.4 Sensitivity Study

We conduct a second sensitivity study of the long-period near-source ground motions, but in this case we focus on determining how the ground motions and rupture behavior change as we vary the initial conditions and parameters of the friction model. We systematically vary the type of friction model, the depth of the top of the fault, the hypocenter location, and the degree of heterogeneity in the initial shear stresses and the parameters of the friction model. Table 10.1 summarizes the general initial conditions and parameters for the scenarios in the sensitivity study, and table 10.2 gives some of the features of the ruptures for the scenarios. We discuss the scenarios in the following sections.

Scenario	Initial Traction	Friction Type
unistress	uniform stress	slip-weakening
unistrain	uniform strain	slip-weakening
unistrain2	same as unistrain	slip-weakening
unichardist	same as unistrain	slip-weakening
shearspeed	same as unistrain	slip-weakening
comboB	uniform strain	slip- and rate-weakening
meltC	same as comboB	melting-refreezing
fault4km	uniform strain	same as unichardist
hymc	uniform strain	same as unistrain2
shearweak	weakly heter. strain	same as unistrain2
shearstrong	strongly heter. strain	same as unistrain2
meltstrong	strongly heter. strain	same as meltC
frictionweak	same as unistrain2	weakly heter. slip-weakening
frictionstrong	same as unistrain2	strongly heter. slip-weakening

Table 10.1: Summary of the initial tractions and the friction model type for each scenario in the sensitivity study with the strike-slip fault. When scenarios share exactly the same parameters, we note the common bond in the latter scenarios.

### Friction Model

We study the sensitivity of the ground motions to the friction model using the slip-weakening friction model (scenario unichardist), the slip- and rate-weakening friction model (scenario comboB), and the shear melting-refreezing friction model (scenario meltC). The minimum sliding stresses remain the same across all three scenarios, but we increase the maximum dynamic stress drop by a factor of 1.44 for scenarios comboB and meltC. As discussed in section 9.5, the friction models with shear re-strengthening require a greater dynamic stress drop to generate the same slip as the slip-weakening friction model. We also scale the coefficient of friction at failure in order to maintain a distance from failure that matches the maximum dynamic stress drop. Equation (10.9) gives the functional forms of the parameters in the friction models for scenarios comboB and meltC. Figure 10.17 gives the initial shear stresses, the shear stresses at failure, and the minimum sliding shear stresses over the depth of the fault. Recall that  $V_o$  denotes the slip rate at which shear re-strengthening occurs in the slip- and rate-weakening friction model, and  $\tau_o$  varies inversely with the rate at which areas

Scenario	Average Slip (m)	Max. Slip (m)	Average Max. Slip Rate (m/sec)	Max. Slip Rate (m/sec)	Moment Magnitude	Average Stress Drop (MPa)
unistress	3.8	11	1.8	11	7.1	1.9
unistrain	1.2	2.3	0.89	1.4	6.8	1.6
unistrain2	1.9	3.5	1.2	3.9	6.9	1.4
unichardist	1.9	3.6	1.2	4.1	6.9	1.4
shearspeed	1.8	3.5	1.2	4.0	6.9	1.4
comboB	1.4	2.4	1.4	4.4	6.8	1.2
meltC	1.5	3.1	1.5	5.2	6.8	1.5
fault4km	1.5	2.8	1.0	1.6	7.0	2.3
hymc	2.0	3.6	1.2	3.7	6.9	1.5
shearweak	2.3	4.4	1.2	4.2	7.0	1.8
shearstrong	1.9	3.8	1.1	5.7	6.9	1.3
meltstrong	1.7	3.8	1.5	7.4	6.9	1.4
frictionweak	1.9	3.6	1.2	4.2	6.9	1.4
frictionstrong	2.0	4.0	1.1	4.5	6.9	1.4

Table 10.2: Summary of the ruptures in the scenarios that we use in the sensitivity study of the strike-slip fault. We compute the average slip using equation (2.39), the moment magnitude using equation (2.40), and the average stress drop using equation (8.9).

“refreeze” in the shear melting-refreezing friction model. These initial conditions for scenarios comboB and meltC produce earthquakes with a moment magnitude of 6.8 and average slips of 1.4 m and 1.5 m.

$$\begin{aligned}
 \mu_{max} &= \begin{cases} 0.227 & z > -1.0 \text{ km} \\ -4.17 \times 10^{-3} \left( \frac{\text{m}^3 \text{sec}^2}{\text{kg}} \right)^{\frac{1}{2}} \frac{\sqrt{\mu}}{z} & z < -1.0 \text{ km} \end{cases} \\
 \mu_{min} &= \begin{cases} 0.0235 & z > -1.0 \text{ km} \\ -4.31 \times 10^{-4} \left( \frac{\text{m}^3 \text{sec}^2}{\text{kg}} \right)^{\frac{1}{2}} \frac{\sqrt{\mu}}{z} & z < -1.0 \text{ km} \end{cases} \\
 \mu_{post} &= \begin{cases} 0.157 & z > -1.0 \text{ km} \\ -2.88 \times 10^{-3} \left( \frac{\text{m}^3 \text{sec}^2}{\text{kg}} \right)^{\frac{1}{2}} \frac{\sqrt{\mu}}{z} & z < -1.0 \text{ km} \end{cases} \\
 D_o &= 0.446 \text{ m (scenario comboB)} \\
 V_o &= 0.150 \text{ m/sec (scenario comboB)} \\
 D_o &= 0.130 \text{ m (scenario meltC)} \\
 \tau_o &= 0.350 \text{ sec (scenario meltC)} \tag{10.9}
 \end{aligned}$$

In scenario comboB the healing portion of the rupture, which is associated with the trailing edge of the rupture front, almost catches the leading edge of the rupture. This narrowing of the rupture front in the central portion of the fault significantly reduces the maximum slip rates and nearly smothers the rupture. Fukuyama and Madariaga (1998) also observed narrowing of the rupture front when they included rate-weakening in

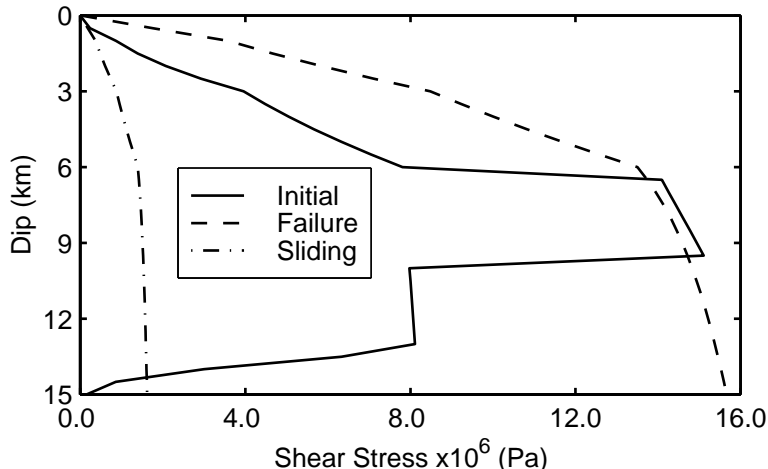


Figure 10.17: Initial, failure, and minimum sliding shear stresses through the center of the asperity on the strike-slip fault as a function of dip for scenarios comboB and meltC.

a similar friction model. The maximum displacements and velocities on the ground surface in figure 10.18 display evidence of this phenomenon. North of the epicenter both distributions exhibit an initial increase in the maximum values followed by a decrease along the central portion of the fault before increasing again. At the north end of the fault, the displacements and velocities on the ground surface return to levels near those observed in scenario unichardist. The local minimum in the maximum displacements occurs approximately two kilometers south of the local minimum in the maximum velocities. This is consistent with the more rapid decay in the maximum displacements off the north end of the fault compared to the maximum velocities. The peak maximum values of 3.3 m and 3.7 m/sec occur 2.3 km south of the north tip of the fault. As in scenario unichardist, these extremely large values occur on the fault where the slip rates are the greatest.

We compare the velocity time histories at sites S1 and S2 for all three scenarios (figure 10.19). At site S1 we find larger amplitudes for scenario meltC (melting-refreezing friction) than for either scenario unichardist (slip-weakening) or scenario comboB (slip- and rate-weakening). The slightly sharper phase arrivals for scenario meltC reflect the faster rupture speed (3.1 km/sec versus 3.0 km/sec) and contributes to the larger amplitudes. Additionally, the increase in the velocity amplitudes may be attributed to the greater tendency for the slip rates to progressively increase in ruptures with the melting-refreezing friction model compared to the other two friction models. At site S2 in the north-south (fault parallel) direction, the velocity amplitudes for scenario unichardist are generally larger than those for scenarios comboB and meltC, but the reverse is true in the east-west (fault normal) direction. While the time histories for scenarios unichardist and comboB match closely at site S1, at site S2 the time histories for scenarios comboB and meltC match closely. Although the velocity time histories exhibit moderate variations in amplitude, at both sites the general shapes of the waveforms do not change across the three friction models.

The maximum displacements and velocities on the ground surface along the east-west line through the north tip of the fault agree with our observations at site S1. Figure 10.20 shows a close match between the

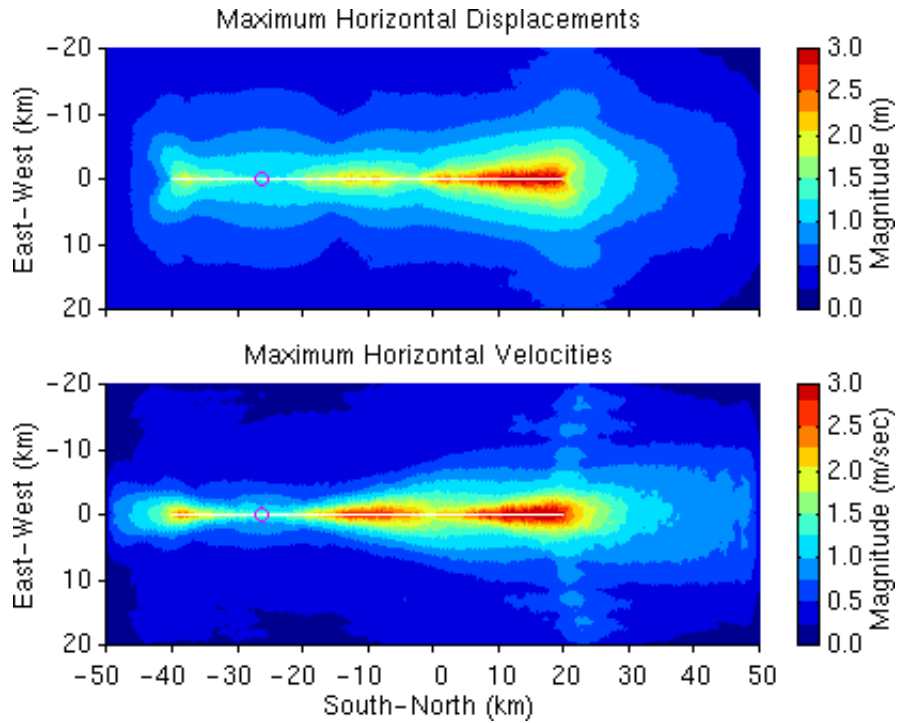


Figure 10.18: Maximum magnitudes of the horizontal displacement and velocity vectors at each point on the ground surface for scenario comboB. The white line indicates the projection of the fault plane onto the ground surface, and the purple circle identifies the epicenter.

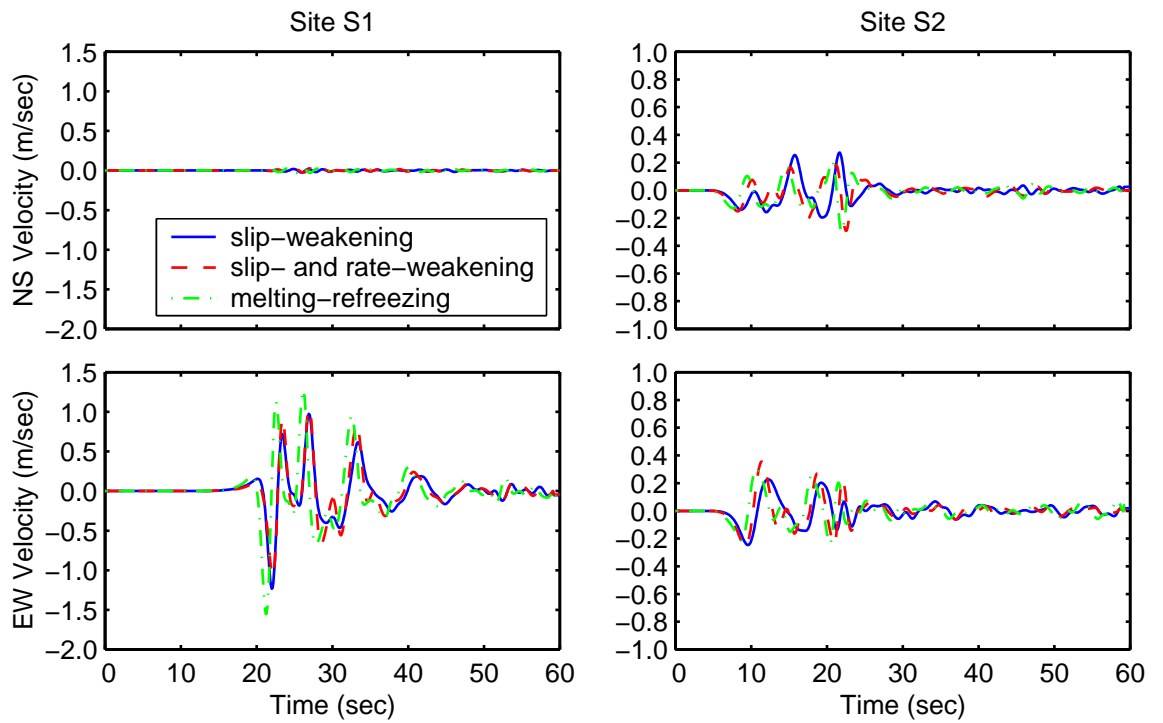


Figure 10.19: Comparison of horizontal velocity time histories at sites S1 and S2 for the three friction models.

maximum displacements and velocities for scenarios unichardist and comboB with slightly larger values for scenario meltC. The maximum velocities for scenario meltC decay at a slightly slower rate from 5.0–10 km away from the fault compared to those from scenarios unichardist and comboB. We attribute these larger maximum velocities to the relatively larger slip rates at the north end of the fault in scenario meltC compared to the other two scenarios. This slower decay more closely matches the shape of the near-source factor,  $N_v$ , from the 1997 Uniform Building Code. Nevertheless, the shapes of the curves of maximum displacements and velocities from all three scenarios match the general shape of the near-source factor curve.

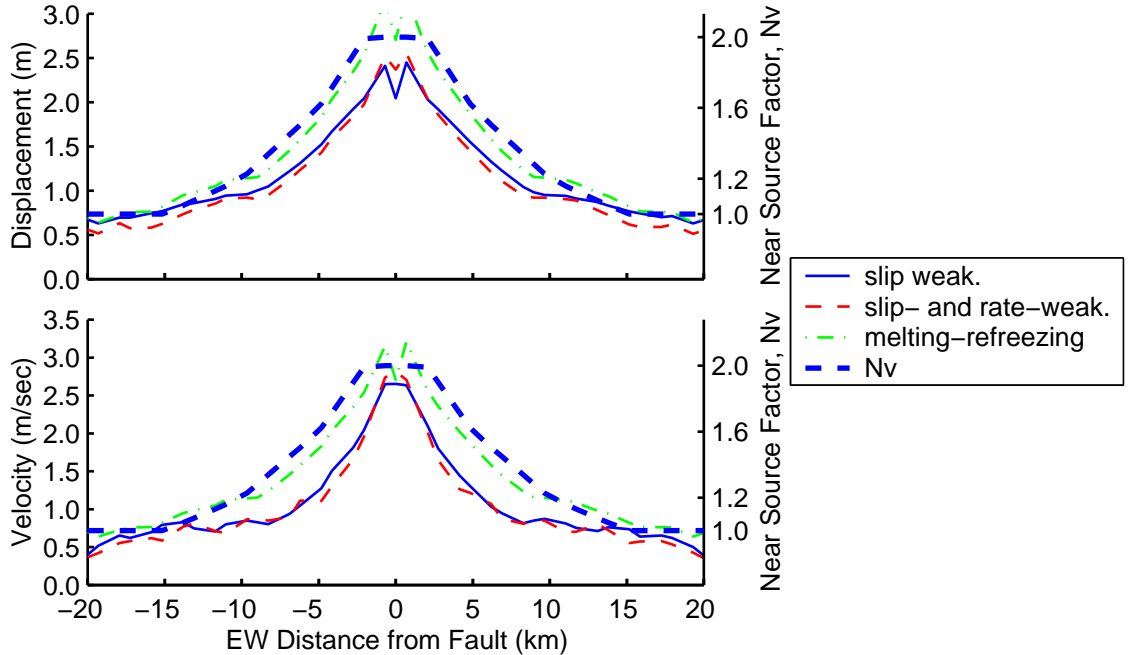


Figure 10.20: Maximum magnitudes of the horizontal displacement and velocity vectors along an east-west line running through the north tip of the fault for the three friction models. The thick, dashed line indicates the near-source ground motion factor,  $N_v$ , from the 1997 Uniform Building Code.

### Fault Depth

We study the sensitivity of the ground motions to the depth of the fault using scenarios unichardist and fault4km. To create scenario fault4km we lower the fault 4.0 km while applying the same initial strain field and using the same slip-weakening friction model litholayeruf2 (given by equation (10.8)). With the buried fault in scenario fault4km, the rupture does not hit the free surface and produces more uniform distributions of final slip and maximum slip rate. The two distributions resemble those from scenario unistrain where the rupture did not penetrate the softer material near the ground surface. With the deeper fault and the increase in shear modulus with depth, the moment magnitude increases from 6.9 to 7.0 even though the average slip decreases from 1.9 m to 1.5 m.

The north-south displacement time histories at site S2 (figure 10.21) reflect this variation in the average

slip. While the shapes of the time histories closely match, we observe larger amplitudes and final displacements for scenario unichardist, where the top of the fault sits at the ground surface, than for scenario fault4km, where the top of the fault sits at a depth of 4.0 km. In the east-west direction at both sites S1 and S2, we generally observe smaller displacement amplitudes with the buried fault. The notable exception is the shear wave arrival at site S1 where the peak displacement for the buried fault exceeds the peak displacement for the fault at the surface by 20% (1.2 m compared to 1.0 m).

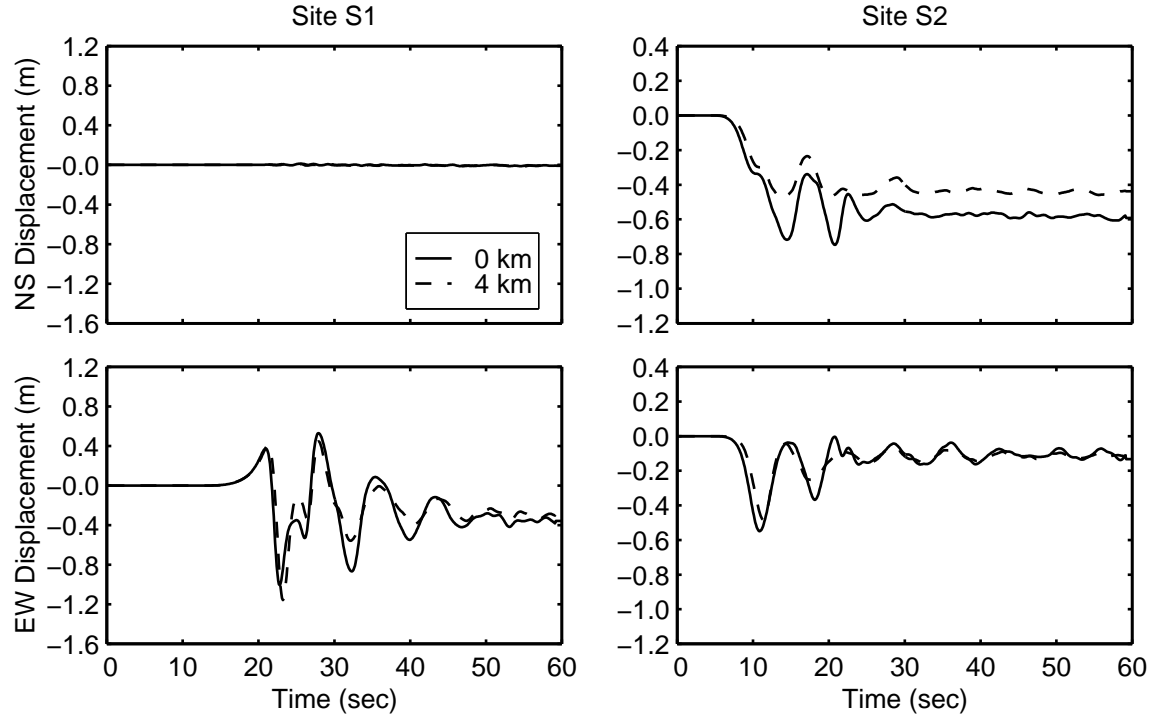


Figure 10.21: Comparison of horizontal displacement time histories at sites S1 and S2 for the two depths of the top of the fault.

In addition to substantially reducing the maximum displacements and velocities along the east-west line running through the north tip of the fault, burying the fault perturbs the shapes of the curves as shown in figure 10.22. The maximum displacements for scenario fault4km become nearly uniform for distances 15–20 km from the fault. On the other hand, the maximum velocities continue to decay at approximately the same rate over this same region. The maximum velocities from scenario unichardist decay at a faster rate closer to the fault before decaying more slowly 10 km from the fault. Consequently, the maximum displacements and velocities from the two scenarios closely agree between 5.0 km and 10 km from the fault. Less than 5.0 km from the fault, the maximum displacements and velocities from scenario fault4km lie well below those from scenario unichardist, while beyond 10 km from the fault, they are only slightly lower. Although the lowering of the fault does reduce the maximum horizontal displacements and velocities, the peak values on this east-west line still exceed 1.0 m and 1.5 m/sec. We continue to find no significant discrepancies between the shape of the near-source factor and the shapes of the maximum displacements and velocities for this strike-slip

fault.

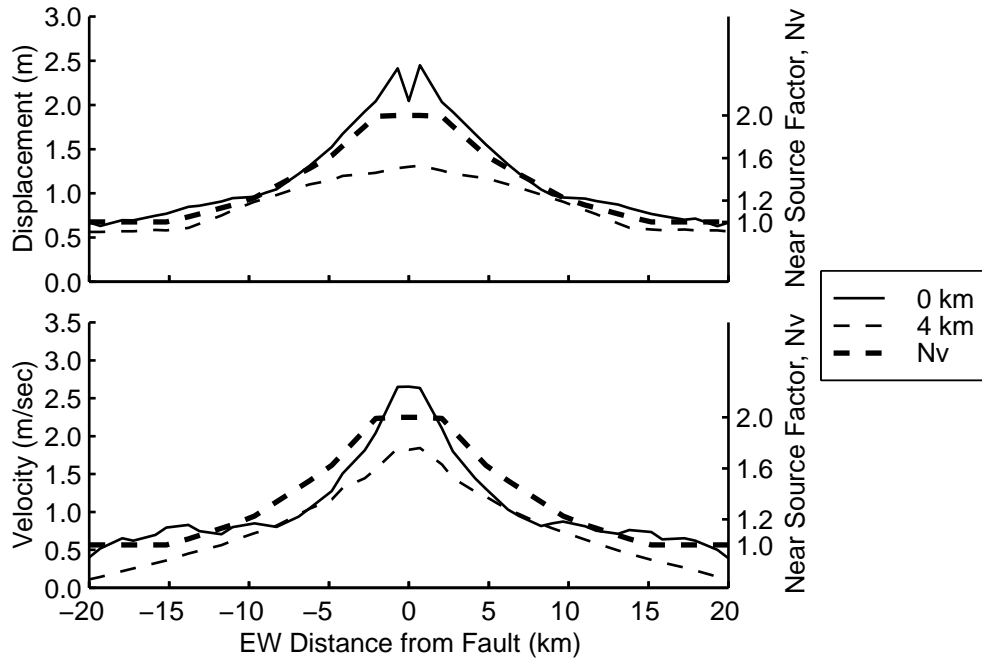


Figure 10.22: Maximum magnitudes of the horizontal displacement and velocity vectors along an east-west line running through the north tip of the fault for the two depths of the top of the fault. The thick, dashed line indicates the near-source ground motion factor,  $N_v$ , from the 1997 Uniform Building Code.

### Hypocenter Location

Moving the asperity to the center of the fault, while maintaining the same 8.0 km depth (scenario hymc), allows examination of the sensitivity of the ground motions to the location of the hypocenter. Besides the adjustment of the asperity in the initial shear tractions, the other initial conditions and parameters do not change from those we use in scenario unistrain2. Figure 10.23 displays the displacement time histories at sites S1 and S2 for scenario unistrain2 with the hypocenter at the southern quarter point (labeled middle quarter<sup>2</sup>) and scenario hymc with the hypocenter at the center of the fault (labeled middle center). As expected, the shear wave arrives earlier at site S1 when we place the hypocenter near the center of the fault. In contrast to the prescribed ruptures where we observe little change in the amplitudes of the motion for the different hypocenter locations, we see that the peak displacement in the east-west direction increases from 0.74 m to 1.0 m as the hypocenter moves from the middle of the fault to the southern quarter point. The shapes of the displacement time histories remain the same.

At site S2 the shear wave arrives more sharply with the central hypocenter location. The energy from the locations within the asperity arrives over a shorter period of time due to the finite size of the asperity and the location of site S2 at an azimuth of precisely 90 degrees. For both hypocenter locations site S1 lies on

<sup>2</sup>The first word in the label of the hypocenter refers to the dip location, and the second word refers to the strike location.

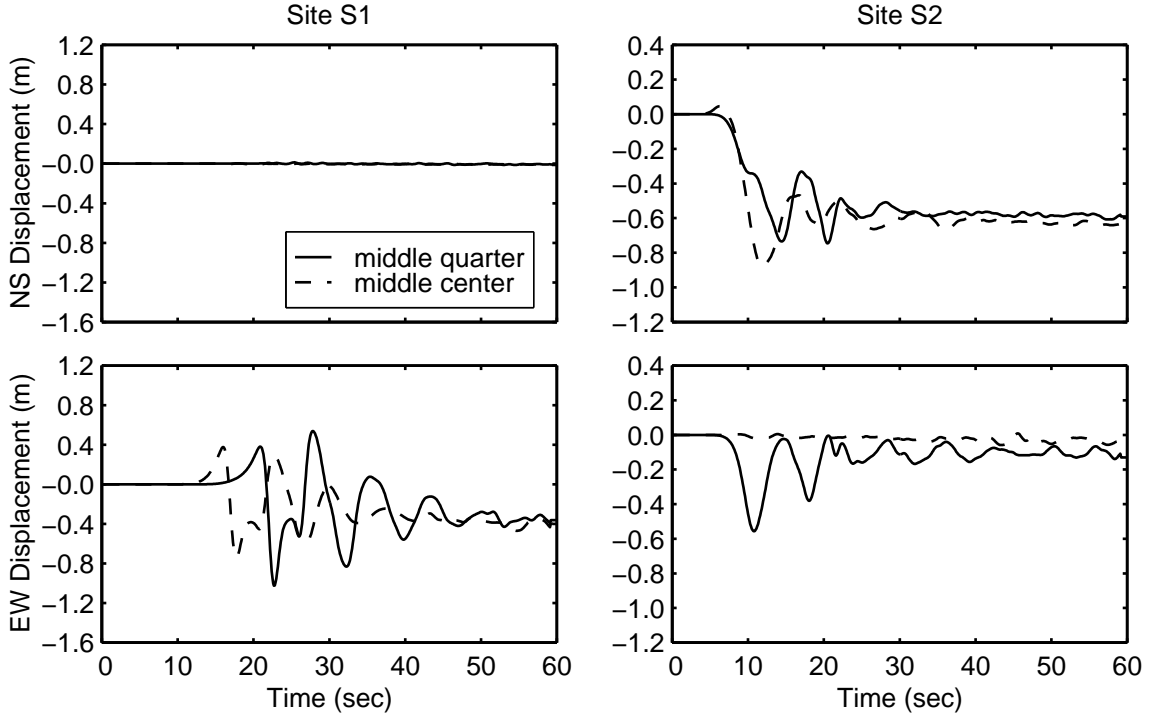


Figure 10.23: Comparison of horizontal displacement time histories at sites S1 and S2 for two the hypocenter locations.

nodal lines for motion in the north-south direction, and for the middle center hypocenter location site S2 lies on a nodal line for motion in the east-west direction. The average slip of 2.0 m from scenario hymc closely matches the average slip of 1.9 m from scenario unistrain2. Consequently, at each site we find minimal differences between the final displacements for the two scenarios.

When we examine the maximum horizontal displacements and velocities along the east-west line through the north tip of the fault given in figure 10.24, we find that the change in the hypocenter location affects the maximum displacements more than the maximum velocities. When we move the hypocenter from near the center of the fault to the southern quarter point, the peak of the curve of maximum displacements increases by 26% while the peak of the curve of maximum velocities increases by only 3.7%. In the prescribed ruptures we find little variation in both the maximum displacements and velocities. The shapes of the curves exhibit little variation and closely agree with the shape of curve for the near-source factor.

### Heterogeneity in Initial Shear Traction

We gauge the sensitivity of the rupture behavior and the ground motions to heterogeneity in the initial shear traction by introducing asperities into the tectonic shear strains. We continue to use the litholayeruf2 slip-weakening friction model (equation (10.8)). We create both weakly heterogeneous (scenario shearweak) and strongly heterogeneous (scenario shearstrong) distributions of the initial shear strains. The distributions each contain 30 asperities with uniform random distributions of radii between 3.0 km and 8.0 km and uniform

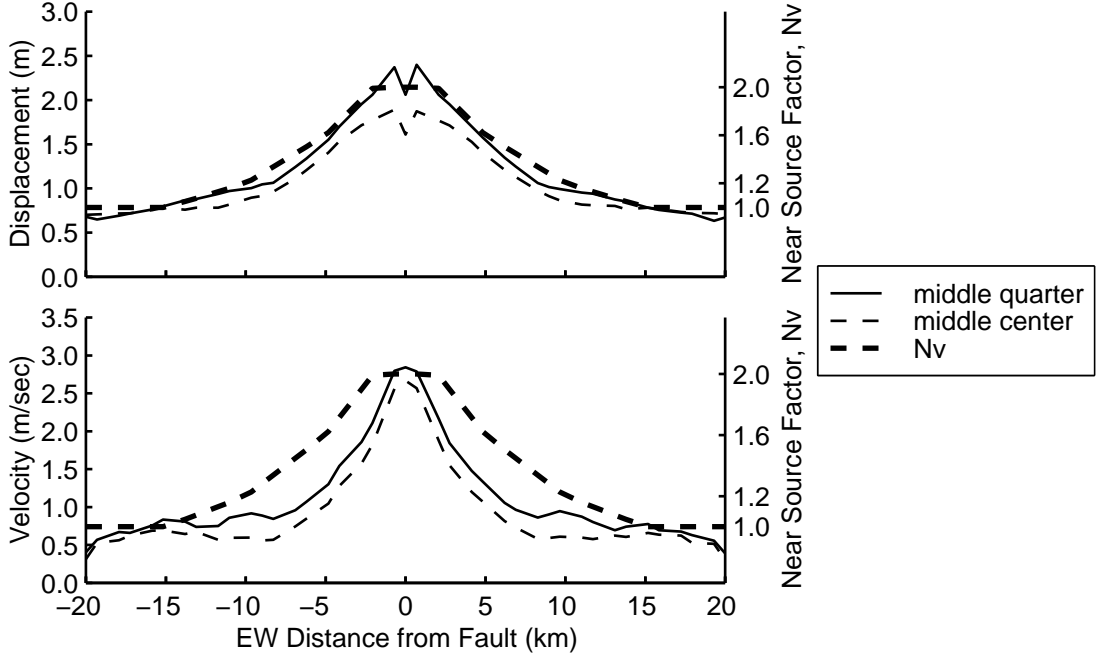


Figure 10.24: Maximum magnitudes of the horizontal displacement and velocity vectors along an east-west line running through the north tip of the fault for the two hypocenter locations. The thick, dashed line indicates the near-source ground motion factor,  $N_v$ , from the 1997 Uniform Building Code.

random distributions of locations along the strike and dip. We do not allow asperities within 2.0 km of the edges of the fault to prevent tampering with the taper in the shear stresses at the edges of the fault. The weakly and strongly heterogeneous distributions contain asperities uniformly distributed within 30% and 60% of the nominal strain field (equation (10.2)). We introduce the heterogeneity directly into the initial shear tractions from the asperities in the strain field. Consequently, the asperities do not affect the effective normal tractions. Figure 10.25 shows the distribution of the initial, failure, and sliding shear stresses on the fault for scenario shearstrong which contains the strongly heterogeneous initial strains.

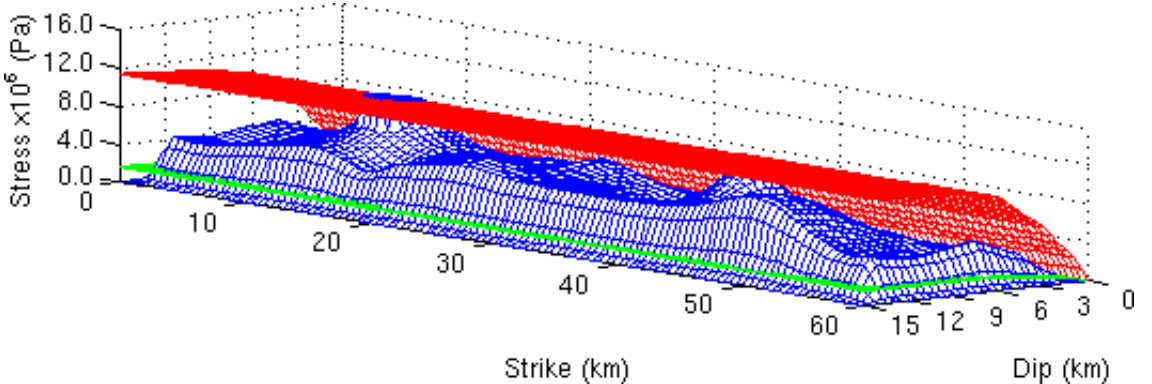


Figure 10.25: Initial (blue), failure (red), and minimum sliding (green) shear stresses on the strike-slip fault for scenario shearstrong.

The heterogeneity in the initial shear stresses provides one of the few means to introduce heterogeneity into the distribution of the final slip. The other methods include using heterogeneity in the parameters of the friction model, which we will discuss below, and using heterogeneity in the material properties. The strongly heterogeneous initial shear stresses do a substantially better job of generating heterogeneity in the distribution of the maximum slip rate than in the distribution of final slip as illustrated by figure 10.26. Compared to the level of heterogeneity in the final slip, the level of heterogeneity in the maximum slip rates more closely matches the level of heterogeneity in the initial shear tractions. We do find an increase in the maximum final slip from 3.5 m to 3.8 m with negligible change in the average slip. We observe an increase in the final slip at a strike of around 40 km, where two asperities create large initial shear stresses. Similarly, the reduced initial shear stresses at the bottom of the north end of the fault effectively prevent slip at the bottom corner of the fault. The asperities also lead to sudden increases and decreases in the maximum slip rate and rupture speed corresponding to regions where they reduce or increase the distance from failure. These fluctuations create the heterogeneous distribution of maximum slip rate visible in figure 10.26.

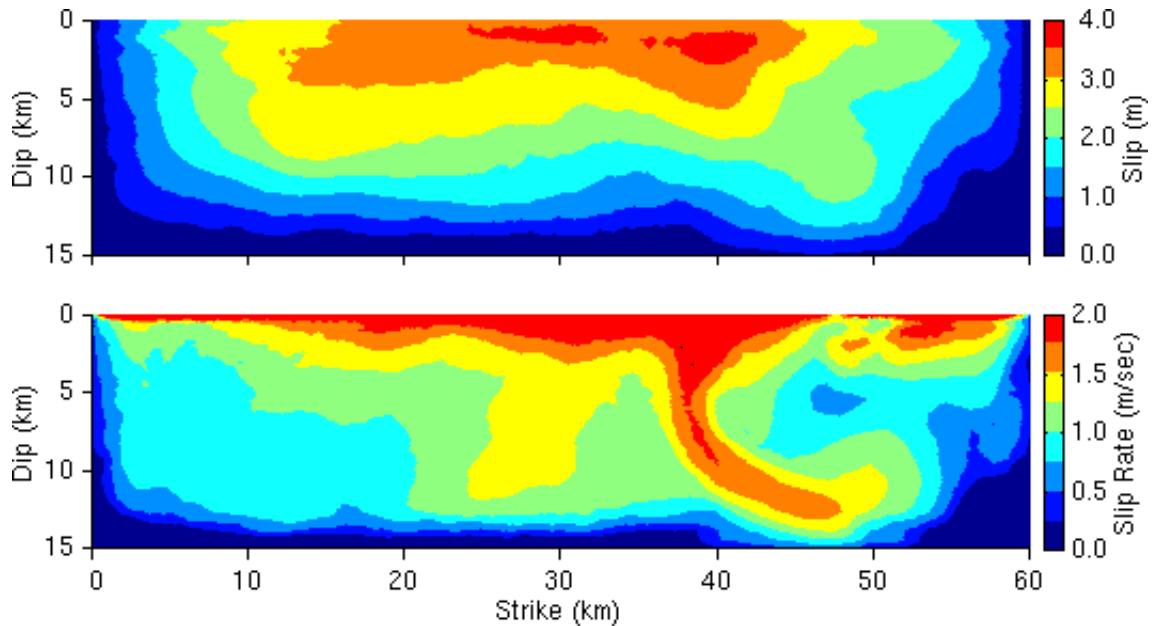


Figure 10.26: Distributions of final slip and maximum slip rate at each point on the strike-slip fault for scenario shearstrong.

The changes in the rupture speed greatly reduce the efficiency of the reinforcement of the shear wave by the rupture. Figure 10.27 shows that the maximum displacements and velocities increase more rapidly as the rupture encounters the two asperities at a north-south location of 0 km (strike of 40 km). This is in response to the relatively larger slip rates and slip that occur when the rupture hits the asperities. These larger slip rates momentarily increase the rupture speed and the efficiency of the reinforcement of the shear wave by the rupture. On the other hand, just north of this region, the maximum displacements and velocities suddenly decrease, because the rupture speed decreases and the efficiency of the reinforcement of the shear

wave returns to near its nominal level. The maximum displacements and velocities increase again as the rupture approaches the north tip of the fault.

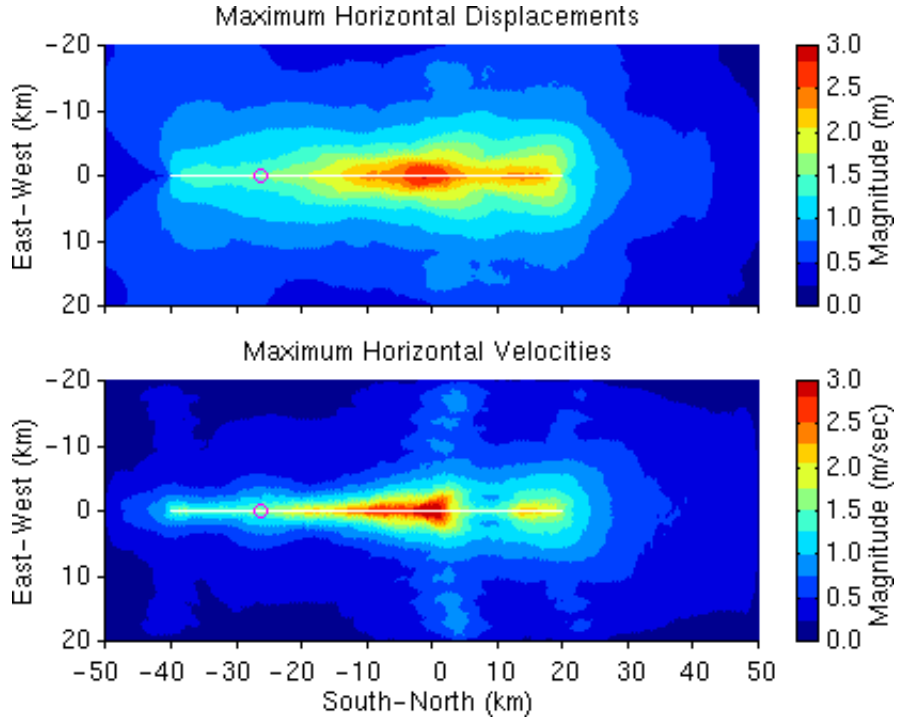


Figure 10.27: Maximum magnitudes of the horizontal displacement and velocity vectors at each point on the ground surface for scenario shearstrong. The white line indicates the projection of the fault plane onto the ground surface, and the purple circle identifies the epicenter.

The limited ability of the strongly heterogeneous initial shear tractions to create large variations in the distribution of final slip inspired the combination of the melting-refreezing friction model with the strongly heterogeneous initial strains (scenario meltstrong). The shear re-strengthening in the melting-refreezing friction model reduces the width of the rupture front and causes the slip to occur at a more local level. We use the melting-refreezing model from scenario meltC and simply add the asperities from the heterogeneous strain field to the initial strain distribution from scenario meltC.

The correlation between the height of the asperities and the final slip increases substantially in scenario meltstrong compared to scenario shearstrong, even though we observe no change in the maximum final slip and minimal change in the average slip. We find local maxima in the final slip in figure 10.28 near the two asperities that sit at a strike of about 40 km. The local variations in the distribution of the maximum slip rate agree with those in scenario shearstrong. This suggests that, while both the slip-weakening and melting-refreezing friction models produce heterogeneity in the slip rates, the friction models with shear re-strengthening more effectively produce heterogeneity in the distribution of final slip.

Figure 10.29 displays the displacement time histories for the four scenarios. The displacement time histories from scenario shearweak differ the most from the other three scenarios, because the rupture happens

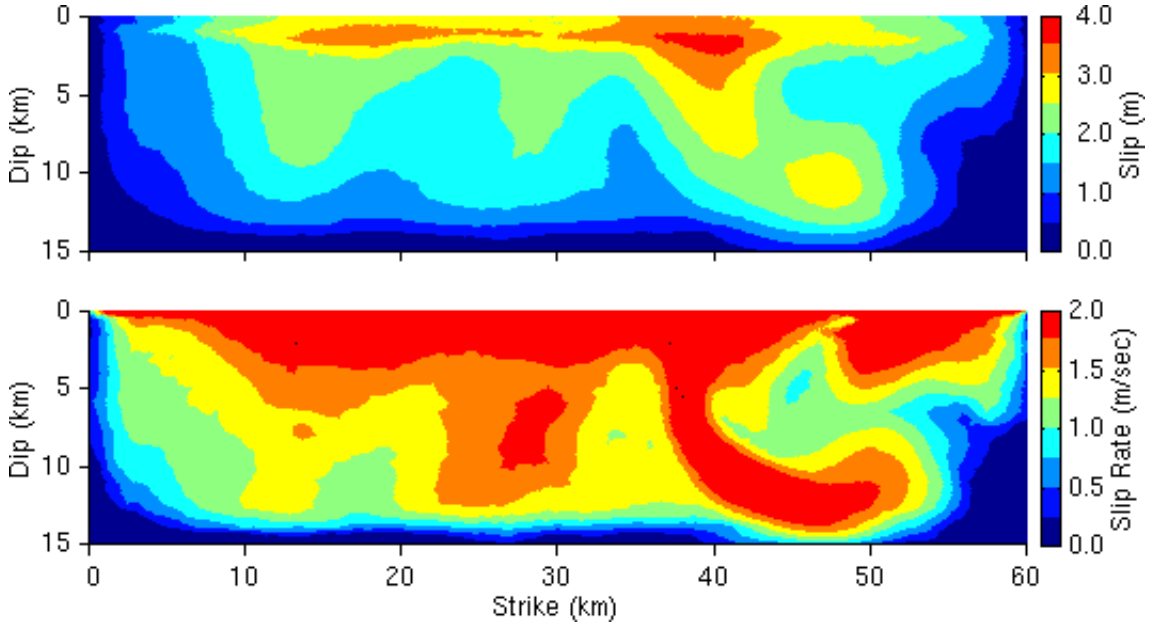


Figure 10.28: Distributions of final slip and maximum slip rate at each point on the strike-slip fault for scenario meltstrong.

to encounter an asperity near the hypocenter and begins propagating at a speed of 4.9 km/sec. By propagating faster than the shear wave, the reinforcement of the shear wave decreases dramatically. This results in the smaller amplitude displacements in the east-west (fault normal) direction at sites S1 and S2. At site S2 the amplitudes in the north-south direction are larger for scenario shearweak, because the faster rupture speed corresponds to higher slip rates. The larger slip rates generate an average slip of 2.3 m in scenario shearweak compared to the 1.9 m of slip in scenario unistrain2. Turning our attention to the other three scenarios, we find only small changes in the displacement amplitudes at site S1 which lies in the forward direction. The displacement amplitudes exhibit greater sensitivity at site S2 which lies at an azimuth of 90 degrees. As we might expect, we find better agreement in the displacement time histories between the scenarios shearstrong and meltstrong, which feature strongly heterogeneous distributions of shear tractions.

Despite wide fluctuations in the maximum displacements and velocities across the four scenarios on the east-west line running through the north tip of the fault, the shapes of the curves match the general shape of the near-source factor from the UBC as shown in figure 10.30. As we noted in our discussion of the time histories, the super-shear rupture speed in scenario shearweak reduces the efficiency of the reinforcement of the shear wave. Consequently, the curve of the maximum velocities for scenario shearweak consistently lies below the other curves. The 20% larger average slip in scenario shearweak compared to scenarios unistrain2 and shearstrong prevents a similar reduction in the maximum displacements. We find the maximum velocities significantly more sensitive to the heterogeneity in shear tractions compared to the maximum displacements. The maximum displacements from scenario unistrain2 match reasonably well with those from scenario meltstrong, but the curves of the maximum velocities do not. Instead, the curve from scenario meltstrong re-

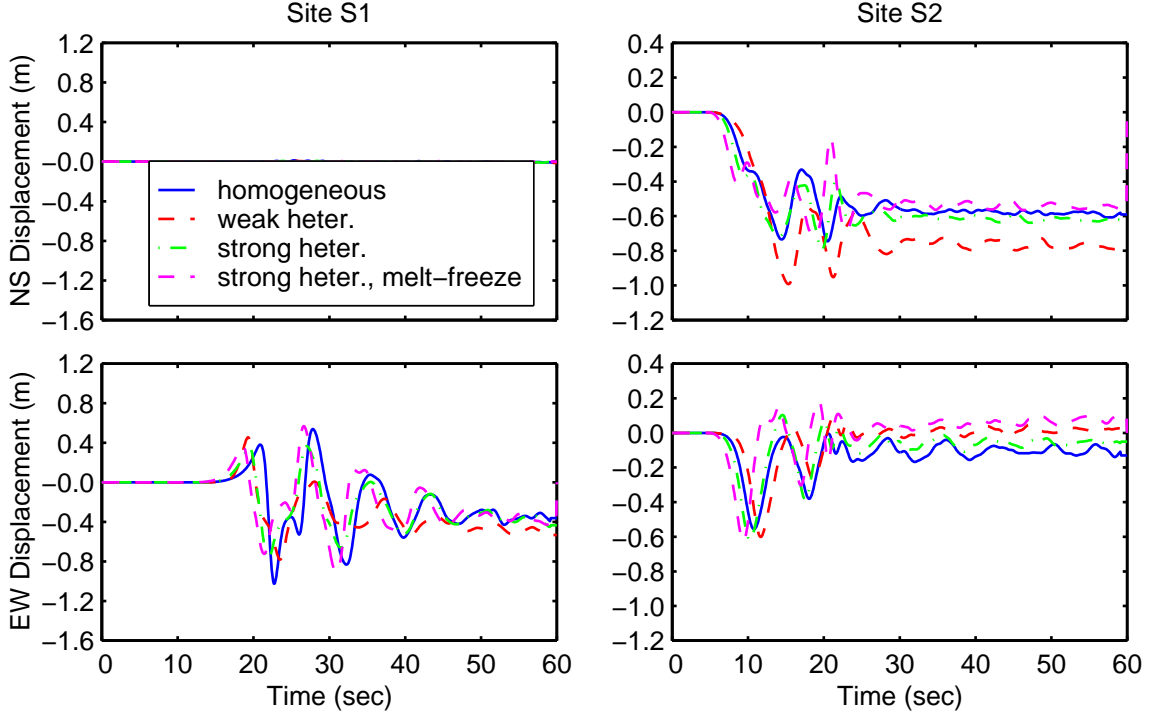


Figure 10.29: Comparison of horizontal displacement time histories at sites S1 and S2 for the four cases of heterogeneity in the initial shear tractions.

sembles the curve from scenario shearstrong. Both curves for the strongly heterogeneous distributions of the initial tractions lie well below the curve for scenario unistrain2, because the strong heterogeneity has a greater impact on the slip rates and velocities.

### Heterogeneity in Friction Model Parameters

We create heterogeneity in the litholayeruf2 friction model by varying the parameters in the friction model over the fault surface. We follow the same procedure that we use for creating heterogeneity in the initial shear tractions and place the 30 asperities using uniform random distributions. The radii vary from 3.0 km to 8.0 km. The asperity heights correspond to variations in the coefficients in the friction model. For example, we independently vary the coefficients in the expressions for  $\mu_{max}$  and  $\mu_{min}$  by 20% and 40% above and below the nominal value to generate weakly and strongly heterogeneous distributions. We do not introduce heterogeneity in the characteristic slip distance, but the fluctuations in the maximum and minimum values of the coefficient of friction cause heterogeneity in the fracture energy. Figure 10.31 shows the initial shear stresses, the shear stresses at failure, and the minimum sliding stresses on the fault surface.

The strong heterogeneity in the friction model parameters has a greater impact on creating heterogeneity in the distribution of the maximum slip rate than in creating heterogeneity in the distribution of final slip. In figure 10.32 the regions with the larger maximum slip rates correlate with the regions of a reduced distance

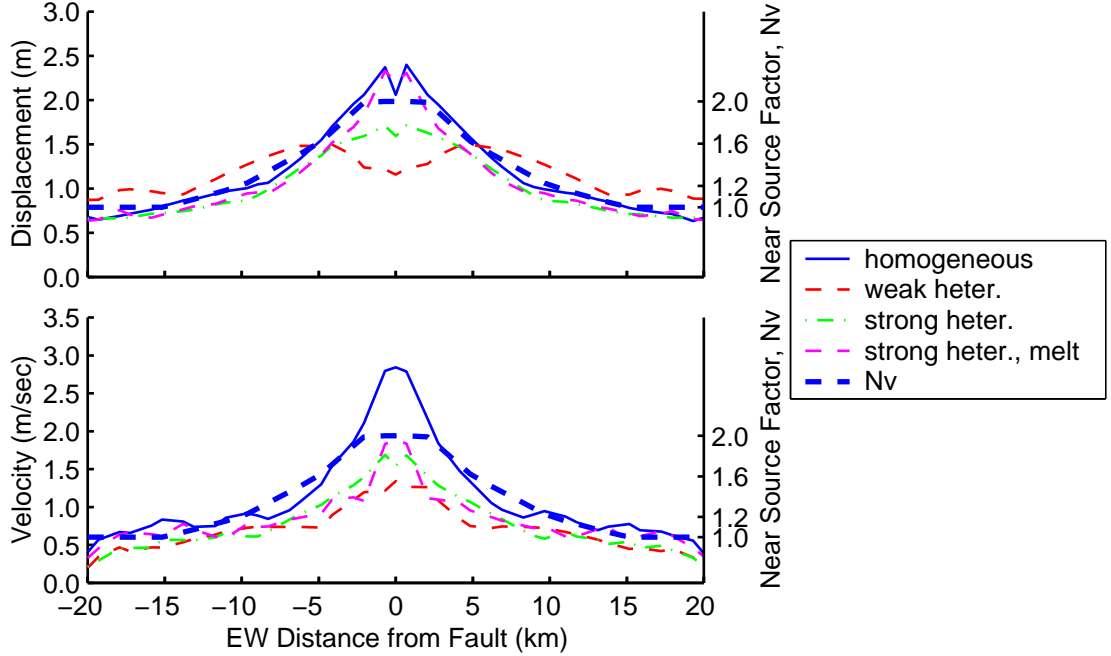


Figure 10.30: Maximum magnitudes of the horizontal displacement and velocity vectors along an east-west line running through the north tip of the fault for the four cases of heterogeneity in the initial shear tractions. The thick, dashed line indicates the near-source ground motion factor,  $N_v$ , from the 1997 Uniform Building Code.

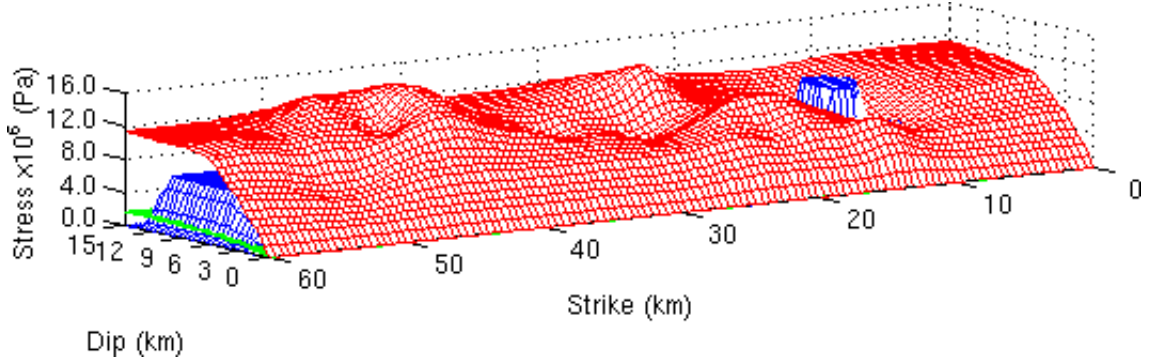


Figure 10.31: Initial (blue), failure (red), and minimum sliding (green) shear stresses on the strike-slip fault for scenario frictionstrong.

from failure, and vice versa. In the central portion of the fault, we observe a relatively uniform increase in slip corresponding to the reduced distance from failure. In our discussion of heterogeneous initial shear tractions, we found similar trends in scenario shearstrong, which uses a strongly heterogeneous distribution in the initial shear stress and a slip-weakening friction model.

Compared to scenario unichardist with homogeneous coefficients in the friction model, the introduction of weak heterogeneity in the coefficients of the friction model (scenario frictionweak) leads to negligible change in the behavior of the rupture. On the other hand, the introduction of strong heterogeneity (scenario frictionstrong) leads to significant changes in the rupture behavior. For the three scenarios the average slip

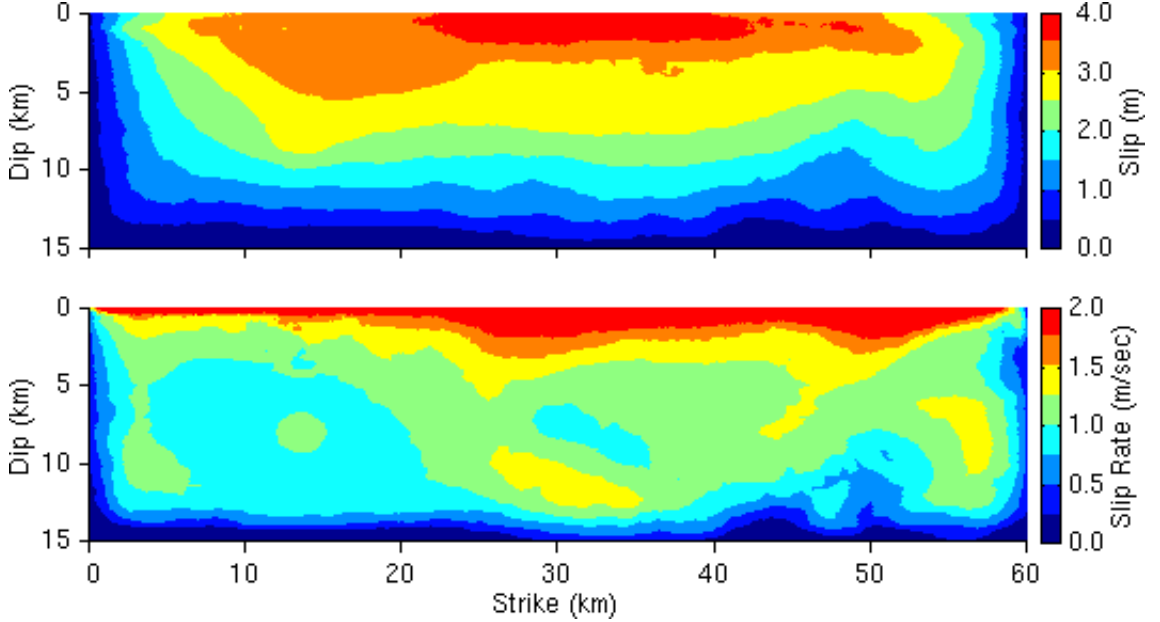


Figure 10.32: Distributions of final slip and maximum slip rate at each point on the strike-slip fault for scenario frictionstrong.

varies less than 0.2 m, but the strongly heterogeneous friction model decreases the maximum horizontal displacement by 20% and the maximum horizontal velocity by 11%.

The displacement time histories at sites S1 and S2 displayed in figure 10.33 illustrate these features. At both sites we see little variation in the final displacements, which is consistent with the nearly identical values of the average slip. As noted above, the rupture behavior does not change with the weak heterogeneity, and we find no noticeable differences between the displacement time histories from scenarios unichardist and frictionweak. At site S1 the strong heterogeneity reduces the peak displacement by 28% (0.72 m for scenario frictionstrong compared to 1.0 m for scenario unichardist). The amplitudes for the remainder of the time histories exhibit similar reductions. At site S2 we observe almost no reduction in the displacement amplitudes in the east-west (fault normal) direction and a small increase in the amplitudes in the north-south direction. The differences in the variations in the displacements between the two sites may be explained by their locations. Site S1 lies at an azimuth of 0 degrees, while site S2 lies at an azimuth of 90 degrees. Consequently, the variation in the rupture speed, which reduces the efficiency of the reinforcement of the shear wave, tends to reduce the amplitude of the motion at site S1. On the other hand, the rapid propagation and large slips near the center of the fault tends to increase the displacement amplitudes at site S2.

The maximum horizontal displacements along the east-west line passing through north tip of the fault support our analysis of the displacement time histories at site S1. As shown in figure 10.34, both the maximum displacements and maximum velocities decrease with the strong heterogeneity in the parameters of the friction model, which we attribute to the fluctuations in the rupture speed. We continue to observe negligible differences in the ground motions between scenarios unichardist and frictionweak (homogeneous and weakly

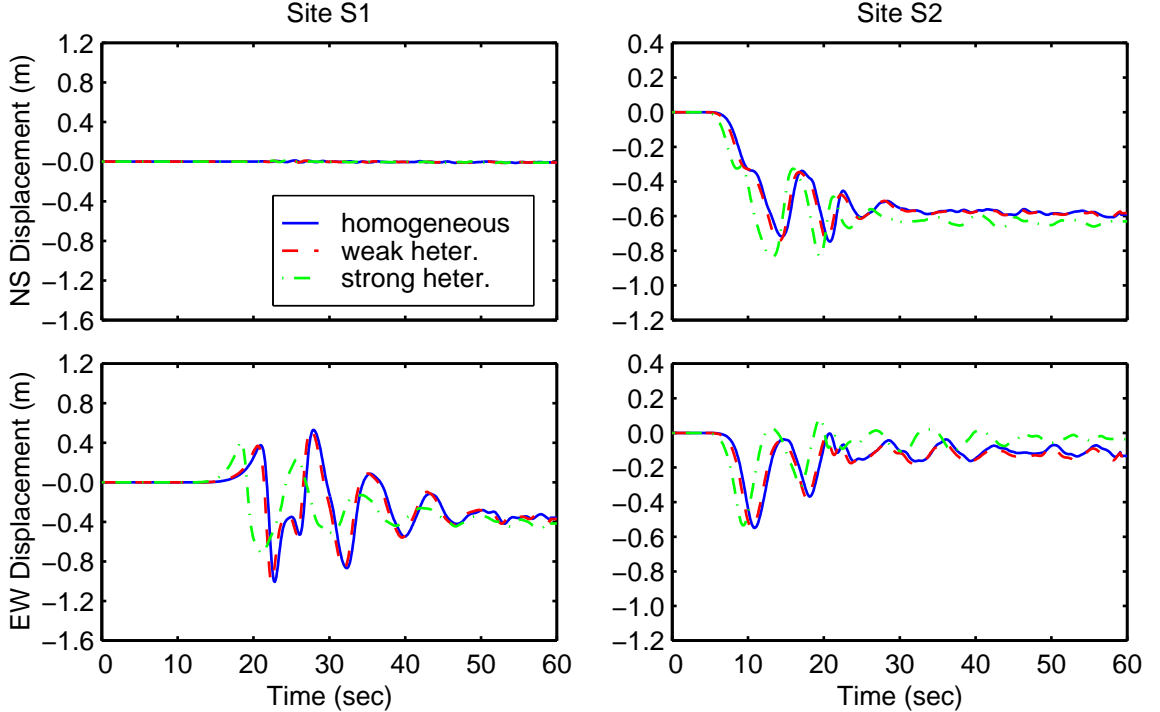


Figure 10.33: Comparison of horizontal displacement time histories at sites S1 and S2 for the three cases of heterogeneity in the parameters of the friction model.

heterogeneous friction model parameters). Once again, we find no significant variations in the shape of the curves of the maximum displacements and maximum velocities, so they continue to match the shape of the curve of the UBC near-source factor.

### 10.1.5 Comparison with Prescribed Ruptures

In our discussion of the sensitivity study, we have highlighted some of the similarities and differences between the prescribed rupture simulations that we discussed in section 7.1 and the dynamic failure simulations. Obviously, we expect similarities in the rupture behavior and the ground motions, because we selected the parameters in the dynamic failure simulations such that the average slip and rupture speeds of the dynamic ruptures generally agree with those that we use in the prescribed ruptures. We will now discuss some of the fundamental similarities and differences in more detail by examining scenario unistrain2, which uses dynamic failure, and scenario hymq, which uses a prescribed rupture. Scenario unistrain2 features an average slip of 1.9 m, a moment magnitude of 6.9, and an average rupture speed of 85% of the local shear wave speed. Scenario hymq has similar characteristics with an average slip of 2.0 m, a moment magnitude of 7.0, and a rupture speed of 80% of the local shear wave speed.

Figure 10.35 gives the horizontal velocity time histories at sites S1 and S2 for the two scenarios. At each site we find that the phases for the two scenarios arrive at nearly the same time, which we expect because

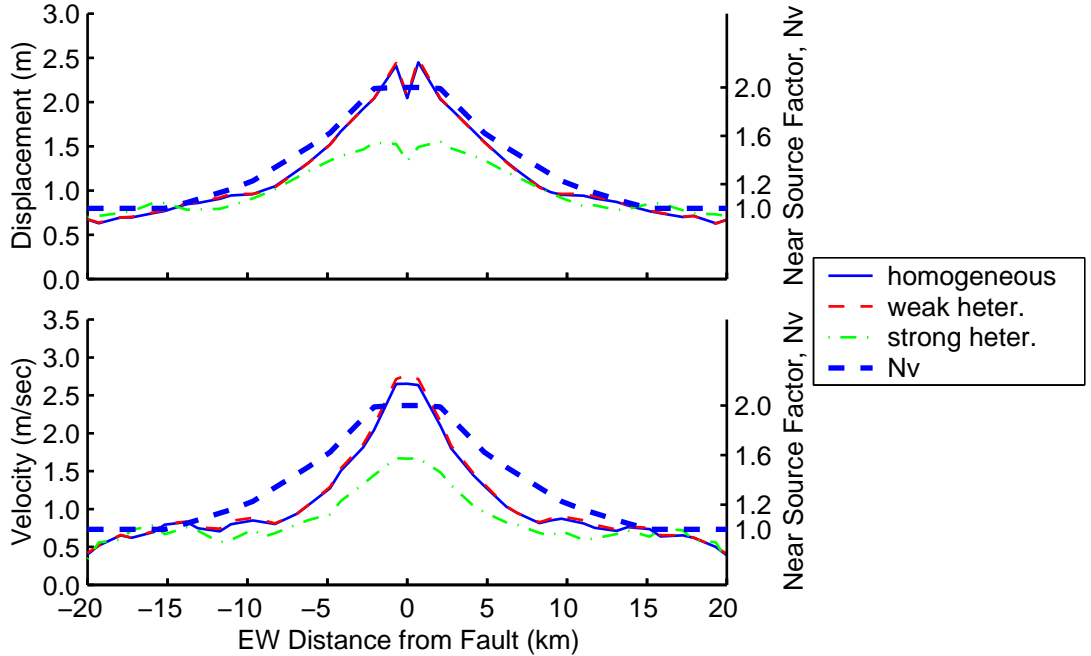


Figure 10.34: Maximum magnitudes of the horizontal displacement and velocity vectors along an east-west line running through the north tip of the fault for the three cases of heterogeneity in the friction model. The thick, dashed line indicates the near-source ground motion factor,  $N_v$ , from the 1997 Uniform Building Code.

the travel time from the hypocenter is the same. At site S1 we see excellent agreement in the shape of the waveforms between the two scenarios with minor discrepancies in the amplitudes. The peak east-west velocity of 1.3 m/sec for scenario unistrain2 exceeds the peak velocity of 1.0 m/sec for scenario hymq by 30%, but the peak displacements (not shown) are within 10% (1.0 m versus 1.1 m). At site S2 we find similar agreement in the east-west component where the amplitudes exhibit minor differences but the shapes match. In the north-south component the phase arrivals match reasonably well, and we find larger differences in the amplitudes; however, the velocity amplitudes are smaller compared to the other components. Thus, the velocity time histories from scenario unistrain2 with dynamic failure and scenario hymq with a prescribed rupture show excellent agreement with only minor discrepancies in the amplitudes of the motion.

The maximum horizontal displacements and velocities along the east-west running line through the north end of the fault highlight the principle difference between the simulations with dynamic failure and the simulations with prescribed ruptures. From figure 10.36 we see that the maximum displacements for the two scenarios match very well except in the region that lies within about three kilometers of the fault. Similarly, the maximum velocities match very well outside the region that lies within about one kilometer of the fault. The large displacements and velocities next to the fault in scenario unistrain2 come from the rapid slip that occurs at the ground surface. The 0.093 MPa effective normal stresses at the ground surface, which come from the tectonic axial strains, provide little resistance to failure. This allows the large, rapid slips at the top of the fault. Harris and Day (1999) found a negative stress drop effectively prevents slip near the surface.

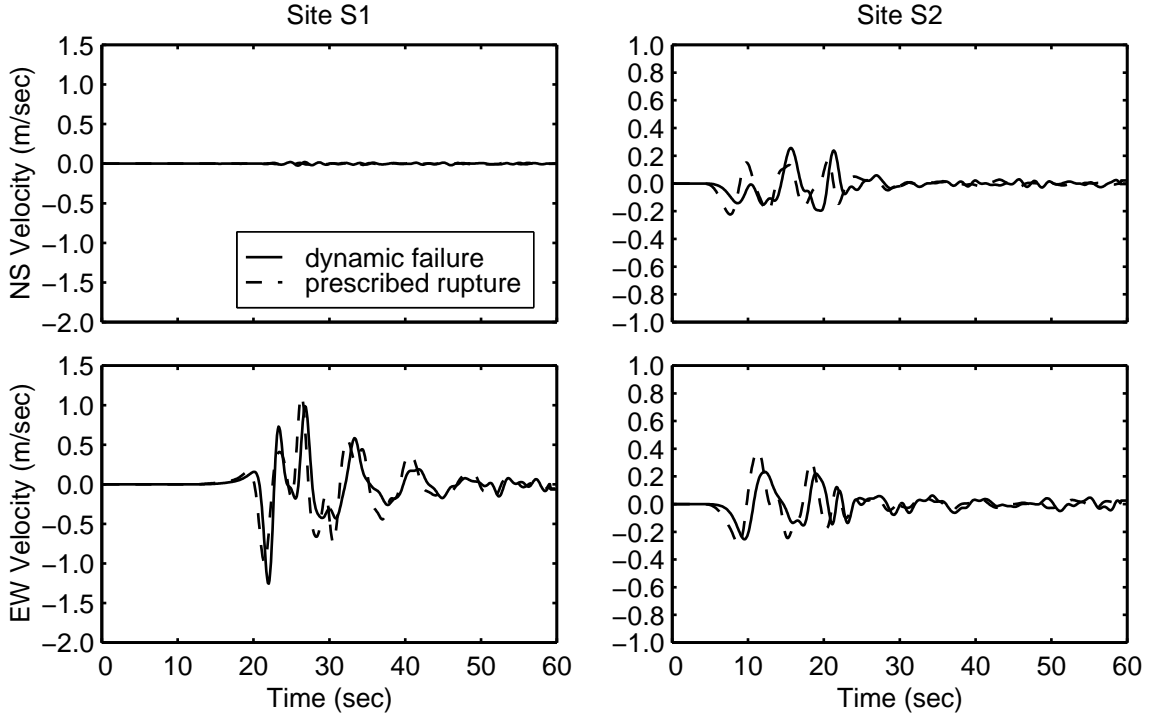


Figure 10.35: Comparison of horizontal velocity time histories at sites S1 and S2 for the dynamic failure scenario unistrain2 and the prescribed rupture scenario hymq.

Alternatively, larger effective normal stresses corresponding to larger tectonic axial strains or modification of the friction model to include cohesion would increase the distance from failure and the fracture energy. These strategies would reduce the slip and slip rates near the surface and bring the maximum displacements and velocities from scenario unistrain2 into better agreement with those from scenario hymq. The general shapes of the curves of the maximum horizontal displacements and velocities from both prescribed rupture scenarios and dynamic failure scenarios match the shape of the near-source factor,  $N_v$ , from the 1997 Uniform Building Code.

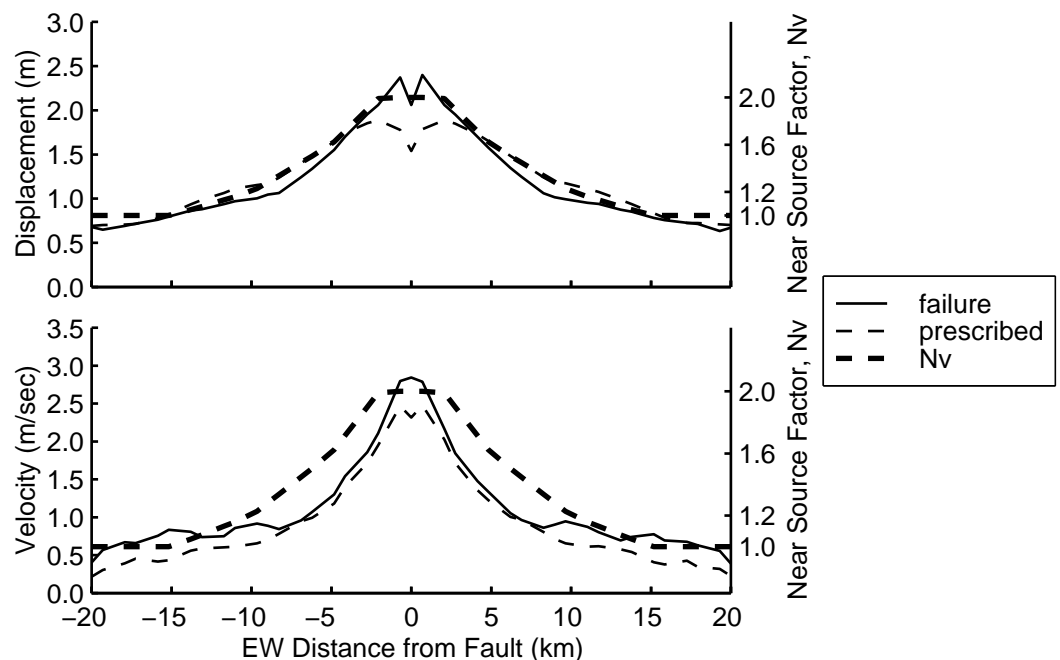


Figure 10.36: Maximum magnitudes of the horizontal displacement and velocity vectors along an east-west line running through the north tip of the fault for the dynamic failure scenario unistrain2 and the prescribed rupture scenario hymq. The thick, dashed line indicates the near-source ground motion factor,  $N_v$ , from the 1997 Uniform Building Code.

## 10.2 Thrust Fault

We follow the same procedure that we use for the strike-slip fault and study dynamic failure on the thrust fault in the layered half-space with the finite-element model from the prescribed ruptures (see section 7.2). Each simulation required 2.6 hours using 16 processors of the Hewlett Packard Exemplar at the CACR. Figure 10.37 shows the partitioning of the mesh among the processors using the METIS library.

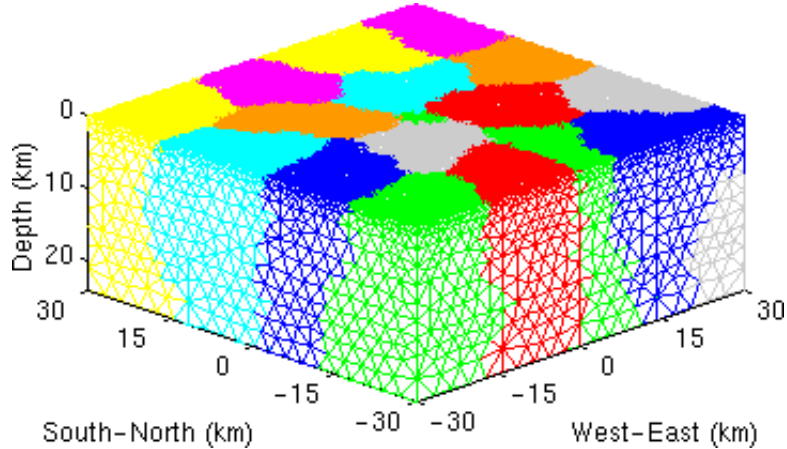


Figure 10.37: Partitioning of the coarse finite-element model among 16 processors for the layered half-space using the METIS library. Each color patch identifies the elements of one processor.

### 10.2.1 Earthquake Source Parameters

We apply uniform horizontal axial and shear strains to generate the shear tractions on the fault. We align the shear tractions with the slip direction of the prescribed ruptures, which has a rake angle of 105 degrees from the strike, and try to match the average slip of 1.0 m from the prescribed ruptures. For inclined faults the average stress drop remains proportional to the product of the shear modulus and average slip, but the proportionality constant depends on the depth of the fault and the dip angle. Consequently, we do not have a simple expression for the average stress drop as a function of the shear modulus and the average slip for inclined faults that we have for strike-slip faults (equation (9.1)) (Parsons et al. 1988). As in the strike-slip fault, the different friction models require different maximum dynamic stress drops to produce comparable slip, so we will discuss the shear tractions on a case by case basis.

We continue to assume that the material contains little water, so that gravity creates lithostatic effective normal stresses. When we bury the fault 8.0 km below the ground surface, the material properties exhibit little change over the depth of the fault. As a result, the uniform tectonic strains will create nearly uniform shear and normal tractions on the fault. The shallow dip of the fault causes the tectonic strains to produce much smaller normal tractions than the normal tractions from gravity. Thus, we will find little change in the normal tractions on the fault surface as we change the maximum dynamic stress drop. We do not change the function form of the friction model; it continues to depend on both the square root of the shear modulus and

the inverse of the depth. We do change the coefficients slightly to create the desired maximum dynamic stress drop and shear stresses at failure.

### 10.2.2 Sensitivity Study

We continue our study of the sensitivity of the long-period near-source ground motion to variations in the initial conditions and parameters of the friction model. In addition to the parameters we examined for the strike-slip fault, we vary the level of the initial shear tractions on the fault. Table 10.3 summarizes the general parameters of the scenarios in the sensitivity study, and table 10.4 displays the basic features of the ruptures for the scenarios. We will examine the scenarios in more detail in the following sections.

Scenario	Initial Traction	Friction Type
unistrain	uniform strain	slip-weakening
unistrain2	uniform strain	same as unistrain
combo8km	uniform strain	slip- and rate-weakening
melt8km	same as combo8km	melting-refreezing
fault4km	uniform strain	same as unistrain
fault0km	uniform strain	same as unistrain
combo0km	uniform strain	same as combo8km
hymc	uniform strain	same as unistrain
shearweak	weakly heter. strain	same as unistrain
shearstrong	strongly heter. strain	same as unistrain
meltstrong	strongly heter. strain	same as melt8km
frictionweak	same as unistrain	weakly heter. slip-weakening
frictionstrong	same as unistrain	strongly heter. slip-weakening

Table 10.3: Summary of the initial tractions and the friction model type for each scenario in the sensitivity study with the thrust fault. When scenarios share exactly the same parameters, we note the common bond in the latter scenarios.

#### Base Case: Scenario unistrain

For the base case we bury the fault 8.0 km below the ground surface. We use a relatively homogeneous distribution of the initial tectonic strains to generate nominal shear tractions of 6.0 MPa on the fault surface; as a result we label the base case scenario unistrain. Equation (10.10) and equation (10.11) give the tectonic strains and the parameters in the lithothrustuf friction model. As in the strike-slip base case, we use the slip-weakening I friction model in the thrust fault base case. We select nominal minimum sliding stresses of 1.5 MPa, a nominal maximum dynamic stress drop of 4.5 MPa, and nominal shear stresses at failure of 10.5 MPa. These correspond to the stresses on the strike-slip fault at similar depths. These initial shear stresses, shear stresses at failure, and minimum sliding shear stresses (shown in figure 10.38) exhibit a small increase over the depth of the fault (8.0 km to 15 km), because the shear modulus increases slightly from a depth of 6.0 km to a depth of 21 km.

Scenario	Average Slip (m)	Max. Slip (m)	Average Max. Slip Rate (m/sec)	Max. Slip Rate (m/sec)	Moment Magnitude	Average Stress Drop (MPa)
unistrain	1.2	2.3	0.79	1.2	6.9	2.6
unistrain2	1.6	2.6	1.1	1.7	7.0	3.5
combo8km	0.72	1.5	0.81	1.4	6.6	1.8
melt8km	0.96	1.7	1.0	1.8	6.8	2.4
fault4km	1.8	3.2	0.91	1.4	7.0	3.1
fault0km	2.5	5.2	1.1	4.7	7.1	1.5
combo0km	1.1	2.6	1.1	6.1	6.8	0.93
hymc	1.2	2.5	0.83	1.4	6.8	1.9
shearweak	1.1	2.0	0.85	1.6	6.8	2.5
shearstrong	1.4	2.5	0.92	1.6	6.9	2.9
meltstrong	1.2	2.3	1.2	2.3	6.8	2.8
frictionweak	1.0	2.2	0.78	1.3	6.8	2.0
frictionstrong	0.83	1.4	0.63	1.2	6.7	1.9

Table 10.4: Summary of the ruptures in the scenarios that we use in the sensitivity study of the thrust fault. We compute the average slip using equation (2.39), the moment magnitude using equation (2.40), and the average stress drop using equation (8.9).

$$\begin{aligned}
 \varepsilon_{yy} &= -2.36 \times 10^{-4} \\
 \varepsilon_{xx} = \varepsilon_{zz} &= 5.84 \times 10^{-5} \\
 \varepsilon_{xy} &= 7.27 \times 10^{-5} \\
 \varepsilon_{yz} = \varepsilon_{xz} &= 0
 \end{aligned} \tag{10.10}$$

$$\begin{aligned}
 \mu_{max} &= \begin{cases} 0.162 & z > -1.0 \text{ km} \\ -2.97 \times 10^{-3} \left( \frac{\text{m}^3 \text{sec}^2}{\text{kg}} \right)^{\frac{1}{2}} \frac{\sqrt{\mu}}{z} & z < -1.0 \text{ km} \end{cases} \\
 \mu_{min} &= \begin{cases} 0.0231 & z > -1.0 \text{ km} \\ -4.24 \times 10^{-4} \left( \frac{\text{m}^3 \text{sec}^2}{\text{kg}} \right)^{\frac{1}{2}} \frac{\sqrt{\mu}}{z} & z < -1.0 \text{ km} \end{cases} \\
 D_o &= 0.338 \text{ m}
 \end{aligned} \tag{10.11}$$

We start the rupture using a shear stress asperity with a radius of 1.8 km located along the north-south running centerline of the fault at a depth of 13.5 km, or 4.0 km up-dip from the bottom of the fault. We taper the shear tractions on all four edges to smother the rupture as it approaches the edges of the fault. Figure 10.39 displays the shear and normal tractions applied to the fault surface.

The rupture begins slowly in response to the placement of the asperity close to the edge of the fault. As shown by the snapshots of slip rate in figure 10.40, at 2.0 sec the rupture is still about the size of the asperity.

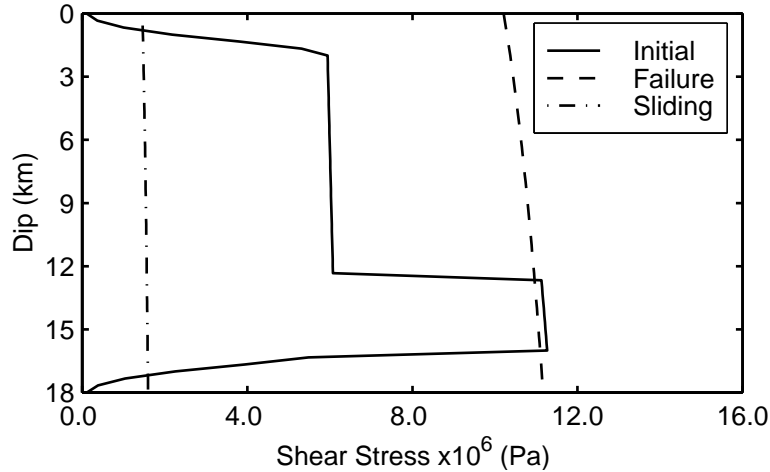


Figure 10.38: Initial, failure, and minimum sliding shear stresses through the center of the asperity on the thrust fault as a function of dip for scenario unistrain.

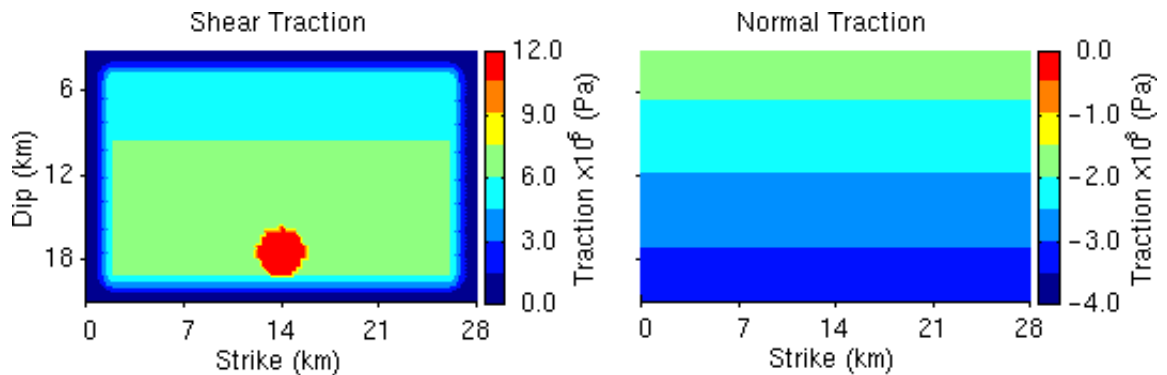


Figure 10.39: Shear and normal tractions on the thrust fault for scenario unistrain.

As the rupture begins to propagate, the rupture front conforms to the familiar elliptic shape with the fastest rupture speed in the direction of slip, which has a rake angle of 105 degrees. The maximum slip rates remain relatively low and the rupture propagates in the direction of slip at a speed of only 2.2 km/sec, or about 67% of the local shear wave speed. The elliptic shape of the rupture front causes the leading edge of the rupture to reach the center of the top of the fault at about 6.5 sec. Meanwhile, the lateral portions of the leading edge of the rupture have propagated a much shorter distance. This gives the rupture a bilateral appearance from 7.0 sec to 9.0 sec. The prescribed ruptures with a uniform rupture speed do not produce this behavior, although we can introduce such behavior with modifications to the algorithm used to set the slip start times which we discussed in section 5.4.

Another phenomenon present in scenario unistrain that fails to appear in the prescribed ruptures is the second slip event near the hypocenter that begins a little before 8.0 sec. The reflection of the dilatational wave off the ground surface generates a shear wave that propagates back down through the fault. As the wave passes through the fault, the dynamic shear stresses cause additional failure on the fault near the hypocenter.

This second slip event lasts only a couple seconds and remains confined to the region around the hypocenter. We will find this second slip strongly sensitive to variations in the initial conditions and the friction model.

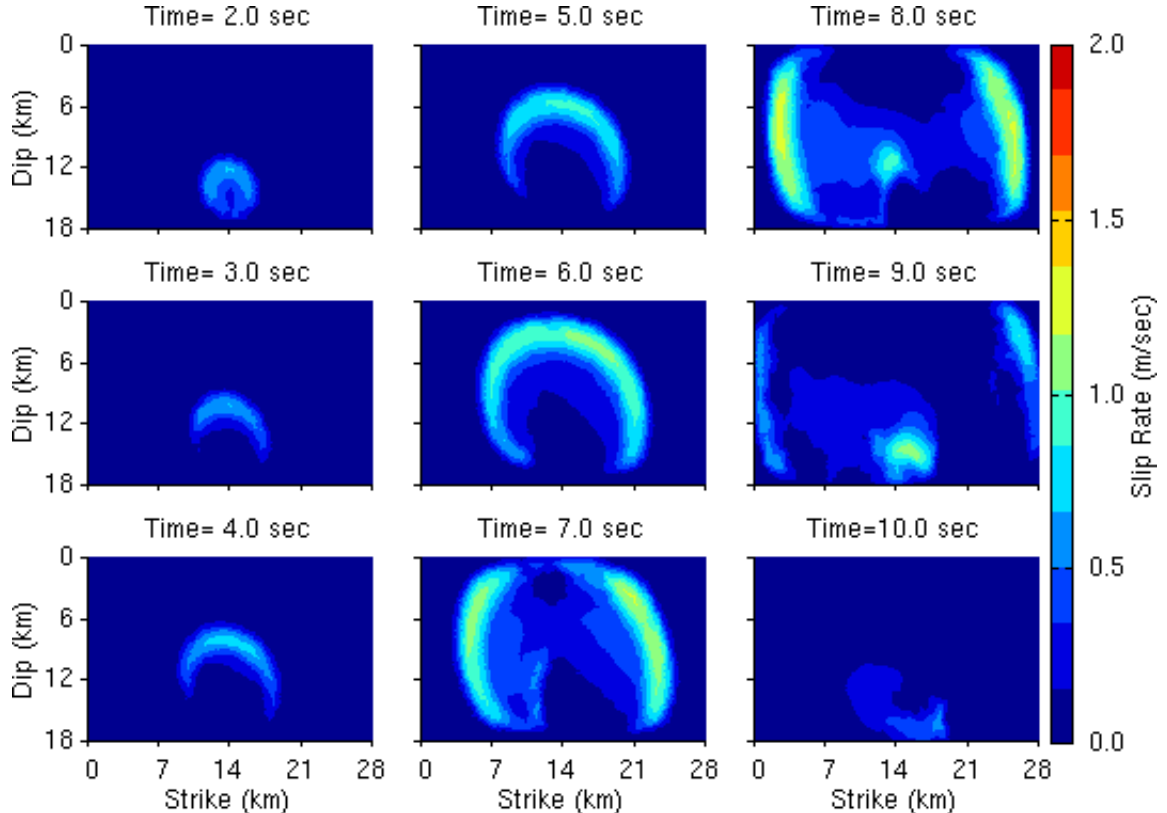


Figure 10.40: Snapshots of slip rate on the thrust fault for scenario unistrain.

The distribution of final slip displayed in figure 10.41 displays no clear trends with depth and resembles the final slip of a uniform stress drop earthquake. The average slip of 1.2 m agrees reasonably well with our target value of 1.0 m. The second slip event caused by the shear wave passing through the fault creates the peak slip of 2.3 m near the hypocenter. The slip rates associated with this second slip event near the hypocenter exceed those in the same region for the first slip event. The maximum slip rates reflect the slow initiation of the rupture. If we neglect the large slip rates near the hypocenter that correspond to the second slip event, then we find the maximum slip rates progressively increase as the rupture propagates. As in the distribution of final slip, we observe no clear trend with depth.

We examine the changes in temperature on the fault surface to determine if melting occurs. As we did for the strike-slip fault, we assume a heat capacity per unit mass of  $1000 \text{ J/(kg}\cdot\text{K)}$  and confinement of the heat to a region that extends 5.0 mm perpendicular to the fault. Figure 10.42 shows the distribution of the change in temperature closely follows the distribution of final slip. This is not surprising because we use a nearly uniform minimum sliding stress coupled with a characteristic slip distance of 0.34 m, which is much smaller than the average slip of 1.2 m. Over most of the fault the maximum temperature change does not exceed 400 degrees Kelvin. Although the temperature change does approach 600 degrees Kelvin in

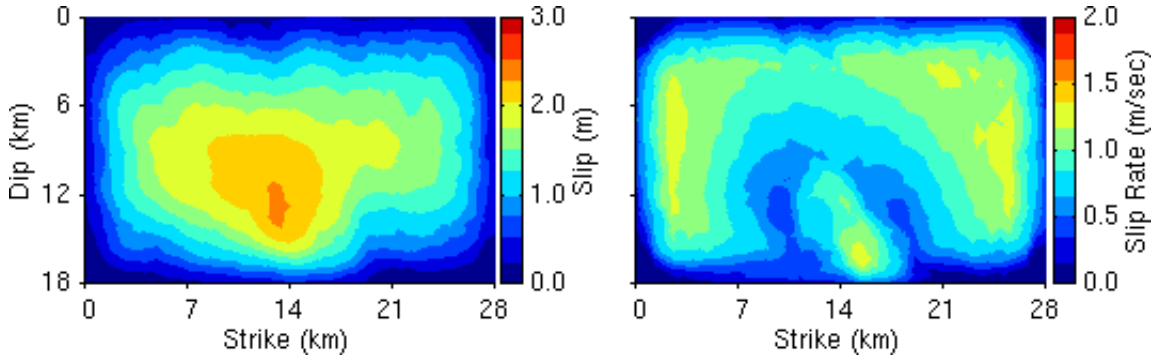


Figure 10.41: Distributions of final slip and maximum slip rate at each point on the thrust fault for scenario unistrain.

the hypocentral region, the changes in temperature remain below the 1000 degrees Kelvin that would imply melting (Kanamori et al. 1998). Thus, we conclude that the level of sliding stress appears realistic based on the lack of melting associated with the estimated changes in temperature.

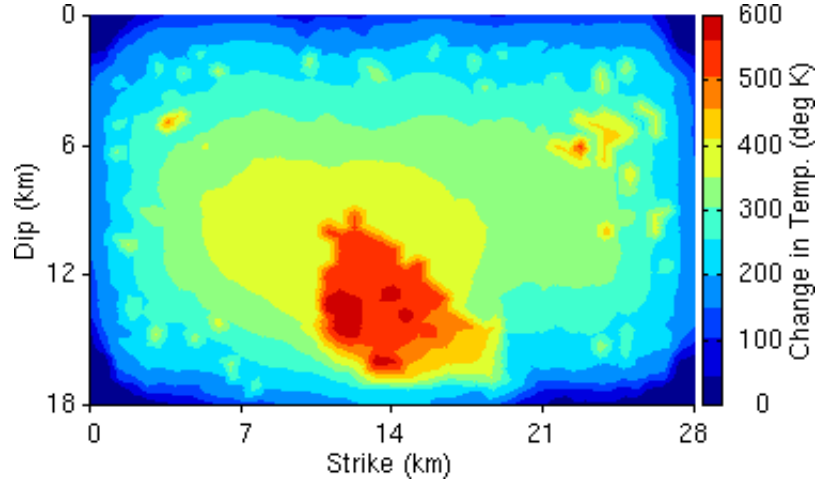


Figure 10.42: Final change in temperature at each point on the thrust fault for scenario unistrain.

The relatively slow rupture speed of 67% of the local shear wave speed allows limited reinforcement of the shear wave by the rupture. Additionally, the bilateral nature of the end of the earthquake directs energy laterally, instead of up-dip from the fault. As a result, we observe significantly smaller ground motions than those from the strike-slip fault with dynamic ruptures and those from the thrust fault with prescribed ruptures. The distribution of the maximum horizontal and vertical displacements given in figure 10.43 shows the directivity of the rupture even at this slow rupture speed. The propagation of the rupture towards the surface along the center of the fault creates the local peaks in the horizontal displacements south of the top of the fault and the vertical displacements just north of the top of the fault. The bilateral nature of the end of the rupture coupled with the south-southeast slip direction creates the large horizontal displacements towards the east. We attribute the local peak in the horizontal displacements north of the epicenter to constructive

interference in the ground motions among the waves coming from the east and west ends of the fault and the second slip event near the hypocenter.

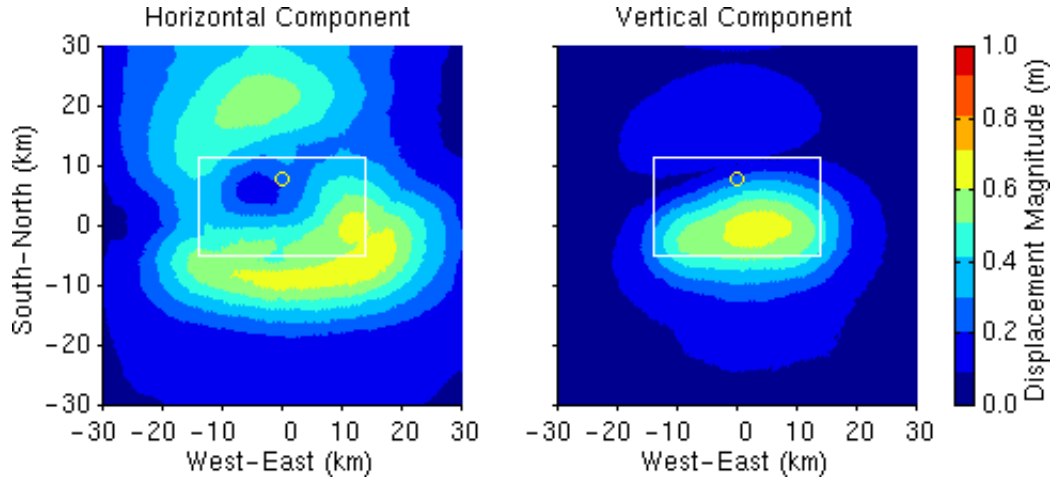


Figure 10.43: Maximum magnitudes of the horizontal and vertical displacement vectors at each point on the ground surface for scenario unistrain. The white line indicates the projection of the fault plane onto the ground surface, and the yellow circle identifies the epicenter.

The peak velocities shown in figure 10.44 exhibit a greater sensitivity to the bilateral nature of the latter part of the rupture. In contrast to the prescribed ruptures where the peak horizontal velocities occur 5.0 km south of the top of the fault, the largest maximum horizontal velocities occur above the east and west edges of the fault. However, we do find locally greater maximum velocities south of the top of the fault. The peak vertical displacement of 0.65 m nearly equals the peak horizontal displacement of 0.68 m, but the peak horizontal velocity of 0.54 m/sec exceeds the peak vertical velocity of 0.29 m/sec by 86%. The prescribed ruptures display a similar discrepancy between the horizontal and vertical velocities compared to the displacements.

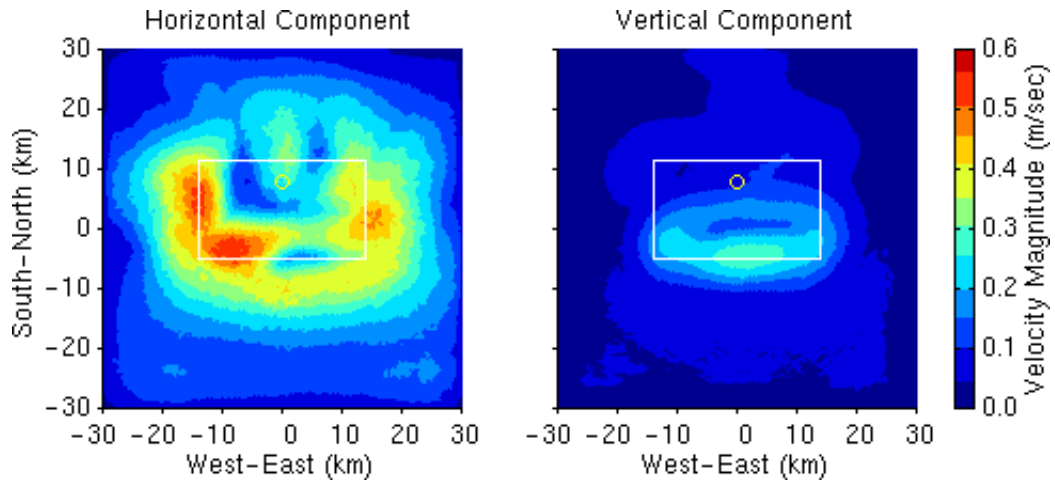


Figure 10.44: Maximum magnitudes of the horizontal and vertical velocity vectors at each point on the ground surface for scenario unistrain. The white line indicates the projection of the fault plane onto the ground surface, and the yellow circle identifies the epicenter.

Figure 10.45 gives the displacement and velocity time histories at site S1, which is located above the southeast corner of the fault, and at site S2, which is located above the middle of the north edge of the fault (see figure 7.31 for a diagram of the site locations). At site S1 we observe pulse-like behavior on all three components with the peak displacements and velocities occurring in the east-west direction. The rebound in displacement creates a single pulse in displacement and a corresponding double pulse in velocity. Based on the slip direction that is only 15 degrees east of south, we would expect larger amplitude motion in the north-south direction compared to the other two directions; however, the bilateral nature of the rupture at the end of the earthquake skews the motion towards the east. At site S2 the largest motion occurs in the north-south direction with a large velocity pulse at 16 sec. This velocity pulse comes predominantly from the second slip event that occurs near the hypocenter, although constructive interference with waves from the east and west ends of the fault also contribute. The rest of the time history features relatively long-period, small amplitude motions that are consistent with the location of the site in the backward direction.

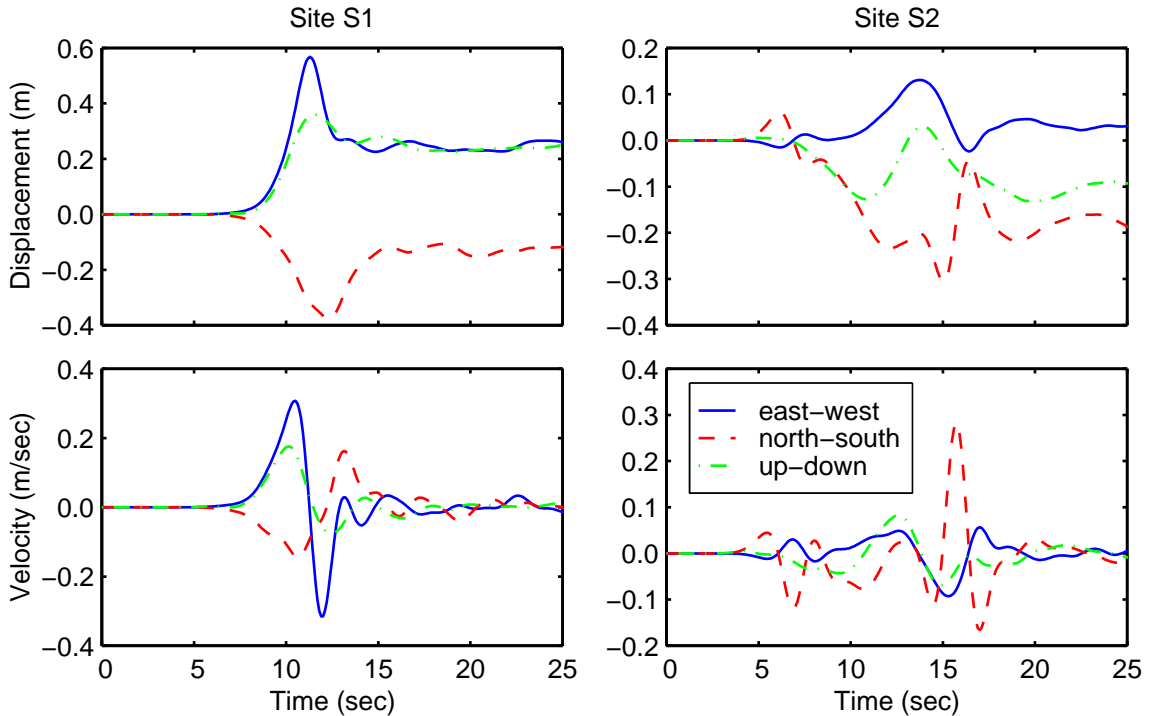


Figure 10.45: Displacement and velocity time histories at sites S1 and S2 for scenario unistrain.

As expected, the uniform strain field and the friction model with dependence on both the shear modulus and depth produces a realistic rupture. The location of the asperity used to start the rupture near the edge of the fault slows the initiation of the rupture and leads to a slow rupture speed. Nevertheless, the rupture creates smooth distributions of final slip and maximum slip rate that agree with our understanding of uniform stress drop earthquakes. Additionally, the average slip of 1.2 m agrees reasonably well with our target value of 1.0 m from the prescribed ruptures. Thus, we choose to use scenario unistrain as the base case for the

sensitivity study.

### Initial Shear Traction

We want to shift the rupture speed to a value near 80–85% of the local shear wave speed that more closely agrees with the rupture speeds observed by Heaton (1990). We accomplish this by increasing the tectonic shear strains given in equation (10.10) by 17% in order to increase the nominal shear tractions from 6.0 MPa to 7.0 MPa. We do not change the friction model or the location of the asperity used to start the rupture from those in scenario unistrain. Comparing the rupture behavior from scenarios unistrain and unistrain2, we observe an increase in the average maximum slip rate from 0.79 m/sec to 1.1 m/sec. This allows the rupture to propagate in the direction of slip at 2.9 km/sec, or 88% of the local shear wave speed, instead of 67% of the local shear wave speed. This increases the reinforcement of the shear wave by the rupture.

Comparing figure 10.43 with figure 10.46, we find substantially larger maximum horizontal and vertical displacements without any significant shifts in the relative distribution. The peak maximum horizontal displacement increases from 0.68 m in scenario unistrain to 1.4 m in scenario unistrain2. Similarly, the peak maximum horizontal velocity increases by 110% from 0.68 m/sec in scenario unistrain to 1.4 m/sec in unistrain2. From figure 10.44 and figure 10.47 we find that the increase in the rupture speed shifts the largest horizontal velocities to the south. The peak horizontal values occur south and east of the top of the fault, which more closely resembles the distributions from the prescribed ruptures. The end of the rupture still retains bilateral characteristics, and we find locally larger horizontal velocities above the east and west edges of the fault. The vertical velocities display only a small shift towards the south with almost no change in the location of the peak value.

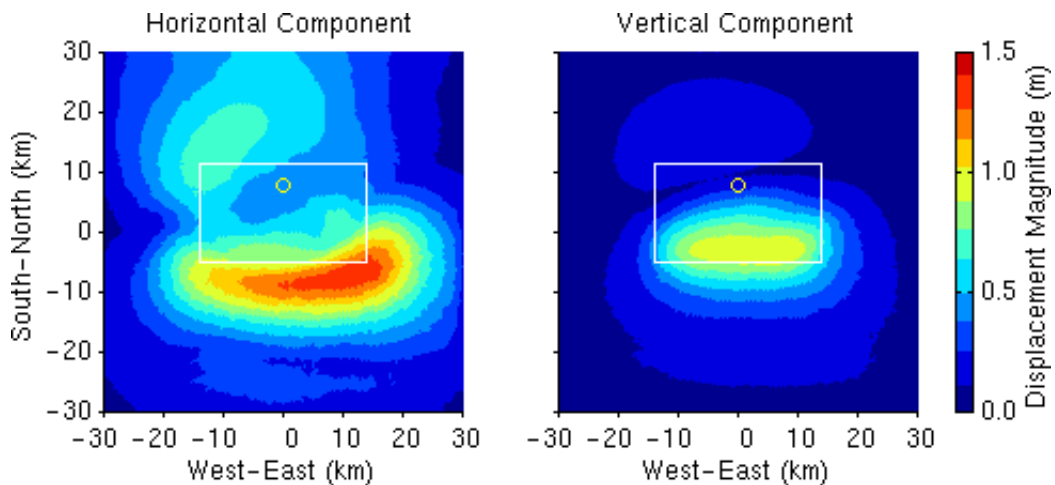


Figure 10.46: Maximum magnitudes of the horizontal and vertical displacement vectors at each point on the ground surface for scenario unistrain2. The white line indicates the projection of the fault plane onto the ground surface, and the yellow circle identifies the epicenter.

At both sites S1 and S2 the increase in the rupture speed causes a dramatic change in the velocity time

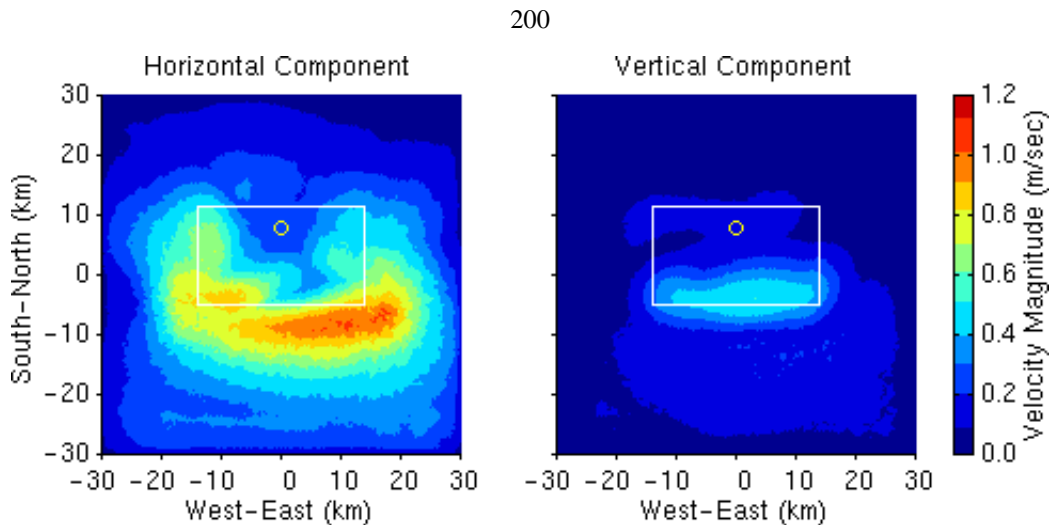


Figure 10.47: Maximum magnitudes of the horizontal and vertical velocity vectors at each point on the ground surface for scenario unistrain2. The white line indicates the projection of the fault plane onto the ground surface, and the yellow circle identifies the epicenter.

histories as shown in figure 10.48. For consistency with the prescribed ruptures we consider motion in the north-south and vertical directions. In the north-south direction at site S1, we see an increase in the peak velocity from 0.16 m/sec to 0.45 m/sec and the waveform for scenario unistrain2 looks like the waveform from unistrain2, but compressed in time. In scenario unistrain2 the double pulse in velocity dominates the time history, while in scenario unistrain the amplitudes of the pulses are only marginally larger than the velocity amplitudes in the latter portion of the time history. The vertical component of velocity at site S1 displays less sensitivity to the increase in the initial tectonic strains with only a 72% increase in the peak velocity and no major changes in the shape of the waveform. The arrival of the shear wave does become sufficiently sharper to create the appearance that the arrival time changes; however, the north-south component clearly shows no change in the arrival time of the shear wave.

The increase in initial tectonic strains allows the second slip event near the hypocenter to propagate farther. This causes significant changes to the amplitude of the motion in the north-south direction at site S2, but little change in the vertical direction. In the north-south direction the initial motion remains nearly identical, but a smaller, double peaked pulse, that arrives at around 12 sec in scenario unistrain2, replaces the narrow velocity pulse, that arrives at 16 sec in scenario unistrain. The vertical component at site S2 shows the compression in time corresponding to the increase in rupture speed but little change in amplitude.

As in the prescribed ruptures, we examine the maximum horizontal displacements and velocities along the north-south line on the ground surface that runs above the center of the fault. Figure 10.49 reflects the increase in the maximum velocities south of the fault in response to the increase in the tectonic strains. The maximum displacements display a similar trend, but the increase is distributed more uniformly across the entire width of the domain. In both scenarios unistrain and unistrain2 the maximum displacements contain a local peak centered approximately 25 km north of the top of the fault. The maximum horizontal velocities do

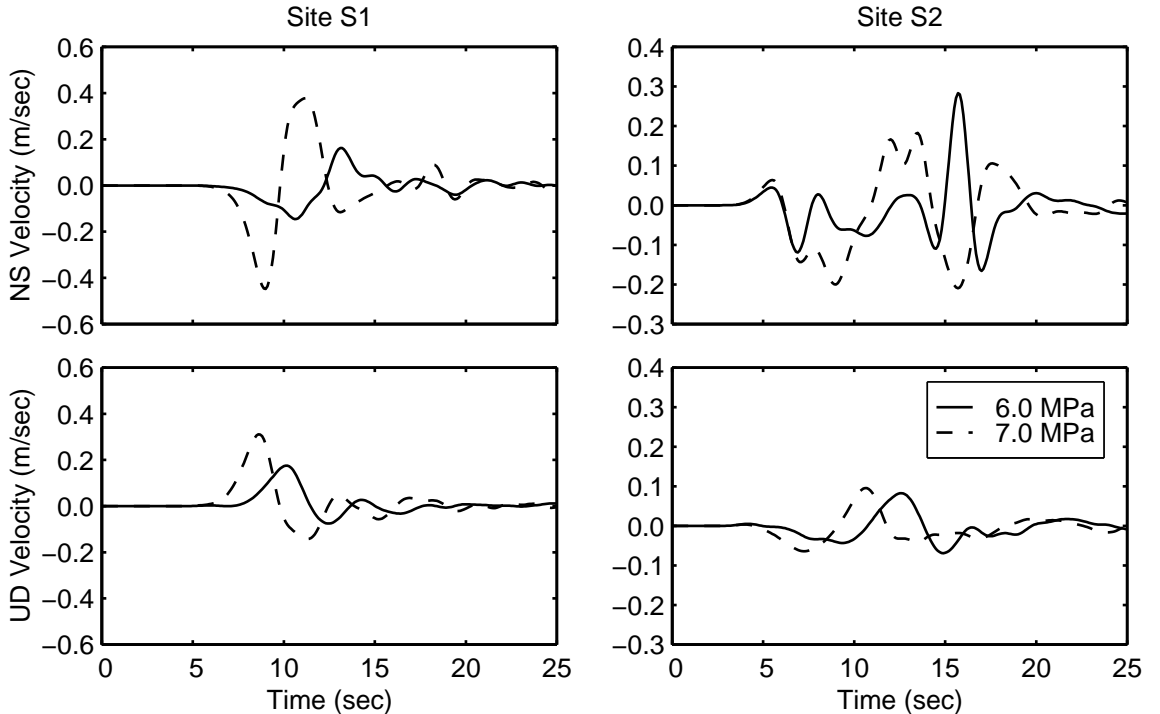


Figure 10.48: Comparison of north-south and vertical velocity time histories at sites S1 and S2 for the two values of the initial shear stress.

not display a corresponding set of peaks.

We overlay the near-source factor,  $N_v$ , from the 1997 Uniform Building even though the California Division of Mines and Geology does not include blind thrust faults on the maps used to determine the near-source factor. The peaks in the curves of the maximum horizontal displacements and velocities both fall outside the region where the near-source factor is a maximum. The shape of the near-source factor does not conform to the peak in the maximum displacements located near the north edge of the domain. We do not find this a significant flaw in the near-source curve, because these local peaks are small relative to the global peak for scenario unistrain2, which contains a more realistic rupture speed compared to scenario unistrain. The peak south of the top of the fault appears in the maximum displacements and velocities for both scenarios. Because this peak dominates the shape of the curves in scenario unistrain2, which has a more realistic rupture speed, and this peak falls outside the region where the near-source factor is at its maximum value, we find the shape of the near-source curve for our blind thrust fault fails to match the distribution of shaking as measured by the maximum horizontal displacements and velocities.

### Friction Model

We examine the sensitivity of the ground motions to the friction model using the slip-weakening friction model (scenario unistrain), the slip- and rate-weakening friction model (scenario combo8km), and the melting-refreezing friction model (scenario melt8km). For scenarios combo8km and melt8km we increase the nom-

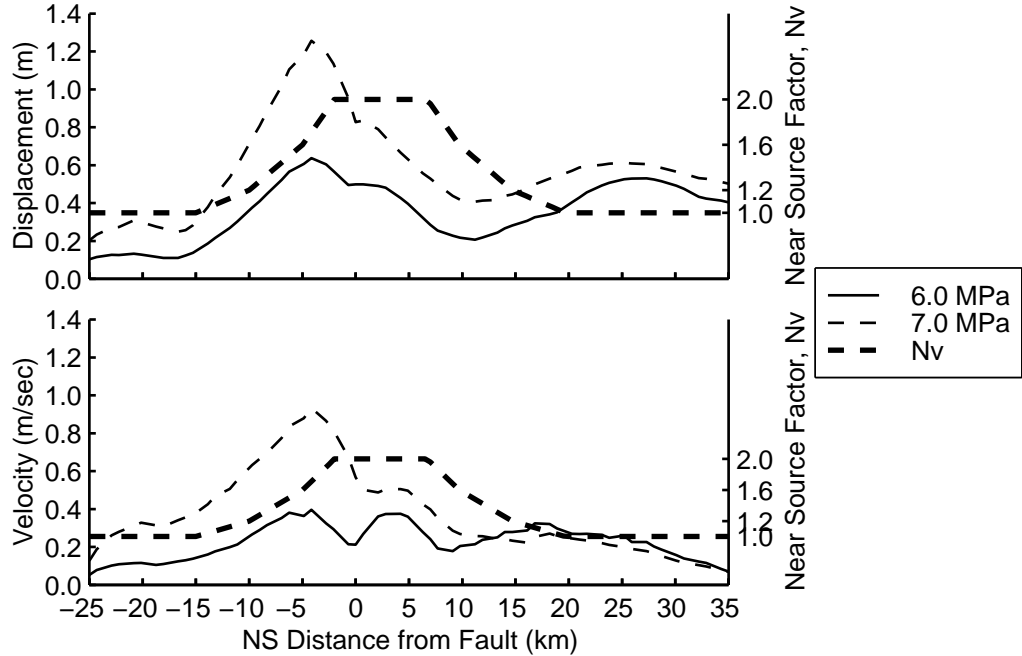


Figure 10.49: Maximum magnitudes of the horizontal displacement and velocity vectors along a north-south line running over the center of the fault for the two values of the initial shear stress. The thick, dashed line indicates the near-source ground motion factor,  $N_v$ , from the 1997 Uniform Building Code.

inal maximum dynamic stresses drop from 4.5 MPa to 6.5 MPa in an attempt to create earthquakes with comparable slip to scenario unistrain. In order to maintain the same nominal minimum sliding shear stresses of 1.5 MPa, we increase the nominal initial shear tractions from 6.0 MPa to 8.0 MPa by scaling the tectonic strains given in equation (10.10) by a factor of 1.33. We scale the distance from failure by the same amount to prevent substantial changes in the rupture speed. Equation (10.12) gives the parameters of the slip- and rate-weakening friction model and the melting-refreezing friction model as a function of depth.

$$\begin{aligned}
\mu_{max} &= \begin{cases} 0.222 & z > -1.0 \text{ km} \\ -4.08 \times 10^{-3} \left( \frac{\text{m}^3 \text{sec}^2}{\text{kg}} \right)^{\frac{1}{2}} \frac{\sqrt{\mu}}{z} & z < -1.0 \text{ km} \end{cases} \\
\mu_{min} &= \begin{cases} 0.0230 & z > -1.0 \text{ km} \\ -4.22 \times 10^{-4} \left( \frac{\text{m}^3 \text{sec}^2}{\text{kg}} \right)^{\frac{1}{2}} \frac{\sqrt{\mu}}{z} & z < -1.0 \text{ km} \end{cases} \\
\mu_{post} &= \begin{cases} 0.153 & z > -1.0 \text{ km} \\ -2.04 \times 10^{-3} \left( \frac{\text{m}^3 \text{sec}^2}{\text{kg}} \right)^{\frac{1}{2}} \frac{\sqrt{\mu}}{z} & z < -1.0 \text{ km} \end{cases} \\
D_o &= 0.446 \text{ m (scenario combo8km)} \\
V_o &= 0.150 \text{ m/sec (scenario combo8km)} \\
D_o &= 0.130 \text{ m (scenario melt8km)} \\
\tau_o &= 0.350 \text{ sec (scenario melt8km)}
\end{aligned} \tag{10.12}$$

The shear re-strengthening friction models with the larger dynamic stress drop produce ruptures with average slips of 0.72 m for scenario combo8km and 0.96 m for scenario melt8km. Hence, despite increasing the maximum dynamic stress drop, the values of average slip do not match as well as we would hope. The final values in the displacement time histories at sites S1 and S2 displayed in figure 10.50 reflect these different values of average slip. Comparing the scenarios with the slip- and rate-weakening friction model and the melting-refreezing friction model with the scenario with the slip-weakening friction model, we notice a decrease in duration of the single pulse in displacement in both the north-south and vertical components at site S1. We associate such compression in time with an increase in the average rupture speed. We observe negligible change in the rupture speed near the end of the rupture, but the larger maximum dynamic stress drop allows the asperity to initiate propagation of the rupture at a faster speed. Thus, the average rupture speed increases due to a faster rupture speed near the beginning of the rupture. The smaller average slip in scenario combo8km produces a peak north-south displacement of only 0.19 m compared to the peak value of 0.43 m in scenario melt8km. In both the north-south and vertical directions the peak displacement in scenario melt8km falls within 17% of the peak values for scenario unistrain.

The shear re-strengthening in the friction models prevents the shear wave that is created from the reflection of the dilatational wave off the ground surface from creating a second slip event on the fault. This leads to a significant reduction in the amplitude of the motion at site S2 for scenarios combo8km and melt8km compared to scenario unistrain. Even with the difference in average slip between scenarios combo8km and melt8km, we find little difference in the displacement time histories. This is not surprising based on the similarity of the friction models and the other features of the ruptures.

Figure 10.51 shows the maximum horizontal displacements and velocities along the north-south line above the center of the fault. The peak horizontal displacements from scenarios combo8km and melt8km

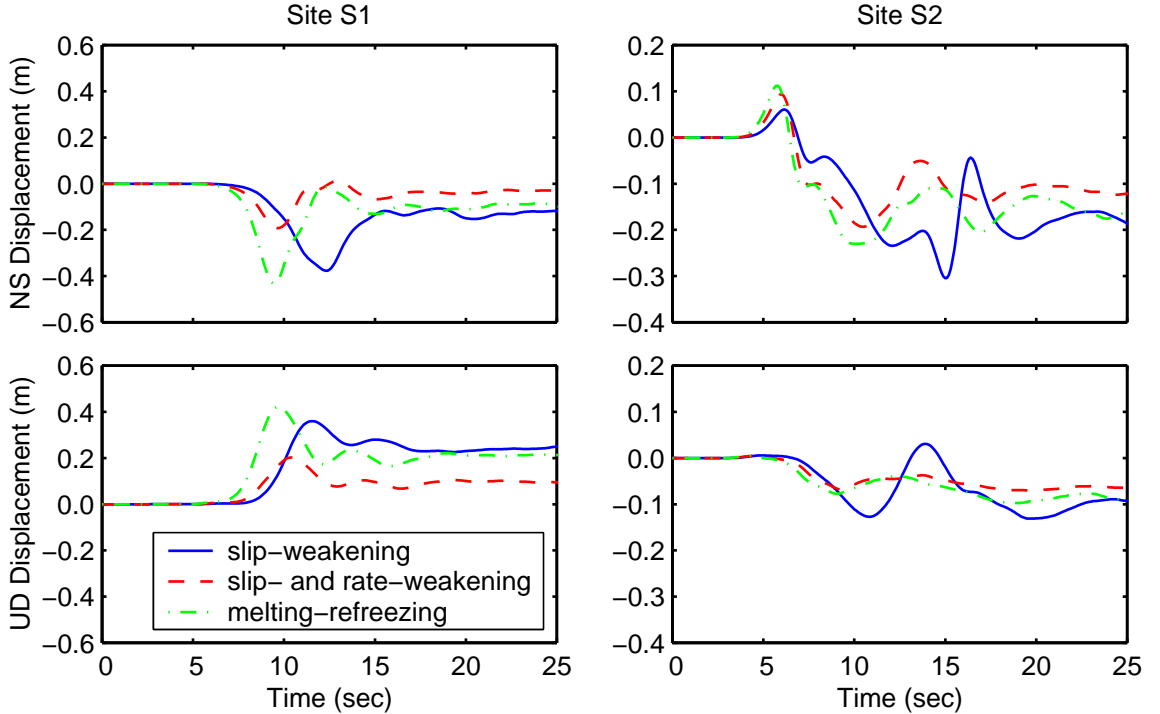


Figure 10.50: Comparison of north-south and vertical displacement time histories at sites S1 and S2 for the three friction models.

do not contain the local peak 25 km north of the top of the fault that we associate with the second slip event near the hypocenter in scenario unistrain. Near the top of the fault, the maximum horizontal displacements from scenarios combo8km and unistrain match, while the maximum horizontal displacements from scenario melt8km are slightly larger. However, the larger slip rates in the scenarios with the larger dynamic stress drop and shear re-strengthening (scenarios combo8km and melt8km) create significantly larger maximum velocities above the top of the fault. We observe no shift in the location of the peak in the curve of maximum displacements or velocities, so it is no surprise that the peak maximum displacements and velocities fall slightly south of the region where the near-source factor is a maximum.

### Fault Depth

We raise the top of the fault in increments of 4.0 km to analyze the sensitivity of the rupture dynamics and the resulting ground motions to the depth of the fault. For scenarios fault4km and fault0km we do not change the strain field (equation (10.10)) or the functions for the parameters of the friction model (equation (10.11)) from those of scenario unistrain where the top of the fault sits at a depth of 8.0 km. Similarly, for scenario combo0km we use the same strain field and slip- and rate-weakening friction model as combo8km. The variation of the parameters in the friction model with the quotient of the square root of the shear modulus and the depth produces the desired variations of the distance from failure and the maximum dynamic stress drop with depth. Figure 10.38 shows the initial shear stresses, the shear stresses at failure, and the minimum

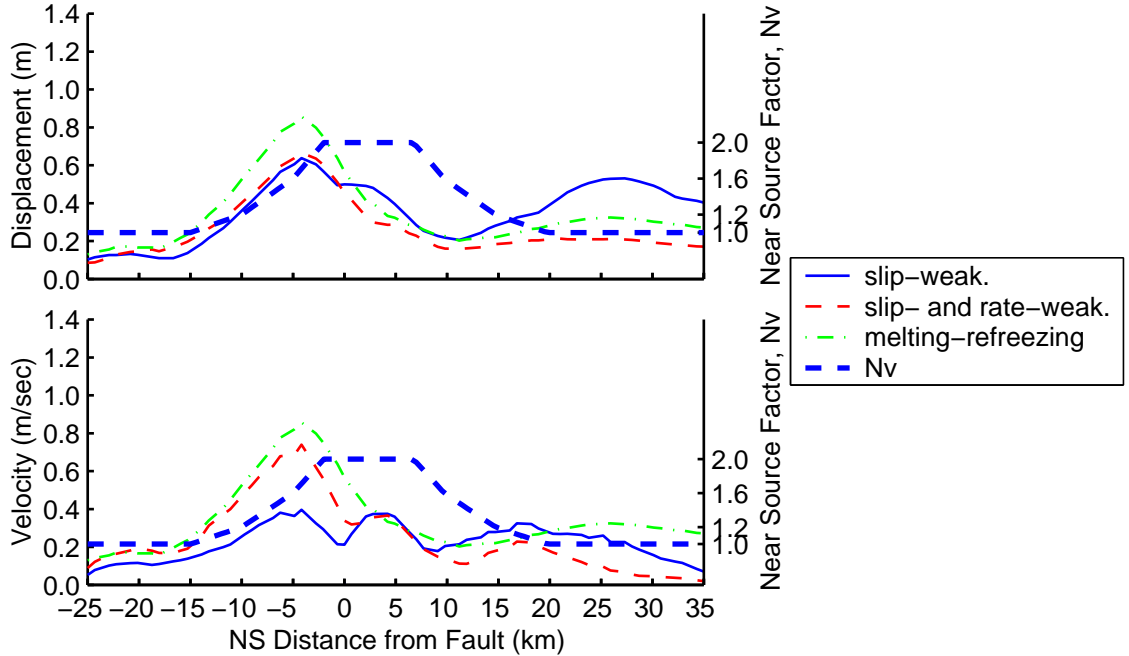


Figure 10.51: Maximum magnitudes of the horizontal displacement and velocity vectors along a north-south line running over the center of the fault for the three friction models. The thick, dashed line indicates the near-source ground motion factor,  $N_v$ , from the 1997 Uniform Building Code.

sliding stresses for scenario fault0km, where the top of the fault sits at the ground surface. Because we use the same material properties and functional form of the slip-weakening friction model for the thrust fault and the strike-slip fault, we find that the shapes of the distributions (figure 10.11 and figure 10.52) look very similar when the top of the faults sit at the ground surface. The principle differences come from the placement of the asperities used to initiate the rupture.

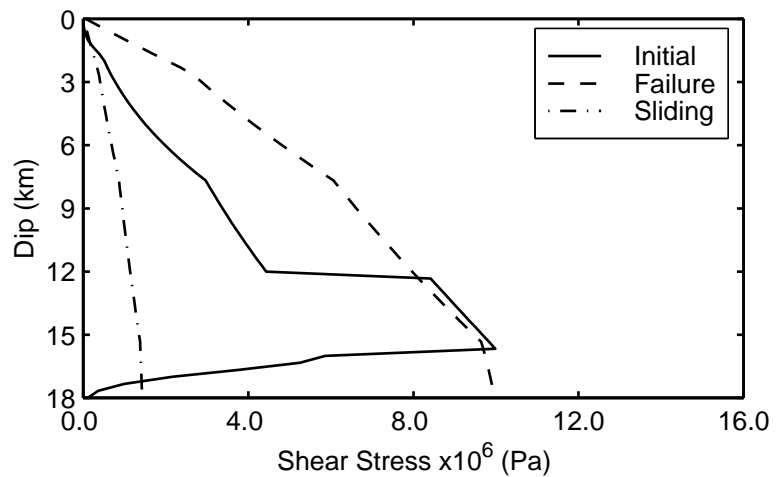


Figure 10.52: Initial, failure, and minimum sliding shear stresses through the center of the asperity on the thrust fault as a function of dip for scenario fault0km.

When the top of the fault reaches the ground surface, the seismic waves become trapped between the fault and the ground surface. For the slip-weakening friction model (scenario fault0km) figure 10.53 provides a closeup view of the snapshots in time of the magnitude of the velocity at each point on a vertical slice through the center of the fault. The snapshots begin at 4.0 sec when the rupture has propagated approximately halfway up the fault, and we observe only minor perturbations in the symmetry of the velocities about the fault plane. We also see the beginning of the amplification of the waves traveling through the softer material on their way to the surface. Beginning at 5.0 sec and continuing until nearly 12.0 sec, we find much larger velocities above the fault than immediately below the fault. The only velocities above 0.2 m/sec below the fault correspond to the motion of the footwall during slip. For a large fraction of this duration, the velocities over a large region saturate the amplitude scale of the plot, so the maximum velocities exceed 0.5 m/sec. When slip occurs on the fault surface, the sliding stresses are low compared to the initial shear stresses, and the fault acts much like a free surface for normally incident shear waves. Consequently, after the seismic waves above the fault reflect off the ground surface and attempt to propagate back through the fault, most of the energy reflects off the fault surface and propagates back towards the ground surface; little of the energy is transmitted across the fault. The energy becomes trapped above the fault and creates severe ground motions above the fault near the surface rupture.

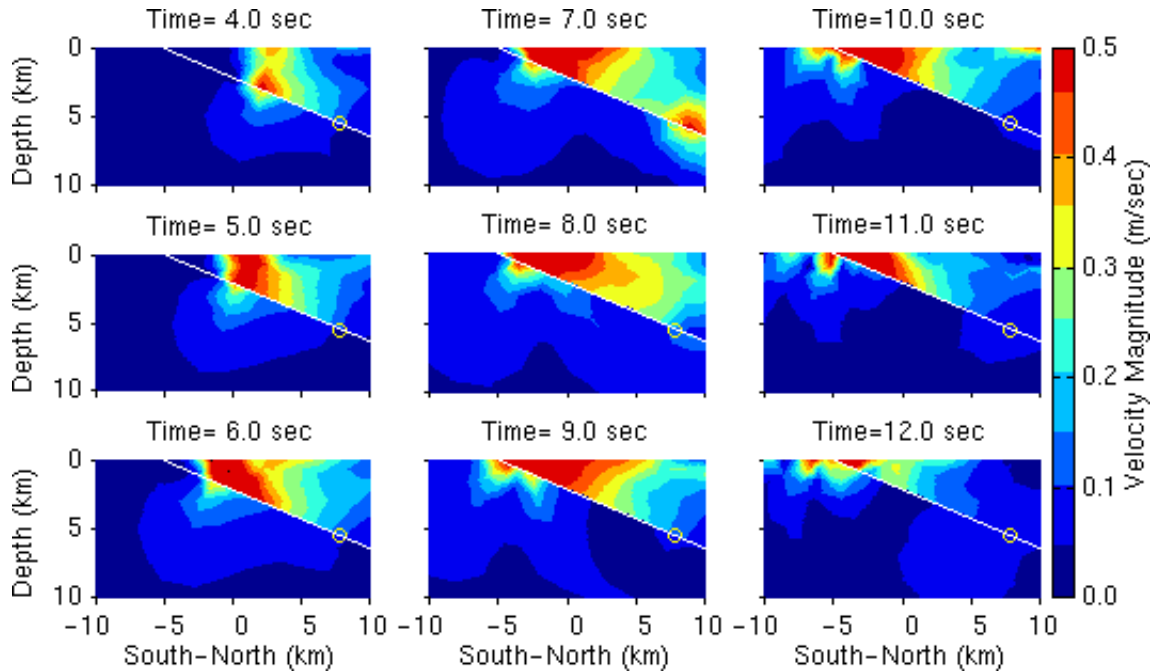


Figure 10.53: Snapshots of the magnitude of the velocity vector on a north-south vertical slice through the center of the fault for scenario fault0km. The white line indicates the projection of the fault onto the vertical slice, and the yellow circle identifies the hypocenter.

The maximum horizontal and vertical displacements in figure 10.54 provide a good indication of the severity of the ground motions near the surface rupture. The entrapment of the seismic waves above the fault

causes nearly all the motion to occur on the hanging-wall side of the fault. The peak maximum horizontal displacements exceed 2.0 m over an area of about 200 square kilometers with a peak value of 6.2 m where the rupture hits the surface. Although the maximum vertical displacements do not reach the same levels as the maximum horizontal displacements, they do exceed 2.0 m along much of the surface rupture.

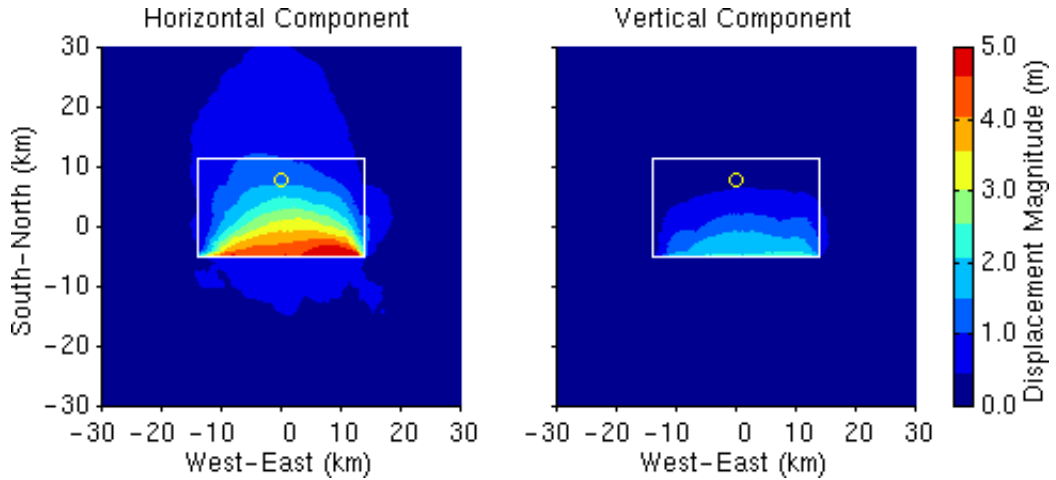


Figure 10.54: Maximum magnitudes of the horizontal and vertical displacement vectors at each point on the ground surface for scenario fault0km. The white line indicates the projection of the fault plane onto the ground surface, and the yellow circle identifies the epicenter.

The extent of the dynamic interaction between the seismic waves and the slip on the fault depends on the width of the rupture front, i.e., the area where slip is occurring. Figure 10.55 displays snapshots of the magnitude of the velocity on the vertical slice through the fault centerline for scenario combo0km, which uses the slip- and rate-weakening friction model. The shear re-strengthening narrows the rupture front which limits the area where the seismic waves may interact with the rupture. Consequently, we do find larger velocities above the fault as in scenario fault0km, but the asymmetry across the fault occurs over a smaller area. Comparing the maximum horizontal displacements from scenario fault0km (figure 10.54) with those from scenario combo0km (figure 10.56), we see a substantial decrease in the values resulting from the smaller amount of dynamic interaction between the seismic waves and the rupture. While the largest motions continue to occur on the hanging wall, the peak maximum horizontal displacement decreases from 6.2 m to 4.0 m. Thus, the lack of any shear re-strengthening in the slip-weakening friction model tends to accentuate the dynamic interaction between the seismic waves and the fault rupture and the entrapment of the waves above the fault.

We now examine the displacement time histories in the north-south and vertical directions at sites S1 and S2 given in figure 10.57 for all three fault depths. At site S1, which sits on the hanging-wall side of the fault, we find a substantial increase in the peak displacements on both components as we move the fault closer towards the surface while using the same slip-weakening friction model; the peak values in the north-south direction increase from 0.38 m to 0.74 m and 1.5 m. When we use the slip- and rate-weakening friction model,

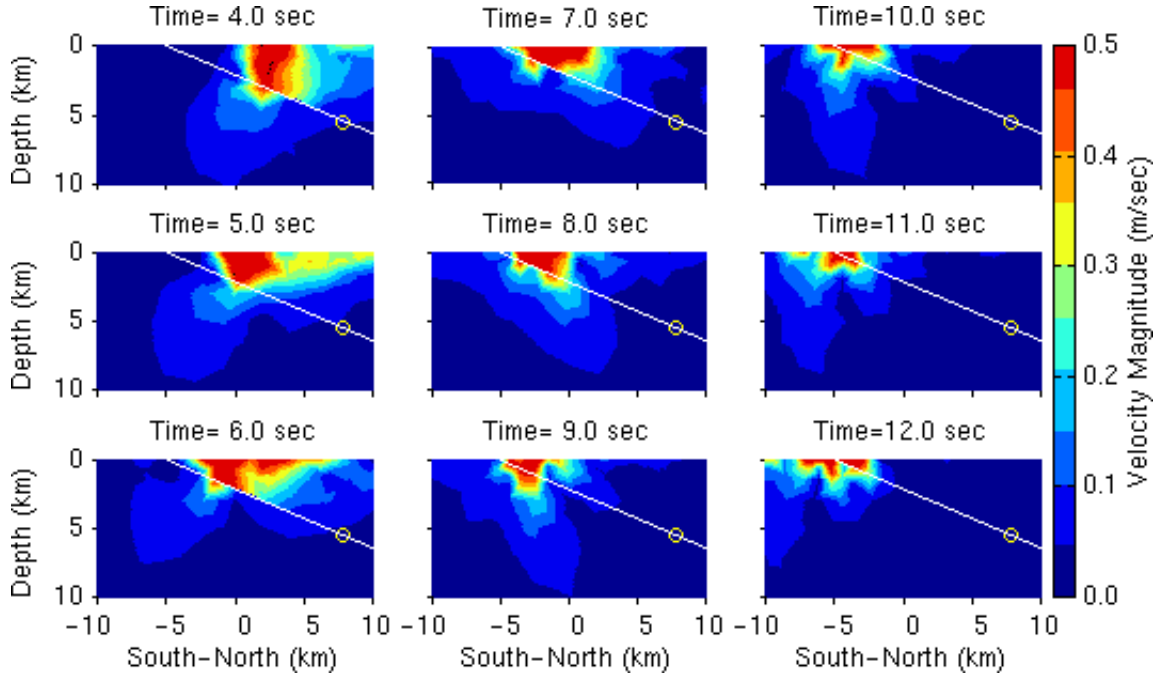


Figure 10.55: Snapshots of the magnitude of the velocity vector on a north-south vertical slice through the center of the fault for scenario combo0km. The white line indicates the projection of the fault onto the vertical slice, and the yellow circle identifies the hypocenter.

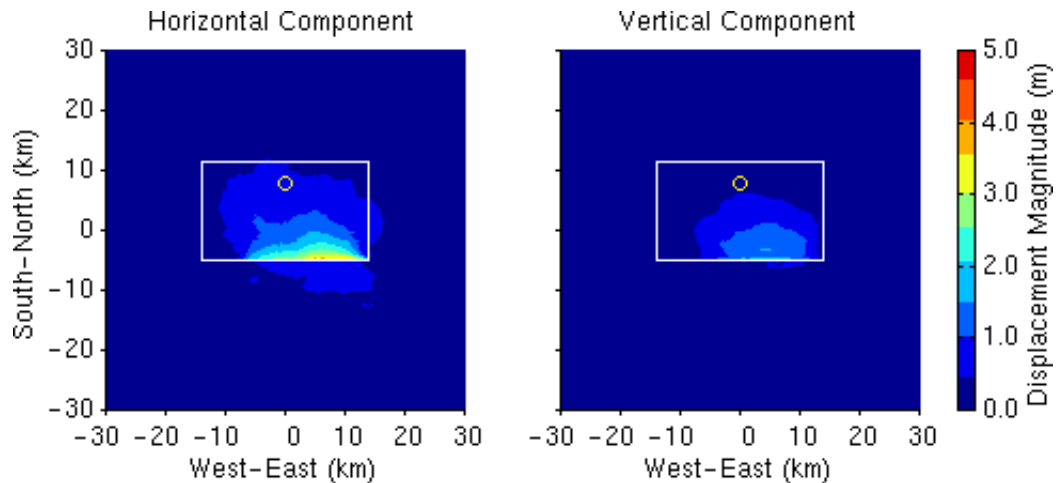


Figure 10.56: Maximum magnitudes of the horizontal and vertical displacement vectors at each point on the ground surface for scenario combo0km. The white line indicates the projection of the fault plane onto the ground surface, and the yellow circle identifies the epicenter.

the smaller amount of dynamic interaction between the seismic waves and the rupture leads to an average slip of 1.1 m compared to the 2.5 m when we use the slip-weakening friction model. As a result, we observe much smaller displacements. The delay in the onset of the large amplitude displacements at site S1 for the two cases of surface rupture stems from the slower rupture speed in the softer material near the surface.

At site S2 we observe little motion in the vertical direction, but the peak displacements in the north-south

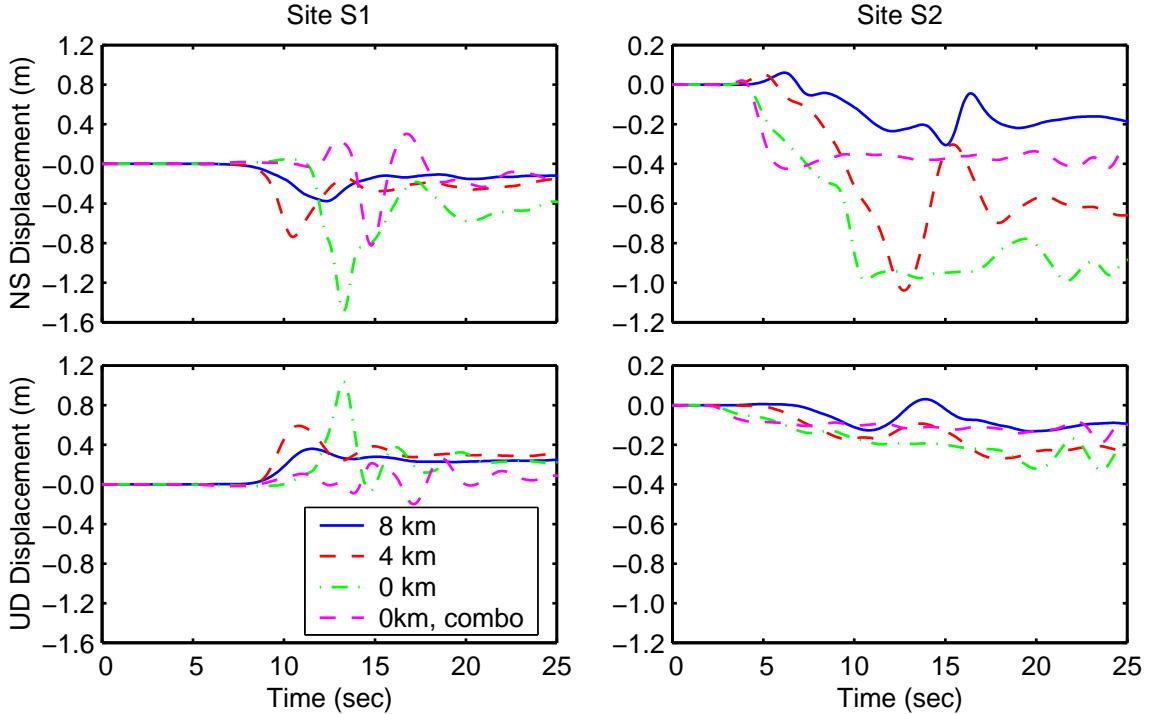


Figure 10.57: Comparison of north-south and vertical displacement time histories at sites S1 and S2 for the three fault depths. The combo in the legend refers to the slip- and rate-weakening friction model.

direction exceed 1.0 m when we use the slip-weakening friction model and the top of the fault lies within 4.0 km of the ground surface. Based on the severity of the ground motions associated with the combination of the slip-weakening friction model and the surface rupture, we are not surprised to find the 1.0 m of displacement at site S2 for scenario fault0km. As we noted in our discussion of site S1, we find much smaller displacements with the top of the fault at the ground surface when we use the slip- and rate-weakening friction model. Comparing the time histories for scenarios fault4km and unistrain we find similar shaped arrivals near the end of the time history. We attribute the pulse in scenario unistrain with a second slip event near the hypocenter, and we find a similar such event in scenario fault4km. Because the fault sits 4.0 km closer to the surface in scenario fault4km, the amplitude of the motion at site S2 from this second slip event exceeds 1.0 m, compared to the peak north-south displacement of 0.30 m in scenario unistrain.

Figure 10.58 shows the maximum horizontal displacements and velocities along the north-south line running over the center of the fault for each of the three fault depths. We also overlay the near-source factor from the 1997 UBC for each case. For the two cases of surface rupture (scenarios fault0km and combo0km), we find that the maximum velocities roughly match (3.3 km/sec and 3.2 km/sec), while the displacements from scenario fault0km (slip-weakening friction model) exceed those from scenario combo0km (slip- and rate-weakening friction model) by 54%. As discussed above, this difference stems from the larger area where the seismic waves interact with the rupture in scenario fault0km compared to scenario combo0km. For these two cases with surface rupture, we find that the peak values of the near-source curve encompass the

locations of the peak maximum displacements and velocities. This should be expected because the California Division of Mines and Geology includes thrust faults with surface rupture in the maps used to determine the near-source factor. As we lower the top of the fault, the peak maximum displacements and velocities shift towards the up-dip direction. When the top of the fault sits 4.0 km below the ground surface, the peak maximum horizontal velocity occurs at the edge of the region where the near-source curve is at a maximum. As discussed in the previous sections, the maximum displacements and velocities along this line fall outside this region when we bury the top of the fault 8.0 km below the ground surface.

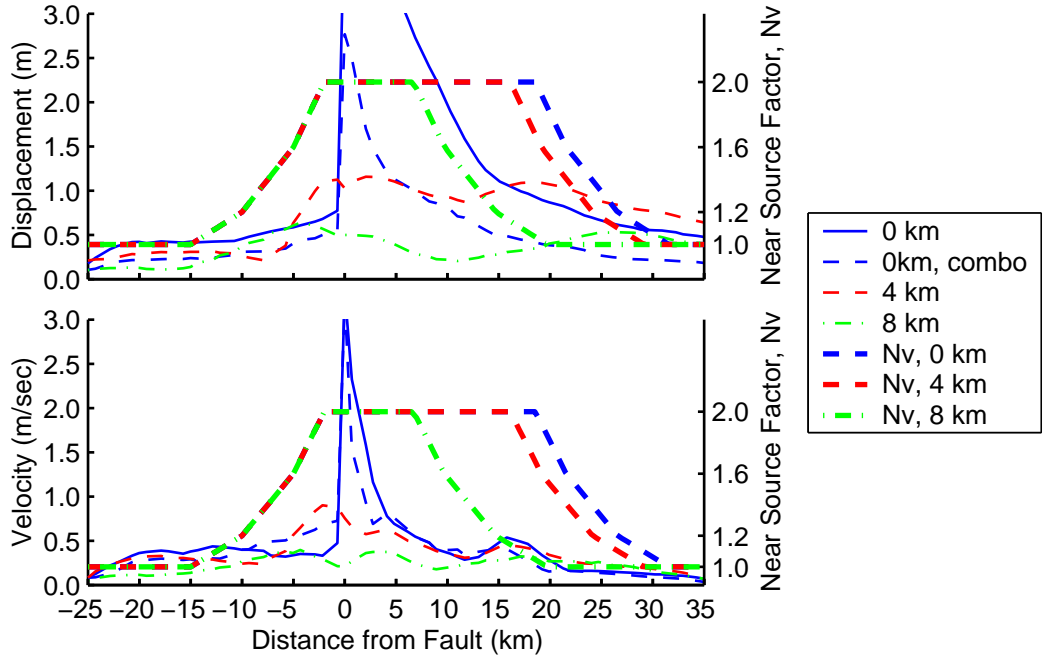


Figure 10.58: Maximum magnitudes of the horizontal displacement and velocity vectors along a north-south line running over the center of the fault for the three depths of the top of the fault. The combo in the legend refers to the slip- and rate-weakening friction model. The thick, dashed line indicates the near-source ground motion factor,  $N_v$ , from the 1997 Uniform Building Code for the three fault depths.

### Hypocenter Location

We move the location of the shear asperity that starts the rupture 6.3 km up-dip along the fault centerline in order to move the hypocenter from a depth of 13.4 km (scenario unistrain) to a depth of 11.0 km (scenario hymc). The deep hypocenter sits roughly 4.0 km up-dip from the one denoted bottom center in the prescribed ruptures and labeled HA in figure 7.31. The shallow hypocenter matches the middle center location in the prescribed ruptures and is labeled HD in the figure. The change in the hypocenter location sufficiently alters the dynamics of the rupture to remove the second slip event near the bottom of the fault that we observe in scenario unistrain. Additionally, in scenario hymc the bilateral nature of the rupture increases with the central location of the hypocenter.

These two factors have little impact on the ground motions at site S1. In figure 10.59 we observe almost no change in the shape of either the north-south or vertical components, and less than a 17% change in the peak velocity. The slightly earlier arrivals correspond to the shorter travel time from the shallow hypocenter compared to the deep hypocenter. In the north-south direction at site S2, the lack of the second slip event in scenario hymc, coupled with the stronger bilateral nature of the rupture, removes the velocity pulse that occurs at 16 sec in scenario unistrain and adds the broad, double pulse in velocity that arrives at 10 sec. In the vertical direction we observe a broadening of the small amplitude pulse, but only a moderate change in amplitude.

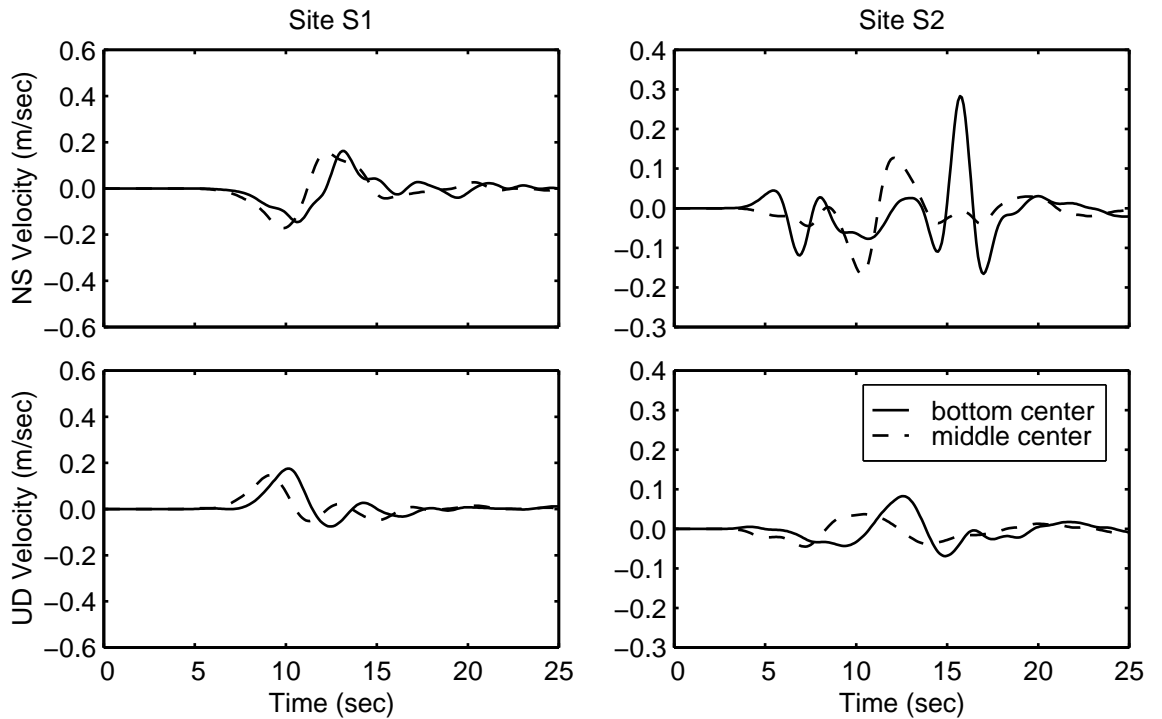


Figure 10.59: Comparison of north-south and vertical velocity time histories at sites S1 and S2 for the two hypocenter locations.

The shift in the hypocenter location to a shallow depth does reduce the ground motions up-dip from the top of the fault. Figure 10.60 displays the maximum horizontal displacements and velocities along the north-south line over the center of the fault. Remarkably, the only significant changes in the curve of the maximum displacements occur in the first 15 km that lie up-dip from the top of the fault. In this region the values decrease with the shallower hypocenter. The maximum velocities exhibit a more uniform decrease along the line with the shift in the hypocenter to the middle of the fault. We do find a slightly greater relative decrease in the peak maximum velocity that occurs 5.0 km up-dip from the top of the fault. This is consistent with the decrease in the maximum displacements in the same region. With the change in the curves of the maximum displacements and velocities, we find a better match between the curves for scenario hymc and the shape of the near-source factor. The near-source factor does not conform to the local peak in the maximum

displacements that in both scenarios sits about 26 km north of the top of the fault. As we noted in our discussion of the scenarios with the different initial shear tractions, this peak becomes significant only when the ground motions near the top of the fault are small, so we do not find this a significant difference between the curves of the maximum horizontal displacements and velocities and the near-source factor.

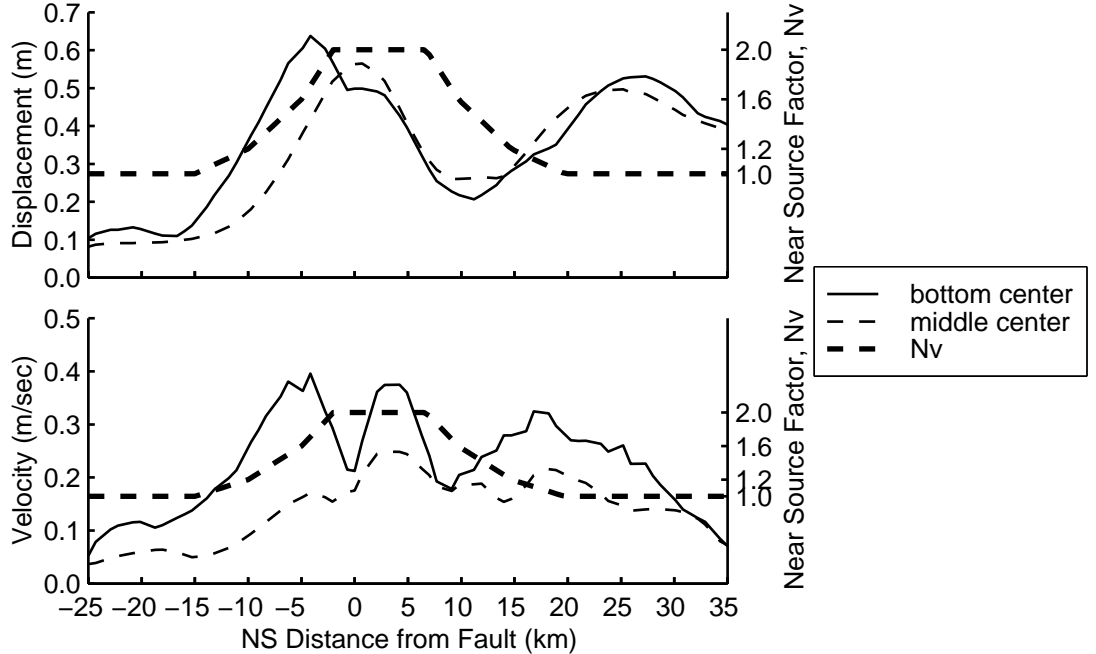


Figure 10.60: Maximum magnitudes of the horizontal displacement and velocity vectors along a north-south line running over the center of the fault for the two hypocenter locations. The thick, dashed line indicates the near-source ground motion factor,  $N_v$ , from the 1997 Uniform Building Code.

### Heterogeneity in Initial Shear Traction

We introduce heterogeneity into the initial shear tractions through the strain field. We create both weakly heterogeneous (scenario shearweak) and strongly heterogeneous (scenario shearstrong) distributions of the initial shear tractions. The distributions each contain 20 asperities with uniform distributions of radii between 3.0 km and 8.0 km and uniform random distributions of locations along the strike and dip. We do not allow the asperities within 2.0 km of the edges of the fault to prevent alteration of the tapering in shear stresses. As in the strike-slip scenarios with heterogeneous shear stresses, we uniformly distribute the asperity heights between plus and minus 30% and 60% of the nominal strain field (equation (10.10)) for the weakly and strongly heterogeneous distributions.

Figure 10.61 shows the initial shear stresses, the shear stresses at failure, and the sliding shear stresses on the fault surface for scenario shearstrong. For scenarios shearweak and shearstrong the friction model remains the same as the one in scenario unistrain, so that the shear stresses at failure and minimum sliding shear stresses remain relatively uniform. We also create scenario meltstrong which features a strongly heteroge-

neous distribution of initial shear tractions and the melting-refreezing friction model (equation (10.12)) from scenario melt8km. To create the strongly heterogeneous shear tractions for scenario meltstrong with the larger dynamic stress drop, we superimpose the tectonic strain asperities from scenario shearstrong on the tectonic strains from scenario melt8km. This creates a strongly heterogeneous distribution of shear tractions with the appropriate nominal maximum dynamic stress drop of 6.5 MPa that we need to generate comparable slip to that in scenario unistrain with the melting-refreezing friction model, which contains shear re-strengthening.

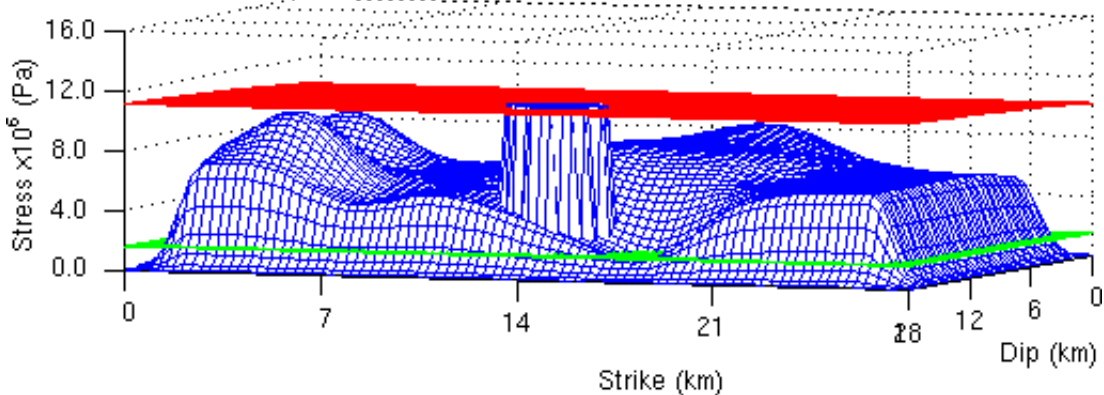


Figure 10.61: Initial (blue), failure (red), and minimum sliding (green) shear stresses on the thrust fault for scenario shearstrong.

We compare the distributions of final slip and maximum slip rate from scenarios shearstrong and meltstrong with those from scenario unistrain (figure 10.41) to determine if the heterogeneous shear tractions introduce heterogeneity in the distributions of final slip and maximum slip rate. As shown in figure 10.62, when we use the slip-weakening friction model, the strongly heterogeneous tractions have little effect on the final slip distribution but do introduce some heterogeneity in the maximum slip rate. The local extrema in the maximum slip rate correlate with the extrema in the initial shear tractions. Comparing the distributions of final slip for scenarios shearstrong and unistrain, we find that the most noticeable difference occurs in the top east corner of the fault, where the slip decreases in response to the smaller maximum slip rates. In scenario meltstrong (figure 10.63) we find a strong correlation between the distributions of final slip and maximum slip rate. While the average maximum slip rate increases from 0.80 m/sec in scenario unistrain to 1.2 m/sec in scenario meltstrong, we observe no change in the average slip (1.2 m). These larger slip rates allow the rupture to generate the same slip over a shorter period of time that corresponds to the narrower width of the rupture front. Thus, we find that the shear re-strengthening in the friction model localizes the slip, which enables the heterogeneity in shear tractions to create a heterogeneous slip distribution.

The heterogeneity in the distribution of final slip in scenario meltstrong influences the maximum velocities. Comparing the maximum horizontal and vertical velocities from scenario unistrain in figure 10.44 with those from scenario meltstrong in figure 10.64, we see a general shift towards larger values in the forward direction. The location of the largest shear stresses near the top of the fault tends to increase the ground

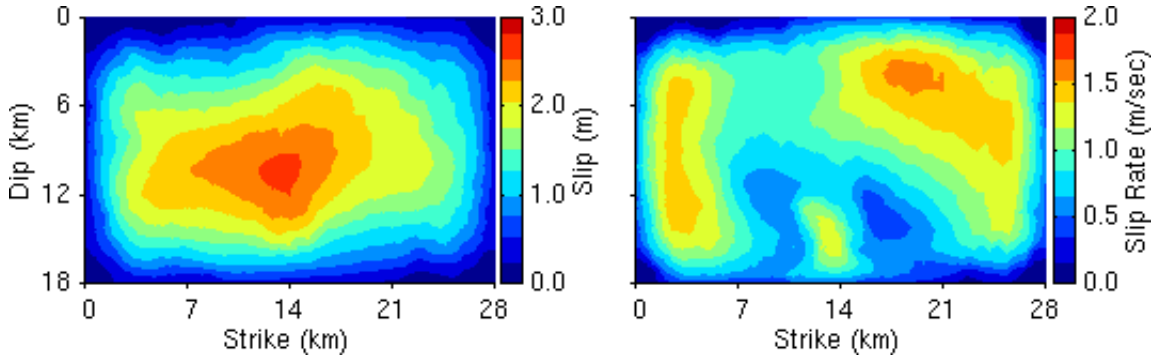


Figure 10.62: Distributions of final slip and maximum slip rate at each point on the thrust fault for scenario shearstrong.

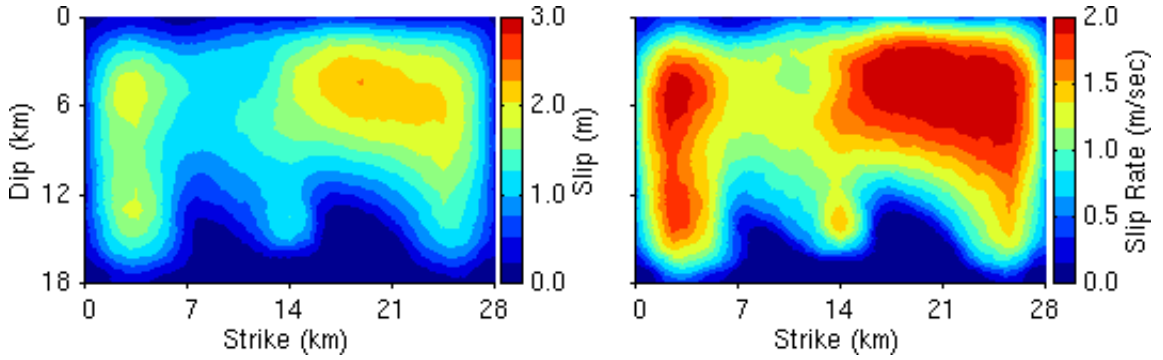


Figure 10.63: Distributions of final slip and maximum slip rate at each point on the thrust fault for scenario meltstrong.

motions above the top of the fault. Thus, for this random distribution of asperities, the local effects of the asperities with large shear stresses, which tend to increase the ground motions, overcome the general effect of the heterogeneity, which tends to decrease the ground motions. The peak maximum vertical velocity remains above the top of the fault, but the largest maximum horizontal velocities shift to above the southwest corner of the fault where the greatest slip and maximum slip rates occur. The distribution of the maximum horizontal velocities continues to contain local maxima along the east, south, and west edges of the surface projection of the fault.

We compare the velocity time histories at sites S1 and S2 to gauge the sensitivity of the ground motions to the heterogeneity in the tectonic strains. The north-south and vertical velocities at site S1, which are displayed in figure 10.65 for the four scenarios (unistrain, shearweak, shearstrong, meltstrong), all have the same general shape. The different timing of the peak velocities reflects the variability in the rupture speed as the ruptures encounter the different degrees of heterogeneity. The peak velocities in the north-south direction vary from 0.16 m/sec in scenario unistrain to 0.31 m/sec in scenario shearweak. At site S2 the vertical velocities exhibit little variation across the four scenarios. In the north-south direction the presence or absence of the second slip event near the hypocenter strongly influences the variability in the ground motion. Scenarios unistrain and shearstrong both contain the second slip event and the large velocity pulses at around

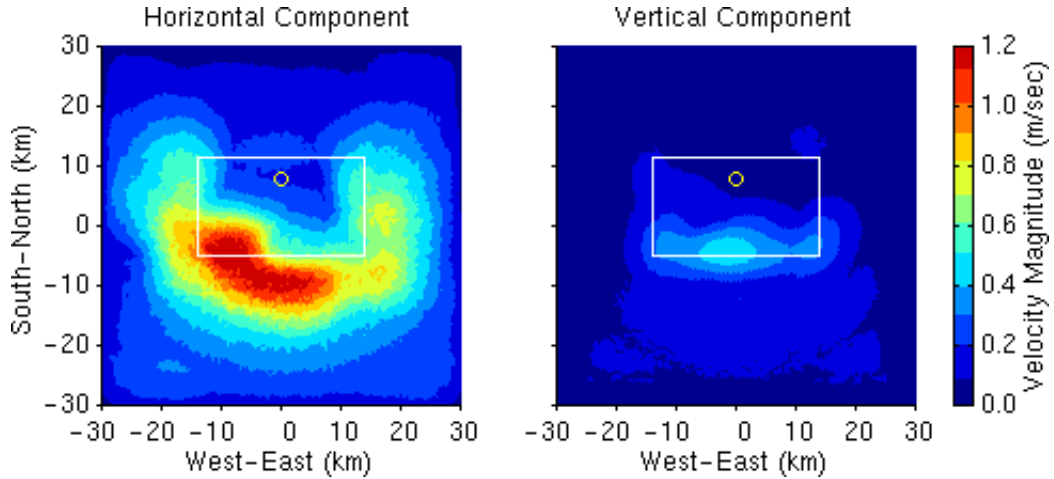


Figure 10.64: Maximum magnitudes of the horizontal and vertical velocity vectors at each point on the ground surface for scenario meltstrong. The white line indicates the projection of the fault plane onto the ground surface, and the yellow circle identifies the epicenter.

15 sec. Moreover, scenarios shearweak and meltstrong do not contain the second slip event, and the velocity time histories differ considerably, both from the other two scenarios and from each other.

Despite the wide variability in the velocity time histories, the maximum horizontal displacements and velocities along the north-south line over the center of the fault change little in shape across the four scenarios, as shown in figure 10.66. In contrast to the strike-slip simulations where the addition of heterogeneity in the initial tractions tends to decrease the motion, the addition of heterogeneity tends to increase the ground motions on the ground surface for the thrust fault. As discussed above, we attribute this increase to the random location of the asperities with large shear stresses near the surface. These asperities are most prevalent in the strongly heterogeneous distribution of the initial shear tractions. The larger slip and faster slip rates near the top of the fault in scenario meltstrong lead to substantially greater peak maximum displacements and velocities compared to the other scenarios. Nevertheless, we observe no shift in the location of the peak relative to the top of the fault; the peak continues to fall 5.0 km south of the top of the fault and outside the region with the largest near-source factor. In the forward direction (south of the top of the fault) the curves for scenarios shearweak and shearstrong show negligible sensitivity to the increase in heterogeneity in the tectonic strains. The second slip event near the hypocenter in scenario shearstrong does create larger maximum displacements and velocities in the backward direction compared to scenario shearweak.

### Heterogeneity in Friction Model Parameters

We create heterogeneity in the lithothrustuf friction model by following the same procedure that we use to create heterogeneity in the friction model for the strike-slip simulations. We independently vary the coefficients in the expressions for  $\mu_{max}$  and  $\mu_{min}$  by 20% and 40% above and below the nominal value to generate weakly and strongly heterogeneous distributions. We do not include heterogeneity in the characteristic slip

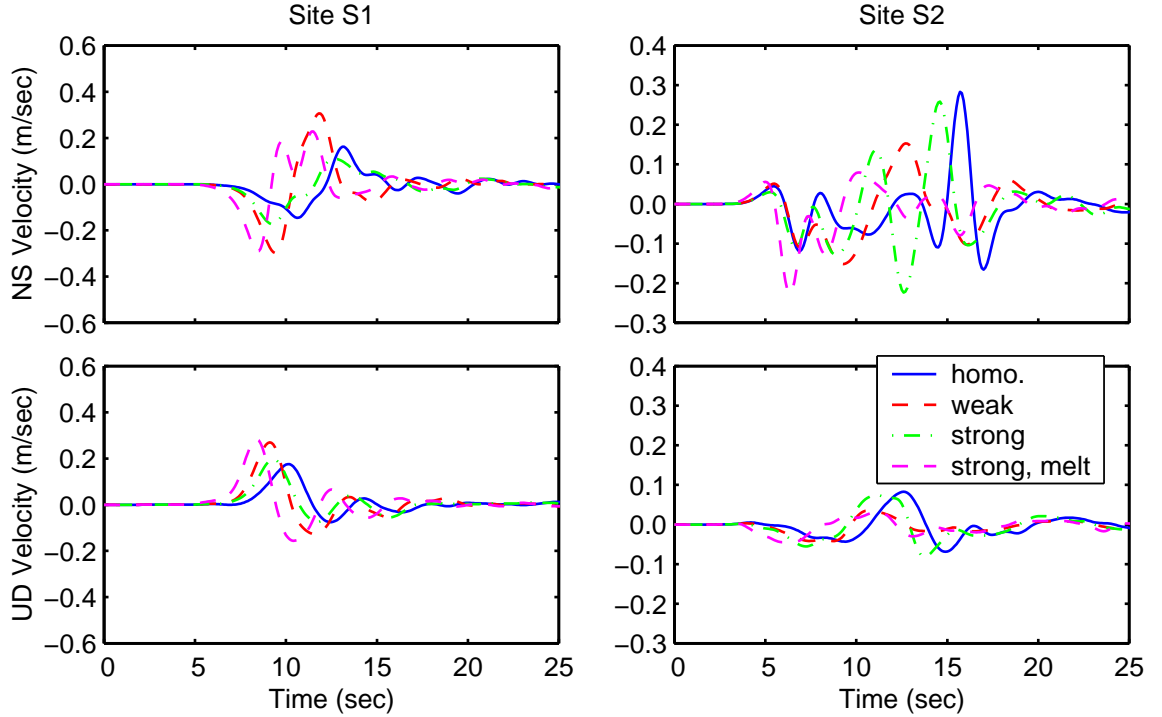


Figure 10.65: Comparison of north-south and vertical velocity time histories at sites S1 and S2 for the four cases of heterogeneity in the initial shear tractions.

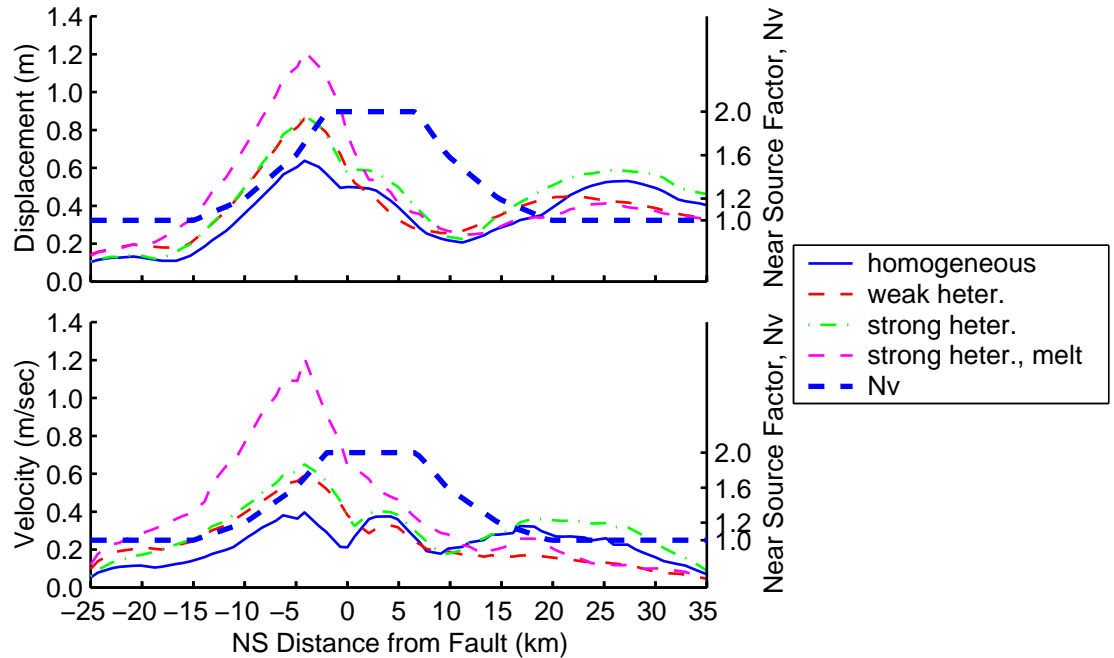


Figure 10.66: Maximum magnitudes of the horizontal displacement and velocity vectors along a north-south line running over the center of the fault for the four cases of heterogeneity in the initial shear tractions. The thick, dashed line indicates the near-source ground motion factor,  $N_v$ , from the 1997 Uniform Building Code.

distance, but the fluctuations in the maximum and minimum values of the coefficient of friction create heterogeneity in the fracture energy. The size and location of the 20 asperities follow the same guidelines as the asperities that we use in the previous section for the initial tectonic strains. We apply the initial shear and normal tractions from scenario unistrain, except that we adjust the height of the shear asperity such that it is 2.0% over the shear stress required for failure. Scenario frictionweak uses the weakly heterogeneous friction model parameters and scenario frictionstrong uses the strongly heterogeneous friction model parameters. Figure 10.67 shows the initial shear stresses, the shear stresses at failure, and the minimum sliding stresses on the fault surface for scenario frictionstrong.

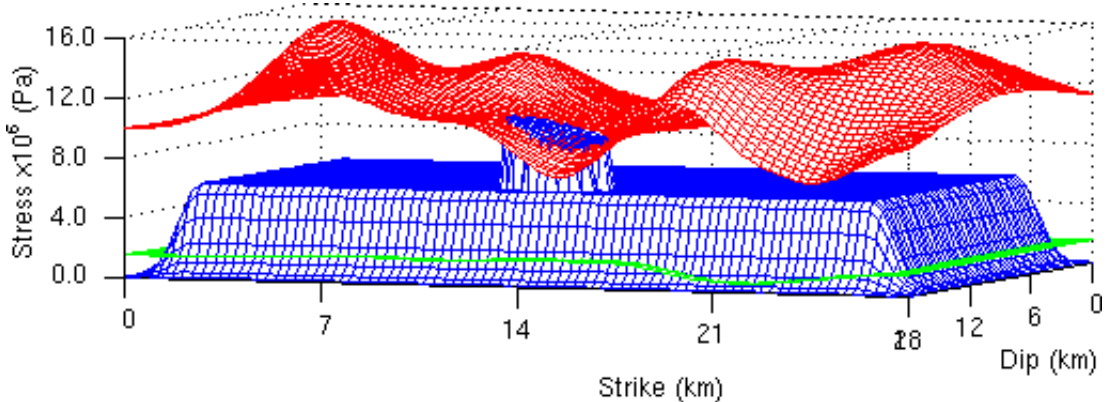


Figure 10.67: Initial (blue), failure (red), and minimum sliding (green) shear stresses on the thrust fault for scenario frictionstrong.

Our strongly heterogeneous failure stresses in scenario frictionstrong degrade the ability of the rupture to propagate and produce an average slip of only 0.83 m. From the distributions of final slip and maximum slip rate in figure 10.68, we find that a large region in the top west corner does not fail. Additionally, the slip along the eastern side of the fault remains relatively low despite the local peak in the maximum slip rate. As in the case of heterogeneity in the tectonic tractions with the slip-weakening friction model, the slip distribution remains relatively homogeneous; the distribution of the maximum slip rate exhibits a greater sensitivity to the heterogeneity than the distribution of final slip.

The heterogeneity in combination with smaller average slips reduces the displacement amplitudes, especially at site S1. Figure 10.69 shows the sharpest shear wave arrival at site S1 occurs in scenario unistrain with the homogeneous parameters in the friction model. As we increase the heterogeneity, the amplitudes decrease and the arrivals become more gradual despite little change in the average rupture speed. Certainly, the reductions in the average slip from 1.2 m in scenario unistrain to 1.0 m and 0.83 m in scenarios frictionweak and frictionstrong reduce the amplitude of the motion. The perturbations in the rupture speed also contribute to the reduction in the amplitude of the motion by disrupting the reinforcement of the shear wave by the rupture. At site S2 we continue to find little variation in the vertical component. We also find the initial portion of the displacement time histories in the north-south direction relatively insensitive to the heterogeneity in the

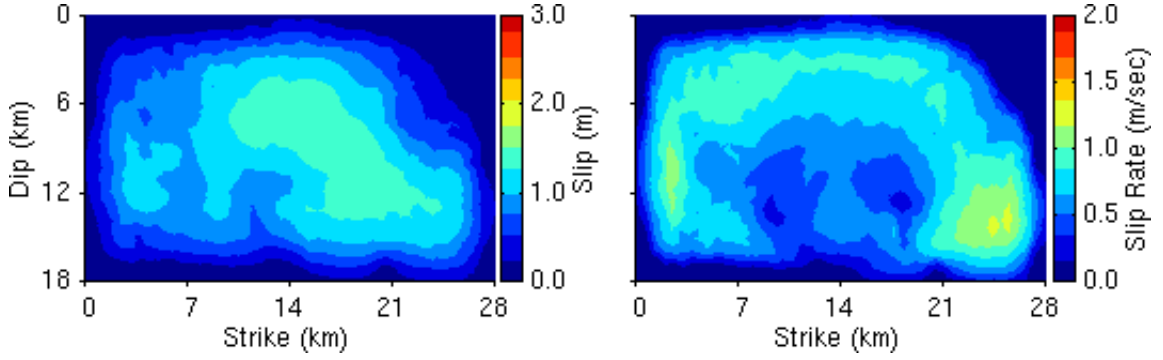


Figure 10.68: Distributions of final slip and maximum slip rate at each point on the thrust fault for scenario frictionstrong.

friction model. The second slip event near the hypocenter in scenario frictionstrong produces significantly less slip than the ones in scenarios unistrain and frictionstrong. This creates the variability in the north-south component towards the central portion of the time history.

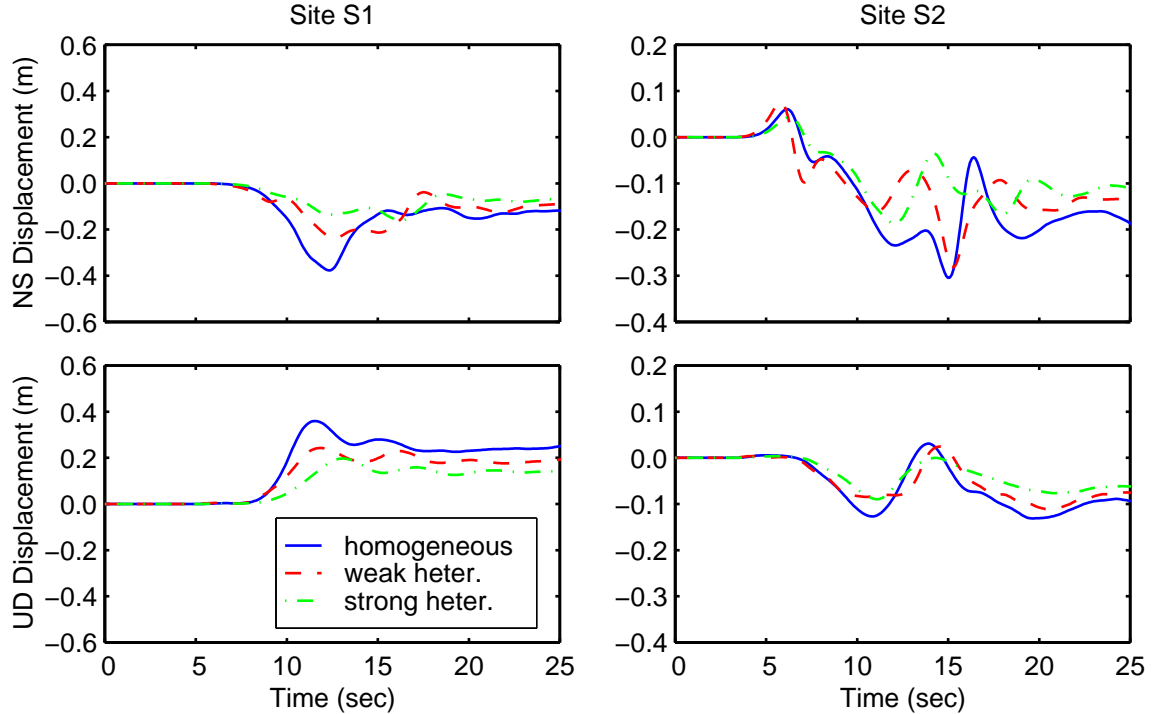


Figure 10.69: Comparison of north-south and vertical displacement time histories at sites S1 and S2 for the three cases of heterogeneity in the parameters of the friction model.

The heterogeneity in the friction model creates moderate perturbations in the shape of the maximum horizontal displacements and velocities along the north-south line that runs over the center of the fault as shown in figure 10.70. Comparing the maximum displacements from scenario frictionweak with those from scenario unistrain, we observe a shift in the peak values towards the north, with the peak value occurring

almost directly above the top of the fault. On the other hand, the peak maximum horizontal displacement for scenario frictionstrong remains at about the same location as that in scenario unistrain. The maximum horizontal velocities display similar trends. The shapes of the curves for scenarios unistrain and frictionstrong match, while the maximum velocities for scenario frictionweak contains a local peak 13 km north of the top of the fault that is not present in the other curves. In general, the maximum displacements and velocities for the homogeneous friction model exceed those from the heterogeneous friction model cases. The near-source curve continues to miss the shape of the maximum displacements and velocities by not extending sufficiently far enough in the up-dip direction.

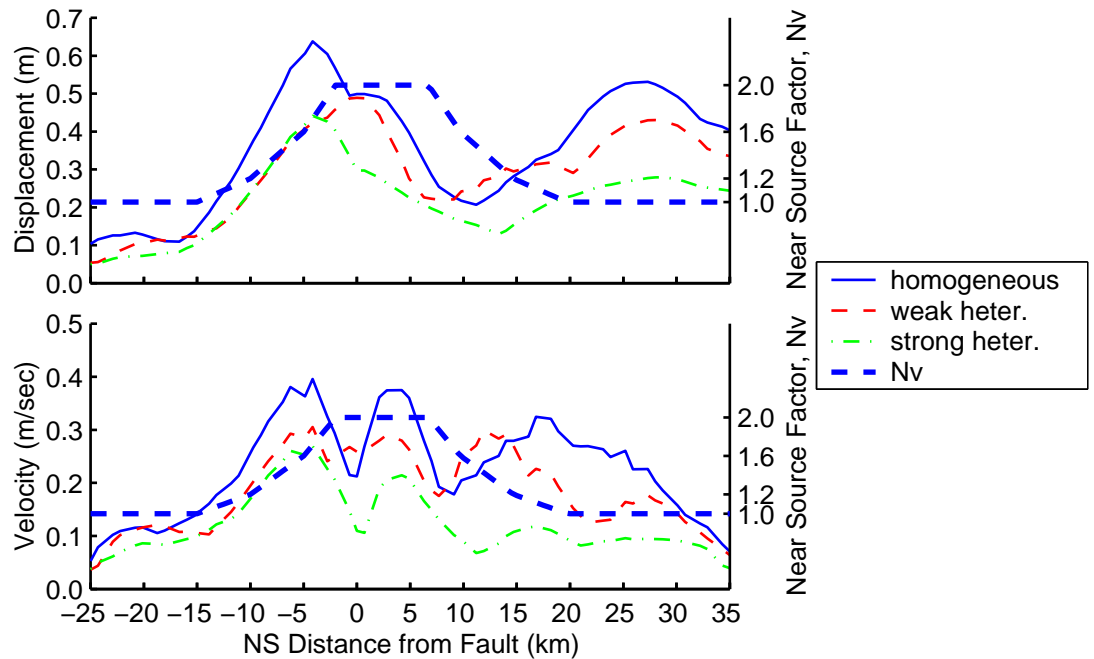


Figure 10.70: Maximum magnitudes of the horizontal displacement and velocity vectors along a north-south line running over the center of the fault for the three cases of heterogeneity in the friction model. The thick, dashed line indicates the near-source ground motion factor,  $N_v$ , from the 1997 Uniform Building Code.

### 10.2.3 Comparison with Prescribed Ruptures

In our analysis of the ground motions during the sensitivity study, we noted some of the similarities and differences between the prescribed ruptures simulations in section 7.2 and the dynamic failure simulations. We will highlight some of the fundamental differences between the prescribed ruptures and the dynamic ruptures by examining a dynamic failure scenario and a prescribed rupture scenario for the case where the top of the fault lies at a depth of 8.0 km and the case where the top of the fault lies at the ground surface.

### **Blind Thrust**

We compare the dynamic failure scenario unistrain2 with the prescribed rupture scenario base, because the rupture features of scenario unistrain2 best fit scenario base. The rupture speed of 88% of the local shear wave speed and peak maximum slip rate of 1.7 m/sec provide a good match to the rupture speed of 80% of the local shear wave speed and uniform maximum slip rate of 1.5 m/sec in scenario base; however, scenario unistrain2 generates an average slip of 1.6 m compared to the 1.0 m slip of scenario base.

Figure 10.71 shows the velocity time histories at site S1 and S2 for both scenarios. At both sites we observe a good match in the general shapes of the time histories for both the north-south and vertical components. In the vertical direction at site S1 the peak velocities differ by less than 15%. Similarly, in the north-south direction the peak negative velocities differ by less than 10%. The narrower velocity pulse for the prescribed rupture scenario creates a peak positive velocity 82% greater than the peak positive velocity in the dynamic failure scenario. This difference corresponds to the direction dependence of the rupture speed in the dynamic failure scenario that we do not include in the prescribed ruptures. The apparent rupture velocity towards site S1 decreases as the rupture becomes more bilateral in nature towards the end of the earthquake. As a result, the energy arrives at site S1 over a longer time interval. This increases the width of the velocity pulse and reduces the peak velocity. At site S2 we find better agreement in the north-south direction than in the vertical direction. Site S2 lies at the epicenter and receives more energy as the rupture becomes more bilateral. Hence, because the bilateral nature of the dynamic rupture increases as it propagates, at site S2 the amplitudes of the motion in the dynamic failure scenario become progressively larger relative to those in the prescribed rupture scenario.

Along the north-south line running over the center of the fault, we observe a close match in the maximum horizontal displacements and velocities as displayed in figure 10.72. The dependence of the rupture speed on the direction of propagation relative to the slip direction has much less impact on the sites near the center of the fault, because they lie close to azimuths of 0 or 180 degrees. As a result, the maximum velocities from scenario unistrain2 exhibit an excellent match with those from scenario base. The larger slip in scenario unistrain2 causes the maximum displacements from the dynamic failure scenario to exceed those from the prescribed rupture scenario. Nevertheless, the shapes of the curves show minimal variation. For both scenarios the peak maximum displacements and velocities occur outside the region where the near-source curve attains its maximum value.

### **Surface Rupture**

When we raise the top of the fault to the ground surface, the low sliding stresses on the fault allow entrainment of the seismic waves above the fault. This generates large slips near the surface and severe ground motion on the hanging-wall side of the surface rupture. The prescribed ruptures do not contain this dynamic interaction between the seismic waves and slip. As we discussed in section 10.2.2, the degree to which this

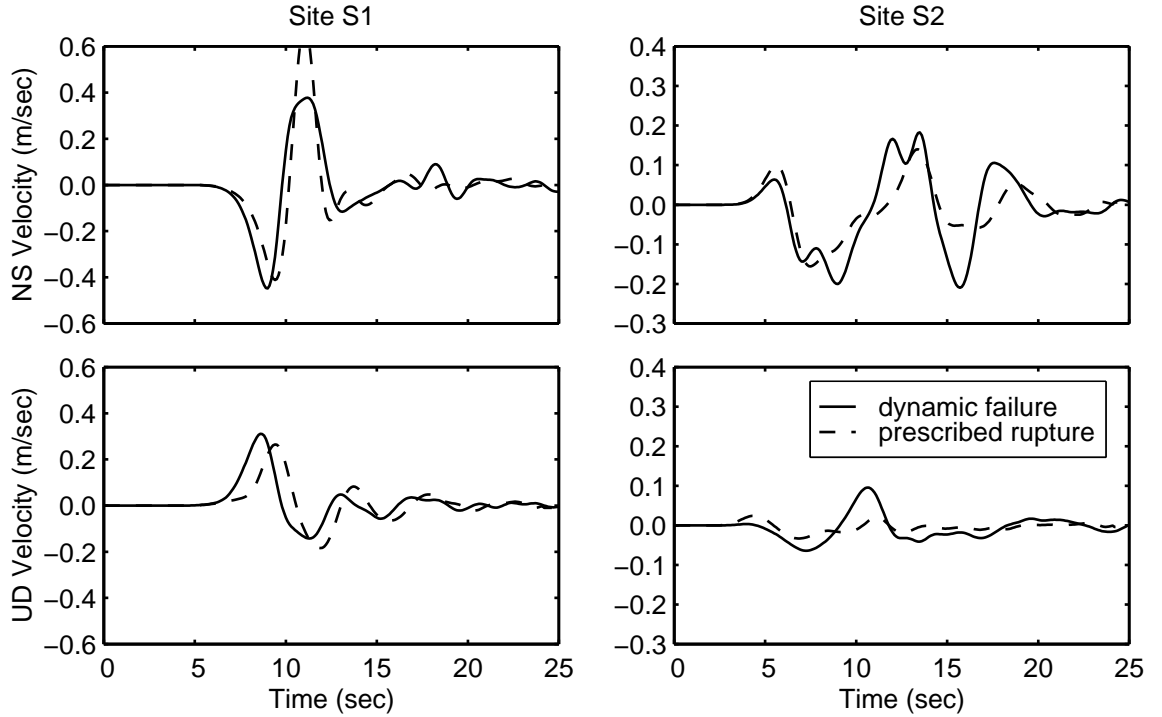


Figure 10.71: Comparison of north-south and vertical velocity time histories at sites S1 and S2 for the dynamic failure scenario unistrain2 and the prescribed rupture scenario base.

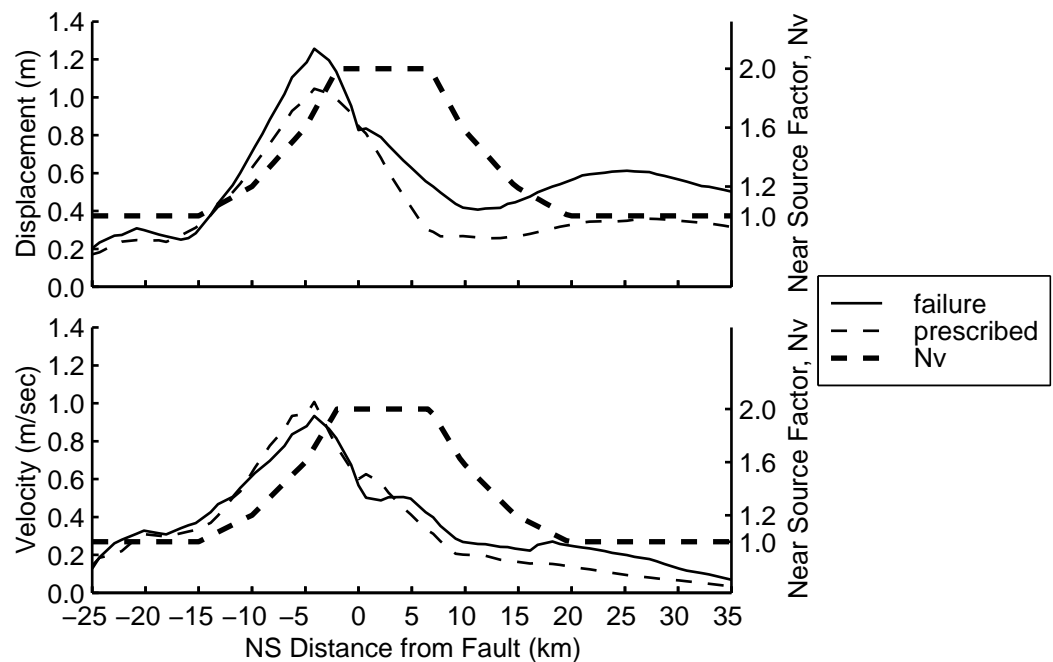


Figure 10.72: Maximum magnitudes of the horizontal displacement and velocity vectors along a north-south line running over the center of the fault for the dynamic failures scenario unistrain2 and the prescribed rupture scenario base. The thick, dashed line indicates the near-source ground motion factor,  $N_v$ , from the 1997 Uniform Building Code.

interaction occurs depends on the width of the rupture front. The slip-weakening friction model, which tends to create wide rupture fronts, accentuates this effect. Consequently, we will compare the dynamic failure scenario combo0km, which uses the slip- and rate-weakening friction model, and the prescribed rupture scenario fault0km to see how the inclusion of the dynamic interaction changes the ground motion. Scenarios combo0km and fault0km have comparable average slips (1.1 m and 1.0 m) and average maximum slip rates (1.1 m/sec and 1.5 m/sec), but scenario combo0km has a much larger peak maximum slip rate (6.1 m/sec compared to 1.5 m/sec).

At site S2 we find little difference in the displacement time histories between the dynamic failure scenario (combo0km) and the prescribed rupture scenario (fault0km). At site S1 we observe no differences in the arrival times of the phases, but the amplitudes differ considerably. The peak displacement in the vertical direction for the prescribed rupture scenario exceeds that of the dynamic failure scenario by 58% (0.41 m compared to 0.26 m). In the north-south direction, we find a larger peak displacement for the dynamic failure scenario (0.82 m) compared to the prescribed rupture scenario (0.56 m). Furthermore, we observe almost no difference between the peak positive and negative displacements for the prescribed rupture, while the peak negative displacement for the dynamic failure simulation is much larger than the peak positive displacement. We attribute this distinct difference in the shape of the waveforms to the dynamic interaction between the seismic waves and the rupture in the dynamic failure scenario. Thus, while the dynamic interaction between the seismic waves and the rupture has little affect on the waveforms away from the surface rupture, it does affect the amplitudes and shapes of the waveforms near the surface rupture.

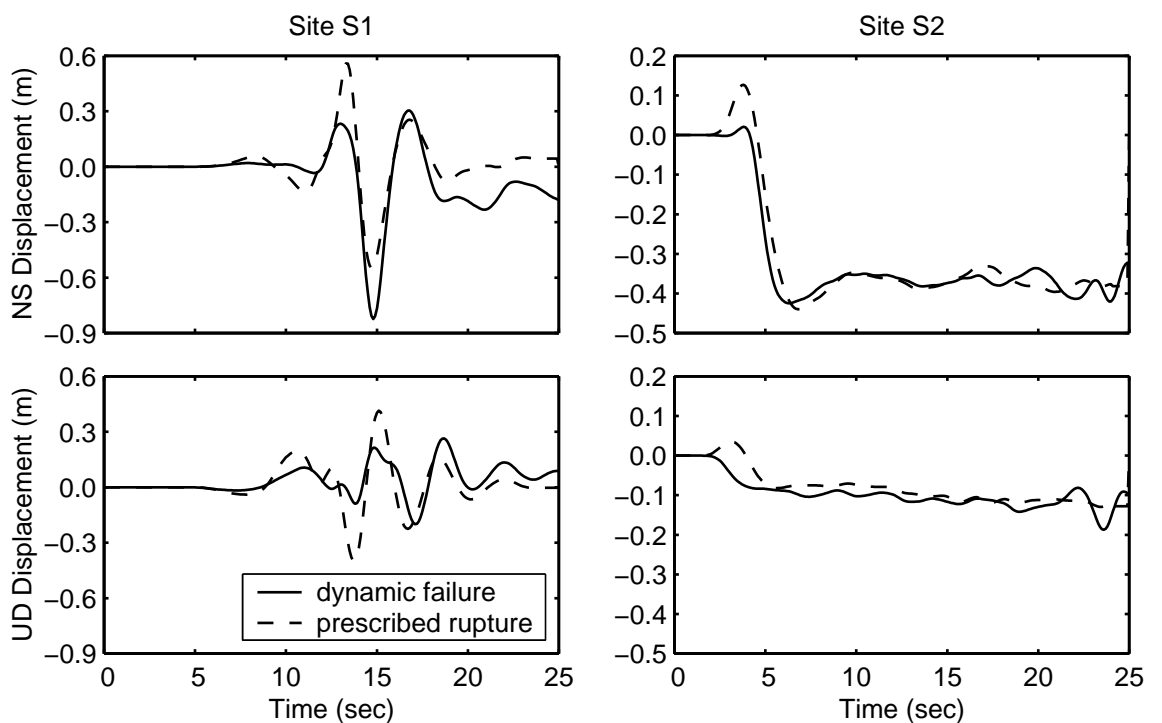


Figure 10.73: Comparison of north-south and vertical displacement time histories at sites S1 and S2 for the dynamic failure scenario combo0km and the prescribed rupture scenario fault0km.

## 10.3 Discussion

### 10.3.1 Summary of Rupture Behavior and Ground Motions

The layered half-space, in contrast to the homogeneous half-space, allows examination of how parameters in the dynamic failure simulations depend on the material properties. This includes distinguishing between application of a uniform strain field and a uniform stress field, and how the coefficient of friction varies with the material properties.

#### Uniform Stress Versus Uniform Strain

The variation of the material properties with depth leads to different distributions of the initial shear tractions on the fault surface depending on whether we apply a relatively uniform stress field or a relatively uniform strain field. On the strike-slip fault with the depth dependence of the coefficient of friction, we find that application of the uniform strain field creates more realistic ruptures. In the simulation with uniform stress, the rupture propagates near the dilatational wave speed and generates slips and slip rates in excess of 10 m and 10 m/sec at the ground surface. On the other hand, in the simulation with uniform strain, the rupture propagates at 88% of the local shear wave speed, and the final slips and maximum slip rates remain below 2.5 m and 1.5 m/sec; however, the rupture fails to reach the ground surface. Of course, the stress state on a fault in the earth evolves over time due to many factors, such as plate tectonics, earthquakes, and viscoelastic creep. It probably looks very different from both a uniform stress field and a uniform strain field. Nevertheless, our simulations lend support for relatively uniform strains with depth compared to relative uniform stresses with depth.

#### Adjustment of Friction Model

We modify the friction model to account for the variation in the material properties with depth, based on the lack of surface rupture that occurs when we apply uniform strains and include only a depth dependence in the friction model. Making the coefficient of friction a function of either the shear wave speed or the square root of the shear modulus introduces reasonable variations with depth of the shear stresses at failure and the shear stresses during sliding. Furthermore, this modification remains consistent with the depth only dependence that we use in the homogeneous half-spaces, because the coefficient of friction depends on the quotient of the square root of the shear modulus and the depth. We adjust the friction model to generate realistic ruptures and adhere to restrictions on the change in thermal energy, but do not invoke any theoretical basis for these modifications. However, a number of mechanisms have been proposed for low dynamic friction during earthquakes (Ben-Zion and Andrews 1998; Melosh 1996; Sleep 1997; Tworzdylo and Hamzeh 1997). This alteration of the friction model moderates the variation of the coefficient of friction with depth in the layered half-space compared to the homogeneous half-space. For example, as we go from a depth of 1.0 km to a depth

of 15.0 km, the coefficient of friction decreases by 93% in a homogeneous half-space, while it decreases by only 80% in the layered-half space. Thus, the increase in the coefficient of friction with the shear modulus partially offsets the decrease in the coefficient of friction with the depth.

### **10.3.2 Sensitivity of Ground Motion to Variations in Parameters**

Using the strike-slip and thrust simulations, we gauge the sensitivity of the ground motions to the variations in the simulation parameters. For those parameters present in both the dynamic failure and prescribed rupture sensitivity studies, we compare the sensitivity of the ground motions from the dynamic failure simulations with those from the prescribed rupture simulations.

#### **Friction Model**

The ground motions exhibit a moderate sensitivity to the introduction of shear re-strengthening in the friction model, i.e., recovery of the coefficient of friction as the slip rates decrease. By increasing the maximum dynamic stress drop when we introduce shear re-strengthening, we preserve the general characteristics of the rupture. As a result, we observe little change in the overall shape of the waveforms. The slip rates increase with the greater maximum dynamic stress drop, which leads to a moderate increase in the velocity amplitudes. The switch from the slip-weakening friction model to either the slip- and rate-weakening friction model or the melting-refreezing friction model has a greater impact on the ground motions for the thrust fault. The location of the hypocenter close to the edge of the thrust fault inhibits the initiation of the rupture. The increase in the dynamic stress drop with the switch in the friction models results in faster initiation of the rupture and larger ground motions. This same behavior does not occur in the simulations with the strike-slip fault, because we place the hypocenter well away from the edges of the fault.

#### **Fault Depth**

The severity of the ground motions increases substantially when we allow the rupture to reach the ground surface. On both the strike-slip and thrust faults the ruptures generate significantly larger slips near the surface than at depth. As the ruptures encounter the reduced resistance to slip approaching the ground surface, the slip and slip rates increase. This leads to a corresponding increase in the amplitudes of the displacements and velocities near the fault. Additionally, when we raise the thrust fault to the surface, the dynamic interaction between low sliding stresses on the fault and the seismic waves above the fault causes large displacements and velocities on the ground surface above the fault. Using a slip-weakening friction model, Oglesby et al. (1998) observed similar behavior during two-dimensional simulations of dynamic failure on a thrust fault subjected to uniform initial stresses in a homogeneous half-space. The slip-weakening friction model which contains no shear re-strengthening accentuates this effect, because it tends to create wide rupture fronts. Using the slip- and rate-weakening friction model, which contains shear re-strengthening, we observe significantly less

dynamic interaction. Nevertheless, we retain asymmetry across the fault plane with much larger ground motions on the hanging wall compared to the footwall. The dependence of the friction model on the material properties exhibits a strong influence on the shallow slip, and our *ad hoc* choice of parameters in the friction model may also accentuate these near-surface effects. However, as in the prescribed ruptures, we find that the depth of the fault displays a strong influence on the ground motions.

### Hypocenter Location

We observe the same trend in the sensitivity of the ground motions to the location of the hypocenter in the dynamic failure simulations that we find in the prescribed rupture simulations. The sensitivity of the ground motions at a given site depends on the relative change in azimuth. As we move the hypocenter location, the ground motions show little variation at sites that remain near the same azimuth. When the azimuth changes significantly with different hypocenter locations, we observe large changes in the ground motions, especially when the site lies near a nodal line for one of the hypocenter locations.

### Initial Shear Tensions

On the thrust fault we find that the ground motions exhibit a strong sensitivity to the level of the initial shear tractions. Increasing the nominal shear traction by 17% with no corresponding increase in the failure stress (or the fracture energy) leads to a 31% increase in the rupture speed and a 200–300% increase in the maximum velocities. We expect that the ground motions display a similar degree of sensitivity to variation of the level of the initial shear tractions on the strike-slip fault. Additionally, introducing heterogeneity into the initial shear tractions generates heterogeneity in the maximum slip rate and variations in the rupture speed. The peak displacements and velocities at sites near regions with larger slip rates tend to increase, but the variation in the rupture speed tends to cause a general decrease in the amplitude of the motion, because it disrupts the reinforcement of the shear wave by the rupture.

At most locations on the ground surface of the strike-slip fault simulations, the general decrease dominates the local increases. These results with heterogeneous maximum slip rates more closely resemble the source parameterization used by Graves (1998) than the prescribed ruptures with heterogeneous slip distributions in chapter 7. As a result, the observed decreases in the maximum displacements and velocities with the introduction of heterogeneity in the initial shear tractions on the strike-slip fault are consistent with the decreases observed by Graves. In the forward direction on the ground surface of the thrust fault simulations, the local increases that we associate with the proximity of the asperities dominate the general decrease that we associate with the disruption of the reinforcement of the shear wave by the rupture.

On both faults replacement of the slip-weakening model with the melting-refreezing friction model leads to a substantial increase in the heterogeneity in the distribution of the final slip. These local changes in slip and slip rate alter the shapes and amplitudes of the time histories. Thus, we find the ground motions exhibit a strong sensitivity to both the level of the initial shear stresses and the degree of heterogeneity. These

observations suggest that shear re-strengthening may play an important role in generating heterogeneous slip distributions. Madariaga and Cochard (1996) suggested that any friction model that produces a large dynamic stress drop compared to the average stress drop will produce heterogeneity in the final shear stress. Ultimately, this will lead to slip heterogeneity. On the other hand, based on kinematic inversions of several recent earthquakes Day et al. (1998) found that heterogeneity in the stress drop alone may generate the heterogeneity in the final slip. Our use of large asperities (3.0–8.0 km in radius) in the initial shear stresses may not provide sufficient heterogeneity in the stress drop to arrest the rupture at a local level when we use the slip-weakening friction model. As a result, the distributions of final slip closely resemble the final slip from a uniform stress drop earthquake. Thus, we cannot dismiss the possibility that the slip-weakening friction model with greater heterogeneity in the initial shear tractions will produce the same level of heterogeneity in the distribution of final slip that is generated by the melting-refreezing friction model which contains shear re-strengthening.

### **Heterogeneity in Friction Model Parameters**

The ground motions generally display less sensitivity to the heterogeneity in the parameters of the friction model than they do to the initial shear tractions. For the strike-slip fault the introduction of weak heterogeneity has negligible impact on the ground motions. On the thrust fault the introduction of the same level of heterogeneity reduces the amplitude of the ground motions. On both faults, the variation in the rupture speed with the strong heterogeneity in the friction model parameters leads to a substantial, general decrease in the peak displacements and peak velocities.

#### **10.3.3 Dynamic Failure versus Prescribed Ruptures**

In the dynamic failure simulations we do not *a priori* know the characteristics of the rupture behavior. In the prescribed ruptures we have complete control over the time histories at each point on the fault, so that we know the behavior of the rupture before running the simulation. Furthermore, many aspects of controlling the rupture still remain a mystery, and reasonable ruptures are often created by trial and error (Madariaga et al. 1998; Olsen et al. 1997). On the other hand, the dynamic failure simulations may generate much more physically realistic ruptures, because the dynamics of the rupture control the rupture speed and slip at each point on the fault; we need to know the initial conditions and the friction model, but not the complex relationships between rupture speed, slip rate, and final slip. Unfortunately, we have only rough estimates of the initial conditions and the friction models.

We find several important differences between the simulations with prescribed ruptures and the simulations with dynamic failure. In the dynamic failure simulations the speed of the rupture depends on the direction of propagation relative to the slip direction. As documented by other researchers, such as Madariaga et al. (1998), the rupture propagates near the shear wave speed in the direction of slip, but at a slower speed

in the direction perpendicular to slip. The absolute and relative speeds in the two directions depend on the fracture energy, but we consistently observe a 20% reduction in the speed of the rupture in the direction perpendicular to the slip compared to the direction parallel to the slip. In the prescribed rupture simulations we assume a uniform rupture speed relative to the shear wave speed. This difference is minimal on long, narrow faults where the direction of slip coincides with the longer dimension, because the rupture propagates along the fault near the shear wave speed. However, when the slip direction is nearly perpendicular to the longer dimension, as is often the case on thrust faults, the rupture propagates near the shear wave speed along the shorter dimension but at a slower speed along the longer dimension. The contrast in rupture speeds in the two directions tends to create a rupture that propagates progressively closer to a right angle from the direction of slip. This reduces the reinforcement of the shear wave by the rupture and decreases the amplitudes of the ground motions at sites away from an azimuth of zero degrees.

When we include heterogeneity in the initial shear stresses (through the tectonic strains) or the shear stresses at failure (through heterogeneity in the friction model parameters), the rupture slows down as it encounters regions farther from failure (where the fracture energy is larger) and speeds up as it encounters regions closer to failure (where the fracture energy is smaller). The degree to which such variations occur depends on the dynamics of the rupture and the state of stress on the fault. Olsen et al. (1997) found similar changes in rupture speed in their simulation of the 1992 Landers earthquake, which used a heterogeneous initial distribution of shear stress. These changes in the rupture speed disrupt the steady reinforcement of the shear wave by the rupture and reduce the amplitude of the ground motions. Additionally, the slip rates increase with the faster rupture speed in regions closer to failure, which in turn generate larger slips. Furthermore, we observe heterogeneity in the final slip only when strong heterogeneity exists in the maximum slip rate. In the prescribed ruptures we allow the rupture to continue propagating at a uniform speed regardless of the heterogeneity in slip. This causes minimal disruption in the steady reinforcement of the shear wave by the rupture. As a result, the ground motions in the dynamic failure simulations exhibit a much stronger sensitivity to introduction of heterogeneity in the slip compared to the prescribed rupture simulations.

The dynamics of the rupture also lead to phenomenon not present in the prescribed ruptures. In most of the strike-slip simulations the rupture reflects off the free surface and generates a second slip event on the fault below. Because the rupture propagates away from the ground surface during this second slip event, it has only a small impact on the ground motions. When we bury the thrust fault, we also observe a second slip event in some of the simulations. The reflection of the dilatational waves off the ground surface generates shear waves that passes through the fault. In some cases the dynamic shear stresses created by the shear waves trigger additional slip near the hypocenter. This creates a significant velocity pulse that we observe late in the time history near the epicenter. When the top of the thrust fault sits at the ground surface, the dynamic interaction between the rupture and the seismic waves causes large ground motions on the hanging wall.

As shown in figure 10.74, the areas subjected to a given level of horizontal displacement or velocity re-

mains nearly the same when we use either prescribed ruptures or dynamic failure. For the strike-slip fault we follow section 10.1.5 and compare the data from the prescribed rupture scenario hymq with the data from the dynamic failure scenario unistrain2, and for the thrust fault we follow section 10.2.3 and compare the data from the prescribed rupture scenario base with the data from the dynamic failure scenario unistrain2. For both the strike-slip and thrust faults we find an excellent match between the curves associated with the maximum velocities. Due to differences in the average slips (2.0 m for scenario hymq versus 1.9 m for scenario unistrain2 for the strike-slip fault, and 1.0 m for scenario base versus 1.6 m for scenario unistrain2 for the thrust fault), the curves associated with the maximum displacements for the thrust fault display less agreement than the curves for the strike-slip fault. The peak maximum horizontal displacements and velocities for the dynamic failure simulations exceed those from the prescribed rupture simulations. This changes the areas where the ground motions exceed a given level only at the most severe levels of motion.

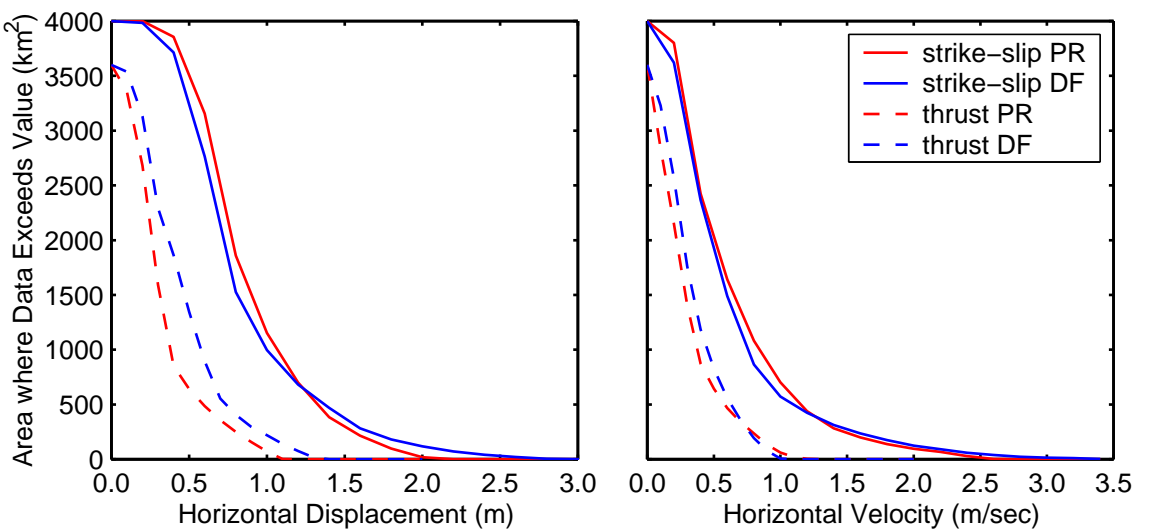


Figure 10.74: Areas on the ground surface in the strike-slip (solid lines) and thrust fault (dashed lines) domains where the maximum horizontal displacements and velocities exceed a given value for prescribed rupture scenarios baseII and base (red) and the dynamic failure scenarios unistrain2 and unistrain2 (blue).

### 10.3.4 Implications for Earthquake Engineering

The simulations with dynamic failure demonstrate several important characteristics of the behavior of earthquake ruptures. Incorporating these characteristics into the prescribed ruptures allows creation of more realistic earthquake simulations without explicitly including the dynamics of the rupture process. With the limited database of strong ground motions, such simulations play an important role in generating ground motions for engineering design. The dependence of the rupture speed on the direction of propagation plays an important role in the ground motions on blind thrust faults, particularly along the lateral edges of the surface projection of the fault. This behavior may be easily incorporated into prescribed ruptures, because the behavior is well defined. Other more complex features that may be difficult to incorporate into the prescribed ruptures include:

the relationship between the maximum slip rate and the rupture speed, and the variation of the rupture speed with heterogeneous slips and slip rates. All of these phenomenon influence the behavior of the rupture and the ground motions. Their inclusion into prescribed ruptures would lead to more physically realistic simulations of earthquakes and more accurate predictions of ground motions.

We revisit our modified near-source factor described in section 7.3.3 to demonstrate that it applies equally well to the thrust fault simulations with dynamic failure. Figure 10.75 reproduces figure 10.58 with the near-source factor from the 1997 UBC replaced by the modified near-source factor for the three fault depths. As in the prescribed ruptures, the peak maximum horizontal displacements and velocities for all three depths of the fault occur near the center of the regions where the corresponding modified near-source factors attain their maximum values. When we apply the 1997 UBC near-source factor to our thrust fault, the peaks generally lie outside this region. Thus, the shape of the modified near-source factor does a better job of matching the general pattern of the severity of shaking for both prescribed rupture simulations and dynamic failure simulations compared to the 1997 UBC near-source factor.

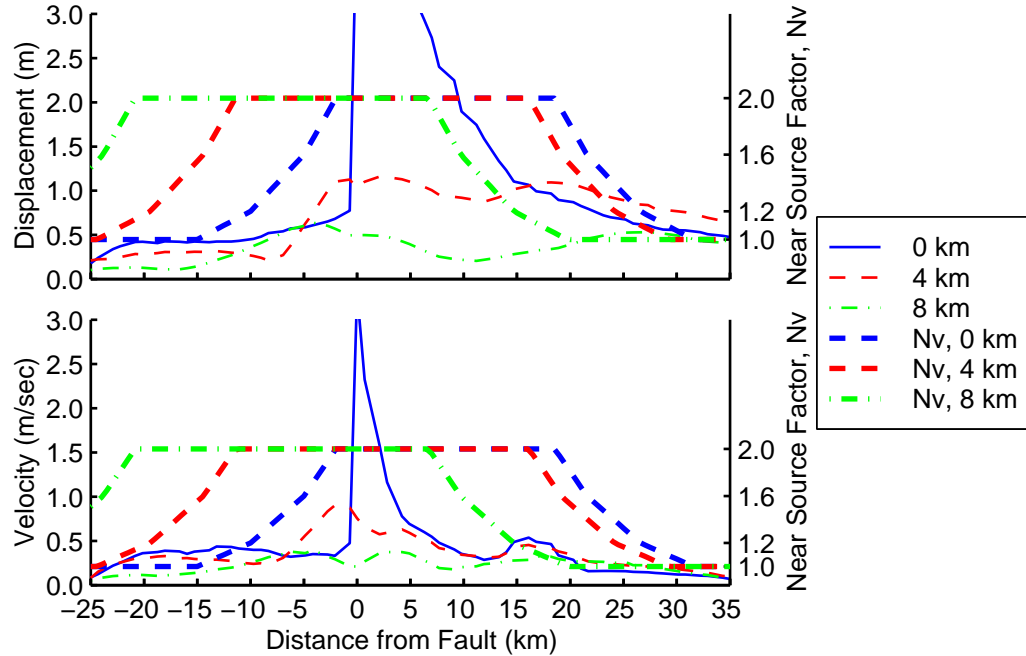


Figure 10.75: Maximum magnitudes of the horizontal displacement vectors and velocity vectors along a north-south line running over the center of the fault for the three depths of the top of the fault. The thick, dashed lines indicate a modified near-source ground motion factor for the three fault depths.

### 10.3.5 Geophysical Implications

Using the strike-slip and thrust fault simulations, we consider how well our earthquakes in the layered half-space fit the proportionality between average stress drop and average slip given by equation (10.13), which

applies to homogeneous half-spaces.

$$\Delta\bar{\sigma} = C\mu \frac{D}{w} \quad (10.13)$$

Using the data from table 10.2 and table 10.4, figure 10.76 shows that the proportionality continues to provide a good description of the relationship. The blue and red lines indicate the average proportionality between the average stress drop and average slip for the simulations on the strike-slip fault and the thrust fault. The blue and red symbols identify the scenarios that we use in determining the proportionality constant. We do not include the scenarios identified by the green symbols, because they correspond to different depths of the fault, which we associate with different proportionality constants. If we use the shear modulus from a depth of 6.0 km, the blue and red lines correspond to  $C = 0.45$  and  $C = 1.5$  in equation (10.13) for the strike-slip fault and the thrust fault. The value of  $C = 0.45$  for the strike-slip fault falls below the value of  $C = 0.7$  from equation (9.1). The difference corresponds to the tendency for the larger slips to occur near the ground surface where the shear modulus and, consequently, the stress drop are smaller. For blind thrust faults no relationships have been found relating the average stress drop to the average slip as a function of the fault dimensions and depth of the top of the fault. As noted by Parsons et al. (1988), the proportionality constant should be less for a thrust fault than for the same sized strike-slip fault, because of the reduction in the relative stiffness above a thrust fault. Equation (9.1) yields a value of  $C$  equal to 1.6 for a deeply buried strike-slip fault with the same dimensions as our thrust fault. Consequently, our value of  $C = 1.5$  falls slightly below that of the strike-slip fault and is consistent with the numerical results of Parsons et al.

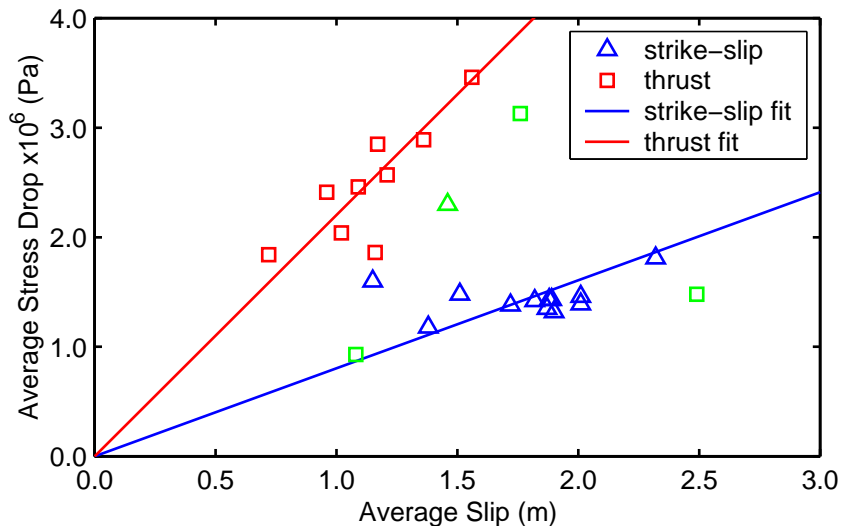


Figure 10.76: Average stress drop as a function of average slip for the scenarios in the sensitivity study with the strike-slip fault (triangle) and the thrust fault (square). The blue and red lines indicate the linear fit created using corresponding blue and red scenarios.

Following the procedure described in chapter 4, we can compute the energy balance for each earthquake

generated using dynamic failure. Restricting our domains to only a small fraction of the earth limits the terms in the energy balance to the change in potential energy, the radiated energy, and the change in thermal energy (which includes the fracture energy). Furthermore, we model the long-period motion, so that we do not include the energy radiated at short periods. In figure 10.77 we display a typical energy balance for a strike-slip simulation (scenario unistrain2) and a thrust fault simulation (scenario unistrain2). On both faults the change in thermal energy generally exceeds the (long-period) radiated energy by a factor of two to three. If we maintain the same dynamic stress drop and distance from failure (fracture energy) but reduce the shear stresses during sliding, the rupture behavior does not change. This leads to smaller changes in the thermal and potential energies with no change in the radiated energy. Because we can determine the general behavior of the rupture from ground motions, the radiated energy is much more severely constrained by data from real earthquakes than either the change in potential energy or the change in thermal energy. Assuming that melting does not occur on the fault surface limits the levels of shear stresses on the fault surface during sliding. Since the shear stresses during sliding determine the change in thermal energy, we may constrain the change in thermal energy by limiting the changes in temperature to values that do not imply melting.

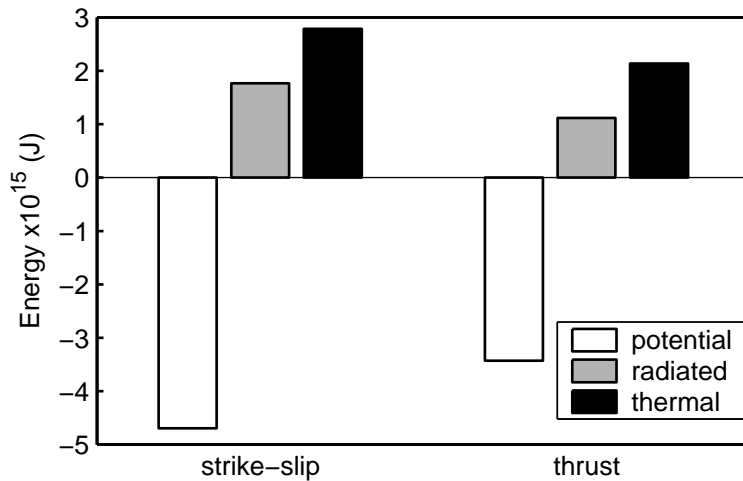


Figure 10.77: Energy balance from the strike-slip and thrust fault scenarios denoted by unistrain2.

With the radiated energies and average slips from the dynamic failure simulations, we revisit the Gutenberg-Richter relationship between radiated energy and magnitude. Figure 10.78 shows the data from the prescribed ruptures scenarios (given in figure 7.64) and the data from the dynamic failure scenarios. Nearly all of the simulations follow the Gutenberg-Richter relationship between the radiated energy and the moment magnitude. The thrust fault simulation with surface rupture and the slip-weakening friction model (the red rectangle on the bottom right) does not fit the relationship, because the dynamic interaction between the rupture and the seismic waves creates very large slips near the surface. The large slips lead to a large moment magnitude. The large area where the dynamic interaction occurs between the rupture and the seismic waves generates much larger slips relative to other earthquakes with the same radiated energy.

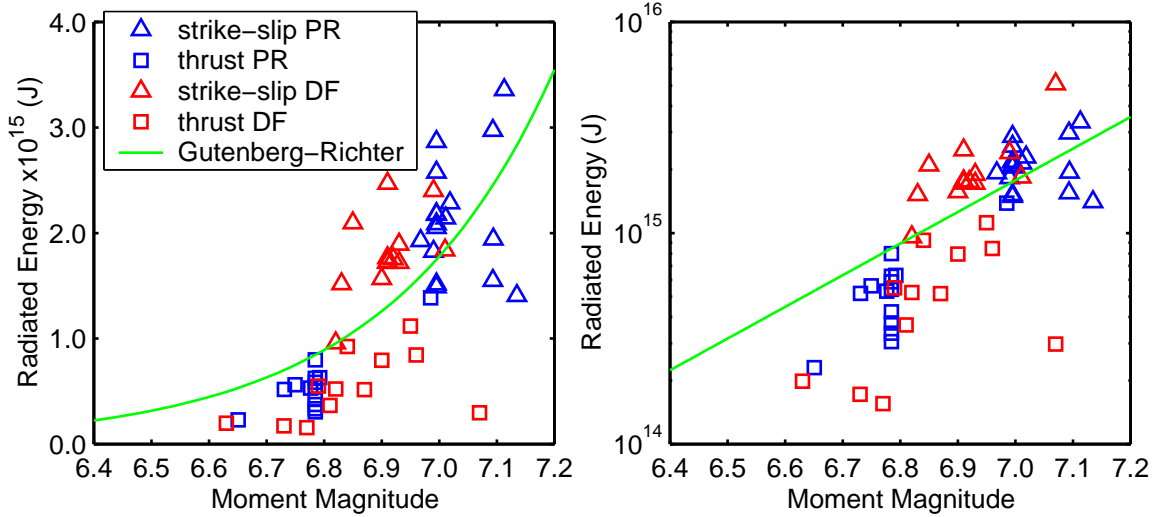


Figure 10.78: Radiated energy as a function of moment magnitude for the strike-slip (triangle) and thrust (square) earthquake simulations with both prescribed ruptures (blue) and dynamic failure (red).

The radiated energies from the strike-slip simulations continue to be slightly larger than those predicted by the Gutenberg-Richter relationship, while the radiated energy from the thrust fault simulations continue to be slightly smaller than those predicted by the Gutenberg-Richter relationship. The scatter of the events about the Gutenberg-Richter relationship appears to be based on the fault geometry (strike-slip versus thrust) with the scatter that falls near the median of the moment magnitude of the simulations centered about the Gutenberg-Richter relationship. This suggests that the radiated energies from the simulations are consistent with those predicted by the Gutenberg-Richter relationship and likely fall within the scatter used in its derivation.

# Chapter 11 Conclusions and Future Work

## 11.1 Conclusions

We simulated the long-period near-source ground motions from earthquakes using both prescribed ruptures and dynamic failure. We modeled the earthquake source by introducing slip degrees of freedom to create dislocations in the finite-element model. For prescribed ruptures we specified the displacement of the slip degrees of freedom to create slip on the fault. In the simulations with dynamic failure, the friction model determined the forces acting on the slip degrees of freedom, and the dynamics of the rupture process controlled the slip on the fault. In both cases the use of slip degrees of freedom allowed arbitrary orientation of the fault plane.

Using prescribed ruptures we examined the sensitivity of the near-source ground motion to variations in the material properties and five earthquake source parameters. The ground motions exhibited the strongest sensitivity to the depth of the rupture and the material properties. The ground motions also showed moderate to strong sensitivities to the rupture speed, the maximum slip rate, and the average slip. Adding heterogeneity to the slip distribution had little impact on the long-period ground motions, especially in the forward direction. Thus, in order to accurately model ground motion, in particular ground motion for engineering design, we must carefully select the values for those parameters that cause the most variability in the resulting ground motion. In all of the simulations, the directivity of the rupture created large displacement and velocity pulses in the forward direction. Additionally, shallow ruptures generated surface waves that caused several cycles of large amplitude motion. When we raised the depth of the fault and maintained the same slip distribution and fault area, the moment magnitude decreased while the ground motions became larger. Consequently, the seismic potency, which does not depend on the shear modulus, provided a slightly better measure of the severity of the shaking.

For strike-slip faults and thrust faults with surface rupture, we found a good match between the severity of the shaking and the shape of the near-source factor from the 1997 Uniform Building Code. On the other hand, for blind thrust faults the region subjected to the most severe shaking fell up-dip from the region where the near-source factor reaches its maximum value. We demonstrated that modifying the near-source factor for blind thrust faults, so that it uses the up-dip projection of the fault plane instead of the top of the fault, extends the region where the near-source factor is at its maximum value. As a result, the region with the maximum near-source factor encompassed the area subjected to the strongest shaking for both strike-slip and thrust faults.

By including the frictional sliding on the fault surface in our simulations, we improved our understanding

of the dynamics of the rupture process. Simulations on a strike-slip fault and a thrust fault demonstrated that it is more realistic to assume that the effective normal stresses increase with depth than remain uniform. In order for ruptures to generate realistic slip distributions under such conditions, the absolute change in the coefficient of friction during sliding must decrease with depth. We found that assuming the coefficient of friction varied inversely with depth and proportionally with either the shear wave speed or the square root of the shear modulus produced reasonable ruptures. Compared to the ground motions from ruptures with the slip-weakening friction model, the velocities from ruptures with either the slip- and rate-weakening or shear melting-refreezing friction models displayed a moderate increase for the same average slip, although the general behavior of the ruptures did not change.

The dynamic failure simulations illustrated several important features of the behavior of ruptures during earthquakes. In the direction of slip the ruptures usually propagated at speeds between 50% and 90% of the shear wave speed, while in the direction perpendicular to slip the ruptures propagated approximately 20% slower. In our prescribed ruptures, we used a uniform rupture speed relative to the shear wave speed. While this difference had minimal impact on the ground motions from strike-slip faults, it tended to increase the amplitude of the ground motions above the lateral sides of the buried thrust fault.

Additionally, the speed of the dynamic rupture changed as it encountered heterogeneity in the distance from failure (fracture energy) and the dynamic stress drop. We found that these changes in the rupture speed had a moderate influence on the ground motions. Locally, the displacements and velocities increased and decreased in response to the changes in the slip and slip rates. The fluctuations in the rupture speed disrupted the reinforcement of the shear wave by the rupture, and generally decreased the amplitude of the motion in the forward direction. Consequently, the ground motions from the dynamics failure simulations exhibited a stronger sensitivity to heterogeneity in the slip than the ground motions from the prescribed rupture simulations. Incorporating these features into prescribed ruptures would allow more realistic simulations of earthquakes without explicitly modeling the rupture dynamics.

Despite these differences between the behavior of the prescribed ruptures and those with dynamic failure, the ground motions displayed many of the same features. In both cases the directivity of the rupture was the principle factor governing the amplitude of the displacements and velocities. We observed relatively minor differences in the shape of the waveforms between the prescribed rupture simulations and the dynamic failure simulations. As expected, when the source parameters from a dynamic rupture resembled those from a prescribed rupture, the ground motions showed excellent agreement.

The radiated energies from both the prescribed rupture simulations and the dynamic failure simulations followed the Gutenberg-Richter energy-magnitude relationship. The strike-slip simulations consistently radiated slightly more energy than that predicted by the Gutenberg-Richter relationship, while the opposite was true for the thrust fault simulations. As in the prescribed rupture simulations, the shape of the near-source factor from the 1997 Uniform Building Code failed to match the distribution of the shaking for the dynamic failure simulations on a blind thrust fault, because the largest maximum displacements and velocities oc-

curred up-dip from the top of the fault. The shape of the modified near-source factor, which uses the up-dip projection of the fault plane in the formulation of the near-source factor, did a better job of matching the general pattern of the severity of the shaking.

## 11.2 Future Work

We still have much to learn about the dynamics of the rupture process. Although the work described above illustrated the qualitative relationships between many of the seismic source parameters, such as dependence of the rupture speed on the slip rate and the dependence of the slip rate on the fracture energy and the dynamic stress drop, quantifying these relationships would lead to more realistic prescribed ruptures and less trial and error in dynamic failure simulations. We also need to test our assumptions of how the coefficient of friction varies with the material properties and depth by attempting to reproduce the rupture dynamics of real earthquakes.

Oglesby et al. (1998) suggested that the ground motions above thrust faults are significantly larger than those above normal faults with the same geometry. However, Oglesby et al. used a homogeneous half-space and uniform effective normal stresses. With our assumptions of how the coefficient of friction varies with the material properties and depth, we need to determine if their observations hold true for more realistic distributions of the material properties and the effective normal stresses. If we find systematic variations in the ground motions between the two types of faults, the building codes may need to be changed to reflect those differences.

Additional work is also necessary to improve our understanding of how ruptures generate the heterogeneous slip distributions that we observe in earthquakes. For different friction models the degree of heterogeneity in the slip distributions may stabilize at different levels with successive simulations of ruptures on the same fault. Although we found that the friction models with shear re-strengthening more efficiently produce heterogeneous slip distributions, based on kinematic inversions of several recent earthquakes, Day et al. (1998) suggested that heterogeneity in the stress drop alone may generate the heterogeneous slip distributions, i.e., ruptures do not require shear re-strengthening to produce heterogeneous slip distributions. Higher resolution simulations with smaller scale heterogeneity in the stress drop may confirm their observations or suggest alternative mechanisms. Investigations in this area will also shed light on whether healing in fault ruptures comes from shear re-strengthening or healing phases emitted by the edges of the fault, i.e., whether faults tend to follow pulse-like behavior or crack-like behavior.

Modeling the friction stresses on fault surfaces has important implications to understanding earthquakes. We can enhance the applicability of the slip degrees of freedom by making the transformation to the slip degrees of freedom local to each degree of freedom. This allows creation of finite-element models with non-planar fault surfaces and arbitrary orientation of any number of fault surfaces. It then becomes possible to model shear and normal stresses on multiple fault surfaces. We can expand on the study of ruptures that prop-

agate along an echelon of faults conducted by Harris and Day (1999) by using realistic fault orientations and curvatures. Including existing three-dimensional topography and density variations will provide constraints on the stress fields. Furthermore, it becomes natural to enforce consistency of the stress field across different faults. Ultimately, this allows modeling of the stress field over a region, such as southern California, and bridging the gap between the inter-seismic and seismic behavior.

## Bibliography

- Bao, H. S., J. Bielak, O. Ghattas, L. F. Kallivokas, D. R. O'Hallaron, J. R. Shewchuk, and J. F. Xu (1998, January). Large-scale simulation of elastic wave propagation in heterogeneous media on parallel computers. *Computer Methods in Applied Mechanics and Engineering* 152(1-2), 85–102.
- Ben-Zion, Y. and D. Andrews (1998, August). Properties and implications of dynamic rupture along a material interface. *Bulletin of the Seismological Society of America* 88(4), 1085–1094.
- Brune, J. N. (1970, September 10). Tectonic stress and spectra of seismic shear waves from earthquakes. *Journal of Geophysical Research* 75, 4997–5009.
- Burridge, R., G. Conn, and L. Freund (1979, May 10). The stability of a rapid mode II shear crack with finite cohesive traction. *Journal of Geophysical Research* 85(B5), 2210–2222.
- California Department of Conservation, Division of Mines and Geology (1998). *Maps of known active fault near-source zones in California and adjacent portions of Nevada: to be used with the 1997 Uniform Building Code*. California Department of Conservation, Division of Mines and Geology. In cooperation with Structural Engineers Association of California, Seismology Committee, International Conference of Building Officials, Whittier, California.
- Chao, B. F. and R. S. Gross (1995, September). Changes in the earth's rotational energy induced by earthquakes. *Geophysical Journal International* 122(3), 776–783.
- Cohen, M. (1980). Silent boundary conditions for transient wave analysis. Technical Report 80-09, California Institute of Technology, Earthquake Engineering Research Laboratory, Pasadena, CA.
- Dahlen, F. (1977). The balance of energy in earthquake faulting. *Geophysical Journal of the Royal Astronomical Society* 48, 239–261.
- Day, S. M., G. Yu, and D. J. Wald (1998, April). Dynamic stress change during earthquake rupture. *Bulletin of the Seismological Society of America* 88(2), 512–522.
- Dieterich, J. (1992, September 30). Earthquake nucleation on faults with rate-dependent and state-dependent strength. *Tectonophysics* 211(1–4), 115–134.
- Freund, L. (1990). *Dynamic Fracture Mechanics*. Cambridge monographs on mechanics and applied mathematics. New York: Cambridge University Press.
- Fukuyama, E. and R. Madariaga (1998, February). Rupture dynamics of a planar fault in a 3D elastic medium: Rate- and slip- weakening friction. *Bulletin of the Seismological Society of America* 88(1), 1–17.

- Fung, Y. C. (1965). *Foundations of Solid Mechanics*. Prentice-Hall international series in dynamics. Englewood Cliffs, NJ: Prentice-Hall.
- Graves, R. W. (1998, August). Three-dimensional finite-difference modeling of the San Andreas fault: Source parameterization and ground-motion levels. *Bulletin of the Seismological Society of America* 88(4), 881–897.
- Hall, J. F., T. H. Heaton, M. W. Halling, and D. J. Wald (1995, November). Near-source ground motion and its effects on flexible buildings. *Earthquake Spectra* 11(4), 569–605.
- Harris, R. and S. Day (1999, July 15). Dynamic 3D simulations of earthquakes on en echelon faults. *Geophysical Research Letters* 26(14), 2089–2092.
- Heaton, T. H. (1979). *Generalized ray models of strong ground motion*. Ph.D. thesis, California Institute of Technology.
- Heaton, T. H. (1990, November). Evidence for and implications of self-healing pulses of slip in earthquake rupture. *Physics of the Earth and Planetary Interiors* 64(1), 1–20.
- Heaton, T. H. (1995). Overview of seismological methods for the synthesis of strong ground motion. In *Proceedings: Modeling Earthquake Ground Motion at Close Distances*, Palo Alto, CA, pp. 15–1 – 15–17. Electric Power Institute. Research Project 3102-04.
- Heaton, T. H. and R. E. Heaton (1989, June). Static deformations from point sources and force couples located in welded elastic Poissonian half-spaces: Implications for seismic moment tensors. *Bulletin of the Seismological Society of America* 79(3), 813–841.
- Heaton, T. H., F. Tajima, and A. Mori (1986, March). Estimating ground motions using recorded accelerograms. *Surveys in Geophysics* 8(1), 25–83.
- Hisada, Y., H. Bao, J. Bielak, O. Ghattas, and D. O'Hallaron (1998, December). Simulations of long-period ground motions during the 1995 Hyogo-Ken Nanbu (Kobe) earthquake using a 3D finite element method. In *2nd International Symposium on Effect of Surface Geology on Seismic Motion*, Yokohama, Japan, pp. 59–66.
- Iwan, W. and X. Chen (1994). Important near-field ground motion data from the Landers earthquake. In *Proceedings of the 10th European Conference on Earthquake Engineering*, Vienna.
- Kamae, K. and K. Irikura (1998, April). Source model of the 1995 Hyogo-Ken Nanbu earthquake and simulation of near-source ground motion. *Bulletin of the Seismological Society of America* 88(2), 400–412.
- Kanamori, H., D. L. Anderson, and T. H. Heaton (1998, February 6). Frictional melting during the rupture of the 1994 Bolivian earthquake. *Science* 279, 839–842.
- Karypis, G., R. Aggarwal, V. Kumar, and S. Shekhar (1999, March). Multilevel hypergraph partitioning:

- Applications in VLSI domain. *IEEE Transactions on Very Large Scale Integration (VLSI) Systems* 7(1), 69–79.
- Langer, J., J. Carlson, C. R. Myers, and B. E. Shaw (1996, April 30). Slip complexity in dynamic models of earthquake faults. *Proceedings of the National Academy of Sciences USA* 93(9), 3825–3829.
- Lay, T. and T. C. Wallace (1995). *Modern global seismology*, Volume 58 of *International geophysics series*. San Diego: Academic Press.
- Madariaga, R. and A. Cochard (1996, April 30). Dynamic friction and the origin of the complexity of earthquake sources. *Proceedings of the National Academy of Sciences of the United States of America* 93(9), 3819–3824.
- Madariaga, R., K. Olsen, and R. Archuleta (1998, October). Modeling dynamic rupture in a 3D earthquake fault model. *Bulletin of the Seismological Society of America* 88(5), 1182–1197.
- Magistrale, H. and S. Day (1999, July 15). 3D simulations of multi-segment thrust fault rupture. *Geophysical Research Letters* 26(14), 2093–2096.
- Marone, C. (1998). Laboratory-derived friction laws and their application to seismic faulting. *Annual Review of Earth and Planetary Sciences* 26, 643–696.
- Melosh, H. (1996, February 15). Dynamical weakening of faults by acoustic fluidization. *Nature* 379(6566), 601–606.
- Oglesby, D. D., R. J. Archuleta, and S. B. Nielsen (1998, May 15). Earthquakes on dipping faults: The effect of broken symmetry. *Science* 280(5366), 1055–1059.
- Olsen, K. and R. Archuleta (1996, June). Three-Dimensional simulation of earthquakes on the Los Angeles fault system. *Bulletin of the Seismological Society of America* 86(3), 575–596.
- Olsen, K., R. Madaraiga, and R. Archuleta (1997, October 31). Three-dimensional dynamic simulation of the 1992 Landers earthquake. *Science* 278, 834–839.
- Parsons, I., J. Hall, and G. Lyzenga (1988, April). Relationships between the average offset and the stress drop for two-dimensional and three-dimensional faults. *Bulletin of the Seismological Society of America* 78(2), 931–945.
- Persson, B. N. (1997). *Sliding Friction: Physical Principles and Applications*. NanoScience and Technology. New York: Springer Verlag.
- Pitarka, A., K. Irikura, T. Iwata, and H. Sekiguchi (1998, April). Three-dimensional simulation of the near-fault ground motion for the 1995 Hyogo-Ken Nanbu (Kobe) earthquake. *Bulletin of the Seismological Society of America* 88(2), 428–440.
- Rao, S. S. (1999). *The finite element method in engineering* (3rd ed.). Boston: Butterworth Heinemann.

- Rice, J. R. and Y. Ben-Zion (1996, April 30). Slip complexity in earthquake fault models. *Proceedings of the National Academy of Sciences USA* 93(9), 3811–3818.
- Rosakis, A., O. Samudrala, and D. Coker (1999, May 21). Cracks faster than the shear wave speed. *Science* 284(5418), 1337–1340.
- Rundle, J. B., S. Gross, W. Klein, C. Ferguson, and D. L. Turcotte (1997, August 15). The statistical mechanics of earthquakes. *Tectonophysics* 277(1–3), 147–164.
- Saikia, C. K. (1993, June). Estimated ground motions in Los Angeles due to  $M_W = 7$  earthquake on the Elysian thrust fault. *Bulletin of the Seismological Society of America* 83(3), 780–810.
- Savage, J. and J. Walsh (1978, December). Gravitational energy and faulting. *Bulletin of the Seismological Society of America* 68(6), 1613–1622.
- Scholz, C. H. (1990). *The mechanics of earthquakes and faulting*. New York: Cambridge University Press.
- Scholz, C. H. (1998, January 1). Earthquakes and friction laws. *Nature* 391(6662), 37–42.
- Sleep, N. H. (1997, February 10). Application of a unified rate and state friction theory to the mechanics of fault zones with strain localization. *Journal of Geophysical Research* 102(B2), 2875–2895.
- Somerville, P., C. Saikia, D. Wald, and R. Graves (1996, February). Implications of the Northridge earthquake for strong ground motions from thrust faults. *Bulletin of the Seismological Society of America* 86(1), S115–S125.
- Tullis, T. E. (1996, April 30). Rock friction and its implications for earthquake prediction examined via models of Parkfield earthquakes. *Proceedings of the National Academy of Sciences USA* 93(9), 3803–3810.
- Tworzydlo, W. W. and O. N. Hamzeh (1997, July 10). On the importance of normal vibrations in modeling of stick slip in rock sliding. *Journal of Geophysical Research* 10(B7), 15091–15103.
- Wald, D. (1996). Slip history of the 1995 Kobe, Japan, earthquake determined from strong motion, teleseismic, and geodetic data. *Journal of Physics of the Earth* 44(5), 489–503.
- Wald, D., D. Helmberger, and T. Heaton (1991, October). Rupture model of the 1989 Loma Prieta earthquake from the inversion of strong-motion and broadband teleseismic data. *Bulletin of the Seismological Society of America* 81(5), 1540–1572.
- Wald, D. J. and R. W. Graves (1998, April). The seismic response of the Los Angeles basin, California. *Bulletin of the Seismological Society of America* 88(2), 337–356.
- Wald, D. J. and T. H. Heaton (1994, June). Spatial and temporal distribution of slip for the 1992 Landers, California, earthquake. *Bulletin of the Seismological Society of America* 84(3), 668–691.
- Wald, D. J., T. H. Heaton, and K. Hudnut (1996, February). The slip history of the 1994 Northridge, California, earthquake determined from strong-motion, teleseismic, GPS, and leveling data. *Bulletin*

*of the Seismological Society of America* 86(1), S49–S70.

Wallace, R. (1984, June). Eyewitness account of surface faulting during the earthquake of 28 October 1983, Borah-Peak, Idaho. *Bulletin of the Seismological Society of America* 74(3), 1091–1094.

Wells, D. and K. Coppersmith (1994, August). New empirical relationships among magnitude, rupture length, rupture width, rupture area, and surface displacement. *Bulletin of the Seismological Society of America* 84(4), 974–1002.

Williams, R. D. (1991, October). Performance of dynamic load balancing algorithms for unstructured mesh calculations. *Concurrency-Practice and Experience* 3(5), 457–481.

Williams, R. D. (1994, August). Unification of spectral and inertial bisection. Unpublished.

Yomogida, K. and T. Nakata (1994, August 15). Large slip velocity of the surface rupture associated with the 1990 Luzon earthquake. *Geophysical Research Letters* 21(17), 1799–1802.